

**CARBON MOLECULAR SIEVE MEMBRANES FOR NATURAL  
GAS SEPARATIONS**

A Dissertation  
Presented to  
The Academic Faculty

by

Mayumi Kiyono

In Partial Fulfillment  
of the Requirements for the Degree  
Doctor of Philosophy in the  
School of Chemical & Biomolecular Engineering

Georgia Institute of Technology  
December 2010

**COPYRIGHT 2010 BY MAYUMI KIYONO**

# **CARBON MOLECULAR SIEVE MEMBRANES FOR NATURAL GAS SEPARATIONS**

Approved by:

Dr. William J. Koros, Advisor  
School of Chemical & Biomolecular  
Engineering  
*Georgia Institute of Technology*

Dr. Satish Kumar  
School of Materials Science & Engineering  
*Georgia Institute of Technology*

Dr. Sankar Nair  
School of Chemical & Biomolecular  
Engineering  
*Georgia Institute of Technology*

Dr. Ronald W. Rousseau  
School of Chemical & Biomolecular  
Engineering  
*Georgia Institute of Technology*

Dr. P. Jason Williams  
Projects and Technology- Innovation,  
Research, and Development  
*Shell Global Solutions (US) Inc.*

Date Approved: September 23, 2010

To whom I love the most:  
my fiancé Manabu and my parents

## ACKNOWLEDGEMENTS

I wish to acknowledge my advisor Dr. William J. Koros who has provided me sincere support, guidance, and encouragement. The lessons I learned from him extend far beyond science and engineering, and he has been invaluable in my growth as a person and a professional. He has set a superb role model for me to follow, and his dedication and strong work ethic have and will always inspire me. I would also like to thank committee members, Dr. Ronald Rousseau, Dr. Sankar Nair, and Dr. Satish Kumar, for their valuable suggestions and comments. The research fund from Shell Global Solutions and numerous discussions with Dr. Arian Nijmeijer and Eric Geers from Shell are greatly acknowledged.

I am also indebted to past group members, Anshu Singh, Cheryl Jones, Keisha Steel, De Vu, Jason Williams, and John Perry for their past work on carbon molecular sieve membranes. Especially I would mention Jason for providing extensive technical opinions and discussions at any time as a committee member/ project sponsor and answering my questions with great patience, long after he graduated. In the early days when I joined the group as an undergraduate student, John, Shu Shu, and Shabbir Husain taught me valuable lessons around the lab and Imona Omole and Wulin Qiu gave me advice on proper polymer synthesis. I would also like to thank JR Johnson, Ryan Adams, Jason Ward, Madhava Kusuri, and Adam Kratochvil, who were always willing to lend a hand. Oguz Karvan, Meha Rungta, Liren Xu, Nitesh Bhuwania, and Xue Ning who joined the project after I did, gave helpful comments from their fresh eyes, and I hope they will find the experience useful in their carbon research. I would also like to thank

Justin Vaughn and Vinod Babu for being supportive towards the end of the study. I would like to thank all past, present and future group members for making this such a great group to be part of.

Finally I wish to thank those who have played a critical role helping me keep my motivation and sanity throughout my stay at Georgia Tech. My fiancé, Manabu Shimobe, has been my strongest supporter and my best friend. He has been extremely encouraging and I cannot imagine completing this without him. The same gratitude goes to my parents for all their love and support. My friends Laura Nunez Patel, Hanae Ishii, Sakurako (Natomi) Honda, and Yuri Sugano were always supportive during the trying times. I am also grateful for my friends at Georgia Tech: Mita Das, Samirkumar Patel, Kaushik Roy Chowdhury, and Anwesha Paladhi were always there for me on good and bad days throughout my PhD work. I will always cherish the time, especially our “coffee sessions”.

# TABLE OF CONTENTS

	Page
ACKNOWLEDGEMENTS	iv
LIST OF TABLES	xii
LIST OF FIGURES	xv
SUMMARY	xii
<u>CHAPTER</u>	
1 INTRODUCTION	1
1.1 NATURAL GAS PROCESSING	1
1.2 MEMBRANES FOR NATURAL GAS SEPARATIONS	3
1.3 OVERVIEW OF MEMBRANE TECHNOLOGY	5
1.4 RESEARCH OBJECTIVES	8
1.5 DISSERTATION OVERVIEW	10
1.5 REFERENCES	11
2 BACKGROUND AND THEORY	13
2.1 OVERVIEW	13
2.2 FUNDAMENTAL GAS TRANSPORT THEORY	13
2.2.1 Transport in membranes	13
2.2.2 Transport in CMS membranes	17
2.2.2.1 Permeation	17
2.2.2.2 Sorption	21
2.2.2.3 Diffusion	22
2.3. STRUCTURE OF CMS MEMBRANES	25
2.4 FORMATION OF CMS MEMBRANES	28

2.4.1 Polymer precursor	28
2.4.2 Pyrolysis temperature	30
2.4.3 Ramp rate	30
2.4.4 Thermal soak time	31
2.4.5 Pyrolysis atmosphere	32
2.5 REFERENCES	35
3 MATERIALS AND EXPERIMENTAL PROCEDURES	38
3.1 INTRODUCTION	38
3.2 MATERIALS	38
3.2.1 Polymer	38
3.2.2 Gases	42
3.3 MEMBRANE FORMATION	43
3.3.1 Formation of polymeric membranes	43
3.3.1.1 Formation of homogeneous films	43
3.3.1.2 Formation of asymmetric hollow fibers: spinning	45
3.3.2 Formation of CMS membranes	50
3.3.2.1 Pyrolysis protocol	50
3.3.2.2 Pyrolysis set-up	50
3.3.2.3 Pyrolysis system cleaning	55
3.4 MEMBRANE CHARACTERIZATION	56
3.4.1 Permeation	56
3.4.1.1 Dense film permeation	56
3.4.1.2 Asymmetric hollow fiber permeation	59
3.4.1.2.1 Hollow fiber pure gas permeation	60
3.4.1.2.2 Hollow fiber mixed gas permeation	62

3.4.2 Sorption	64
3.4.3 Fourier transform infra-red spectroscopy (FTIR)	65
3.4.4 Thermal gravimetric analysis (TGA)	65
3.4.5 Thermal gravimetric analysis connected with FTIR (TGA-IR)	65
3.4.6 Gel permeation chromatography (GPC)	66
3.4.7 Nuclear Magnetic Resonance Spectroscopy (NMR)	66
3.4.8 Differential scanning calorimetry (DSC)	66
3.4.9 Density gradient column	66
3.4.10 Scanning electron microscopy (SEM)	67
3.4.11 Wide angle X-ray diffraction (XRD)	67
3.5 REFERENCES	68
4 DEVELOPMENT OF EFFECTIVE “INERT” PYROLYSIS CONDITIONS FOR ATTRACTIVE CMS MEMBRANES	70
4.1 INTRODUCTION AND OVERVIEW	70
4.1.1 Effect of pyrolysis atmosphere on separation performance of CMS membranes	70
4.1.2 Effect of oxygen exposure on separation performance	71
4.2 EFFECT OF OXYGEN EXPOSURE ON CMS MEMBRANES	73
4.2.1 6FDA/BPDA-DAM CMS membranes	74
4.2.1.1 Weight loss	74
4.2.1.2 Production of flat CMS films	75
4.2.1.3 Correlation between oxygen exposure and consumption	77
4.2.1.4 Correlation between total amount of oxygen exposure and CMS separation performance	81
4.2.2 Matrimid® CMS membranes	86
4.2.2.1 FTIR	86



4.2.2.2 Correlation between oxygen exposure and CMS separation performance	87
4.2.2.2.1 Permeation	87
4.2.2.2.1 Equilibrium sorption	89
4.2.3 Structural differences between 6FDA/BPDA-DAM and Matrimid <sup>®</sup> CMS membranes	94
4.2.3.1 TGA-FTIR	94
4.2.3.2 Sorption isotherms	98
4.2.3.3 “Molecular-ruler”	102
4.2.4 Effect of pyrolysis temperature	106
4.3 EFFECT OF OXYGEN CONCENTRATION ON CMS FORMATION	109
4.3.1 Review	109
4.3.2 Effect of thermal soak time	111
4.3.3 Effect of inert flow rate: external transfer limitation	117
4.3.4 Effect of precursor film thickness: internal transfer limitation	120
4.3.5 Oxygen-carbon reaction mechanism: chemical reaction limitation consideration	122
4.4 POSSIBLE MECHANISM OF OXYGEN “DOPING” PROCESS DURING PYROLYSIS	122
4.5 SUMMARY	126
4.6 REFERENCES	127
5 ASYMMETRIC HOLLOW FIBER CMS MEMBRANES FOR NATURAL GAS (CO <sub>2</sub> /CH <sub>4</sub> ) SEPARATION	131
5.1 OVERVIEW	131
5.2 DEFECT-FREE POLYMER PRECURSOR DEVELOPMENT	132
5.2.1 Defect-free polymeric fiber spinning	132
5.2.2 Pyrolysis of defect-free asymmetric hollow polymeric fibers	136

5.3 EFFECT OF PYROLYSIS ATMOSPHERE ON ASYMMETRIC HOLLOW FIBER CMS MEMBRANES	137
5.3.1 Review	137
5.3.2 Effect of oxygen exposure during pyrolysis process	138
5.3.2.1 Shrinkage	138
5.3.2.2 Correlation between oxygen exposure and consumption	139
5.3.2.3 Correlation between oxygen exposure and CMS separation performance	140
5.4 SUMMARY	145
5.6 REFERENCES	146
6 CHARACTERIZATION OF CMS MEMBRANES UNDER AGGRESSIVE OPERATING CONDITIONS	148
6.1 INTRODUCTION	148
6.2 PRACTICAL CONSIDERATION OF PERMEATE PRESSURE	148
6.3 PRACTICAL CONSIDERATION OF HUMIDITY EXPOSURE	152
6.3.1 Review	152
6.3.2 CMS dense films	153
6.3.2.1 Humidity exposure	153
6.3.2.2 Regeneration study	160
6.3.3 Asymmetric hollow fiber CMS membranes	162
6.4 SUMMARY	166
7 SUMMARY AND RECOMMENDATIONS	169
7.1 SUMMARY AND CONCLUSIONS	169
7.2 RECOMMENDATIONS	171
7.2.1 Properties of CMS membranes	171
7.2.1.1 Morphology	171

7.2.1.2 Physical properties	172
7.2.2 “Other “dopants”	173
7.2.3 “Doping” method for other gas separations	173
7.2.4 Prevention of permeance loss	174
7.2.5 Alternative regeneration method	175
7.2.6 Alternative hydrophobic coating	175
7.2.7 Scale-up of CMS membrane production	176
7.3 REFERENCES	177
APPENDIX A: MANUFACTURE OF LAB-SCALE HOLLOW FIBER MODULES	179
A.1 INTRODUCTION	179
A.2 PARTS	179
A.3 PROCEDURE	180
A.4 REFERENCES	182

## LIST OF TABLES

	Page
Table 1.1: Composition of natural gas required for delivery to the US national pipeline.	1
Table 2.1: Transport properties of asymmetric hollow fiber CMS membranes, adapted from [40].	33
Table 2.2: Summary of transport properties with calculated values of the total oxygen exposure factor, $q_{O_2}$ , adapted from [36].	34
Table 3.1: Chemical structures of polymers used in this work.	39
Table 3.2: Polymer properties used in this work. The decomposition temperature is symbolized as $T_{decomp}$ .	39
Table 3.3: Preliminary screening test results for spinning Matrimid <sup>®</sup> 5218. Syringe tests, which are described by Carruthers [5], were conducted to check the spinnability. Unspinnable polymer was insoluble to any combination of solvent mixtures. The results indicate that molecular weight more than 57K with $2 < PDI < 3.6$ is preferred for hollow fiber spinning.	41
Table 3.4: Kinetic diameters [7] and critical temperatures [8] of gasses used in this work.	42
Table 3.5: List of equipment used to build the pyrolysis system used in this work. Note that equipment marked with “*” indicates that it was purchased by previous Koros group members. Adjustments on the vacuum sealing assembly were made by GTRI machine shop to have vacuum tight fittings with NPT.	53
Table 4.1: Success rates of producing flat CMS dense films under different pyrolysis environments. In parenthesis, the numerator indicates numbers of flat CMS films, depicted in Figure 4.2 (c), and the denominator represents numbers of polymeric films pyrolyzed under the specified conditions.	76
Table 4.2: Langmuir hole filling capacity $C_H'$ and Langmuir affinity constant $b$ calculated based on Matrimid <sup>®</sup> CMS sorption isotherms on Figure 4.11.	90
Table 4.3: Langmuir hole filling capacity $C_H'$ and Langmuir affinity constant $b$ calculated based on Matrimid <sup>®</sup> CMS sorption isotherms on Figure 4.12.	91
Table 4.4: Langmuir hole filling capacity $C_H'$ and Langmuir affinity constant $b$ calculated based on Matrimid <sup>®</sup> CMS sorption isotherms on Figure 4.13.	92

Table 4.5: Langmuir hole filling capacity $C_H'$ and Langmuir affinity constant $b$ calculated based on 6FDA/BPDA-DAM CMS sorption isotherms.	101
Table 4.6: Langmuir hole filling capacity $C_H'$ and Langmuir affinity constant $b$ calculated based on Matrimid <sup>®</sup> CMS sorption isotherms.	101
Table 4.7: Permeability of 6FDA/BPDA-DAM and Matrimid <sup>®</sup> CMS membranes pyrolyzed under 1 ppm O <sub>2</sub> /Ar inert gas. Tests were conducted at 35 °C with a pressure of 50 psia. Units are in Barrer with % deviation of less than 10%.	103
Table 4.8: Sorption coefficients of 6FDA/BPDA-DAM and Matrimid <sup>®</sup> CMS membranes in ccSTP/(ccCMS-psia). Experiments were repeated and had less than 10% of deviation.	103
Table 4.9: Diffusion coefficients of 6FDA/BPDA-DAM and Matrimid <sup>®</sup> CMS membranes in 10 <sup>-8</sup> cm <sup>2</sup> /s. Experiments were repeated and had less than 10% of deviation.	103
Table 4.10: Diffusion selectivity among challenging gas separations. This was referenced to construct ultramicropore size distribution curves.	106
Table 4.11: Normalized values of the total amount of oxygen at different soak time obtained with 6FDA/BPDA-DAM. Inert pyrolysis under 200 cc/min of 7 ppm O <sub>2</sub> /Ar was conducted by eight hours soak time while the other was pyrolyzed for two hours 8 ppm O <sub>2</sub> /Ar. Experiments were repeated and have a standard deviation of less than 10%.	112
Table 4.12: Normalized values of the total amount of oxygen at different soak time obtained with Matrimid <sup>®</sup> . Inert pyrolysis under 200 cc/min of ~30 ppm O <sub>2</sub> /Ar was conducted in both cases. Experiments were repeated and have a standard deviation of less than 10%.	115
Table 4.13: Normalized values of the total amount of oxygen at different inert flow rates of 50 and 200 cc(STP)/min with Matrimid <sup>®</sup> . Inert gas of ~30 ppm O <sub>2</sub> /Ar was used in both cases. Experiments were repeated and have a standard deviation of less than 10%.	118
Table 4.14: Normalized values of the total amount of oxygen with different polymer precursor thickness. Inert gas of ~35 ppm O <sub>2</sub> /Ar was used in both cases. Experiments were repeated and have a standard deviation of less than 10%.	121
Table 5.1: Dope composition of Ultem <sup>®</sup> .	133
Table 5.2: Dope composition of Matrimid <sup>®</sup> .	133

Table 5.3: Optimized spinning conditions for defect-free asymmetric hollow fiber membranes.	134
Table 5.4: Separation performance of Ultem <sup>®</sup> and Matrimid <sup>®</sup> asymmetric hollow fibers. Measurements were repeated and data has less than 5% deviations. CO <sub>2</sub> /CH <sub>4</sub> selectivity from dense film study is also listed as a reference.	136
Table 5.5: Dimensions of Matrimid <sup>®</sup> polymeric and CMS fibers, pyrolyzed under various oxygen exposure. Measurements were the average of three samples, and the deviation was less than 10%.	138
Table 5.6: Amount of oxygen available and consumed during Matrimid <sup>®</sup> asymmetric polymeric hollow fiber pyrolysis process. All was repeated and has standard deviation less than 10%.	139
Table 6.1: CMS membrane performance, pyrolyzed with 1ppm O <sub>2</sub> /Ar, and various permeate pressures. Experiments were conducted at feed pressure of 80 atm with 50/50 CO <sub>2</sub> /CH <sub>4</sub> at 35 °C.	151
Table 6.2: Langmuir hole filling capacity C <sub>H</sub> ' and Langmuir affinity constant <i>b</i> calculated based on Matrimid <sup>®</sup> CMS sorption isotherms on Figure 6.9.	158
Table 6.3: Langmuir hole filling capacity C <sub>H</sub> ' and Langmuir affinity constant <i>b</i> calculated based on Matrimid <sup>®</sup> CMS sorption isotherms on Figure 6.10.	159
Table 6.4: Separation performance of Matrimid <sup>®</sup> CMS membranes evaluated under 50/50 CO <sub>2</sub> /CH <sub>4</sub> mixed gas feed of 80 atm at 35 °C. CMS membranes were prepared by 550 °C with 1ppm O <sub>2</sub> /Ar. Tests were repeated at least twice and deviation was less than 10%.	165
Table A.1: Parts required for manufacture of double-ended lab scale hollow fiber module.	178

## LIST OF FIGURES

	Page
Figure 1.1: Robeson's upper bound for CO <sub>2</sub> /CH <sub>4</sub> separation, adapted from [11], along with a performance of carbon molecular sieve membranes.	4
Figure 1.2: Schematic showing a two stage membrane process to purify a natural gas stream using (a) a cellulose acetate membrane and (b) a yet to be developed high performance membrane [2].	4
Figure 1.3: Principal gas separation membrane module configurations [2].	6
Figure 1.4: Graph representing the surface area/volume achievable in various module types [2].	7
Figure 2.1: Four possible general mechanisms for selective membrane based gas and vapor separations adapted from Koros [8].	14
Figure 2.2: Schematic of CO <sub>2</sub> /CH <sub>4</sub> separation process.	16
Figure 2.3: (a) Idealized gas molecule's equilibrium positions at various locations inside the pore structures and (b) potential energy of penetrants associated with the locations.	21
Figure 2.4: The structure of graphite made of the AB stacking of graphene sheets [22].	25
Figure 2.5: Structures of carbon material, adapted from (a) Jenkins and Kawamura [4] and (b) Pierson [5].	26
Figure 2.6: Idealized "slit-like" carbon structure and bimodal pore size distribution [1-3].	27
Figure 2.7: Transport properties of CMS dense film using two different polyimide precursors. The points on the graph are average of 2-3 samples and the circles around the points represent the spread of data , adapted by [2, 3].	29
Figure 2.8: Transport properties of CMS dense films pyrolyzed with different soak time, adapted from [2].	31
Figure 3.1: Synthesis steps for 6FDA/BPDA-DAM (1:1) polyimide.	40
Figure 3.2: Schematic showing the solution-casting method for dense film production.	44

Figure 3.3: Resulting Matrimid <sup>®</sup> CMS membranes with polymer films casted with (a) a ring on a glass plate and (b) a Teflon dish. While a ring casting associated 44% flat film production rate, the Teflon casting resulted in more than 89% flat film production tested with at least 36 polymeric films.	44
Figure 3.4: SEM images of Matrimid hollow fibers. Characteristic dimensions of the nodular, porous support layer are similar in size to the skin thickness [10].	45
Figure 3.5: Schematic of spinning process for producing asymmetric hollow fiber membranes.	46
Figure 3.6: Ternary phase diagrams of polymer, solvent, and non-solvent for spinning hollow fibers. On this ternary phase diagram, desired dope composition is represented as a star.	47
Figure 3.7: Spinning process depicted on a ternary phase diagram.	48
Figure 3.8: Schematic diagram of the old pyrolysis system.	51
Figure 3.9: Schematic diagram of the new pyrolysis system.	51
Figure 3.10: Flanges with two silicon O-rings for vacuum tightening (MTI Co., CA).	52
Figure 3.11: Baseline after installing a new pyrolysis tube.	54
Figure 3.12: Schematic of a permeation cell. A cross section through the cell is shown with a “sandwich” type masked membrane. The membrane assembly is composed of membrane (yellow), filter paper (light gray), epoxy (brown), adhesive backed aluminum (chechered). Bolts at both ends and O-rings shown by solid black circles assure a leak tight seal [24].	57
Figure 3.13: A schematic of dense film permeation system [24].	58
Figure 3.14: Schematic showing a hollow fiber membrane in a module housing.	60
Figure 3.15: A schematic of the pure gas permeation set-up for asymmetric hollow fiber membranes [6]. In this figure, six modules are connected to the feed and could be tested simultaneously.	61
Figure 3.16: Schematic showing a variable volume system.	63
Figure 3.17: Schematic of pressure decay sorption system used for gas sorption experiments.	64
Figure 4.1: Schematic of oxygen “doping” process during pyrolysis.	72



Figure 4.2: (a) Polymeric films, (b) untestable “curled” CMS films, and (c) flat CMS films.	75
Figure 4.3: Oxygen profile during pyrolysis of 6FDA/BPDA-DAM. A specified amount of oxygen levels in argon gas was used as inert pyrolysis and vacuum pyrolysis was conducted at ~0.005 torr.	78
Figure 4.4: Correlation between the total amount of oxygen and the amount of oxygen consumption normalized by weight of polymer precursors. A linear relationship was observed with $R^2 = 99.7\%$ .	80
Figure 4.5: Separation performance of 6FDA/BPDA-DAM CMS dense films. All were tested at 35 °C. A circular data point represents polymeric properties and square points represent properties of CMS membranes. Pyrolysis atmospheres are indicated with data points for both vacuum and inert pyrolysis. A dash line represents a trend between separation performance and oxygen concentration prior to pyrolysis. The Robeson curve shows the trade-off from currently available polymer [22].	82
Figure 4.6: Trend on CO <sub>2</sub> /CH <sub>4</sub> selectivity as a function of the total amount of oxygen.	83
Figure 4.7: Trend on CO <sub>2</sub> permeability as a function of the total amount of oxygen.	84
Figure 4.8: Hypothetical effective “diffusivity based ultramicropore distribution” along with CMS slit like structures: (a) undoped “intrinsic” structure when pyrolyzed under no oxygen presents, (b) optimal selective structure with adequate amount of oxygen doped, (c) overdoped structure when slightly higher oxygen was introduced during pyrolysis.	85
Figure 4.9: FTIR spectra of Matrimid <sup>®</sup> CMS membranes.	87
Figure 4.10: Separation performance of Matrimid <sup>®</sup> CMS dense films. Tests were conducted at 35 °C with an upstream pressure of ~50 psia. A circular data point represents polymeric properties and square points represent properties of CMS membranes. On vacuum pyrolysis, oxygen concentration was ~1 ppm. A dash arrow line represents a trend between separation performance and oxygen concentration prior to pyrolysis [24]. Experiments were repeated and all had less than 10% deviation.	88
Figure 4.11: Sorption isotherms for Matrimid <sup>®</sup> CMS membranes prepared with 1 ppm O <sub>2</sub> /Ar inert pyrolysis. Test temperature was 35 °C. The experiments were repeated, had deviation less than 5%, and fitted with Langmuir isotherm model described in lines.	90

- Figure 4.12: Sorption isotherms for Matrimid<sup>®</sup> CMS membranes prepared with 30 ppm O<sub>2</sub>/Ar inert pyrolysis. Test temperature was 35 °C. The experiments were repeated, had deviation less than 5%, and fitted with Langmuir isotherm model described in lines. 91
- Figure 4.13: Sorption isotherms for Matrimid<sup>®</sup> CMS membranes prepared with 100 ppm O<sub>2</sub>/Ar inert pyrolysis. Test temperature was 35 °C. The experiments were repeated, had deviation less than 5%, and fitted with Langmuir isotherm model described in lines. 92
- Figure 4.14: Normalized sorption selectivity values of CMS membranes pyrolyzed at 1, 30, and 100 ppm O<sub>2</sub>/Ar. The normalization was based on S<sub>CO<sub>2</sub></sub>/S<sub>CH<sub>4</sub></sub> of 1ppm O<sub>2</sub>/Ar CMS membranes. 93
- Figure 4.15: TGA-FTIR result of 6FDA/BPDA-DAM [23]. 95
- Figure 4.16: TGA-FTIR result of Matrimid<sup>®</sup> [24]. 95
- Figure 4.17: Schematic of folded graphite-like layers (top) [27] and graphene sheets (bottom): (a) the carbon atoms in the dotted circles are removed by electron beam, and (b) four dangling bonds are saturated by hydrogen (cyan), while the other four dangling bonds together with their carbon atoms are replaced by nitrogen atoms (green). The pore electron density isosurface of the nitrogen functionalized porous graphene presumably has 3.0 Å pore window, adapted from [28]. 97
- Figure 4.18: Sorption isotherms for 6FDA/BPDA-DAM CMS membranes prepared with 1 ppm O<sub>2</sub>/Ar inert pyrolysis. The isotherms were obtained with six different gases: ○ CO<sub>2</sub>, ● CH<sub>4</sub>, ■ O<sub>2</sub>, □ N<sub>2</sub>, △ He, ▲ SF<sub>6</sub>. The experiments were repeated, had less than 5% of deviations, and fitted with Langmuir isotherm model described in dot lines. 99
- Figure 4.19: Sorption isotherms for Matrimid<sup>®</sup> CMS membranes prepared with 1 ppm O<sub>2</sub>/Ar inert pyrolysis. The isotherms were repeated and obtained with six different gases: ○ CO<sub>2</sub>, ● CH<sub>4</sub>, ■ O<sub>2</sub>, □ N<sub>2</sub>, △ He, ▲ SF<sub>6</sub>. The experiments were repeated, had less than 5% of deviations, and fitted with Langmuir isotherm model described in dot lines. 100
- Figure 4.20: Diffusion coefficient based ultramicropore size distribution. The dot line represents the distribution of 6FDA/BPDA-DAM CMS membrane and the solid line represents the distribution of Matrimid<sup>®</sup> CMS membranes. The x-axis is linearly scaled with an indication of molecule's kinetic diameters. 105
- Figure 4.21: Effect of pyrolysis temperature reported by Steel [8]. All data was from vacuum pyrolysis. 107

- Figure 4.22: Separation performance of Matrimid<sup>®</sup> CMS membranes pyrolyzed by different temperatures, 500 and 500 °C, with oxygen “doping” process. Oxygen concentration in argon inert is listed. A dot line represents a trend observed for CMS films pyrolyzed at 500 °C. All data were repeated and had deviation of less than 10%. 108
- Figure 4.23: Correlation between the total amount of oxygen and the amount of oxygen consumption normalized by weight of polymer precursors. Circles (●) represent data of two hour thermal soak time from previous study [37], and the rectangular (□) represents data of eight hour thermal soak time. Inert compositions are listed along with data points. The data with longer thermal soak time falls within the trend seen with two hour soak time [47]. 113
- Figure 4.24: Separation performance of 6FDA/BPDA-DAM CMS films. A filled circle (●) represents CMS pyrolyzed with eight hour thermal soak time, and open circles (○) represent CMS pyrolyzed with two hour soak time. Each was repeated at 35 °C [47]. 114
- Figure 4.25: Separation performance of Matrimid<sup>®</sup> CMS films pyrolyzed with two different thermal soak times of two hours (●) and eight hours (○). The thickness of the films was ~80 μm. Inert carrier of ~30 ppm O<sub>2</sub>/Ar was used with a flow rate of 200 cc(STP)/min. All was repeated at 35 °C[47]. 116
- Figure 4.26: Schematic of experiments to investigate external transfer limitation by applying two different inert flow rates. Total of ~0.02g polymeric films,  $m_1 + m_2 = m_3 + m_4$  were pyrolyzed at 550 °C with two hour soak time. Experiments were repeated twice. 117
- Figure 4.27: Separation performance of Matrimid<sup>®</sup> CMS films pyrolyzed with two different inert flow rates of 200 (●) and 50 (○) cc(STP)/min. Inert carrier of ~30 ppm O<sub>2</sub>/Ar was used. All was repeated at 35 °C. 119
- Figure 4.28: Schematic design of experiments testing the internal mass transfer limitation. About 0.02g of polymer precursor,  $m_1 + m_2 = m_3$ , was prepared. Gas mixture of argon and a slightly higher than 30 ppm of oxygen in argon gas was used as an inert with the flow of 200 cc(STP)/min. Experiments were repeated twice. 120
- Figure 4.29: Separation performance of Matrimid<sup>®</sup> CMS films pyrolyzed with two different precursor thickness, 60 (●) and 120 (○) μm. Inert carrier of ~35 ppm O<sub>2</sub>/Ar was used. All was repeated at 35 °C. 121
- Figure 4.30: Possible carbon-oxygen reactions suggested by Marsh et al. [12]. In the temperature of the interests, the O<sub>2</sub> adsorption dominates the reaction [15, 48]; therefore, there is no actual carbon loss with “O<sub>2</sub> doping” CMS production. 123

Figure 4.31: Carbon-oxidation equilibrium reactions.	123
Figure 5.1: SEM images of asymmetric hollow fiber precursors: Ultem <sup>®</sup> (top) and Matrimid <sup>®</sup> (bottom).	135
Figure 5.2: SEM images of asymmetric hollow fiber CMS membranes: Ultem <sup>®</sup> CMS fiber (left) and (b) Matrimid <sup>®</sup> CMS fiber (right).	136
Figure 5.3: Separation performance of Matrimid <sup>®</sup> CMS membranes using 50/50 CO <sub>2</sub> /CH <sub>4</sub> mixed gas with $P_{\text{feed}} = 80$ atm and $P_{\text{permeate}} = 1$ atm at 35 °C. Stage cut less than 1% was used.	140
Figure 5.4: Comparison between Matrimid <sup>®</sup> CMS film and asymmetric hollow fiber membranes tested at 35 °C. The red circles represent transport properties obtained on asymmetric hollow fiber membranes with 50/50 CO <sub>2</sub> /CH <sub>4</sub> mixed gas of $P_{\text{feed}} = 80$ atm and $P_{\text{permeate}} = 1$ atm, and the blue lines represent properties based on dense film experimental data obtained with single gas feed of ~3 atm. The permeability of the dense films was converted to a unit of permeance with 30 to 100% skin thickness of the 40µm wall. Robeson curves were converted with assumption of 0.1 to 10 µm of fiber skin thickness. Rectangular points represent separation performance of cross-linked PDMC. The filled point was measured at 35 °C with 10/90 CO <sub>2</sub> /CH <sub>4</sub> mixed gas of $P_{\text{feed}} = 57$ atm and $P_{\text{permeate}} = 1$ atm, and the open was measured with 100 ppm toluene exposure [16].	141
Figure 5.5: Comparison of CO <sub>2</sub> /CH <sub>4</sub> selectivity between experimental (asymmetric hollow fibers) and model (dense films) made under 50/50 CO <sub>2</sub> /CH <sub>4</sub> mixed gas at a feed pressure of 80 atm at 35 °C.	144
Figure 6.1: Calculated permeate CO <sub>2</sub> concentration as a function of selectivity with various pressure ratios ( $R$ ). The feed CO <sub>2</sub> concentration is 50%.	150
Figure 6.2: Schematic of fiber permeation system modified to measure separation performance with various permeate pressures.	151
Figure 6.3: Schematic of a humidity controlled sample box.	154
Figure 6.4: Matrimid <sup>®</sup> CMS dense films exposed to humidified conditions.	154
Figure 6.5: Effect of humidity during ageing process on normalized CO <sub>2</sub> permeability values ( $P_{\text{CO}_2}/P_{\text{CO}_2,0}$ ). $P_{\text{CO}_2,0}$ of 6FDA/BPDA-DAM CMS was 7169 Barrer and $P_{\text{CO}_2,0}$ of Matrimid <sup>®</sup> CMS was 1050 Barrer. The experiments were conducted at 35 °C. They were repeated and had less than 10% deviation.	155

Figure 6.6: Effect of humidity during ageing process on normalized CO <sub>2</sub> /CH <sub>4</sub> selectivity. $\alpha_0$ of 6FDA/BPDA-DAM CMS is 31 and $\alpha_0$ of Matrimid <sup>®</sup> CMS is 48. The experiments were repeated and had less than 10% deviation.	156
Figure 6.7: Possible explanation of water adsorption taking place after a week.	157
Figure 6.8: Possible explanation of water adsorption taking place after 1 month.	157
Figure 6.9: CO <sub>2</sub> sorption isotherm for Matrimid <sup>®</sup> CMS membranes with different levels of humidity exposure: 80% RH vs. in vacuum (~0% RH) in a month. The experiment was conducted at 35 °C.	158
Figure 6.10: CH <sub>4</sub> sorption isotherms of Matrimid <sup>®</sup> CMS membranes with different levels of humidity exposure: 80% RH vs. in vacuum (~0% RH) in a month. The experiment was conducted at 35 °C.	159
Figure 6.11: Recovery from humidity effect on CO <sub>2</sub> permeability of CMS membranes. Data in red represents separation properties of regenerated CMS membranes.	160
Figure 6.12: TGA profile of 6FDA/BPDA-DAM CMS membranes exposed to 80%RH for 1 month.	161
Figure 6.13: Schematic of the permeation system used to measure separation performance of asymmetric hollow fiber CMS membranes under humidified feed conditions.	163
Figure 6.14: Chemical structure of Teflon AF2400 which consists of m:n mole fraction of 87:13 [9, 10].	163
Figure 7.1: Matrimid <sup>®</sup> CMS fibers twisted to depict its flexibility.	172
Figure 7.2: Example of hydrocarbon dendrimers: (left) chemical structure and (right) space-filling molecular model [22].	176
Figure A.1: Picture of fiber modules in production: (a) Parts for a “blank” module, (b) the “blank” module, (c) a brass male adapter with Tygon tubing piece, and (d) the final module for permeation tests.	182

## SUMMARY

A new innovative polymer pyrolysis method was proposed for creation of attractive carbon molecular sieve (CMS) membranes. Oxygen exposure at ppm levels during pyrolysis was hypothesized and demonstrated to make slit-like CMS structures more selective and less permeable, which is contrary to one's expectation. Indeed prior to this work, any exposure to oxygen was expected to result in removal of carbon mass and increase in permeability. The results of this study indicated that the separation performance and CMS structure may be optimized for various gas separations by careful tuning of the oxygen level. This finding represents a breakthrough in the field of CMS membranes. Simple replacement of pyrolysis atmospheres from vacuum to inert can enable scale-up. The deviation in CMS membrane performance was significantly reduced once oxygen levels were carefully monitored and controlled. The method was shown to be effective and repeatable not only with dense films but also with asymmetric hollow fiber membranes. As a result, this work led the development of the “inert” pyrolysis method which has overcome the challenges faced with previously studied pyrolysis method to prepare attractive CMS membranes.

The effect of oxygen exposure during inert pyrolysis was evaluated by a series of well-controlled experiments using homogeneous CMS dense films. Results indicated that the oxygen “doping” process on selective pores is likely governed by equilibrium limited reaction rather than (i) an external or (ii) internal transport or (iii) kinetically limited reaction. This significant finding was validated with two polyimide precursors: synthesized 6FDA/BPDA-DAM and commercial Matrimid<sup>®</sup>, which implies a possibility

of the “inert” pyrolysis method application extending towards various precursors. The investigation was further extended to prepare CMS fibers. Despite the challenge of two different morphologies between homogeneous films and asymmetric hollow fibers, the “inert” pyrolysis method was successfully adapted and shown that separation performance can be tuned by changing oxygen level in inert pyrolysis atmosphere. Moreover, resulting CMS fibers were shown to be industrially viable. Under the operating condition of ~80 atm high pressure 50/50 CO<sub>2</sub>/CH<sub>4</sub> mixed gas feed, the high separation performance of CMS fibers was shown to be maintained. In addition, elevated permeate pressures of ~20 atm did effect the theoretically predicted separation factor. While high humidity exposures (80%RH) resulted in reduced permeance, high selectivity was sustained in the fibers. Recommendations to overcome such negative effects as well as future investigations to help CMS membranes to be commercialized are provided.

# CHAPTER 1

## INTRODUCTION

### 1.1 NATURAL GAS PROCESSING

According to Baker and Lokhandwala, consumption of natural gas in the United States is around 22 trillion scf/yr and around 95 trillion scf/yr worldwide (scf is defined as standard cubic feet) [1]. Natural gas is one of the fastest growing energy sources because it is abundant and relatively cleaner than liquid fossil fuels or coal [1]. Raw natural gas contains methane with various impurities, such as carbon dioxide, hydrogen sulfide, water, heavy hydrocarbons, and inert gases [1, 2], and these impurities must be removed to meet pipeline standards for the natural gas to be fed to the mainline gas transportation system. The specifications are shown in Table 1.1.

Table 1.1: Composition of natural gas required for delivery to the US national pipeline [3].

Component	Specification
CO <sub>2</sub>	<2 %
H <sub>2</sub> O	<120 ppm
H <sub>2</sub> S	<4 ppm
C <sub>3+</sub>	95-1050 Btu/scf
Content	Dew point, -20 °C
Total inert (N <sub>2</sub> , CO <sub>2</sub> , He, etc)	<4 %



Among the natural gas impurities, CO<sub>2</sub> is usually the most abundant and can be above 50% in some cases [1, 4]. In enhanced oil recovery application, CO<sub>2</sub> contents can be >70% of the natural gas stream [5]. The removal of CO<sub>2</sub> is usually an important step and it became the main focus of this research. The presence of H<sub>2</sub>O and acid gases such as CO<sub>2</sub> and H<sub>2</sub>S may cause corrosion in pipelines; thus their removal is essential to the functioning of a stable pipeline network grid. Moreover, removal of non-fuel gases like CO<sub>2</sub> and N<sub>2</sub> increases heating value of the natural gas which can reduce compression cost required for the gas transportation.

Currently, separation technologies, specifically for CO<sub>2</sub> removal from natural gas, include various absorption processes, such as Benfield<sup>TM</sup> process (hot potassium carbonate solutions) and Amine Guard-FS<sup>TM</sup> processes (formulated solvents), cryogenic distillation, adsorption processes, such as pressure swing adsorption (PSA) and thermal swing adsorption (TSA), and membranes [6]. Cryogenic distillation is an energy intensive process since the gas must be cooled to very low temperatures to achieve a separation [7]. Amine absorption processes are currently well accepted and are considered the standard for such applications because they have been used extensively in the past with success [8]. Despite these facts, the capital and maintenance costs associated with these absorption units can be high since the size of the absorption tower and the amount absorbent liquid required scales with the amount of CO<sub>2</sub> that must be removed [1]. Moreover, additional costs are associated with regeneration of the solvents used in the absorption processes; and the environmental restrictions on the disposal of such solvents make the processes more cumbersome especially where the level of CO<sub>2</sub> to be removed is high.

While each processes has its own advantages and disadvantages, membranes are excellent candidates for applications that have large flows, have high CO<sub>2</sub> contents, or are in remote locations. The high CO<sub>2</sub> content typical of raw natural gas wells makes the

current amine technologies less competitive and gives membranes an opportunity to prove itself as a viable technology for the future [1].

## **1.2 MEMBRANES FOR NATURAL GAS SEPARATIONS**

Membrane systems are attractive over the other, rather traditional, separations methods, due to their lower cost, lower energy consumption, smaller size, and smaller environmental impact. Membrane systems require lower capital cost since site preparation are minimal and the installation costs are significantly lower than alternative technologies, especially for remote areas. Membrane units do not require the additional facilities, such as solvent storage and water treatment, required by other processes, which saves capital cost as well. Another advantage is the lower operating cost because the only major operating cost for single-stage membrane systems is membrane replacement [6]. Membranes systems have high adaptability. It should be also noted that membrane systems are environmentally friendly because they do not involve periodic removal and handling of spent solvents or adsorbents. Permeate gases can be flared, used as fuel, or reinjected into well [6] in many cases.

Polymer membranes have gained attention as a separation material due to the processability of polymers and their inherent permselectivity for different molecules. The transport properties of these glassy polymer membranes can be tailored by introducing packing-inhibiting bulky groups and intrinsically rigid linkages in the polymer backbone [9, 10]. However, the separation performance of these polymeric membrane materials has stagnated at an “upper bound curve” trade-off [11] relating CO<sub>2</sub> permeability and CO<sub>2</sub>/CH<sub>4</sub> selectivity as shown in Figure 1.1. This trade-off can result in relatively high methane loss associated with removing high amount of CO<sub>2</sub>. Expensive cost also associates with the compressors for recycle stream as shown in Figure 1.2.

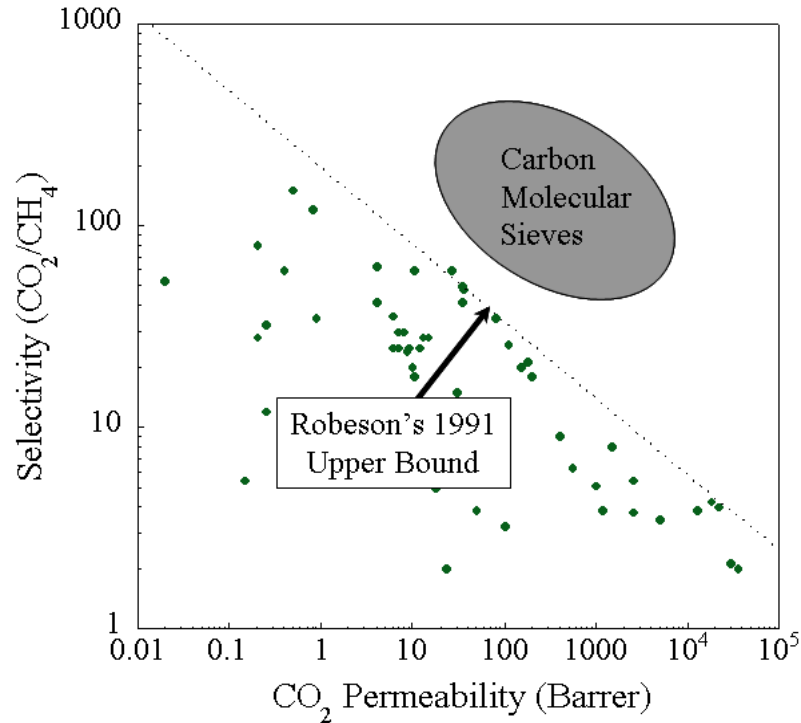
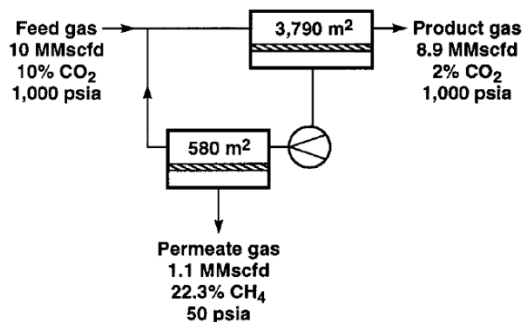


Figure 1.1: Robeson's upper bound for CO<sub>2</sub>/CH<sub>4</sub> separation, adapted from [11], along with a performance of carbon molecular sieve membranes.

**(a) Cellulose Acetate Membranes**

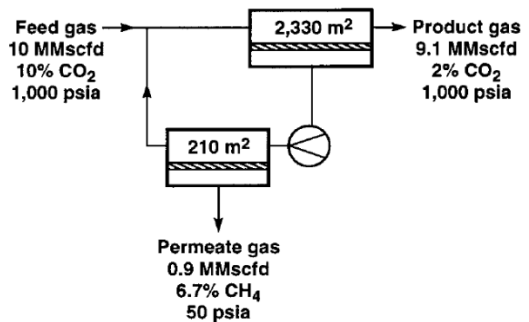
CO<sub>2</sub> flux:  $50 \times 10^{-6} \text{ cm}^3(\text{STP})/\text{cm}^2 \cdot \text{s} \cdot \text{cmHg}$   
CO<sub>2</sub>/CH<sub>4</sub> selectivity: 15



Membrane area 4,290 m<sup>2</sup>  
Compressor load 547 hp (theoretical)  
Methane loss 2.6% of feed methane

**(b) High Performance Membranes**

CO<sub>2</sub> flux:  $100 \times 10^{-6} \text{ cm}^3(\text{STP})/\text{cm}^2 \cdot \text{s} \cdot \text{cmHg}$   
CO<sub>2</sub>/CH<sub>4</sub> selectivity: 40



Membrane area 2,540 m<sup>2</sup>  
Compressor load 346 hp (theoretical)  
Methane loss 0.65% of feed methane

Figure 1.2: Schematic showing a two stage membrane process to purify a natural gas stream using (a) a cellulose acetate membrane and (b) a yet to be developed high performance membrane [2].

Ideally, the higher flux reduces the membrane area required to achieve the separation requirements and the higher separation efficiency reduces the compression required to recycle the methane that would otherwise be lost to the permeate stream. Moreover, such higher methane recoveries translate to higher returns on investment as well.

While polymer membranes have a trade-off performance, carbon molecular sieve (CMS) membranes are known to have outstanding separation performance. CMS membranes are formed from high temperature pyrolysis of polymeric membranes and perform well for many challenging gas separations, such as oxygen/nitrogen, ethane/ethylene, and olefin/paraffin [12-16], including natural gas due its amorphous and unique nature of its structure [12, 17]. One of the barriers to be overcome, however, is the economical feasibility of the CMS production. While cost of the polymer membranes is estimated to be  $\sim 20$   $\$/\text{m}^2$  [18], CMS membranes are estimated to be 50-100  $\$/\text{m}^2$  [19]. Traditionally, this economical barrier comes from the required polymer processing method, especially use of vacuum pyrolysis as opposed to inert pyrolysis for attractive CMS production. This research will aim to develop an economically favored process to form CMS membranes with attractive  $\text{CO}_2/\text{CH}_4$  separation performance using polymer precursors.

### **1.3 OVERVIEW OF MEMBRANE TECHNOLOGY**

A number of practical requirements must be met to develop a membrane for commercial application. An article by Koros identifies four elements for membrane technology advancement [7]: (i) development of high-efficiency modules with high surface area/volume for large scale processes, (ii) development of advanced materials, (iii) development of a capability to tailor morphologies at multiple levels along the cross section of a membrane, and (iv) development of manufacturing methods to rapidly and efficiently link the previous three elements.

To meet such requirement, the asymmetric hollow fiber membrane morphology was chosen over other membrane module configurations that are shown in Figure 1.3.

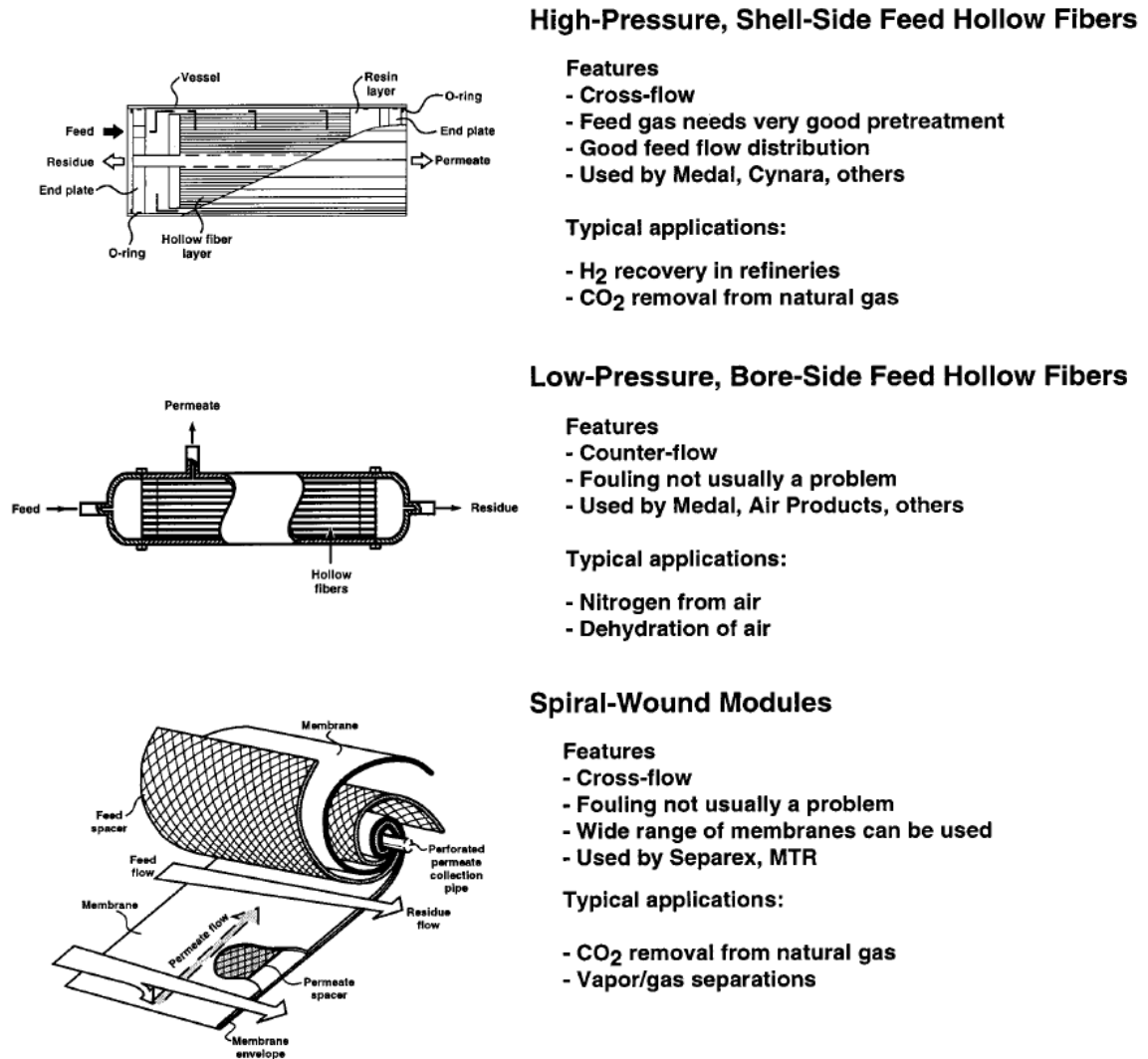


Figure 1.3: Principal gas separation membrane module configurations [2].

Asymmetric hollow fibers are tubular forms of a membrane and provide high fluxes required for productive separations due to the ability to reduce the separating layer to a thin integral “skin” on the outer surface of the membrane [20]. Specifically for CMS membranes, the asymmetric hollow morphology is also practically preferred over homogeneous flat sheets because of better strength and/or flexibility, presumably due to the selective “skin” layer supported by the micropore structure. Such small diameter, cylindrical morphologies also can provide high surface area to volume ratios and high packing densities, with the ability to withstand large transmembrane driving force pressure differences, as shown in Figure 1.4.

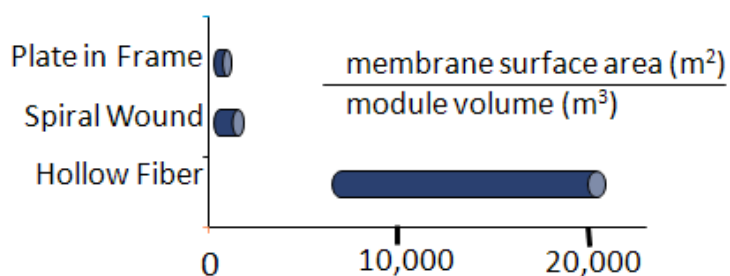


Figure 1.4: Graph representing the surface area/volume achievable in various module types [2].

In this work, all of the elements described above are addressed for production of attractive CMS membranes. Advanced material, CMS membranes, and its economically feasible production method were developed based on fundamental studies with homogeneous dense film morphology. The study was advanced by applying the method from dense film to asymmetric hollow fiber morphology. The following are the main research objectives for this dissertation.

## **1.4 RESEARCH OBJECTIVES**

### **1. Develop economically favored method to control separation performance properties of CMS membranes.**

While CMS membranes have excellent separation performance, its production cost is speculated to be much more than for commercially available polymer membranes. One of the reasons for this is the use of vacuum as pyrolysis atmosphere because it consumes large amount of energy to pump down the pyrolysis oven in commercial scale. Moreover, large vacuum vessels are costly and difficult to control. In the past, researchers have tried inert pyrolysis to produce CMS membranes, but the separation performance was not as attractive as ones produced under vacuum and the performance was unpredictable. In this work, chemical composition of inert atmosphere is monitored. Specifically, the effect of oxygen partial pressure in the pyrolysis atmosphere is investigated. A polymer precursor 6FDA/BPDA-DAM was synthesized and used to benchmark against literature values of homogeneous flat CMS membranes pyrolyzed under vacuum. Then the investigations of oxygen exposure during inert pyrolysis to produce CMS membranes were conducted with the 6FDA/BPDA-DAM and extended to commercially available polymer Matrimid<sup>®</sup>. The effect of oxygen exposure to CO<sub>2</sub>/CH<sub>4</sub> separation performance and the resulting CMS structures are discussed. CMS membranes are amorphous in nature and difficult to characterize their structure. In order to have a better understanding of the structure, diffusion coefficients are used to probe the pore size distributions. As a result of these investigations, a guidance to produce and control CMS separation performance was developed using an economically preferred pyrolysis method.

**2. Create “first generation” asymmetric hollow fiber CMS membranes by adapting method developed in Objective 1.**

Asymmetric hollow fiber membrane morphology is preferred in industry due to its high surface area to volume ratio. For CMS membranes, it appears to have an additional advantage of better mechanical strength and flexibility due to the combination of a thin integral “skin” on the outer surface of the membranes supported by microporous layer. Defect-free asymmetric hollow fibers are spun and used to evaluate efficacy of the CMS membrane production method developed in objective 1. Mixed gas feed with high feed pressure are used to characterize the asymmetric hollow fiber CMS membranes. In addition to the method demonstration, the experimental mixed gas separation properties are compared with theoretical values predicted using the single gas permeation and sorption experimental results.

**3. Characterize the asymmetric hollow fiber CMS membranes under realistic feed and permeate conditions.**

For the CMS membranes to be scaled-up, it is essential to demonstrate its ability under realistic conditions. The asymmetric hollow fiber CMS membranes produced with the method investigated in objective 1 and 2 are further characterized under aggressive feed conditions. Using the mixed gas feed of 80 atm, permeate pressures are varied from 1 to 20 atm and the experimental results were compared with theoretical values.

CMS membranes are known to lose capabilities with humidity exposure. Homogeneous dense CMS membranes are exposed to 80%RH air for a term of (i) a week and (ii) a month and the effect to the separation performance is evaluated. Moreover, humidified mixed gas feed is used to characterize asymmetric hollow fiber CMS



membranes. An amorphous Teflon coating technique is also applied to demonstrate the possibility of humidity effect prevention.

## **1.5 DISSERTATION OVERVIEW**

Chapter 2 presents background and theory of the concepts referred to in this dissertation, chapter 3 contains the material development details and description of the experimental methods used; chapter 4 describes the effective “inert” pyrolysis method developed with two polyimide precursors using homogeneous dense films, 6FDA/BPDA-DAM and Matrimid<sup>®</sup> to produce attractive CMS membranes; chapter 5 contains description of the process translation from dense films to asymmetric hollow fiber membranes; chapter 6 contains results from characterizing the membrane performance (i) with realistic permeate pressures and (ii) in the presence of humidity containing natural gas feeds; and chapter 7 summarizes the results and scientific contributions made from this work and mentions recommendations for future work.

## 1.6 REFERENCES

- [1] Baker RW, Lokhandwala K. Natural gas processing with membranes: An overview. *Ind Eng Chem Res* 2008; 47:2109-21.
- [2] Baker RW. Future directions of membrane gas separation technology. *Ind Eng Chem Res* 2002; 41:1393-411.
- [3] Baker RW. *Membrane technology and applications*. New York: McGraw-Hill; 2000.
- [4] Hugman RH, Springer PS, Vidas EH. *Chemical composition in discovered and undiscovered natural gas in the lower-48 United States*. Arlington, VA: Energy and Environmental Analysis, Inc; 1990.
- [5] Tataryzyn J, Brimm A. Salt creek CO<sub>2</sub> enhanced oil recovery (EOR) project. 74th Annual GPA Convention; 1995; San Antonio, TX USA. 1995. p. 12.
- [6] Dortmund D, Doshi K. *Recent developments in CO<sub>2</sub> removal membrane technology*. Des Plaines, Illinois: UOP LLC; 1999.
- [7] Koros WJ. Evolving beyond the thermal age of separation processes: Membranes can lead the way. *AIChE J* 2004; 50(10).
- [8] Kohl AL, Nielsen RB. *Gas purification*. 5th ed. Houston, TX: Gulf Publishing; 1997.
- [9] Coleman MR, Koros WJ. The transport properties of polyimide isomers containing hexafluoroisopropylene in the diamine residue. *J Poly Sci Part B* 1994; 32:1915.
- [10] Pixton MR, Paul DR. Gas transport properties of polyarylates: Substituent size and symmetry effects. *Macromolecules* 1995; 28:8277.
- [11] Robeson LM. Correlation of separation factor versus permeability for polymeric membranes. *J Membr Sci* 1991; 62(2):165-85.
- [12] Steel KM. *Carbon membranes for challenging gas separations*. Austin TX USA, The University of Texas at Austin, PhD thesis, 2000.
- [13] Hayashi J-i, Mizuta H, Yamamoto M, Kusakabe K, Morooka S. Separation of ethane/ethylene and propane/propylene systems with a carbonized BPDA–pp'ODA polyimide membrane. *Ind Eng Chem Res* 1996; 35(11):4176-81.
- [14] Okamoto K-i, Kawamura S, Yoshino M, Kita H. Olefin/paraffin separation through carbonized membranes derived from an asymmetric polyimide hollow fiber membrane. *Ind Eng Chem Res* 1999; 38(11):4424-32.
- [15] Suda H, Haraya K. Alkene/alkane permselectivities of a carbon molecular sieve membrane. *Chem Comm* 1997(1):93.
- [16] Lee K-R, Hwang S-T. Separation of propylene and propane by polyimide hollow-fiber membrane module. *J Membr Sci* 1992; 73(1):37-45.

- [17] Vu DQ. Formation and characterization of asymmetric carbon molecular sieve and mixed matrix membranes for natural gas purification. Austin TX USA, University of Texas at Austin, PhD thesis, 2001.
- [18] Koros WJ. Membrane opportunities and challenges for large capacity gas and vapor feeds. European Membrane Society's 20th Summer School; 2003; NTNU, Trondheim, Norway. 2003.
- [19] Kiyono M, Koros WJ, Williams JP. Generalization of effect of oxygen exposure on formation and performance of carbon molecular sieve membranes. NAMS/ICIM; 2010; Washington DC, USA. 2010.
- [20] Baker RW. Membrane technology and applications. 2nd ed. New York: John Wiley & Sons, Ltd.; 2004.

## **CHAPTER 2**

### **BACKGROUND AND THEORY**

#### **2.1 OVERVIEW**

Carbon molecular sieve (CMS) membranes are an attractive alternative to polymeric materials due to their unique structure and morphology. The unique structure of such membranes results in excellent performance for many challenging gas separations, such as  $O_2/N_2$ ,  $CO_2/CH_4$ ,  $C_2H_4/C_2H_6$ , and  $C_3H_6/C_3H_8$  [1, 2]. In this chapter, a background of gas transport through membranes, especially through CMS membranes is described in section 2.2. The structure of CMS membranes is described in section 2.3 and the formation of CMS membranes is described in section 2.4.

#### **2.2 FUNDAMENTAL GAS TRANSPORT THEORY**

##### **2.2.1 Transport in membranes**

Membranes are defined as selective barriers between two phases [3], and several mechanisms are associated to describe the transport of small gas molecules through membranes. When a membrane consists of pores, the size of the pores and the mean free path of the penetrant govern the transport process. When the pore radius is much larger than the mean free path of the penetrants molecule at a given temperature and pressures, viscous flow occurs and there is no discrimination among penetrants. When pore size is reduced to the point where it is less than the mean free path of the penetrants molecules, Knudsen flow occurs, and there may be discrimination between the small penetrants depending on their molecular weights. For selective membrane-based gas and vapor

separations our possible mechanisms are discussed: (i) the Knudsen diffusion, (ii) surface diffusion, (iii) molecular sieving, and (iv) sorption-diffusion as shown in Figure 2.1.

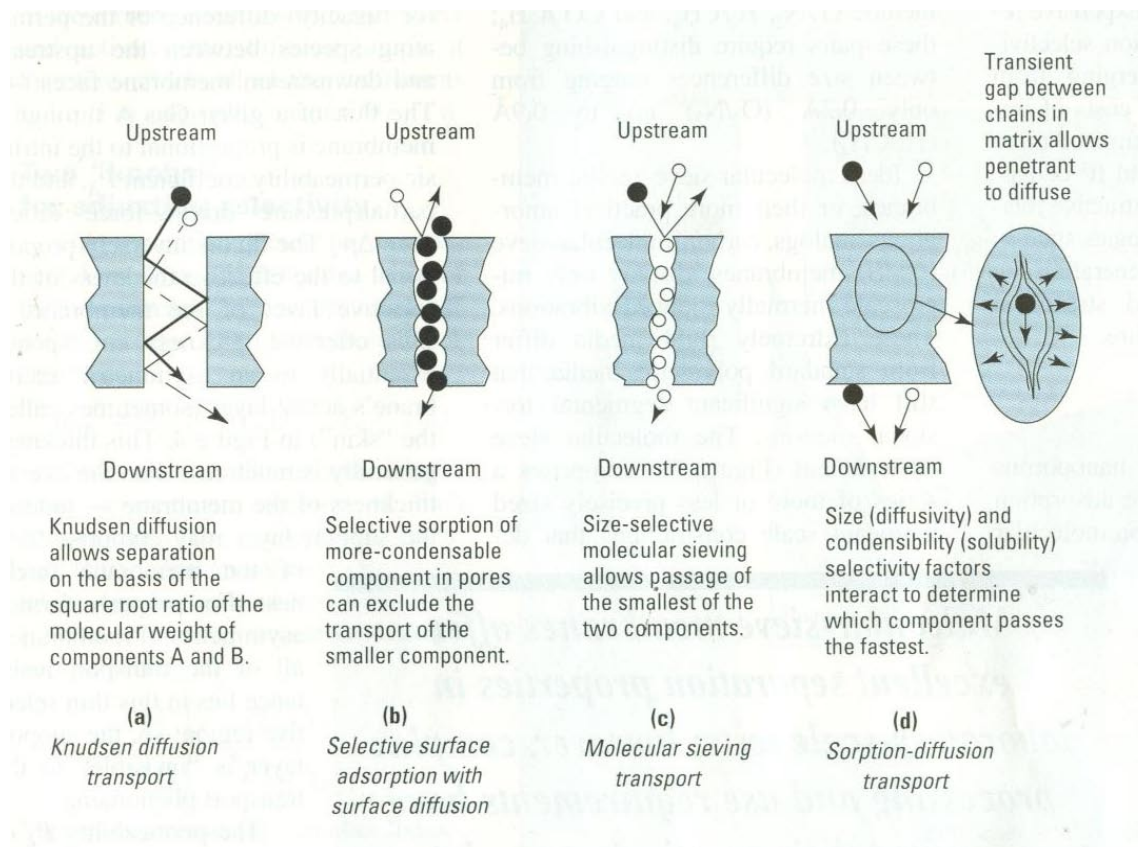


Figure 2.1: Four possible general mechanisms for selective membrane based gas and vapor separations adapted from Koros [4].

Selective adsorption occurs when one or more penetrants are preferentially adsorbed into the membrane, followed by diffusion of the adsorbed species across the membrane from one sorbed site to the other. The physiochemical nature of the pore surface and the pore size governs the efficacy of this mechanism, and exclusion of the rejected penetrant from sorption sites is known to be critical for successful application [5]. Unlike other mechanisms, the driving force of the selective adsorption is the difference in adsorbed phase concentration of the diffusion species; therefore, only low partial pressure

is required as the driving force for strong adsorbing gases. One of the commercial membranes developed to utilize this mechanism is called selective surface flow, SSF<sup>TM</sup>, membranes, and this type has caught attention for the separation of low sorbing hydrogen from highly sorbing hydrocarbon streams [5-7].

While size selective molecular sieving allows passage of the smallest of the multiple components in molecular sieving transport mechanism, a combination of size (diffusivity) and condensability (solubility) determine which component passes the fastest in sorption-diffusion mechanism. Gas transport through glassy polymers and molecular sieves is commonly described by a sorption-diffusion mechanism. Here the transport is governed by the polymer/penetrant or sieve/penetrant thermodynamic partitioning and thermally activated transient gaps within the molecular sieves for diffusion. The diffusion of a penetrant molecule in an isotropic medium can be described as a function of the frequency of the diffusion jumps and the average jump length that takes place in the sieving medium according to Equation 2.1 [8]:

$$D_i = \frac{f_i \cdot \lambda_i^2}{6} \quad (2.1)$$

where  $f$  is the frequency of diffusive jump and  $\lambda$  is the effective diffusion jump length. The frequency of diffusive jump,  $f$ , can be further expressed by:

$$f = \exp\left(\frac{\Delta S^*}{R}\right) \cdot \exp\left(\frac{-\Delta E^*}{RT}\right) \quad (2.2)$$

where  $\Delta S^*$  is related to the control of configurational degrees of freedom of the molecule required to make a diffusive jump,  $R$  is the ideal gas constant, and  $T$  is the absolute temperature.  $\Delta E^*$  is related to the repulsion between the penetrants and the pore mouth of the molecular sieves [9].

In solution-diffusion membranes, the thermodynamic partitioning between the membrane and the penetrants is influenced by the condensability of the penetrant gas and the membrane/penetrant chemical affinity. The critical temperature or boiling point of penetrant gases correlates well with their condensabilities. Gases with higher critical temperatures tend to have higher sorption [10], and to permeate faster through dense membranes where sorption is the dominating mechanism for transport and diffusion is not highly size dependent. This is usually the case for rubbery polymers. The diffusivity of the gas depends on the kinetic diameter of the penetrants, and smaller molecules tend to have higher permeation rates through membranes where diffusion is dominant, which is the case for molecular sieves and many glassy polymers. In the solution-diffusion driven process, a separation can be implemented by maintaining a chemical potential gradient between the upstream and downstream sides of the membrane with lower pressures on the permeate side of the membrane compared to the feed side. When this is satisfied, for a gas feed containing CO<sub>2</sub> and CH<sub>4</sub>, purification of CH<sub>4</sub>, nonpermeable product, can be achieved as shown in Figure 2.2.

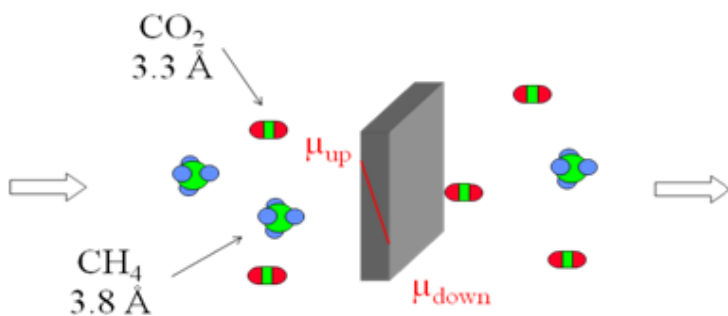


Figure 2.2: Schematic of CO<sub>2</sub>/CH<sub>4</sub> separation process.

The stage cut is defined as the ratio of the permeate flow rate to the feed flow rate and can be adjusted to achieve the desired product purity. Membranes are primarily governed by the intrinsic separation capability of the membrane material which largely determines the amount of product lost in the permeate stream.

## 2.2.2 Transport in CMS membranes

### 2.2.2.1 Permeation

As mentioned previously, gas transport through CMS membranes is modeled by the sorption-diffusion mechanism. Specifically, gas molecules sorb into the membrane at the upstream, then diffuse under the influence of a chemical potential gradient, and finally desorb from the membrane at the downstream. Two intrinsic properties, “permeability” and “selectivity,” are used to evaluate the performance of membrane materials. Permeability is a measure of the membrane material’s intrinsic productivity, and the selectivity is a measure of the membrane’s separation efficiency. The permeability equals the pressure and thickness normalized flux, described as:

$$P_i = \frac{n_i l}{\Delta p_i} \quad (2.3)$$

where  $n_i$  represents the flux of component “ $i$ ” gas molecules through the membrane of the membrane thickness,  $l$ , and  $\Delta p_i$  is the transmembrane partial pressure difference that acts as the driving force across the membrane. In asymmetric hollow fibers, which will be considered later, the actual membrane thickness is not readily known, so the productivity in these membranes is described by the permeance, which is simply the pressure normalized flux as follows:

$$\left(\frac{P}{l}\right)_i = \frac{n_i}{\Delta p_i}. \quad (2.4)$$



A most common unit for permeability is the Barrer which is defined as:

$$1 \text{ Barrer } [=] 10^{-10} \frac{\text{cm}^3 \cdot (\text{STP}) \cdot \text{cm}}{\text{cm}^2 \cdot \text{s} \cdot \text{cmHg}} \quad (2.5)$$

, and the permeance unit is the GPU defined as:

$$1 \text{ GPU } [=] 10^{-6} \frac{\text{cm}^3 \cdot (\text{STP})}{\text{cm}^2 \cdot \text{s} \cdot \text{cmHg}}. \quad (2.6)$$

Diffusion of a gas through a membrane is governed by Fick's law, and the diffusion coefficient is assumed to be independent of the concentration of the penetrants, and the flux is given by Fick's law, viz.,

$$n_i = -D_{i,m} \cdot \frac{dC_i}{dx}. \quad (2.7)$$

where  $C_i$  is the concentration of the component “ $i$ ”. Using the definition of flux and substituting into the equation for permeability, Equation 2.3, or permeance, Equation 2.4, the following equation is obtained:

$$\frac{P_i}{l} = \frac{-D_{i,m} \frac{dC_i}{dx}}{\Delta p_i}. \quad (2.8)$$

Integrating Equation 2.8 over the membrane thickness,  $l$ , and representing the concentrations of component “ $i$ ” in the upstream and downstream faces of the membrane as  $C_{i,U}$  and  $C_{i,D}$  respectively, Equation 2.9 is obtained.

$$\int_0^l \frac{P_i}{l} dx = - \int_{C_{i,D}}^{C_{i,U}} \frac{D_{i,m}}{\Delta p_i} dC_i = \int_{C_{i,D}}^{C_{i,U}} \frac{D_{i,m}}{\Delta p_i} dC_i \quad (2.9)$$

The average diffusion coefficient in the membrane is defined by Equation 2.10 and can be substituted into Equation 2.9 to yield Equation 2.11.

$$\bar{D}_{i,m} = \frac{\int_{C_{i,D}}^{C_{i,U}} D_{i,m} dC_i}{C_{i,U} - C_{i,D}}. \quad (2.10)$$

$$P_{i,m} = \bar{D}_{i,m} \cdot \frac{C_{i,U} - C_{i,D}}{\Delta p_i}. \quad (2.11)$$

Also, the average sorption coefficient can be defined as:

$$\bar{S}_i = \frac{C_{i,U} - C_{i,D}}{\Delta p_i}. \quad (2.12)$$

Therefore, when the diffusion process is Fickian, the permeability can also be described in terms of the governing kinetic and thermodynamic parameters, namely the diffusion coefficient,  $D_i$ , and the sorption coefficient,  $S_i$ , by:

$$P_i = \bar{D}_i \cdot \bar{S}_i. \quad (2.13)$$

The selectivity is a measure of the membrane's separation efficiency. The “ideal selectivity” (for pure gas feeds) of a membrane is described by the ratio of the component permeabilities or permeances for the case of a negligible downstream permeate pressure:

$$\alpha_{i/j} = \frac{P_i}{P_j} = \frac{(P/l)_i}{(P/l)_j} = \frac{\bar{D}_i \cdot \bar{S}_i}{\bar{D}_j \cdot \bar{S}_j}. \quad (2.14)$$

In the case of mixed gas feeds where interactions between the permeating gases and the polymer occur or where nonzero downstream pressured exist, the separation factor is a more practical measure used to describe the separation by:

$$S.F. = \frac{(x_i/x_j)_D}{(x_i/x_j)_U} \quad (2.15)$$

, where  $x$  represents the mole fractions of the gas components in the downstream,  $D$ , and upstream,  $U$ , sections of the membrane. The mixed gas separation factor (Equation 2.15) can also be written in terms of the diffusion and solubility coefficients by including a driving force controlled factor, viz. [8]:

$$S.F. = \frac{D_i}{D_j} \cdot \frac{S_i}{S_j} \cdot \frac{\Delta p_i / (p_i)_U}{\Delta p_j / (p_j)_U}. \quad (2.16)$$

Therefore the ideal selectivity or permselectivity can still be obtained using mixed gases once the downstream compositions and pressures are known. The permselectivity is more reflective of the membrane's intrinsic separation capability since the separation factor is dependent of the downstream pressure. The separation factor in Equation 2.16 approaches the ideal selectivity in Equation 2.14 as the downstream partial pressure approaches zero as long as  $D$ 's and  $S$ 's applicable in the actual mixed gas feed condition are considered. In commercial applications of membranes, the permeability and selectivity must be balanced to achieve a practical optimum, since there is usually a trade-off between the two parameters [11].

### 2.2.2.2 Sorption

The sorption coefficient describes the amount or concentration of gas taken up by a membrane material at a given pressure at equilibrium. It depends on the condensability of the gas penetrant and the gas penetrant's interactions with the membrane material. For molecular sieving material, like carbon molecular sieves with rigid saturatable capacities, a Langmuir isotherm is commonly used. Using the Langmuir isotherm, the sorption coefficient is given by:

$$S_i = \frac{C_i}{p_i} = \frac{C_{Hi}' b_i}{1 + b_i p_i} \quad (2.17)$$

where  $C_i$  is the equilibrium uptake of penetrant “ $i$ ” by the sorbent,  $p_i$  is the partial pressure,  $C_{Hi}'$  is the Langmuir hole filling capacity and  $b_i$  is the Langmuir affinity constant. In CMS materials, the majority of the penetrants are assumed to sorb into large pores characterized by  $d_{TV}$  and  $d_c$  in Figure 2.3(a) since CMS membranes presumably consist of these pores and the interaction energy of the molecule sorbed in the large pores is generally lower than the critical pore windows,  $d_c$ , as shown in Figure 2.3(b).

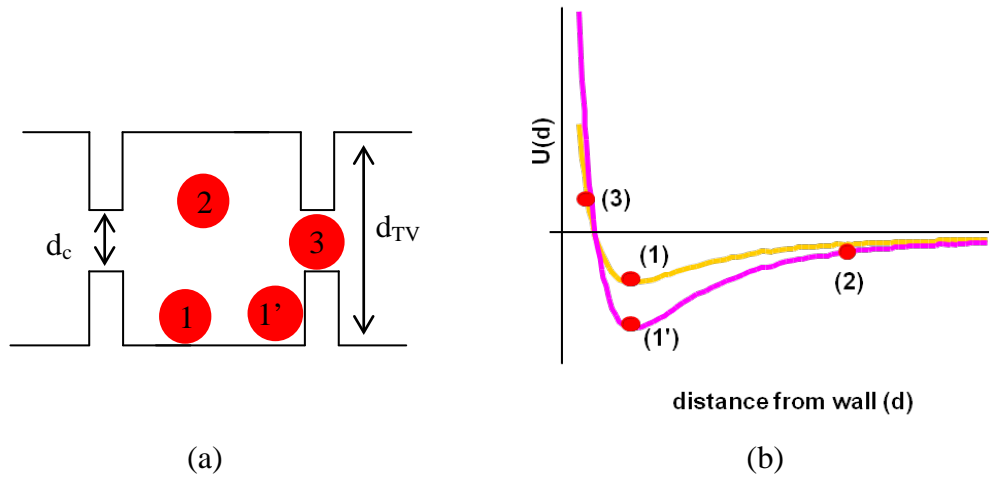


Figure 2.3: (a) Idealized gas molecule's equilibrium positions at various locations inside the pore structures and (b) potential energy of penetrants associated with the locations.

### 2.2.2.3 Diffusion

As previously mentioned, four transport mechanisms are discussed for selective membrane separations: (i) Knudsen diffusion, (ii) selective surface adsorption with surface diffusion, (iii) molecular sieving and (iv) sorption-diffusion [4, 5, 7]. Assuming that the pores are straight and round, when pore size is smaller than the mean free path of the molecule, Knudsen diffusion can occur. The diffusion coefficient of component “ $i$ ”,  $D_{i,K}$  in m<sup>2</sup>/s, is represented as:

$$D_{i,K} = 97.0 \cdot r \cdot \left(\frac{T}{M_i}\right)^{0.5} \quad (2.18)$$

, where  $r$  is the pore radius in m,  $T$  is the absolute temperature in Kelvin, and  $M$  is the molecular weight of the component. The Knudsen diffusivity selectivity can be written as:

$$\alpha_{i/j} = \sqrt{\frac{M_j}{M_i}} \quad (2.19)$$

The Knudsen selectivity is relatively low, especially for gases of similar molecular weight such as oxygen and nitrogen of being 1.07.

Molecular sieving occurs when the penetrants are separated by the size of the molecules relative to the size of pore windows of the membranes. Smaller pores limit the diffusion of the penetrant and therefore control efficacy of the separation performance. Diffusion through the smaller pores requires penetrating molecules to overcome the repulsive interaction energy with the pore walls. Molecules of similar sizes can be effectively separated because very small changes in size result in considerable differences in the activation energy of the diffusion. The diffusivity is correlated with temperature by the energy of the activation for the diffusion jump and can be expressed by an Arrhenius relationship:

$$D_i = D_{i,O} \exp\left(\frac{-E_d}{RT}\right) \quad (2.20)$$

where  $D_{i,O}$  is the pre-exponential term,  $E_d$  is the activation energy of diffusion,  $R$  is the ideal gas constant, and  $T$  is the absolute temperature. Singh and Koros evaluated the importance of entropic selectivity and found that there is a substantial difference in the pre-exponential factor for separations which diffusion activation energy is similar, such as  $O_2/N_2$  separation [12]. The pre-exponential factor can be represented as:

$$D_{i,O} = e \lambda^2 \frac{kT}{h} \exp\left(\frac{S_d}{R}\right) \quad (2.21)$$

where  $k$  is the Boltzmann constant,  $h$  is the Planck's constant, and  $S_d$  is the activation entropy of diffusion [13]. The thermodynamic sorption coefficient decreases with temperature according to the van-Hoff's equation:

$$S_i = S_{i,O} \exp\left(\frac{-H_s}{RT}\right) \quad (2.22)$$

where  $S_{i,O}$  is the pre-exponential term and  $\Delta H_{i,j}$  is the apparent heat of sorption for a penetrants. Entropic selectivity,  $\exp\left(\frac{\Delta S_{i,j}}{R}\right)$ , and enthalpic selectivity,  $\exp\left(\frac{\Delta H_{i,j}}{RT}\right)$ , can be combined to give the overall diffusivity selectivity since  $\lambda^2$ , the jump length, is effectively the same between equilibrium sorption size, viz.,

$$\frac{D_i}{D_j} = \exp\left(\frac{\Delta S_{i,j}}{R}\right) \exp\left(\frac{-\Delta H_{i,j}}{RT}\right). \quad (2.23)$$

According to Glasstone et al., diffusion is accompanied by a negligible volume change:  $-\Delta H$  is essentially the same as  $-E_d$ . The jump length  $\lambda$  correlates with the pore structure and penetrant size, and Equation 2.20 can be written as [13]:

$$D = \lambda^2 \frac{kT}{h} \frac{F^+}{F} \exp\left(\frac{-E_d^+}{R}\right) \quad (2.24)$$

where  $F$  is the partition function in the normal state and  $F^+$  is in the transition state [13]. For molecular sieving material, the sorbed state is in the large pores and the transition state is in the selective pores. The overall partition function in either state is expressed as the product of translational, rotational, and vibrational contributions:

$$F = F_{trans} \cdot F_{rot} \cdot F_{vib}. \quad (2.25)$$

Note that the partition function in the activated state  $F^+$  does not consider the translational partition in the direction of the gas diffusion since the factor  $kT/h$  in Equation 2.23 accounts for it [12]. Combining Equation 2.21 and 2.24, the entropic selectivity can be written as:

$$\exp\left(\frac{S_{d,i}-S_{d,j}}{R}\right) = \frac{(F^+/F)_i}{(F^+/F)_j}. \quad (2.26)$$

For separating gas molecules which have different dimensions, pores can limit rotational freedom for one molecule while allowing it for the other. For CMS membranes, it is known that the entropic selectivity plays a major role in the enhanced separation performance. For instance, oxygen has an approximate diameter of 2.8 Å with a length of 3.7 Å while nitrogen has a length of 4 Å with a diameter of 3.7 Å. If CMS material has a selective pore window of ~3.8 Å in diameter, oxygen is allowed to rotate freely while nitrogen loses its freedom, leading to the entropically selective separation mechanism.

### 2.3. STRUCTURE OF CMS MEMBRANES

CMS membranes are formed by thermal decomposition of polymer precursors and result in an almost pure carbon material, in many cases above 95 % carbon [14-18]. When polymers are pyrolyzed, either coke or char is formed [14, 19].

Coke forms graphite at a temperature above 2200 °C and results in a layer of many graphene sheets in a form of AB stacking as depicted in Figure 2.4. The density of hexagonal graphite is  $\sim 2.25 \text{ g/cm}^3$ , and the distance between the layers is 0.335 nm with two bonded carbon atoms 0.142 nm being apart [20]. Within the layers, the bonding is trigonal  $\text{sp}^2$ -hybrid sigma-bonds with delocalized pi-bonds within the layers. There is no chemical bond between the layers, and the force of attraction is limited to van der Waals forces.

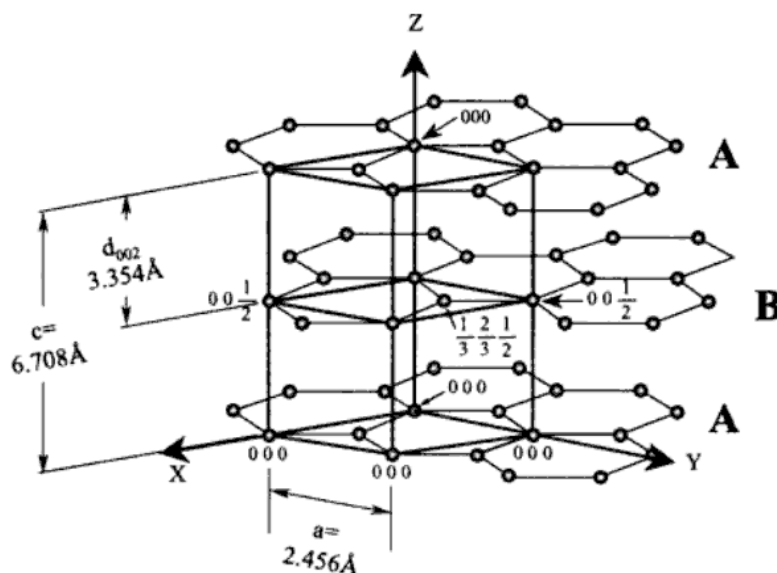


Figure 2.4: The structure of graphite made of the AB stacking of graphene sheets [21].

Graphene is a single sheet of condensed aromatic hydrocarbons to an infinite dimension. In the rigid graphene sheet, the  $\text{sp}^2$  bonded carbon atoms form a 2D extended electronic structure [21]. The single graphite layer of honeycomb structure with solid density  $> 1 \text{ g/cm}^3$  comes with strong covalent binding. Carbon consists of six electrons in the ground



state,  $1s^2 2s^2 2p^2$ . Moreover, in the lattice, the 2s and 2p electrons form an  $sp^2$  hybrid orbital, where three electrons are localized. Graphene has attractive mechanical strength, far exceeding graphite. In addition, it has been measured to be 200 times greater in a breaking strength than steel [22].

While coke forms crystalline structure, char remains in an amorphous structure [14, 19]. Such amorphous materials are believed to have a highly aromatic structure comprised of disordered  $sp^2$  hybridized carbon sheets with angles of disorientation that can attain values of several degrees as illustrated in Figure 2.5(a) [19]. The structure can be envisioned to comprise roughly parallel layers of condensed hexagonal rings with no three-dimensional crystalline order. The majority of CMS membranes used for gas separation have a turbostratic structure [23] with very little long range order and are considered essentially isotropic as shown in Figure 2.5(b).

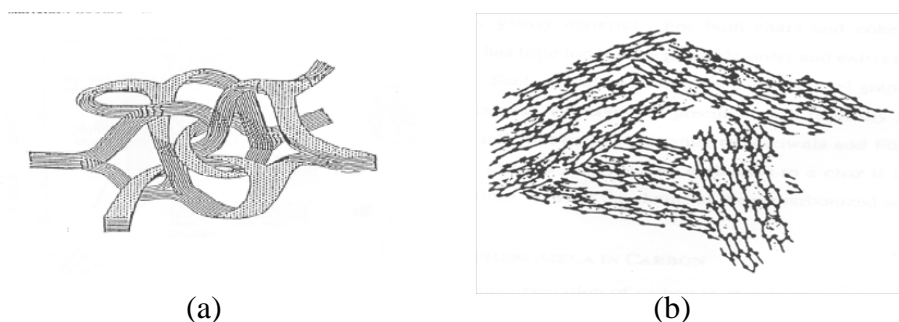


Figure 2.5: Structures of carbon material, adapted from (a) Jenkins and Kawamura [19] and (b) Pierson [14].

Pores are formed from packing imperfections between microcrystalline regions in the material, and the pore structure in CMS membranes is described as “slit-like” with an “idealized” pore structure illustrated in Figure 2.6(a). This pore structure can be further represented as shown in Figure 2.6(b) in terms of an idealized bimodal pore distribution.

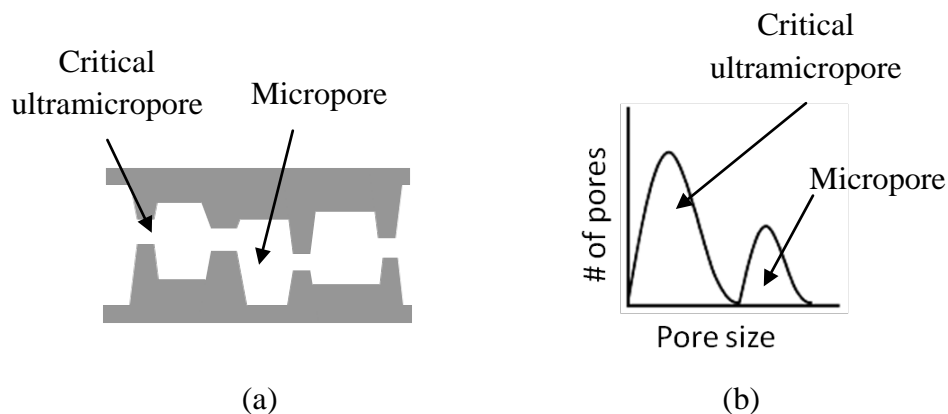


Figure 2.6: Idealized “slit-like” carbon structure and bimodal pore size distribution [2, 9, 24].

The distribution consists of large pores of 6 to 20 Å connected by smaller pores known as “ultramicropores” [2]. Such a combination of ultramicropores and micropores is believed to provide the combined molecular sieving function and high permeability characteristic of these unusual materials. The disordered structure of the carbon material is different from zeolites, which have a uniform, well defined set of pores. Despite the distribution of the ultramicropores, CMS materials offer the important advantage of facile formation of defect free membranes for use in gas separation applications. Structures of CMS membranes have been investigated by many researchers using traditional techniques, such as X-ray diffraction (XRD), transmission electron microscopy (TEM), and adsorption. Unfortunately, due to the amorphous nature of CMS, it has been difficult to determine the structure, especially the ultramicropore region that governs the molecular sieving process. When XRD was performed, as shown in Figure 2, broad peaks were observed due to its amorphous nature. Therefore, the accuracy with which one can deconvolute information to estimate actual pore structure is poor [9, 16, 25, 26]. The results of high resolution TEM were also inconclusive due to the amorphous structure, and the image hardly showed any pores in the material [2, 15]. Chen, Loo, Wang, and

Do conducted an argon adsorption isotherm to obtain a pore size distribution of CMS membranes, but the argon molecule was too large to analyze the selective ultramicropore region [27]. Similarly, Steel and Koros and Campo and Mendes concluded that the pore size distribution derived from CO<sub>2</sub> adsorption equilibrium may not be enough to explain CMS pore structures that are responsible for molecular sieving [25, 28]. A part of this chapter describes an investigation of the CMS structures, namely the applicable ultramicropore distribution, by using various gas molecules as probes. Details of the investigation are described in chapter 4.

## **2.4 FORMATION OF CMS MEMBRANES**

The separation performance and morphology of CMS membranes is influenced by many factors, such as the polymer processing method and polymer precursors. In this section, some of the primary factors are described: (i) polymer precursor composition, (ii) pyrolysis temperature, (iii) ramp rate, (iv) thermal soak time at maximum pyrolysis temperature, and (v) pyrolysis atmosphere.

### **2.4.1 Polymer precursor**

In 1983, Koresh and Soffer pioneered the production of defect-free hollow fiber CMS membranes by pyrolyzing cellulose hollow fibers [29], and since then many polymers have been used to produce CMS membranes in fiber and the dense film forms. Viable precursors include cellulose derivatives [29], phenolic resin [30, 31], poly(vinylidene) based polymers [32], polyetherimide [33, 34], and polyimides. Among them, polyimides have preferably been used because of their high glass transition temperature, ease of processability, and good separation performance as polymeric membranes. Indeed, Jones and Koros mentioned that polyimides are the best currently

available polymer precursors for CMS membrane based on separation performance and mechanical strength [17, 35].

Using the polyimide Matrimid<sup>®</sup>, Steel and Koros worked on dense CMS films [2, 9]. The films were pyrolyzed at 550 °C and 800 °C in a vacuum with a maximum pressure of 0.03 torr. In addition to Matrimid<sup>®</sup>, non-commercial polyimide 6FDA/BPDA-DAM was synthesized and pyrolyzed in the same manner. The results in Figure 2.7 show that Matrimid based membranes are more selective and less permeable than the 6FDA based membranes produced. This was caused primarily by differences in precursor chemical structures. In addition, differences in evolved gases during decomposition also contributed to the differences in performance. According to Williams, Matrimid<sup>®</sup> evolves volatile products, such as aniline, toluene, CO<sub>2</sub>, and CO. In addition to these products, 6FDA/BPDA-DAM also evolves large amount of CF<sub>3</sub>- compounds [36]. This evolution of the large molecule apparently contributes to higher permeability.

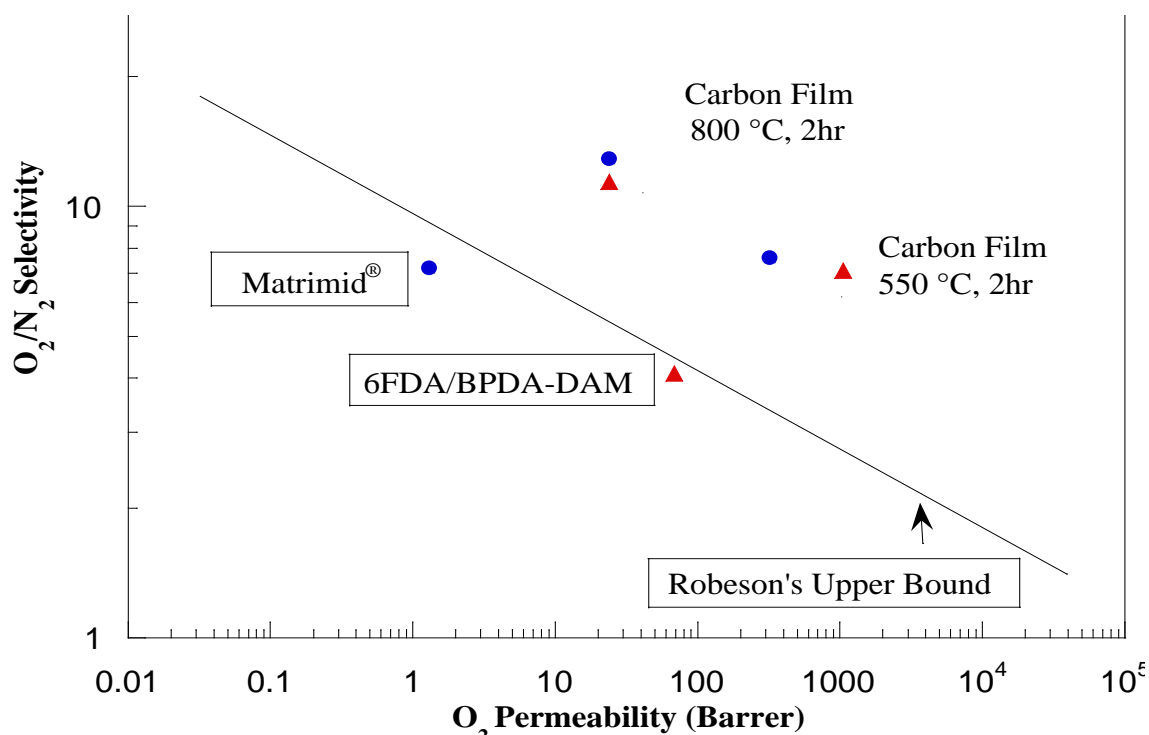


Figure 2.7: Transport properties of CMS dense film using two different polyimide precursors. The points on the graph are average of 2-3 samples and the circles around the points represent the spread of data, adapted by [2, 9].

The effect of polymer precursor on asymmetric hollow fiber CMS membranes was demonstrated by previous researchers in the Koros group. Vu investigated carbon dioxide/methane separation using Matrimid<sup>®</sup> and 6FDA/BPDA-DAM CMS fibers [18, 24]. Results indicate that CO<sub>2</sub> permeance of 6FDA/BPDA-DAM CMS fibers are higher than Matrimid<sup>®</sup> CMS fibers while its selectivity is somewhat similar. This trend with asymmetric hollow fibers is the same as that observed with dense films shown in Figure 2.7. Normalization of these two studies indicates that the choice of polymer precursor does indeed affect CMS performance.

#### **2.4.2 Pyrolysis temperature**

The term pyrolysis temperature is defined as the highest temperature to which a precursor is heated during the pyrolysis process. The pyrolysis temperature is chosen in a range between the decomposition of the polymer and the graphitization temperature. The previous Figure 2.7 shows that an increase in pyrolysis temperature lowers the permeability of the CMS membranes and increases the selectivity [9, 24, 37].

#### **2.4.3 Ramp rate**

An increase in the ramp rate is known to increase permeability and lower the selectivity of the membrane. Suda and Haraya prepared Kapton<sup>®</sup> based CMS membranes in inert pyrolysis and found that the permeability of the membranes to all gases decreased with lower heating rates by varying the heating rate from 13.3 K/min to 1.33 K/min [15]. Williams and Koros suggest two reasons for this dependence: (i) the rate of evolution of by-products and (ii) an increased pyrolysis time that allows pore sintering to occur [38].

#### 2.4.4 Thermal soak time

The term “thermal soak time” is defined as the duration of time at the pyrolysis temperature. This thermal soak time can be used to tune the microstructure of the carbon membranes. Several researchers found that increasing the thermal soak time results in more selective yet less permeable CMS membranes. In Figure 2.8, results by Steel show that increasing the soak time led to a decrease in the permeability and increase in the selectivity [2]. In addition, data with the higher pyrolysis temperature has smaller effect on the selectivity, yet a larger effect on the permeability than the lower pyrolysis temperature.

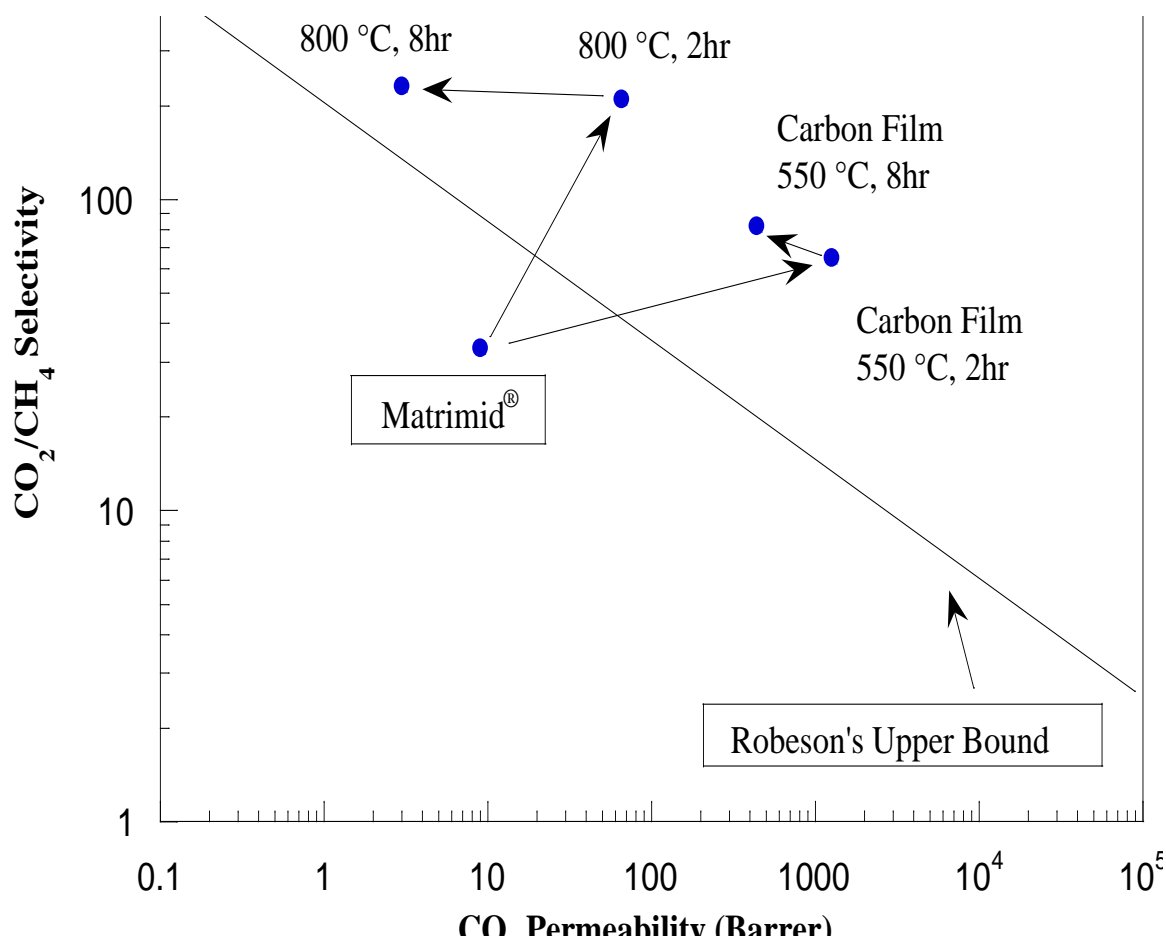


Figure 2.8: Transport properties of CMS dense films pyrolyzed with different soak time, adapted from [2].

The effect of shorter soak times was investigated on BTDA–ODA polyimide dense films by Kim et al [39]. The polymer precursor was pyrolyzed at 700 °C with various thermal soak times from 0 to 60 minute. Comparison showed that changing soak time from 0 to 60 minute resulted in decreasing O<sub>2</sub> permeability from 632 to 136 Barrer while increasing the O<sub>2</sub>/N<sub>2</sub> selectivity from 9 to 15.

This thermal soak effect was also investigated on asymmetric hollow fiber CMS membranes. Vu performed mixed-gas separation of 10%/90% carbon dioxide/methane using Matrimid<sup>®</sup>. Results show that reducing the thermal soak time from 2 hours to 1 hour at 550 °C in a vacuum environment increases CO<sub>2</sub> permeance by 35% while maintaining CO<sub>2</sub>/CH<sub>4</sub> selectivity [24]. These three studies show that the effect of thermal soak time is a strong function of polymer precursor and pyrolysis temperature.

#### **2.4.5 Pyrolysis atmosphere**

Suda and Haraya investigated pyrolysis under different environments. CMS dense films were prepared from polyimide Kapton<sup>®</sup> at 1000 °C in either argon or in vacuum of 10<sup>-5</sup> torr. According to their permeation properties, the results of an O<sub>2</sub>/N<sub>2</sub> separation were almost the same between membranes formed under the different atmosphere [15]. In addition, Geiszler and Koros conducted work on asymmetric hollow fiber CMS membranes using 6FDA/BPDA-DAM [40, 41]. Considering the uncertainty of the permeance data, Geiszler concludes that there is no difference between fibers produced in helium and argon for both O<sub>2</sub>/N<sub>2</sub> and H<sub>2</sub>/N<sub>2</sub> separations. However, a slightly higher selectivity and less permeability was observed with the vacuum pyrolysis than the inert pyrolysis. Using the same pyrolysis equipment as Geiszler, Vu also experienced this trend using the asymmetric hollow fiber CMS membranes of Matrimid<sup>®</sup> for 10%/90% carbon dioxide/methane separations [24].

In addition, Geiszler and Koros have also investigated the effect of inert purge flow rate on the separation performance of CMS hollow fiber membranes [40, 41]. Two different flow rates of 20 and 200 ccSTP/min were investigated at atmospheric pressure.

Table 2.1: Transport properties of asymmetric hollow fiber CMS membranes, adapted from [40].

Pyrolysis atmosphere	Flow rate (cc(STP)/min)	O <sub>2</sub> flux (GPU)	$\alpha_{O_2/N_2}$
Argon	200	$174 \pm 75$	$4.3 \pm 1.4$
Argon	20	$0.24 \pm 0.21$	$4.5 \pm 2.5$
Helium	200	$97 \pm 37$	$5.4 \pm 0.7$
Helium	20	$0.08 \pm 0.05$	$4.6 \pm 0.9$

Table 2.1 shows that CMS membranes produced at 200 cc(STP)/min have higher permeability than those at 20 cc(STP)/min. This shows that the purge flow rate appears to influence the effective decomposition of the polyimide and ultimately the performance of CMS membrane.

In order to understand this phenomenon as well as the trend of emerging transport properties obtained in vacuum and in inert gases, Williams proposed a hypothesis that oxygen content affects separation performance of CMS membranes [36]. Jones and Koros also speculated that trace amount of oxygen may be a critical factor [17]. In Williams' work, polymer 6FDA/BPDA-DAM was used to pyrolyze CMS dense films under different atmospheres. Table 2.2 shows permeation data along with total exposure factors. This term "total oxygen exposure factor,  $q_{O_2}$ " describes the total number of moles of oxygen available for reaction during the pyrolysis. For each condition, this total oxygen exposure factor was calculated using the ideal gas law.



Table 2.2: Summary of transport properties with calculated values of the total oxygen exposure factor,  $q_{O_2}$ , adapted from [36].

Purge gas	Flow rate (cm <sup>3</sup> STP/min)	P <sub>O<sub>2</sub></sub> (Barrer)	$\alpha_{O_2/N_2}$	Calculated $q_{O_2}$ (10 <sup>-8</sup> mol)
0.005 torr Air	-	630	8.8	9.3
0.042 torr Air	-	52	10	3100
He ( $\leq 0.1$ ppm O <sub>2</sub> )	50	620	7.5	2.8
He ( $\leq 0.1$ ppm O <sub>2</sub> )	200	581	7.3	11.2
Ar ( $\leq 4$ ppm O <sub>2</sub> )	50	537	7.1	110
Ar ( $\leq 4$ ppm O <sub>2</sub> )	200	647	6.4	440

Results in Table 2.2 show that both the permeability and selectivity are correlated with the total oxygen exposure factor. In the case of vacuum pyrolysis, a lower total oxygen exposure factor leads to a much higher permeability while selectivity is maintained relatively high. In the case of both helium and argon inert purges, a similar trend was observed. This indicates that pyrolysis atmospheres can be tuned by considering the “total oxygen exposure coefficient.”

## 2.5 REFERENCES

- [1] Baker RW. Membrane technology and applications. New York: McGraw-Hill; 2000.
- [2] Steel KM. Carbon membranes for challenging gas separations. Austin TX USA, The University of Texas at Austin, PhD thesis, 2000.
- [3] Mulder M. Basic principles of membrane technology. 2nd ed. Dordrecht Netherlands: Kluwer Academic Publishers; 1997.
- [4] Koros WJ. Membranes: learning a lesson from nature. Chem Eng Prog 1995; 91(10):68-81.
- [5] Rao MB, Sircar S. Nanoporous carbon membrane for separation of gas mixtures by selective surface flow. J Membr Sci 1993; 85:253-64.
- [6] Naheiri T, Ludwig KA, Anand M, Rao MB, Sircar S. Scale-up of selective surface flow membrane for gas separation. Sep Sci Technol 1997; 32(9):1589-602.
- [7] Rao MB, Sircar S. Nanoporous carbon membrane for gas separation. Gas Sep Purif 1993; 7(4):279-84.
- [8] Koros WJ, Fleming GK. Membrane-based gas separation. J Membr Sci 1993 1993; 83:1-80.
- [9] Steel KM, Koros WJ. Investigation of porosity of carbon materials and related effects on gas separation properties. Carbon 2003; 41(2):253-66.
- [10] Cussler EL. Diffusion, mass transfer in fluid system. 2nd ed. Cambridge, UK: Cambridge University Press; 1997.
- [11] Robeson LM. Correlation of separation factor versus permeability for polymeric membranes. J Membr Sci 1991; 62(2):165-85.
- [12] Singh A, Koros WJ. Significance of entropic selectivity for advanced gas separation membranes. Ind Eng Chem Res 1996; 35(4):1231-4.
- [13] Glasstone S, Laidler KJ, Eyring H. The theory of rate processes. 1st ed. New York: McGraw-Hill Book Co., Inc.; 1941.
- [14] Pierson HO. Handbook of carbon, graphite, diamond, and fullerenes. New York: Noyes Publication; 1993.
- [15] Suda H, Haraya K. Gas permeation through micropores of carbon molecular sieve membranes derived from Kapton polyimide. J Phys Chem B 1997; 101(20):3988-94.
- [16] Singh A. Membrane materials with enhanced selectivity: an entropic interpretation. Austin TX USA, The University of Texas at Austin, PhD thesis, 1997.

- [17] Jones CW, Koros WJ. Carbon molecular sieve gas separation membranes-I. Preparation and characterization based on polyimide precursors. *Carbon* 1994; 32(8):1419-25.
- [18] Vu DQ, Koros WJ, Miller SJ. High pressure CO<sub>2</sub>/CH<sub>4</sub> separation using carbon molecular sieve hollow fiber membranes. *Ind Eng Chem Res* 2002; 41(3):367-80.
- [19] Jenkins GM, Kawamura K. Polymeric carbons - carbon fiber, glass and char. London: Cambridge University Press; 1976.
- [20] Marsh H, Rodríguez-Reinoso F. Activated carbon. Great Britain: Elsevier; 2006.
- [21] Enoki T, Endo M, Suzuki M. Graphite intercalation compounds and applications. New York: Oxford University Press, Inc; 2003.
- [22] Lee C, Wei X, Kysar JW, Hone J. Measurement of the elastic properties and intrinsic Strength of monolayer graphene. *Science* 2008; 321:385-8.
- [23] Biscoe J, Warren BE. An x-ray study of carbon black. *J Appl Phys* 1942; 13:364-71.
- [24] Vu DQ. Formation and characterization of asymmetric carbon molecular sieve and mixed matrix membranes for natural gas purification. Austin TX USA, University of Texas at Austin, PhD thesis, 2001.
- [25] Campo MC, Magalhaes FD, Mendes A. Comparative study between a CMS membrane and a CMS adsorbent: Part I - Morphology, adsorption equilibrium and kinetics. *J Membr Sci* 2010; 346(1):15-25.
- [26] Park HB, Kim YK, Lee JM, Lee SY, Lee YM. Relationship between chemical structure of aromatic polyimides and gas permeation properties of their carbon molecular sieve membranes. *J Membr Sci* 2004; 229(1-2):117-27.
- [27] Chen J, Loo LS, Wang K, Do DD. The structural characterization of a CMS membrane using Ar sorption and permeation. *J Membr Sci* 2009; 335(1-2):1-4.
- [28] Steel KM, Koros WJ. An investigation of the effects of pyrolysis parameters on gas separation properties of carbon materials. *Carbon* 2005; 43:1843-56.
- [29] Koresh JE, Soffer A. Molecular sieve permselective membrane. Part I. Presentation of a new device for gas mixture separation. *Sep Sci Technol* 1983; 18(8):723-34.
- [30] Centeno TA, Fuertes AB. Supported carbon molecular sieve membranes based on a phenolic resin. *J Membr Sci* 1999; 160:201-11.
- [31] Fuertes AB, Menendez I. Separation of hydrocarbon gas mixtures using phenolic resin-based carbon membranes. *Sep Purif Technol* 2002; 28:29-41.
- [32] Centeno TA, Fierres AB. Carbon molecular sieve gas separation membranes based on poly(vinylidene chloride-co-vinyl chloride). *Carbon* 2000; 38:1067-73.

- [33] Sedigh MG, Jahangiri M, Liu PK, Sahimi M, Tsotsis TT. Structural characterization of polyetherimide-based carbon molecular sieve membranes. *AIChE J* 2000; 46(11):2245-55.
- [34] Sedigh MG, Xu L, Tsotsis TT, Sahimi M. Transport and morphological characteristic of polyetherimide-based carbon molecular sieve membranes. *Ind Eng Chem Res* 1999; 38:3367-80.
- [35] Jones CW, Koros WJ. Carbon molecular sieve gas separation membranes-II. Regeneration following organic exposure. *Carbon* 1994; 32(8):1427-32.
- [36] Williams PJ. Analysis of factors influencing the performance of CMS membrane for gas separation. Atlanta GA USA, Georgia Institute of Technology, PhD thesis, 2006.
- [37] Barsema JN, Vegt NFA, Koops GH, Wessling M. Carbon molecular sieve membranes prepared from porous fiber precursor. *J Membr Sci* 2002; 205(1-2):239-46.
- [38] Li NN, Fane AG, Ho WSW, Matsuura T. Advanced membrane technology and applications. New Jersey: A John Wiley & Sons, Inc; 2008.
- [39] Kim YK, Park HB, Lee YM. Preparation and characterization of carbon molecular sieve membranes derived from BTDA-ODA polyimide and their gas separation properties. *J Membr Sci* 2005; 255:265-73.
- [40] Geiszler VC, Koros WJ. Effects of polyimide pyrolysis conditions on carbon molecular sieve membrane properties. *Ind Eng Chem Res* 1996; 35(9):2999-3003.
- [41] Geiszler VC, Koros WJ. Polyimide precursors for carbon molecular sieve membranes. Austin, TX, University of Texas at Austin, 1997.

## **CHAPTER 3**

### **MATERIALS AND EXPERIMENTAL PROCEDURES**

#### **3.1 INTRODUCTION**

This chapter contains a description of the materials and experimental methods. Section 3.2 discusses the polymers and gases used for membrane formation and characterization. Section 3.3 describes the procedures to synthesize polymeric and CMS membranes for both homogeneous dense and asymmetric hollow fiber membranes. Section 3.4 presents the characterization techniques and equipment.

#### **3.2 MATERIALS**

##### **3.2.1 Polymer**

CMS membranes were formed by high temperature decomposition of polymeric precursor membranes. Among polymers, polyimides probably are the best precursors [1, 2]. In this work, in-house synthesized polyimide 6FDA/BPDA-DAM was first used to benchmark against literature and to develop an inert pyrolysis method for high performance CMS membrane production. The method was then advanced by demonstrating with a commercially available polymer. For commercially available polymers, polyimide Matrimid<sup>®</sup> 5218, provided by Vantico, Inc. and polyetherimide Ultem<sup>®</sup>, provided by GE Plastics were chosen for various reasons including their relative low costs and availability. The chemical structure and the characteristics of the polymers are shown in Table 3.1 and 3.2.

Table 3.1: Chemical structures of polymers used in this work.

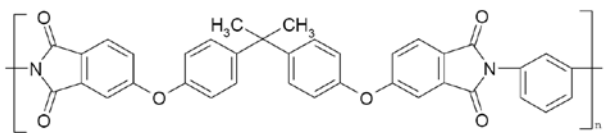
Polymer	Chemical structure
6FDA/BPDA-DAM	2,4,6-trimethyl-1,3-phenylene diamine (DAM), 3,3',4,4'-biphenyl tetracarboxylic dianhydride (BPDA), and 5,5'-[2,2,2-trifluoro-1-(trifluoromethyl)ethylidene]bis-1,3-isobenzofurandione (6FDA). The ration of X to Y is 1:1.
Matrimid <sup>®</sup> (BTDA-DAPI)	3,3',4,4'-benzophenonetetracarboxylic acid dianhydride-5(6)-amino-1-(4' aminophenyl)-1,3,3-trimethylindane
Ultem <sup>®</sup> (BPADA-mPDA)	 2,2-bis[4-(3,4-dicarboxyphenoxy)phenyl] propane dianhydride - 1,3-phenylenediamine

Table 3.2: Polymer properties used in this work. The decomposition temperature is symbolized as  $T_{\text{decomp}}$ .

Polymer	MW	PDI	$T_g$ (°C)	$T_{\text{decomp}}$ (°C)
6FDA/BPDA-DAM	103,170	2.2	424	450
Matrimid <sup>®</sup>	99,369	3.1	302	425
Ultem <sup>®</sup>	62,161 [3]		215 [4]	

The synthesis of 6FDA/BPDA-DAM was conducted via a polycondensation reaction by addition of the dianhydride, 5,5'-[2,2,2-trifluoro-1-(trifluoromethyl)ethylidene]bis-1,3-isobenzofurandione (6FDA, Aldrich), and diamines, 2,4,6-trimethyl-1,3-phenylene diamine (DAM, Fluka) and 3,3',4,4'-biphenyl tetracarboxylic dianhydride (BPDA, Aldrich), in solution using the solvent, n-methylpyrrolidone (NMP). The 6FDA, DAM, BPDA monomers and the reaction sequence are shown in Figure 3.1.

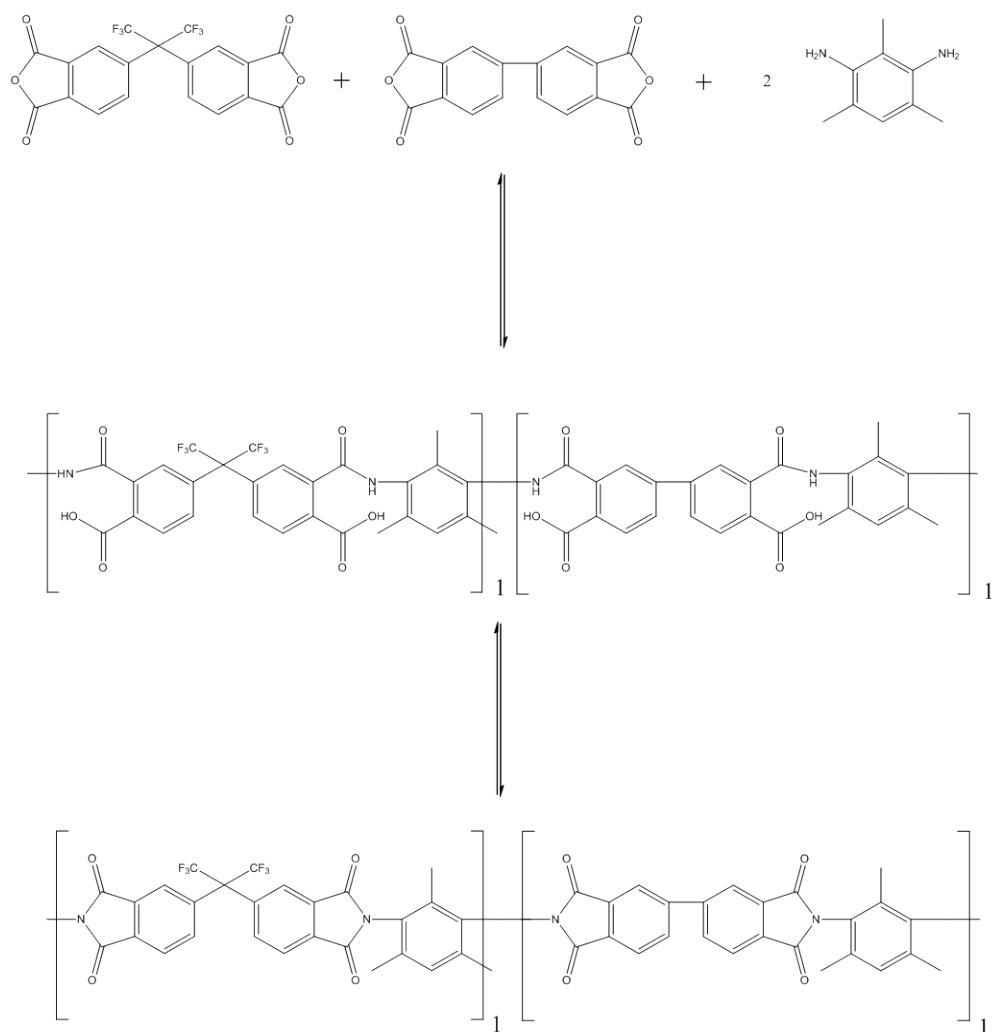


Figure 3.1 Synthesis steps for 6FDA/BPDA-DAM (1:1) polyimide.

All monomers were purified by sublimation prior to use. This sublimation was essential for the end product to have high molecular weight and lower polydispersity index (PDI). A low PDI was speculated to be required for the polymer to be spinnable as shown in Table 3.3.

Table 3.3: Preliminary screening test results for spinning Matrimid<sup>®</sup> 5218. Syringe tests, which are described by Carruthers [5], were conducted to check the spinnability. Unspinnable polymer was insoluble in any combination of solvent mixtures. The results indicate that molecular weight more than 57K with  $2 < \text{PDI} < 3.6$  is preferred for hollow fiber spinning.

Matrimid <sup>®</sup> supplier	MW	PDI	Spinnable?
Ciba (Lot # 47718442)	57K	3.6	Y
Ciba-Geigy (Lot # 30948912)	66K	2.5	Y
Vantico, Inc. (Lot # 778, used in this work)	99K	3.1	Y
Huntsman (Lot # AG6605014)	69K	2.1	Y
Huntsman (Lot # AG06005006)	76K	4.5	N

In this study, the reaction stoichiometry was adjusted to have the ratio of BPDA to DAM of 1:1. The polycondensation is sensitive to water and minimal exposure to moisture was ensured. The reaction produced polyamic acid, which is the precursor to polyimide. Thermal imidization was chosen to dehydrate the polyamic acid to form a polyimide. The reaction solution was heated to a temperature of  $\sim 180$  °C in order for the imidization to occur [6].



### 3.2.2 Gases

All gases used were provided by Air Products/Air Gas. Pure gases (He, O<sub>2</sub>, N<sub>2</sub>, CO<sub>2</sub>, CH<sub>4</sub>, and SF<sub>6</sub>) were of purity 99.999 % or greater. The kinetic diameters and the critical temperatures of these gases are shown in Table 3.4.

Table 3.4: Kinetic diameters [7] and critical temperatures [8] of gasses used in this work.

Gas penetrants	He	O <sub>2</sub>	N <sub>2</sub>	CO <sub>2</sub>	CH <sub>4</sub>	SF <sub>6</sub>
Kinetic diameter (Å)	2.6	3.46	3.64	3.3	3.8	5.5
Critical temperature (K)	5.2	154.6	126.2	304.2	190.6	318.7

In addition, a mixed 50.0 mol % CH<sub>4</sub> with balance CO<sub>2</sub> was used. Mixed gases of argon with a specific amount of oxygen (1-100 ppm O<sub>2</sub>) were used as purge for the “inert” pyrolysis process.

### **3.3 MEMBRANE FORMATION**

Production of CMS membranes involves two steps: (i) formation of polymeric membranes and (ii) pyrolysis of the polymeric membranes. This section describes the procedure to prepare dense film and asymmetric hollow fiber membranes.

#### **3.3.1 Formation of polymeric membranes**

##### 3.3.1.1 Formation of homogeneous films

Homogeneous polymeric dense films were prepared by first drying the polymer powder in a vacuum oven at 110 °C for at least 12 hours to remove moisture. Immediately after removal from the oven, a polymer solution, usually 3-5 wt%, was prepared by dissolving in dichloromethane (99.99% purity from Aldrich), in 40 ml ICHEM vials (Fisher Scientific), and placed on rollers for at least 12 hours. After mixing, dense films were prepared by a solution casting method as shown in Figure 3.2 at room temperature. The polymer solution was placed in a glass syringe, filtered with pressure through a Millex<sup>®</sup>-RH 0.45 micron PTFE filter (Millipore Corporation), and slowly extruded onto the glass surface inside of the stainless steel ring or Teflon dish. An inverted glass funnel with open end covered with a Kimwipe was placed over the solution, or the entire procedure was done in a glove bag to achieve a minimum solvent evaporation rate. It was essential to prepare flat polymeric films to produce flat CMS membranes during the solution casting procedure. In particular with Matrimid<sup>®</sup>, the Teflon dish was preferred to a casting ring because the films produced were flat as shown in Figure 3.3.

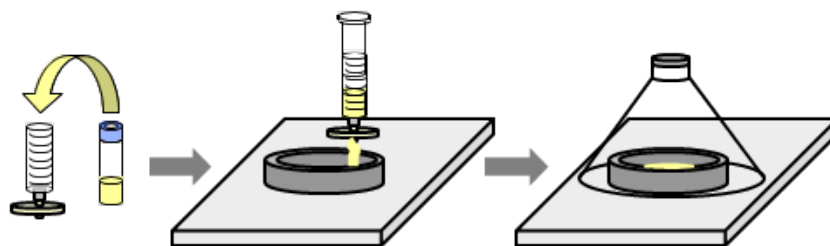
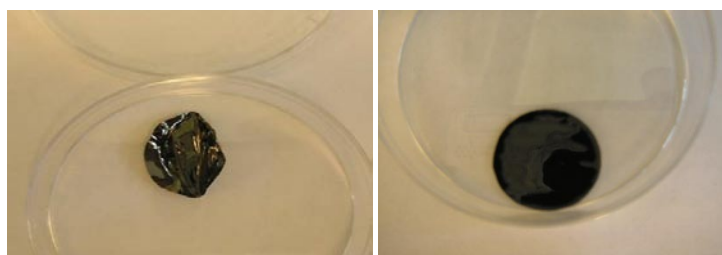


Figure 3.2: Schematic showing the solution-casting method for dense film production.



(a) “Crinkled” CMS films      (b) Flat CMS films

Figure 3.3: Resulting Matrimid<sup>®</sup> CMS membranes with polymer films casted with (a) a ring on a glass plate and (b) a Teflon dish. While a ring casting achieved 44% flat film production rate, the Teflon casting resulted in more than 89% flat film production tested with at least 36 polymeric films.

After the solvent was evaporated, films were removed with tweezers from the casting surface. Occasionally films were removed by lifting the edge of the film with a razor blade and then squirting a few drops of deionized water under the exposed edge. This caused the film to lift off the plate. After the removal, films were placed in the vacuum oven at 110 °C for at least 12 hours to remove residual solvent. Once films were removed from the oven, they were cut into small discs with a one inch die. Any visible stress points in the film during removal from the casting setting were not used for further CMS production. It is also worth mentioning that the disc cutting was one of the critical steps for resulting CMS films to be flat and testable. The film was cut by hitting the die

with a hammer only once to apply uniform forces across the edges. Occasionally, scissors were used to cut out any small attachment points of the films.

### 3.3.1.2 Formation of asymmetric hollow fibers: spinning

For industrial application of novel membrane materials, it is essential to be formed into thin, low cost membranes that can be eventually packed into high surface area modules [9]. Asymmetric hollow fibers are the preferred industrial standard compared with other module configurations, such as spiral wound and plate-in-frame types, because of the high surface area to volume ratios. Asymmetric hollow fiber membrane modules can achieve active surface to volume ratios as high as  $10,000 \text{ m}^2/\text{m}^3$  and offer high productivities [4]. In addition, asymmetric hollow CMS fibers offer higher mechanical strength compared with CMS dense films. These are believed to be caused by the cylindrical geometry of the membrane which consists of the actual separating “skin” layer with the bulk of the membrane acting as support. The support is a porous substructure that ideally has negligible resistance and lies underneath the outer skin layer as shown in Figure 3.4.

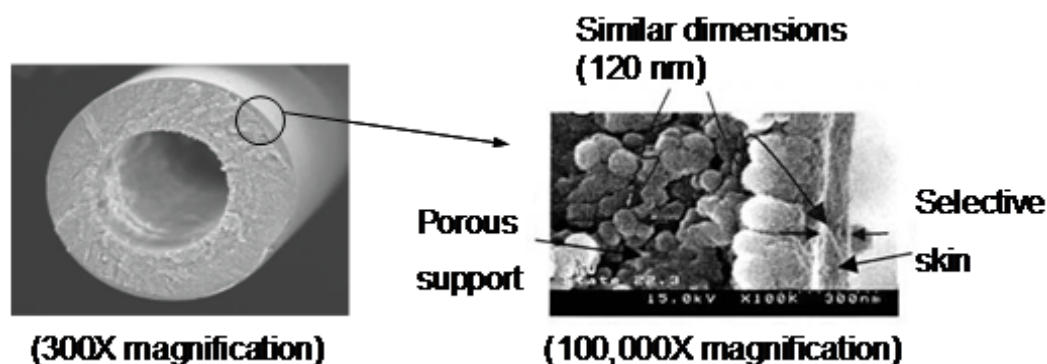


Figure 3.4: SEM images of Matrimid hollow fibers. Characteristic dimensions of the nodular, porous support layer are similar in size to the skin thickness [10].

The process of making asymmetric hollow fiber membranes is called spinning. This occurs by co-extruding a polymer solution and a bore fluid through an annular die called a spinneret into an aqueous quench bath, where the polymer solution precipitates and is drawn up with a take-up device. The method of spinning used in this work is referred to as the dry jet/wet quench method [5, 11-13]. In this process, the polymer solution passes through an air-gap before it precipitates in the aqueous quench bath. The spinning process is depicted in Figure 3.5.

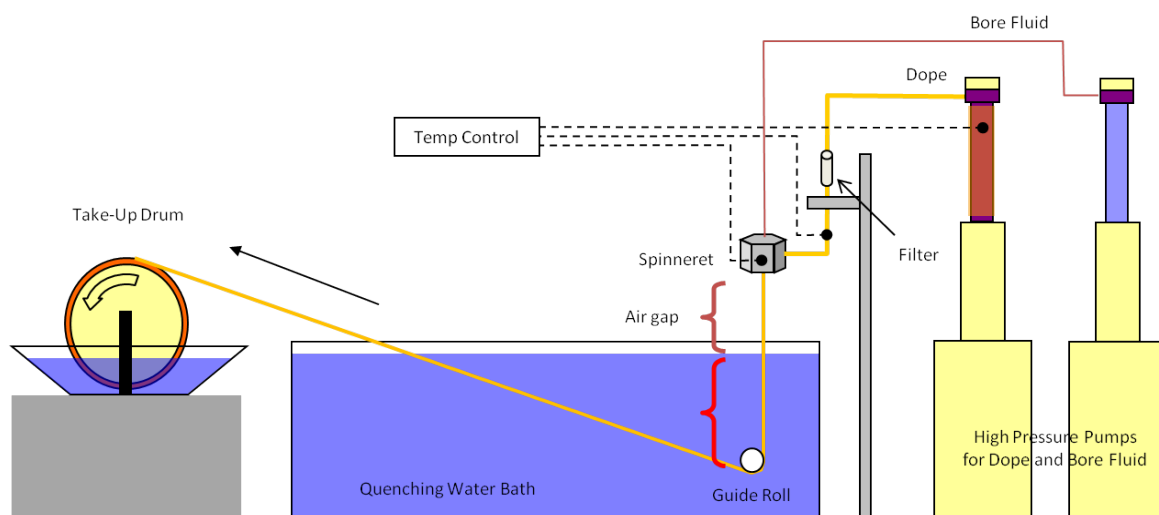


Figure 3.5: Schematic of spinning process for producing asymmetric hollow fiber membranes.

The polymer solution used in making the membranes is commonly called a “dope”. This dope typically consists of the polymer, a solvent, and a non-solvent. N-methylpyrrolidone (NMP) is generally used as the solvent for dopes because it dissolves many of the polyimides used for these applications and is relatively environmentally friendly. The non-solvent is usually chosen to bring the polymer solution close to the two phase unstable region on a ternary phase diagram, shown in Figure 3.6, so that rapid phase separation will occur when the dope is immersed in the quench bath. The non-solvent is

also chosen to be relatively environmentally benign. Water is typically adequate for most of the systems since most of the polymers used for gas separations are hydrophobic. Aliphatic alcohols, such as ethanol, are commonly used as non-solvents, because they provide a greater window for use than water, which tends to be too strong a non-solvent. Additives such as lithium nitrate salts are sometimes used in dopes for various reasons such as viscosity enhancement, phase separation enhancement, and pore formation.

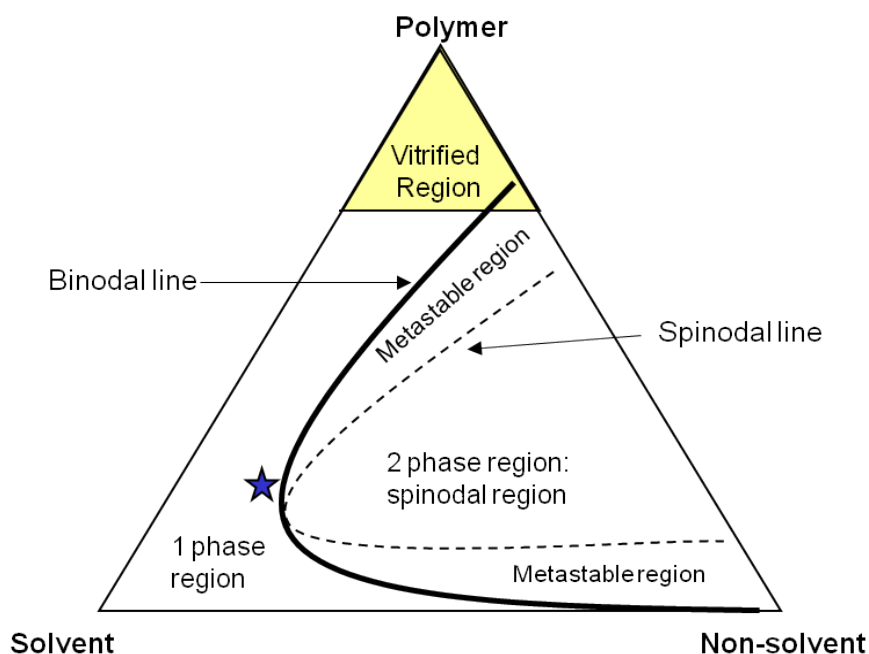


Figure 3.6: Ternary phase diagrams of polymer, solvent, and non-solvent for spinning hollow fibers. On this ternary phase diagram, desired dope composition is represented as a star.

In the ternary phase diagram, the vertices of the triangle represent each of the three pure components, while points on the interior of the triangle represent ternary compositions. Phase diagrams that are relevant to this discussion display a stable one-phase region and an unstable two-phase region where phase separation occurs. Strictly speaking, a metastable two-phase region also exists. In the two-phase region, the polymer solution phase separates into a polymer-lean phase and a polymer-rich phase.

The compositions of these polymer-lean and polymer-rich phases are given by equilibrium tie-lines. The spin dope “A” on Figure 3.7 is formulated to lie close to the two-phase region. While the detailed processes during dry jet/wet quench spinning that causes the outer region of the spinning dope to transition into a defect free skin remains unclear, it is believed that the formation of the defect-free skin and the porous substructure follow two separate composition paths on the ternary phase diagram, as shown in Figure 3.7.

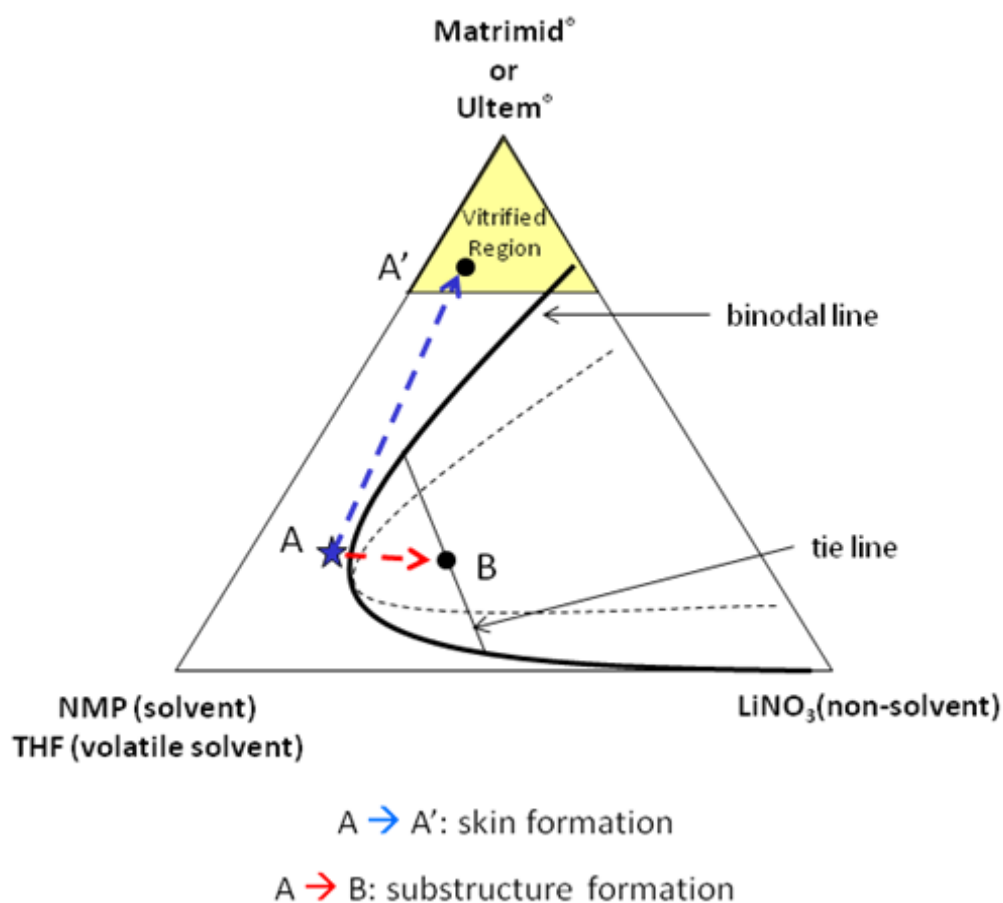


Figure 3.7: Spinning process depicted on a ternary phase diagram.

When the dope passes through the air gap, solvent evaporates from the outer diameter of the fiber, and the outer region of the fiber is represented by “A’,” while the bulk of the

fiber still remains at composition “A.” Upon immersion in the non-solvent bath, solvent efflux and non-solvent influx results in a high non-solvent composition “B” which leads to phase separation along equilibrium tie lines to a polymer rich and lean phase. The composition at “A” is kinetically limited from phase separation if it is sufficiently high in polymer concentration.

Spinning is a complex process and relies upon various parameters, such as composition of dope and bore fluids, air gap, spinneret temperature, extrusion rate, and draw ratio. The draw ratio is defined as the ratio of the take-up to the extrusion rate. Therefore increasing the take-up speed of the fiber at a set extrusion rate increases the draw ratio and ultimately reduces the radial dimensions of the hollow fiber. After a fiber is spun, it is usually dehydrated by exchanging with non-solvent fluids of decreasing surface tension before finally being dried. This fluid exchange is done to minimize capillary forces that would act on the fiber if dried directly from high surface tension fluids like water. Such capillary forces could collapse the porous support. Details of the spinning parameters used in this work are described in chapter 5.



### 3.3.2 Formation of CMS membranes

#### 3.3.2.1 Pyrolysis protocol

The polymer films were placed on a corrugated quartz plate, which was ridged to allow for the diffusion of volatile by-products from the top and bottom of the films into the effluent stream, and loaded into the pyrolysis setup. In order to maintain consistency based on prior optimization, a pyrolysis temperature of 550 °C and a two hour soak time was used, which was the same temperature protocol used in the work by Geiszler and Koros [14], Vu and Koros [15], and Williams [16] as a benchmark. Specifically, the system was heated from room temperature to 50 °C in 15 min and soaked for 15 min, raised to 250 °C in 15 min, from 250 to 535 °C in 74 min, from 535 to 550 °C in 60 min, and soaked for 120 min. In case of the 500 °C protocol, a consistent heating rate and soak time was used and only the final temperature was differed from 550 to 500 °C.

#### 3.3.2.2 Pyrolysis set-up

Initially, a pyrolysis system was equipped with a customized quartz tube as shown in Figure 3.8; however, after many uses by various researchers [1, 16-21] the system was found to be leaky, especially after integrating the oxygen sensor (Cambridge Sensotec Ltd., Rapidox 2100 series, Cambridge, England,  $\pm 1$  % accuracy between  $10^{-20}$  ppm and 100 % [22]). The leaks took place on almost all of the connecting parts, and it prevented one from accurately measuring the oxygen level in the system. Therefore, a new system, depicted below, was designed and constructed.

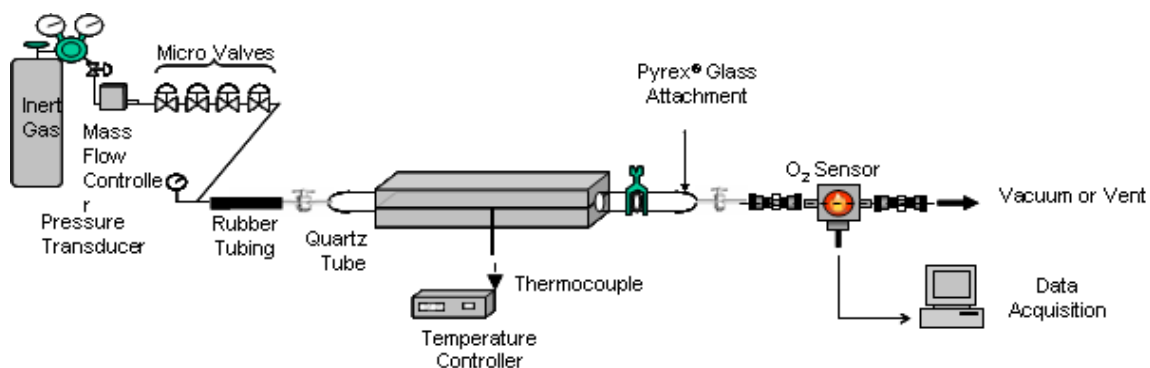


Figure 3.8: Schematic diagram of the old pyrolysis system.

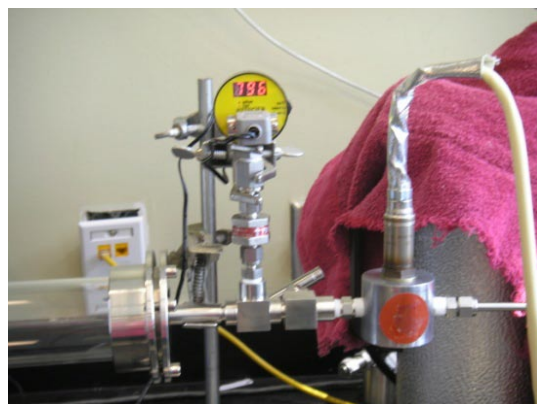
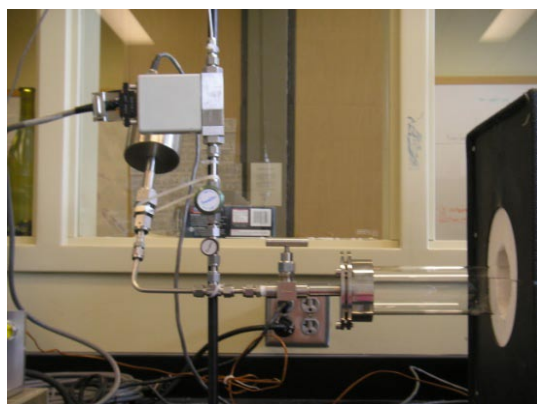
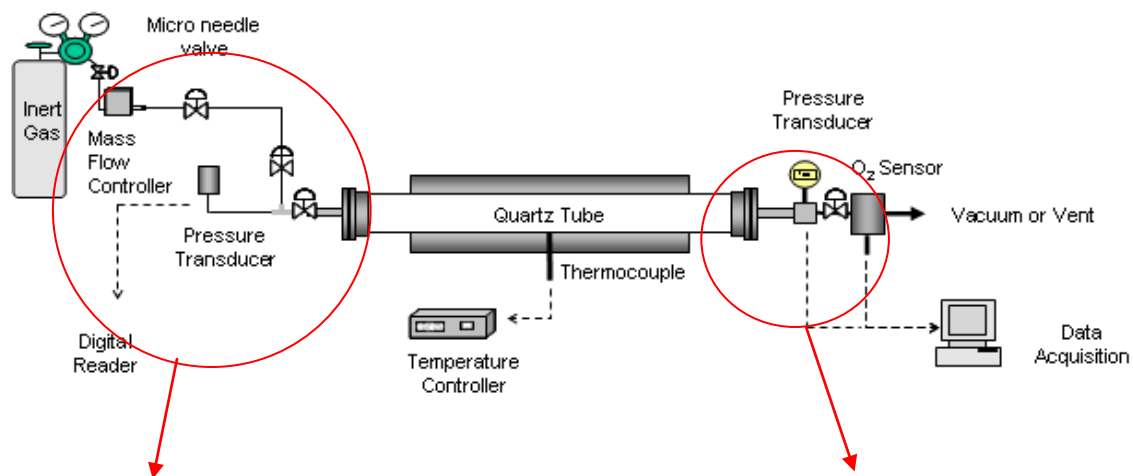


Figure 3.9: Schematic diagram of the new pyrolysis system.

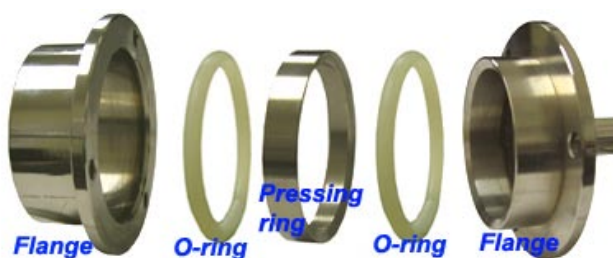


Figure 3.10: Flanges with two silicon O-rings for vacuum tightening (MTI Co., CA).

A new apparatus shown in Figure 3.9 was designed to provide a more controllable system under vacuum and/or an inert purge. Instead of using the customized quartz tube, a cylindrical quartz tube, 55 mm ID x 59 mm OD x 4 ft length (National Scientific, PA) was used. One should note that the cost of the tube was significantly reduced to 1/6 compared with the custom made. The tube is sealed with a flange with two silicon O-rings (described in Figure 3.10) on both ends. The diameter of the quartz tube is slightly larger than before to reduce the gap between furnace wall and the tube. A new pressure reader (MTI Co., CA) was introduced to measure outlet pressure, and a 0.5 micron filter from Swagelok was attached to avoid the accumulation of byproducts from carbonation. A temperature controller (Omega, CT), an upstream pressure transducer (MKS Instrument, MA), and an oxygen analyzer (Cambridge Sensotec Limited, England) from the previous set-up were kept. The transducer, temperature controller, and mass flow controllers (MKS Instrument, MA) were sent to the manufacture for periodic calibrations. All connecting parts, such as T-valves and Swagelok<sup>®</sup> valves, were replaced by new ones. Parts used in the system are listed in Table 3.5.

Table 3.5: List of equipment used to build the pyrolysis system used in this work. Note that equipment marked with “\*” indicates that it was purchased by previous Koros group members. Adjustments on the vacuum sealing assembly were made by GTRI machine shop to have vacuum tight fittings with NPT.

Name of equipments	Specifications and/or catalog number	Manufacture
Furnace*	Model 23-24-1ZH	Thermocraft
Temperature controller	CN8241	Omega
Thermocouple	K-type	Omega
Vacuum pump	Model RV3	Edwards
Pressure reader and power supply	PDR2000	MKS
Pressure transducer	Baratron <sup>®</sup> 628B capacitance manometer (0.5 % accuracy below 1 torr)	MKS
Quartz tube	55mm ID and 4 ft long	National Scientific Company
Quartz sample folder plate*		
Vacuum sealing assembly	Model EQ-FI-60	MTI Corporation
High temperature silicone O-rings	60mm diam.	MTI Corporation
SS tubings and bellow & needle valves		Swagelok
Oxygen analyzer	Rapidox 2100	Cambridge Sensotec Ltd
Desktop computer		Dell
Mass flow controller	Type 247	MKS
Bubble flow meter	Model 520	Fisher Scientific
Micron filter	Nupro FW Filter 0.5	Swagelok

After assembling, leak tests were performed and to confirm that the pressure of 0.005 torr was maintained for at least the duration of pyrolysis even with both system ends closed. In addition, an inert pyrolysis blank run was performed as follows: pyrolysis experiments were run with argon flow of 200 cc(STP)/min and the oxygen level was monitored using the oxygen analyzer. The resulting baseline is shown in Figure 3.11.

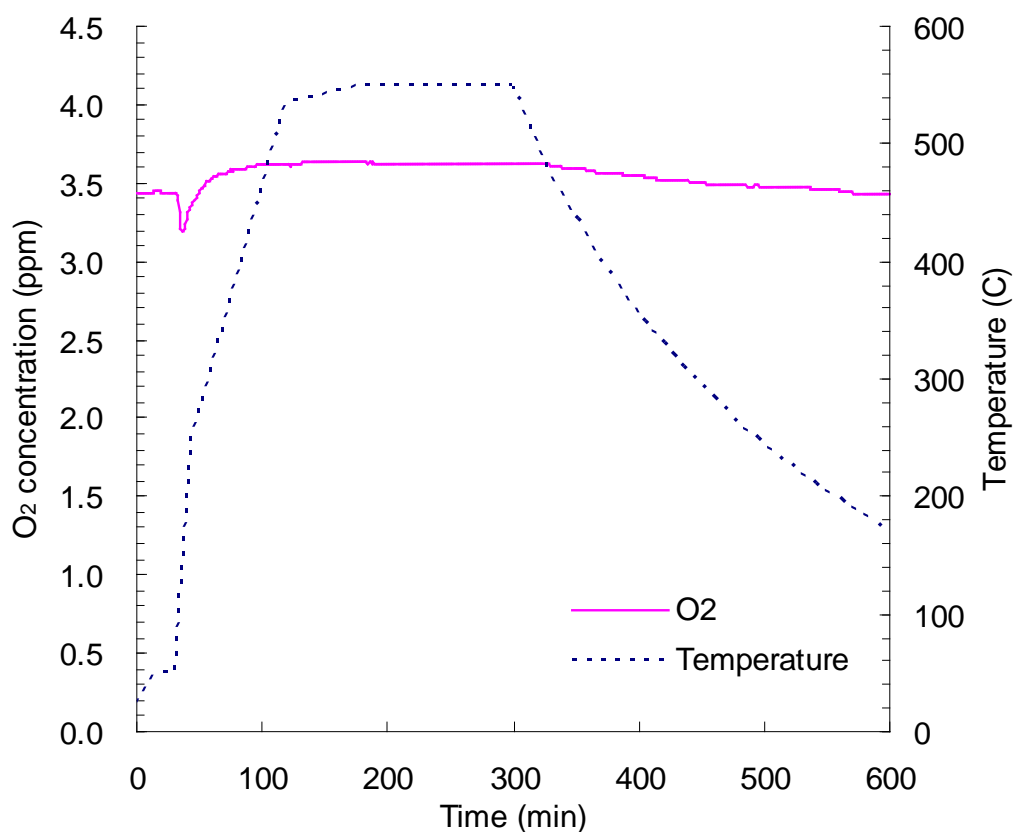


Figure 3.11: Baseline after installing a new pyrolysis tube.

This baseline experiment was repeated twice and similar results were observed. The constant oxygen level in the baselines indicates a negligible leak and negligible oxygen chemisorption on the system, these confirming that pyrolysis system was successfully constructed.

Pyrolysis atmospheres consisted of either continuous vacuum or continuous inert gas. For vacuum pyrolysis, a pump (Edwards) was used to create a low pressure, below 0.005 torr, and a liquid nitrogen trap was used to prevent any back diffusion of oil vapor. The pressure inside the tube was monitored by a pressure transducer (MKS Instruments) attached to a readout (MKS Instruments). For experiments using purged gas during pyrolysis, the flow rate of the gas was controlled with a mass flow controller (MKS Instruments) and confirmed with a bubble flow meter (Fisher Scientific) before and after each experiment. Between experiments, the quartz tube and plate were rinsed with acetone (Aldrich) and baked in air at 800 °C to remove any deposited materials which could affect consecutive runs.

#### 3.3.2.3 Pyrolysis system cleaning

Pyrolysis of polyimide materials produces large amounts of evolved by-products, which were observed to deposit on the inner tube surface. In particular, it was observed that Matrimid<sup>®</sup> produces more “debris” than 6FDA/BPDA-DAM or Ultem<sup>®</sup>. In order to prevent any of the by-products from consuming oxygen during pyrolysis, the tube was cleaned prior to each experiment. As mentioned earlier, the cleaning normally involved two steps: (i) rinsing the entire tube in acetone with a bundle of long handled bottle brushes and (ii) burning out at 800 °C for at least 2 hours. It was important to use acetone instead of tap water since minerals calcinate and reside after burning, which made it impossible to remove them afterwards. When this cleaning procedure was found to be ineffective after many pyrolysis runs, the tube was treated with more care. First, the surface was cleaned with base solution. This was done by first rinsing it with laboratory detergent (Alconox, NY) and DI water. Then the surface was washed in KOH (8M) with a bundle of long handled bottle brushes (McMaster-Carr). Since brown deposits were still observed adhering to the surface, the tube was filled with KOH solution overnight

(>12 hours.) After the soak, the tube was rinsed with DI water and acetone to remove oils from fingerprints or other organic contaminants. In order to remove any residual solvent, the tube was burned out at 800 °C for 2 hours. If any additional oxygen consumption was observed by the baseline experiments, acid cleaning was used to remove remaining residuals on the surface. The quartz tube was first washed with the laboratory detergent and rinsed with HF solution (5% by vol.) for 5 min. The concentration and duration of HF cleaning were carefully measured. After cleaning with acid, the tube was rinsed with DI water and acetone and burned at 800 °C for 2 hours. When this procedure was used, water condensation was sometimes observed during the burn out as a result of HF “eating” the quartz surface [23]. This indicates that most of the residuals on the surface were removed, and silicon surface was exposed, leaving the pyrolysis system free of oxygen consumption during pyrolysis.

### **3.4 MEMBRANE CHARACTERIZATION**

#### **3.4.1 Permeation**

Once dense films and asymmetric hollow fiber membranes were prepared, permeation experiments were conducted as a part of membrane characterization.

##### **3.4.1.1 Dense film permeation**

After dense films were prepared as described in section 3.3.1.1 (polymeric films) and 3.3.2 (CMS films), the samples were immediately loaded into permeation cells, usually within 24 hours to minimize humidity exposure especially on CMS membranes. The films were first masked using impermeable aluminum tape, and only a specific area was exposed for permeation. Five minute epoxy (Devcon, Danvers, MA) was applied at

the interface of the tape and the film to further minimize any gas leak. This assembly was placed in a double O-ring flange permeation cell as depicted in Figure 3.12.

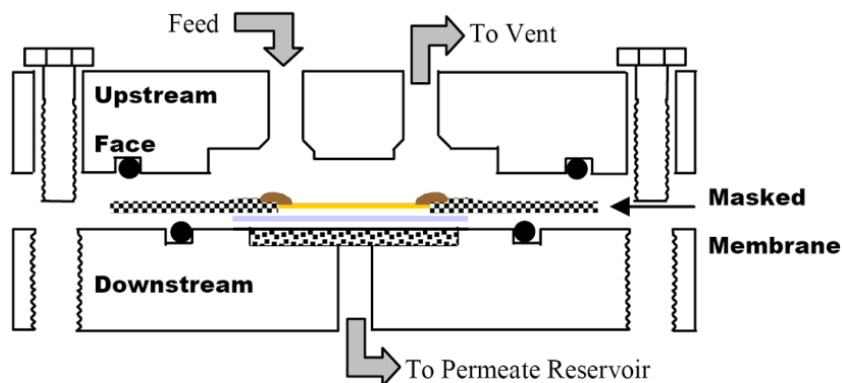


Figure 3.12: Schematic of a permeation cell. A cross section through the cell is shown with a “sandwich” type masked membrane. The membrane assembly is composed of membrane (yellow), filter paper (light gray), epoxy (brown), adhesive backed aluminum (chequered). Bolts at both ends and O-rings shown by solid black circles assure a leak tight seal [24].

The cell was placed in a permeation system in which a constant-volume variable-pressure method [25, 26] was applied. The schematic of the isochoric variable pressure permeation system is depicted in Figure 3.13.





$$P = \frac{(1.1583 \times 10^3) \cdot \left(\frac{dp}{dt}\right) \cdot l \cdot V_R}{A \cdot T \cdot \Delta p} \quad (3.1)$$

where  $dp/dt$  is in torr/min,  $l$  is the membrane thickness in microns,  $V_R$  is the downstream reservoir volume in  $\text{cm}^3$ , which was calibrated using the ideal gas law,  $T$  is the operating temperature in Kelvin, and  $\Delta p$  is transmembrane pressure in psi. The permeability,  $P$ , is in the units of Barrer as defined below:

$$\text{Barrer} = 10^{-10} \frac{\text{cc(STP)} \cdot \text{cm}}{\text{cm}^2 \cdot \text{cmHg} \cdot \text{s}} \quad (3.2)$$

The system was evacuated each time before experiments with different gases for at least 12 hours for CMS membranes and for at least ten times the time-lag for polymeric membranes.

#### 3.4.1.2 Asymmetric hollow fiber permeation

Hollow fibers were potted into modules according to the method described by Wallace [27]. The modules contained fibers with active membrane lengths varying from ~5-20 cm depending on the types of fibers and permeation experiments performed (pure or mixed gas). The number of fibers in a module was also chosen depending on the type of permeation to be performed. For polymeric hollow fibers, for instance, as many as 40 fibers in a module could be used for pure gas experiments; however, for mixed gas permeation experiments, the number of fibers is reduced to 1-2 to reduce the membrane surface area for the experiments. A lower surface area reduces the amount of gas that is vented off the retentate stream since the stage cuts used are typically less than 1% (see section 3.4.1.2.2 for more information on mixed gas experimental set-up). The reasons

for the low stage cuts are explained in the same section. The pictures below in Figure 3.14 shows typical hollow fiber module, and the module assembly is described in Appendix A.

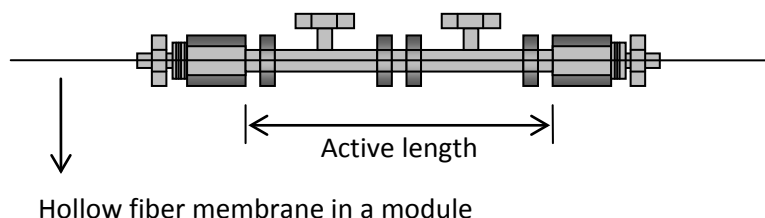


Figure 3.14: Schematic showing a hollow fiber membrane in a module housing.

#### *3.4.1.2.1 Hollow fiber pure gas permeation*

Counter-current flow scheme with the bore side feed was used to conduct pure gas permeation. The entire feed stream permeates through the membrane and is collected only on the permeate side, the shell side, where the flow-rate can be measured using a bubble flow-meter. Figure 3.15 shows a schematic of the pure gas permeation set-up for asymmetric hollow fibers.

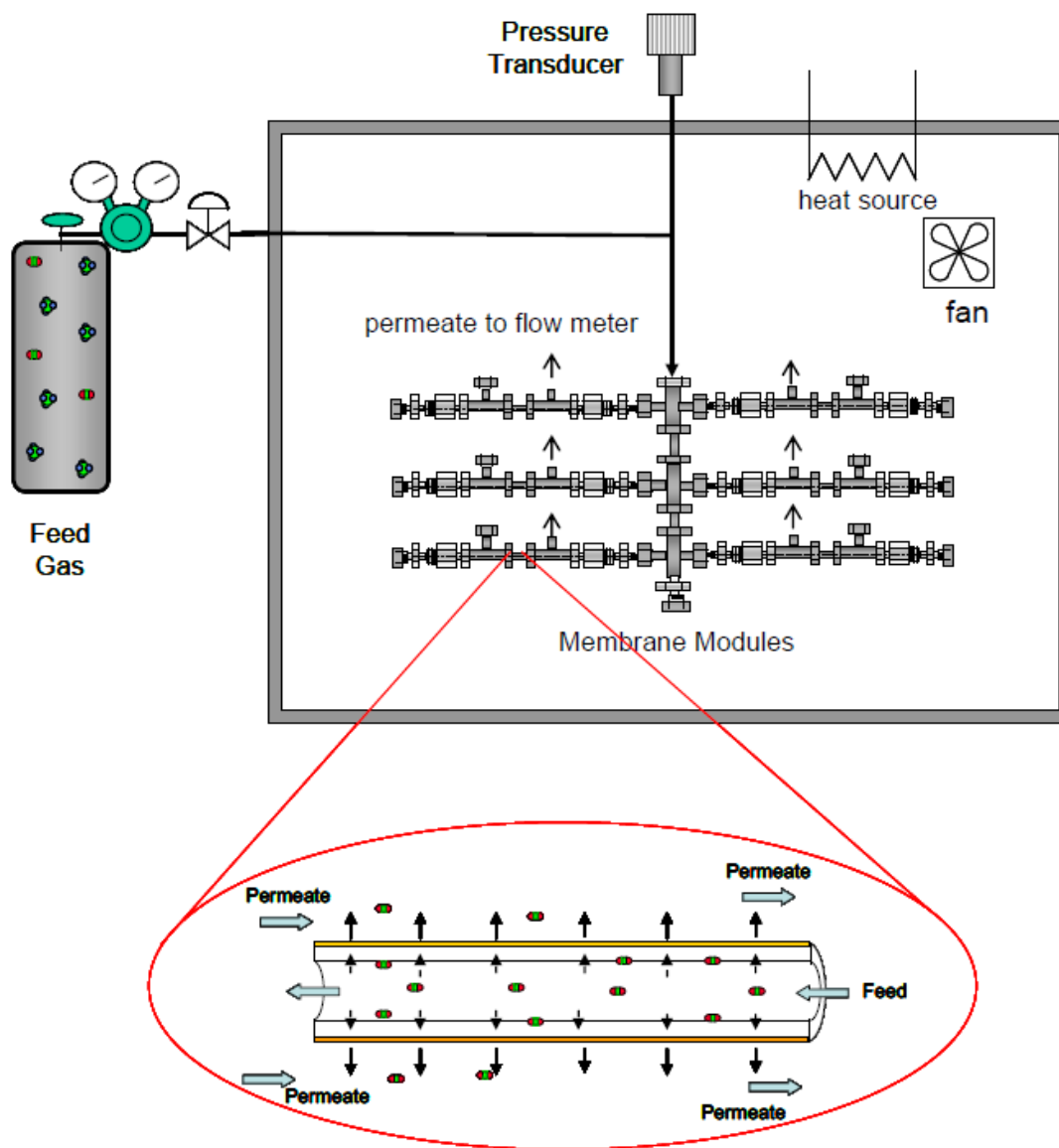


Figure 3.15: A schematic of the pure gas permeation set-up for asymmetric hollow fiber membranes [6]. In this figure, six modules are connected to the feed and could be tested simultaneously.

This configuration allows for multiple fiber modules to be tested head-on, with a common feed and under the same test conditions. The permeance ( $P/l$ ) can be obtained from multiple modules at the same time using the following equations:

$$\frac{P}{l} = 10^{-6} \cdot \frac{(v_p) \cdot 273.15}{5.17 \cdot A \cdot T \cdot \Delta p} \quad (3.3)$$

where  $v_p$  is the volumetric flowrates in cc(STP)/sec,  $T$  is the operating temperature in Kelvin,  $A$  is the membrane area in  $\text{cm}^2$ , and  $\Delta p$  is the transmembrane pressure in psia. The permeance ( $P/l$ ) is in the units of GPU, which is defined as:

$$GPU = 10^{-6} \frac{\text{cc(STP)}}{\text{cm}^2 \cdot \text{cmHg} \cdot \text{s}} \quad (3.4)$$

#### 3.4.1.2.2 Hollow fiber mixed gas permeation

Mixed gas permeation experiments were carried out using a counter-current flow scheme with the feed on the shell side of the hollow fibers. The feed stream flows over the surface of the membrane and the permeate flux is controlled by a needle valve on the retentate side. The percentage of the feed that permeate through the membrane is called the stage cut. In determining intrinsic membrane properties, stage-cuts less than 1% were used to minimize concentration polarization and to minimize feed composition variation, as the membrane selectively permeates the penetrants along the module. The permeate stream, collected on the bore side, is measured with a bubble flow-meter to determine the flux and can also be sent to a GC (EG&G Chandler Engineering Carle AGC Series 100, OK) to analyze the compositions. A schematic of mixed gas permeation set-up is shown in Figure 3.16.

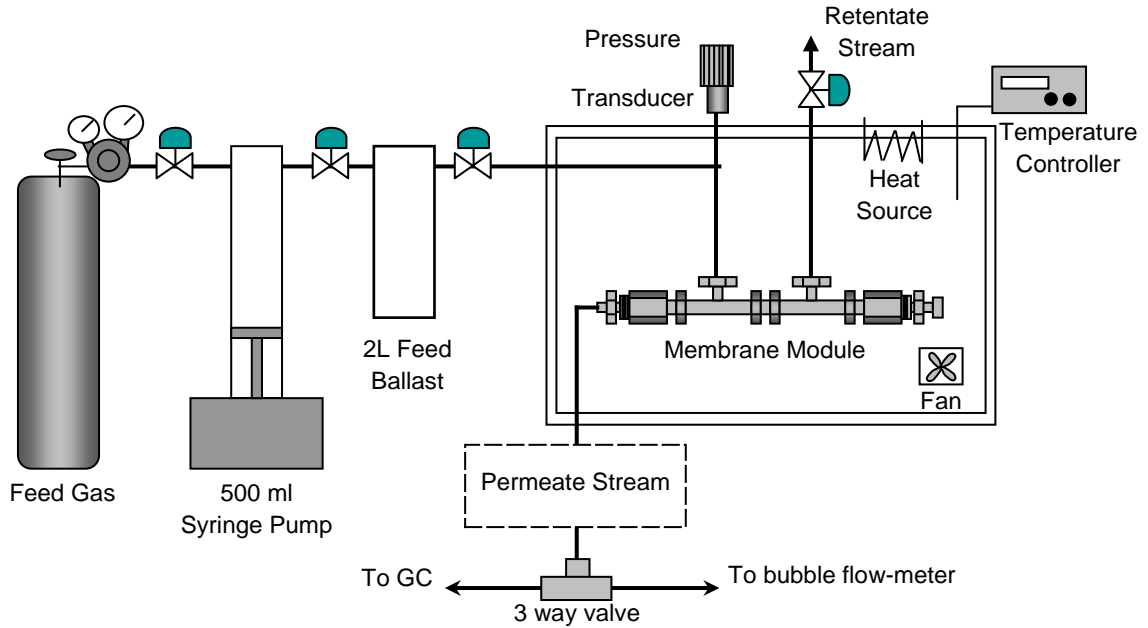


Figure 3.16: Schematic showing a variable volume system.

Using the set-up shown in Figure 3.16, the permeance,  $P_i/l$  in GPU, is obtained by following equation:

$$\frac{P_i}{l} = 10^{-6} \cdot \frac{v_p \cdot y_i \cdot 273.15}{5.17 \cdot A \cdot T \cdot (p_y \cdot \phi_{x,i} \cdot x_i - p_y \cdot \phi_{y,i} \cdot y_i)} \quad (3.5)$$

where  $l$  is the membrane thickness,  $v_p$  is the volumetric flow-rate of permeate in cc/sec,  $y_i$  is mole fraction of component  $i$  in permeate,  $x_i$  is mole fraction of component  $i$  in the upstream, which is essentially equal to the mole fraction of  $i$  in the feed at low stage cut,  $A$  is the membrane active area in  $\text{cm}^2$ ,  $T$  is the testing temperature in Kelvin,  $p_x$  and  $p_y$  are feed and permeate pressures respectively in psia, and  $\phi_{xi}$  and  $\phi_{yi}$  are fugacity coefficients of component  $i$  in the upstream and permeate streams respectively. Most of the work was done with ambient permeate pressure, and when it was necessary, a backpressure regulator was used to vary the permeate pressure.

### 3.4.2 Sorption

In this study, a pressure decay method [28, 29] was mainly used to measure sorption capacity of samples. In the pressure decay method, the equilibrium sorbed concentration at a given pressure can be used to calculate the solubility coefficient. The pressure decay sorption system is depicted in Figure 3.17.

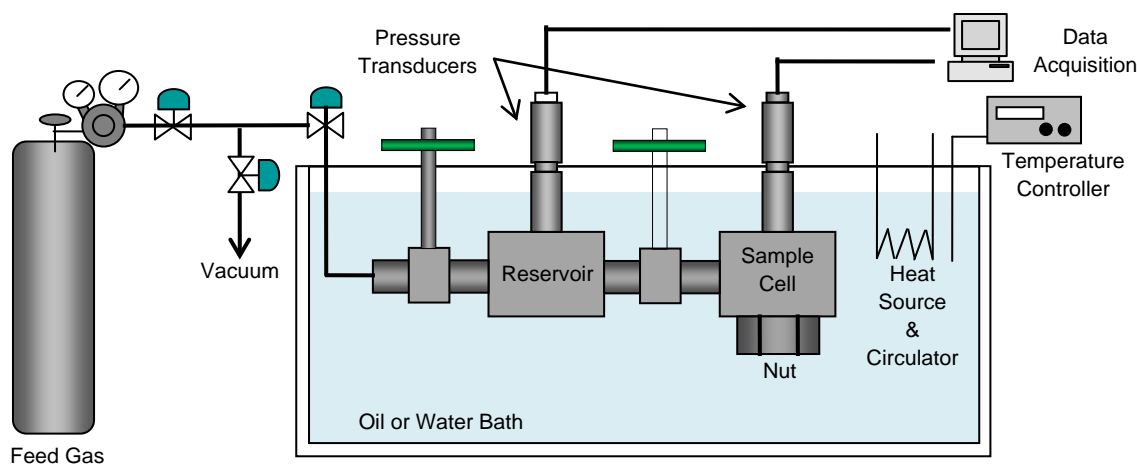


Figure 3.17: Schematic of pressure decay sorption system used for gas sorption experiments.

Once samples were loaded, the system was evacuated for ~24 hours. A feed reservoir was pressurized with a certain amount of gas, allowing the system to equilibrate thermally. The entire system was kept in a heated water bath with a circulator to maintain constant temperature. Once the feed reservoir came to equilibrium, the pressure valve between the feed and the sample cell was opened and then quickly closed to introduce a dose of the feed gas into the cell. The pressure in both chambers was monitored with pressure transducers. The amount of gas sorbed was then calculated using a mole balance shown below:

$$n_P = \frac{1}{R \cdot T} \cdot \left[ (V_C - V_{CMS}) \cdot \left( \frac{p_{C,i}}{z_i \cdot p_{C,i}} - \frac{p_{C,f}}{z_f \cdot p_{C,f}} \right) + V_R \cdot \left( \frac{p_{R,i}}{z_i \cdot p_{R,i}} - \frac{p_{R,f}}{z_f \cdot p_{R,f}} \right) \right] \quad (3.6)$$

where  $n_P$  is the amount of gas sorbed into the CMS samples at equilibrium,  $T$  is the temperature,  $R$  is the ideal constant,  $V_C$  is the volume of the sample cell,  $V_{CMS}$  is the volume of CMS sample,  $V_R$  is the volume of reservoir,  $p_{C,i}$  is the initial pressure of the sample cell,  $p_{C,f}$  is the final pressure of the sample cell,  $p_{R,i}$  is the initial pressure of the reservoir,  $p_{R,f}$  is the final pressure of the reservoir, and  $z$  is the compressibility factor for the testing gas at the pressures measured. The compressibility factors were obtained using software Supertrapp (NIST) and used to correct for non-idealities.

#### **3.4.3 Fourier transform infra-red spectroscopy (FTIR)**

The FTIR was done using a Bruker Tensor 27 FTIR spectrometer. For polymer powder, samples were analyzed using a Harrick MVP2 micro ATR with at least 32 scans at a resolution of 2 cm<sup>-1</sup>.

#### **3.4.4 Thermal gravimetric analysis (TGA)**

TGA was performed to analyze the decomposition process on polymeric samples. TGA was provided from Netzsch, STA 409 PC Luxx TGA/DSC.

#### **3.4.5 Thermal gravimetric analysis connected with FTIR (TGA-IR)**

Thermal gravimetric analysis combined with Fourier transform infrared spectroscopy (TGA-FTIR), provided from Netzsch, STA 409 PC Luxx TGA/DSC) was performed to characterize the decomposition process of polymers.



### **3.4.6 Gel permeation chromatography (GPC)**

Molecular weight (MW) and polydispersity index (PDI) of polymer batches were obtained by dissolving the polymer in solvent THF at 10 mg/ml. The 1 ml samples were filtered through a Millex<sup>®</sup>-FG 0.20 micron PTFE filter (Millipore Corporation) into 2 ml vial before analysis and loaded into Viscotek GPCmax VE2001 GPC solvent/sample module, which was located in Prof. Jones laboratory at Georgia Institute of Technology.

### **3.4.7 Nuclear Magnetic Resonance Spectroscopy (NMR)**

<sup>1</sup>H NMR experiments were done in solution. The solution NMR studies were performed by dissolving samples in deuterated dimethyl sulfoxide (DMSO) at ~2.5 wt%. The solutions were analyzed using a Varian Mercury Vx 300 spectrometer.

### **3.4.8 Differential scanning calorimetry (DSC)**

DSC was performed to determine the glass transition temperature ( $T_g$ ) of polymers with a Seiko DSC 220. It was located in Prof. Shofner laboratory at Georgia Institute of Technology.

### **3.4.9 Density gradient column**

The densities of membranes were determined using a Techne density gradient column. The 70 cm long column was prepared by mixing solutions of calcium nitrate and water, placed in a water bath, and temperature controlled using a temperature controller. The density gradient in the column was calibrated using glass balls calibrated to  $\pm 0.0001 \text{ g/cm}^3$  from Techne.

#### **3.4.10 Scanning electron microscopy (SEM)**

SEM images were obtained by first cryogenically fracturing the fibers in liquid nitrogen. Most times, fibers were soaked in hexane prior to fracturing in liquid nitrogen. This helped to freeze the fibers and ensure a smooth cut. The machine used in this work was a LEO 1530 thermally assisted field emission (TFE) scanning electron microscope. For polymeric fibers, samples were coated with gold prior to experiments.

#### **3.4.11 Wide angle X-ray diffraction (XRD)**

XRD was performed to analyze pore sizes of porous materials using a Phillips Panalytical X-ray diffractometer in Prof. Nair's laboratory at Georgia Institute of Technology.

### 3.5 REFERENCES

- [1] Jones CW, Koros WJ. Carbon molecular sieve gas separation membranes-I. Preparation and characterization based on polyimide precursors. *Carbon* 1994; 32(8):1419-25.
- [2] Jones CW, Koros WJ. Carbon molecular sieve gas separation membranes-II. Regeneration following organic exposure. *Carbon* 1994; 32(8):1427-32.
- [3] Husain S. Mixed matrix dual layer hollow fiber membranes for natural gas separation. Atlanta GA USA, Georgia Institute of Technology, 2006.
- [4] Kesting RE, K. FA. Polymeric gas separation membranes. New York: John Wiley and Sons Inc.; 1993.
- [5] Carruthers SB, Ramos GL, Koros WJ. Morphology of integral-skin layers in hollow-fiber gas separation membranes. *J Appl Polym Sci* 2003; 90:399-411.
- [6] Omole IC. Crosslinked polyimide hollow fiber membranes for aggressive natural gas feed streams. Atlanta GA USA, Georgia Institute of Technology, PhD thesis, 2008.
- [7] Mulder M. Basic principles of membrane technology. 2nd ed. Dordrecht Netherlands: Kluwer Academic Publishers; 1997.
- [8] Green DW, Perry RH. Perry's chemical engineer's handbook. 8th ed.: McGraw-Hill; 2008.
- [9] Baker RW. Future directions of membrane gas separation technology. *Ind Eng Chem Res* 2002; 41:1393-411.
- [10] Punsalan DT. A sorption and dilation investigation of amorphous glassy polymers and physical aging. Austin TX USA, University of Texas at Austin, 2001.
- [11] McKelvey SA, Clausi DT, Koros WJ. A guide to establishing hollow fiber macroscopic properties for membrane applications. *J Membr Sci* 1997; 124:223-32.
- [12] Pesek SC, Koros WJ. Aqueous quenched asymmetric polysulfone membranes prepared by dry/wet phase separation. *J Membr Sci* 1993; 81:71-88.
- [13] Pesek SC, Koros WJ. Aqueous quenched asymmetric polysulfone hollow fibers prepared by dry/wet phase separation. *J Membr Sci* 1994; 1994:1-19.
- [14] Geiszler VC, Koros WJ. Effects of polyimide pyrolysis conditions on carbon molecular sieve membrane properties. *Ind Eng Chem Res* 1996; 35(9):2999-3003.
- [15] Vu DQ, Koros WJ, Miller SJ. High pressure CO<sub>2</sub>/CH<sub>4</sub> separation using carbon molecular sieve hollow fiber membranes. *Ind Eng Chem Res* 2002; 41(3):367-80.
- [16] Williams PJ. Analysis of factors influencing the performance of CMS membrane for gas separation. Atlanta GA USA, Georgia Institute of Technology, PhD thesis, 2006.

- [17] Geiszler VC, Koros WJ. Polyimide precursors for carbon molecular sieve membranes. Austin, TX, University of Texas at Austin, 1997.
- [18] Perry JD. Formation and characterization of hybrid membranes utilizing high-performance polyimides and carbon molecular sieves. Atlanta GA USA, Georgia Institute of Technology, 2007.
- [19] Singh A. Membrane materials with enhanced selectivity: an entropic interpretation. Austin TX USA, The University of Texas at Austin, PhD thesis, 1997.
- [20] Steel KM. Carbon membranes for challenging gas separations. Austin TX USA, The University of Texas at Austin, PhD thesis, 2000.
- [21] Vu DQ. Formation and characterization of asymmetric carbon molecular sieve and mixed matrix membranes for natural gas purification. Austin TX USA, University of Texas at Austin, PhD thesis, 2001.
- [22] Rapidox 2100 oxygen analyser instruction manual. Cambridge, England: Cambridge Sensotec Limited; 2004.
- [23] Iler RK. The chemistry of silica: Solubility, polymerization, colloid and surface properties and biochemistry of silica. New York: John Wiley & Sons; 1979.
- [24] Moore TT. Effects of materials, processing, and operating conditions on the morphology and gas transport properties of mixed matrix membranes. Austin TX USA, University of Texas at Austin, 2004.
- [25] Pye DG, Hoehn HH, Panar M. Measurement of gas permeability of polymers. I. Permeabilities in constant volume/variable pressure apparatus. *J Appl Polym Sci* 1976; 20(7):1921-31.
- [26] Pye DG, Hoehn HH, Panar M. Measurement of gas permeability of polymers. II. Apparatus for the determination of permeabilities of mixed gases and vapors. *J Appl Polym Sci* 1976; 20(2):287-301.
- [27] Wallace DW. Crosslinked hollow fiber membranes for natural gas purification and their manufacture from novel polymers. Austin TX USA, University of Texas at Austin, 2004.
- [28] Costello LM, Koros WJ. Temperature dependence of gas sorption and transport properties in polymers: measurement and applications. *Ind Eng Chem Res* 1992; 31(12):2708-14.
- [29] Koros WJ, Paul DR. Design considerations for measurements of gas sorption in polymers by pressure decay. *J Polym Sci, Polym Phys Ed* 1976; 14(10):1903-7.

## **CHAPTER 4**

### **DEVELOPMENT OF EFFECTIVE “INERT” PYROLYSIS CONDITIONS FOR ATTRACTIVE CMS MEMBRANES**

#### **4.1 INTRODUCTION AND OVERVIEW**

##### **4.1.1 Effect of pyrolysis atmosphere on separation performance of CMS membranes**

Gas separation performance of CMS membranes depends on the critical pore size and the pore size distribution. These properties are known to be affected by many factors, such as polymer precursor [1-5] and pyrolysis temperature [4-6]. The effect of pyrolysis atmosphere has also been investigated and identified as one of the key factors. When vacuum and inert pyrolysis are compared, some researchers observed that an inert pyrolysis provides much higher permeability and lower selectivity [5, 7, 8]. To the contrary, Suda and Haraya reported that CMS films prepared from polyimide Kapton<sup>®</sup> at 1000 °C in either argon or in high vacuum of  $10^{-5}$  torr showed negligible differences [9]. Geiszler and Koros conducted work on asymmetric hollow fiber CMS membranes using 6FDA/BPDA-DAM and reported negligible differences between fibers produced under argon, helium, and carbon dioxide inerts for both O<sub>2</sub>/N<sub>2</sub> and H<sub>2</sub>/N<sub>2</sub> separations [7]. When high vs. low inert flows were compared, Geizler observed that the inert purge flow rate per se does not have a significant impact on a permeability of CMS membranes within the standard deviations of  $\pm 20$  % typically observed for CMS membranes [7] formed under the same conditions. These various discrepancies reveal the need to identify at least one additional factor to unite and explain the rather disparate observations in this CMS field, and this chapter addresses this need.

#### 4.1.2 Effect of oxygen exposure on separation performance

To explain the discrepancies between reported studies regarding effects of the pyrolysis atmosphere, a hypothesis regarding CMS formation was proposed. The hypothesis relates the formation mechanism to the amount of oxygen exposure during pyrolysis as the key missing factor controlling CMS properties. As mentioned in chapter 2, CMS consists of irregularly packed sheets of  $sp^2$  hybridized carbon. The CMS structures illustrated in Figure 2.4 have micropores providing adsorption sites and ultramicropores acting as molecular sieve sites. These ultramicropores are speculated to be created at “kinks or defects” in the carbon sheet or at the edge of a carbon sheet. These sites have more reactive unpaired sigma electrons prone to oxidation as compared to other sites in the membrane [10-12]. In fact, studies on the electrochemical oxidation of carbon give evidence that the rate of gas-phase oxidation of carbon on the edge plane is close to 20 times greater than on the basal plane [10]. In addition, various characterizations have been performed by prior researchers to indicate the existence of chemisorbed oxygen. Ishiguro et al. showed FTIR spectrum that indicates existence of the C-O bonding group on carbon samples heated at  $\sim 500^\circ\text{C}$  [13]. When pyrolyzed in the presence of oxygen, it is hypothesized that oxygen reacts and binds to the reactive sites on CMS membranes at locations comprising the ultramicropores, thereby narrowing the average ultramicropore size. This process, in turn, is hypothesized to lower the permeability of the membrane, and to increase the selectivity. A schematic drawing of this hypothetical process is depicted in Figure 4.1. Tests of the above hypothesis are discussed in section 4.2.

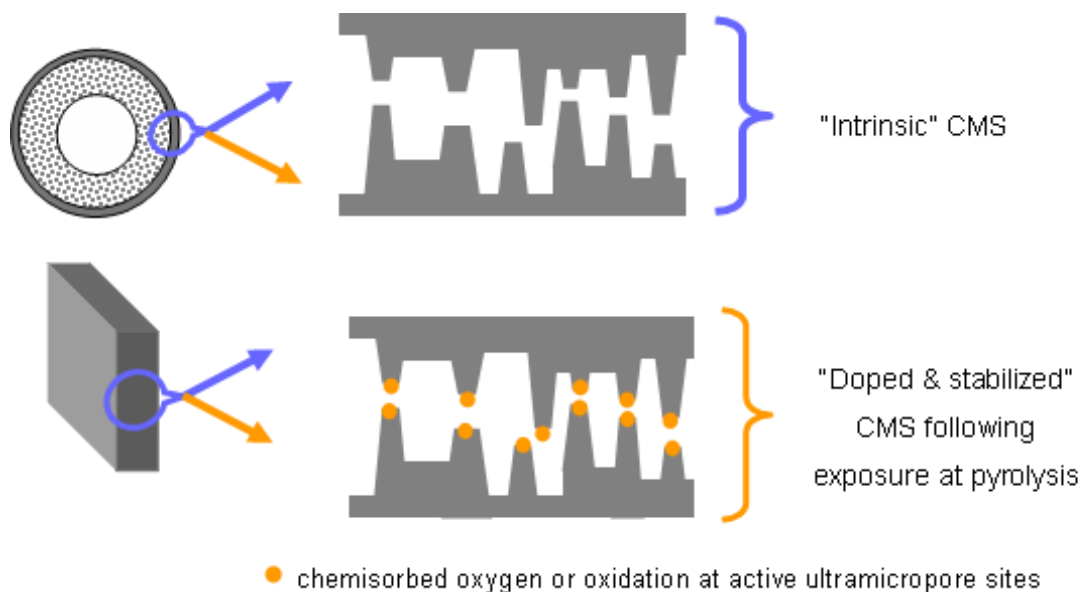


Figure 4.1: Schematic of oxygen “doping” process during pyrolysis.

The exact mechanism of the oxidation reaction that takes place during formation of pyrolytic carbon is not fully known, but as mentioned above, studies have shown that three stable oxides, CO, CO<sub>2</sub>, and surface oxides, such as carbonyls, are produced by oxygen molecules during the electrochemical oxidation on carbon [11, 12, 14]. de Soete showed measured adsorption and desorption rates of oxides at temperatures between 350 and 700 °C using high surface area active carbons and concluded that the adsorption is the limiting step [15]. During CMS formation, the main source of oxygen in the pyrolysis system comes from the pyrolysis atmosphere. As the highly reactive pores on the surface are oxidized, oxygen diffuses into the membrane and reacts with the next available site. The limiting step of this complex carbon-oxygen reaction is investigated in section 4.3 and hypothetical reaction mechanisms are proposed in section 4.4.

## 4.2 EFFECT OF OXYGEN EXPOSURE ON CMS MEMBRANES

The oxygen doping method described in section 4.1.2 was tested using two polymer precursors: in house synthesized polyimide, 6FDA/BPDA-DAM (1:1), and a commercially available polymer, Matrimid<sup>®</sup>. The 6FDA/BPDA-DAM was chosen due to (i) high gas separation performance among other polymer materials prior to pyrolysis processing and (ii) data availability for benchmarking against literature and against data from previous Koros group members. Among many commercial polymers, Matrimid<sup>®</sup> and Ultem<sup>®</sup> were chosen due to ease of accessability and processability, and their attractive CMS separation performance [3, 8, 16-21]. Between Matrimid<sup>®</sup> and Ultem<sup>®</sup>, Matrimid<sup>®</sup> was chosen because of its high glass transition temperature ( $T_g$ ) and mechanical strength. Also it was observed that Ultem<sup>®</sup> CMS films broke into small pieces due to its softening point around 230 °C while Matrimid<sup>®</sup> CMS films remained evenly flat. A pyrolysis temperature of 550 °C and a two hour soak time was chosen to observe effectiveness of the oxygen doping process. By creating more permeable and larger numbers of ultramicropore windows with 550 °C pyrolysis protocol [8], compared with higher temperature such as 800 °C, the probability of oxygen to penetrate and be sorbed during the doping process increases. This makes the oxygen “doping” process more efficient. The purge gas of argon with specific amount of oxygen in ppm level was supplied by AirGas.



## 4.2.1 6FDA/BPDA-DAM CMS membranes

### 4.2.1.1 Weight loss

After each pyrolysis experiment, percentage weight losses were calculated using Equation 4.1.

$$\% \text{ weight loss} = \frac{(\text{weight})_{\text{before pyrolysis}} - (\text{weight})_{\text{after pyrolysis}}}{(\text{weight})_{\text{before pyrolysis}}} \times 100 \quad (4.1)$$

As described before, all the polymer films were pyrolyzed using the same thermal process of 550 °C. Based on the hypothesis developed in this study, all films produced with the same thermal profile should have an *intrinsic* percentage weight loss, a weight loss solely based on the pyrolysis process without the doping oxygen. This weight loss would remain the same regardless of oxygen content in the pyrolysis atmosphere. In addition, the amount of oxygen doped would be higher as a concentration of oxygen in inert increases according to the aforementioned hypothesis. This means that a weight loss as a result of the pyrolysis process would decrease as the amount of oxygen exposure increases since an exposure to higher amount of oxygen results in a larger amount of “doping”. Results show a slight trend for the weight loss to actually decrease with increasing O<sub>2</sub> exposure (and consumption); however, the percentages of the average weight losses remain in a range of 32-35 % in all cases and were not considered to be significant beyond experimental uncertainty. Clearly, at some higher level of O<sub>2</sub>, one would expect actual losses in weight due to consumption of carbon with CO and CO<sub>2</sub> emission; however, at the lower level of O<sub>2</sub> used here, this was not observed.

#### 4.2.1.2 Production of flat CMS films

An additional observation was that pyrolysis with higher oxygen exposure of inert gases leads to a larger amount of stressed, mostly untestable, films. Unsuccessful films were “curled” or bent to a degree that inhibited the ability to test their performance as shown in Figure 4.2.

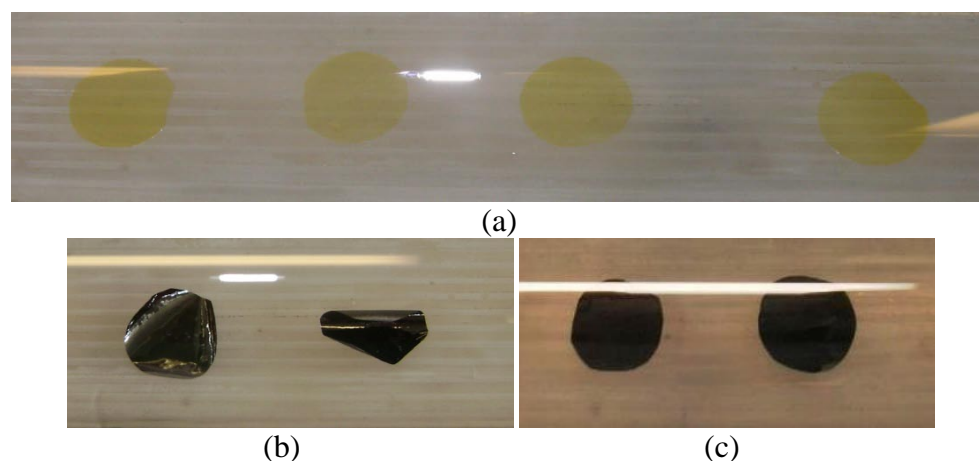


Figure 4.2: (a) Polymeric films, (b) mostly untestable “curled” CMS films, and (c) flat CMS films.

One should note that the shape of the untestable Teflon dish casted precursor CMS film is different from that observed using a ring casting technique, previously shown in Figure 3.3: the pyrolysis of the ring casted polymer film resulted in “crinkled” films whereas the pyrolysis of an untestable Teflon dish cast polymer resulted in “curled” films. Additional experiments were conducted to soak polymer films at the  $T_g$  for 2-3 hours prior to pyrolysis, and this showed that the  $T_g$  annealing does not affect the shape of resulting CMS membranes significantly. In fact, polymer films which just experienced  $T_g$  were

*flat* due to relaxation of polymer chains but the resulting CMS *was* most of times “crinkled or curled”. This suggests that the precursor polymer film has “intrinsic” stress or chain orientation which is not easily removed by the relaxation or annealing. This, among many other possibilities, could cause the different shapes of “crinkled” and “curled” films. The stress or the unique polymer chain orientation could be developed by different hydrophobicity of casting substrate’s surface (either glass or Teflon), and this may cause the resulting CMS films to be either “crinkled or curled”.

Of those Teflon casted polymer films, the success rate of producing the flat CMS films was evaluated and the results are shown in Table 4.1.

Table 4.1: Success rates of producing flat CMS dense films under different pyrolysis environments. In parenthesis, the numerator indicates numbers of flat CMS films, depicted in Figure 4.2 (c), and the denominator represents numbers of polymeric films pyrolyzed under the specified conditions.

Pyrolysis environment	Vacuum	Inert (200 cm <sup>3</sup> (STP)/min of O <sub>2</sub> doped in Ar gas)			
		4 ppmO <sub>2</sub>	8 ppmO <sub>2</sub>	30 ppmO <sub>2</sub>	50 ppmO <sub>2</sub>
Success rate	80% (8 / 10)	100% (10 / 10)	80% (8 / 10)	40% (4 / 10)	11% (3 / 27)

The success of flat CMS production rate decreased as the oxygen exposure increases. This indicates that the number of curled films increased by increasing oxygen exposure. Based on the preceding hypothesis, a lower oxygen exposure results in less oxygen to diffuse into polymer films and be consumed. Ultimately, using thicker polymeric precursors increased the success rate of producing flat films, due to greater resistance to curling and subsequent failure during subsequent handling.

#### 4.2.1.3 Correlation between oxygen exposure and consumption

The previous section 4.1.2 hypothesizes that the controlled oxidation of carbon at ultramicropores occurs during pyrolysis. It was hypothesized to control the amount of “dopants” on carbon edges by varying total amount of oxygen exposure during pyrolysis. The total amount of oxygen is defined to be “total oxygen exposure coefficient,  $q_{O_2, \text{tot}}$ ,” that expresses the amount of oxygen present to react during the pyrolysis process. The polymer precursor 6FDA/BPDA-DAM was pyrolyzed with a mixed gas of argon and a specific amount of oxygen in ppm level flowing at a rate of  $200 \text{ cm}^3(\text{STP})/\text{min}$ . In this controlled study, the total amount of oxygen exposure was varied by changing oxygen concentration in the purge gas. All experiments were conducted at least three times to demonstrate repeatability.

During each experiment,  $0.12 \pm 0.02 \text{ mg}$  of 6FDA/BPDA-DAM polymer films were pyrolyzed under specified atmospheres. The oxygen analyzer was calibrated with air before and after the experiments and a blank run without polymer samples, the “base line experiment”, was performed to confirm no oxygen consumption by the system, as described in chapter 3. Once the oxygen profiles like Figure 4.3 were obtained, the total amount of oxygen available, which is equivalent to the aforementioned parameter  $q_{O_2, \text{tot}}$ , and the amount of oxygen consumed were calculated using Equation 4.2 and 4.3.

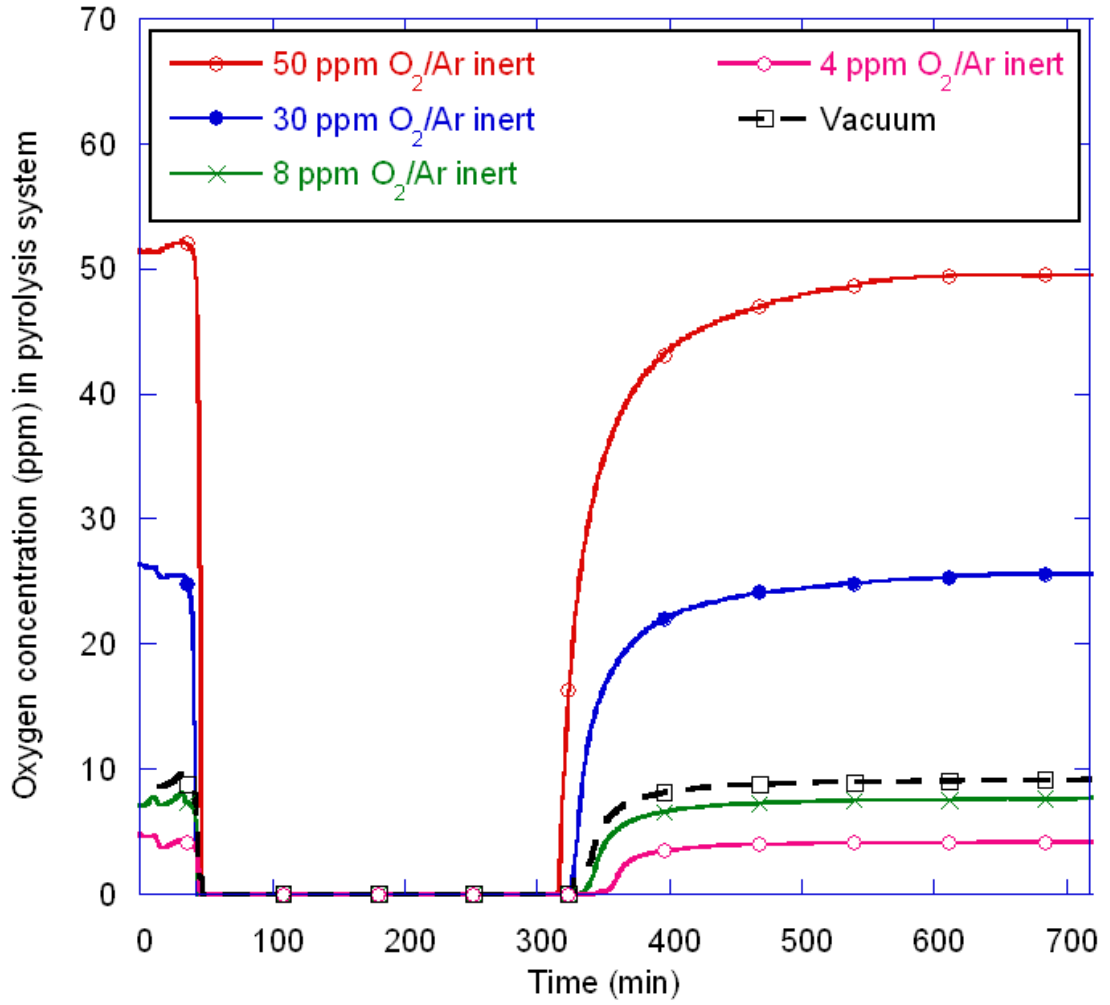


Figure 4.3: Oxygen profile during pyrolysis of 6FDA/BPDA-DAM. A specified amount of oxygen levels in argon gas was used as inert pyrolysis and vacuum pyrolysis was conducted at  $\sim 0.005$  torr.

$$\text{Total amount of } O_2 (q_{O_2, \text{total}}) = \dot{Q}_{\text{purge}} \times [(\text{ppm } O_2)_{\text{feed}}] \times t \quad (4.2)$$

$$\text{Amount of } O_2 \text{ consumed } (q_{O_2, \text{consumed}})$$

$$= \dot{Q}_{\text{purge}} \times [(\text{ppm } O_2)_{\text{feed}} - (\text{ppm } O_2)_{\text{measured}}] \times t \quad (4.3)$$

The parameter  $\dot{Q}_{\text{purge}}$  is the volumetric flow rate of the “inert” gas containing the controlled amount of  $\text{O}_2$  impurity. For vacuum pyrolysis,  $\dot{Q}_{\text{purge}}$  was determined by a curve supplied by BOC Edwards, and by direct measurement by bubble flow meter for inert pyrolysis. The values  $(\text{ppm O}_2)_{\text{Feed}}$  and  $(\text{ppm O}_2)_{\text{Measured}}$  are obtained by the oxygen analyzer at the entrance and exit of the pyrolysis chamber. The value  $(\text{ppm O}_2)_{\text{Feed}}$  was the measured oxygen entering the pyrolysis chamber for both vacuum and inert pyrolysis prior to the initiation of the pyrolysis. A duration of 720 minutes, time from onset of heating to cooling, was used to make an initial attempt to observe oxygen consumption during pyrolysis of polymer membranes.

The oxygen consumption profile in Figure 4.3 shows that the oxygen level prior to the pyrolysis process, between 4-30 ppm level, dropped to an order of  $10^{-16}$  ppm once the temperature reached the polymer decomposition temperature either in inert or vacuum pyrolysis. The oxygen consumption slowly decreased when the temperature started to cool down and eventually stopped. Considering all pyrolysis atmospheres, the polymer precursor tends to consume more oxygen as the amount of oxygen fed increased. This is illustrated as the linearity in Figure 4.4 between the amount of consumed,  $\bar{q}_{\text{O}_2, \text{consumed}}$ , and the total amount of oxygen available for consumption,  $\bar{q}_{\text{O}_2, \text{tot}}$ .

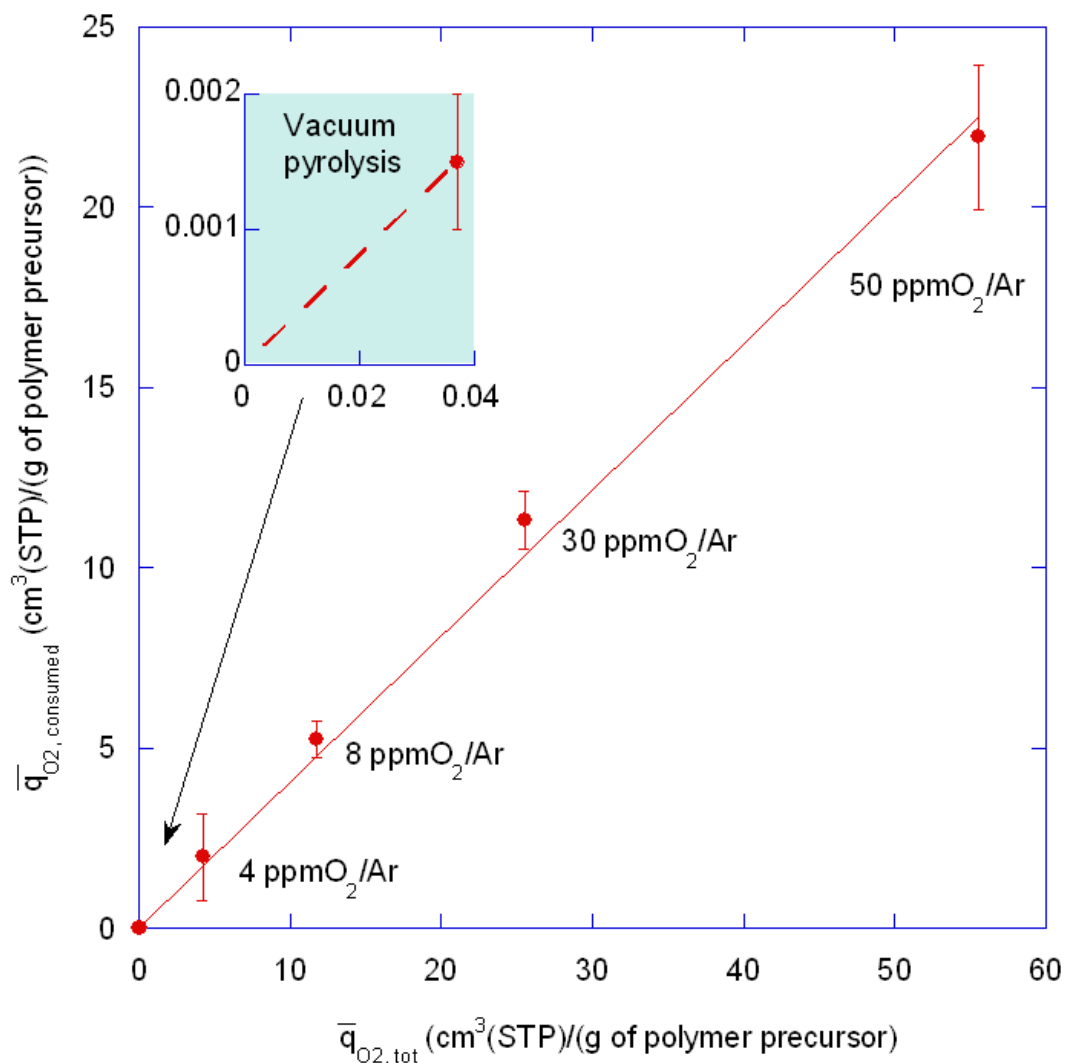


Figure 4.4: Correlation between the total amount of oxygen and the amount of oxygen consumption normalized by weight of polymer precursors. A linear relationship was observed with  $R^2 = 99.7\%$ .

It is speculated that a majority of the oxygen supplied is consumed by by-products evolved during pyrolysis process since the polymer precursor loses 40-45 % of the initial weight as a result of pyrolysis [8]. This indicates that the relatively large amount of “total amount of oxygen available” was consumed by the by-products, rather than as “dopants,” so the situation is complicated. In addition, TGA analysis by Steel showed that most of the weight loss occurred just before the temperature protocol reaches the two

hour soak period: it is speculated that the majority of the by-products evolve before the two hour soaking period and consume a majority of the oxygen supplied in the bulk flow. Once the by-products flowing out of the pyrolysis system is completed, the remaining oxygen fed is speculated to be used mainly to treat the active carbon edges.

#### 4.2.1.4 Correlation between total amount of oxygen exposure and CMS separation performance

Figure 4.5 shows separation properties of homogeneous dense CMS films pyrolyzed under each pyrolysis condition. Each data point on the figure represents an average of at least three CMS dense films, and standard deviations of less than  $\pm 10\%$  in both permeability and selectivity were achieved. It was demonstrated that CMS films pyrolyzed under inert gases with an oxygen concentration in a range of 4 to 30 ppm perform as attractively as CMS films pyrolyzed under vacuum, well exceeding the upper bound curve. This finding leads one to believe that a selectivity as high as was obtained under vacuum pyrolysis can be accomplished by tuning the oxygen exposure.



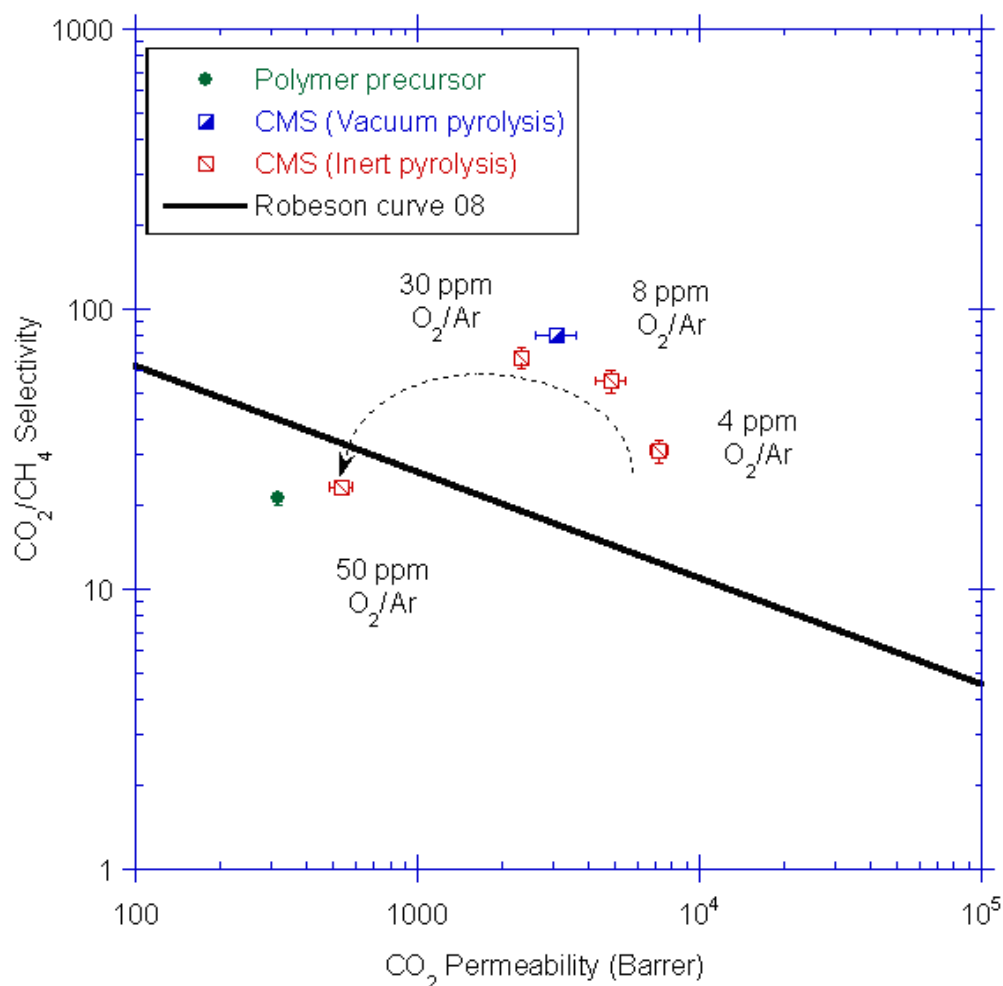


Figure 4.5: Separation performance of 6FDA/BPDA-DAM CMS dense films. All were tested at 35 °C. A circular data point represents polymeric properties and square points represent properties of CMS membranes. Pyrolysis atmospheres are indicated with data points for both vacuum and inert pyrolysis. A dash line represents a trend between separation performance and oxygen concentration prior to pyrolysis. The Robeson curve shows the trade-off from currently available polymer [22].

Figure 4.5 clearly shows that a strong relationship exists between the total amount of oxygen and the transport properties for inert pyrolysis. Performance differences between the various “inert” atmospheres are especially revealing. Selectivity increases and permeability decreases as the amount of oxygen in the inert gas increases. However,

there is a cut-off point on the benefit to the amount of oxygen exposure such that once it exceeds a critical level, low values of both selectivity and permeability are observed as shown in Figure 4.6 and Figure 4.7.

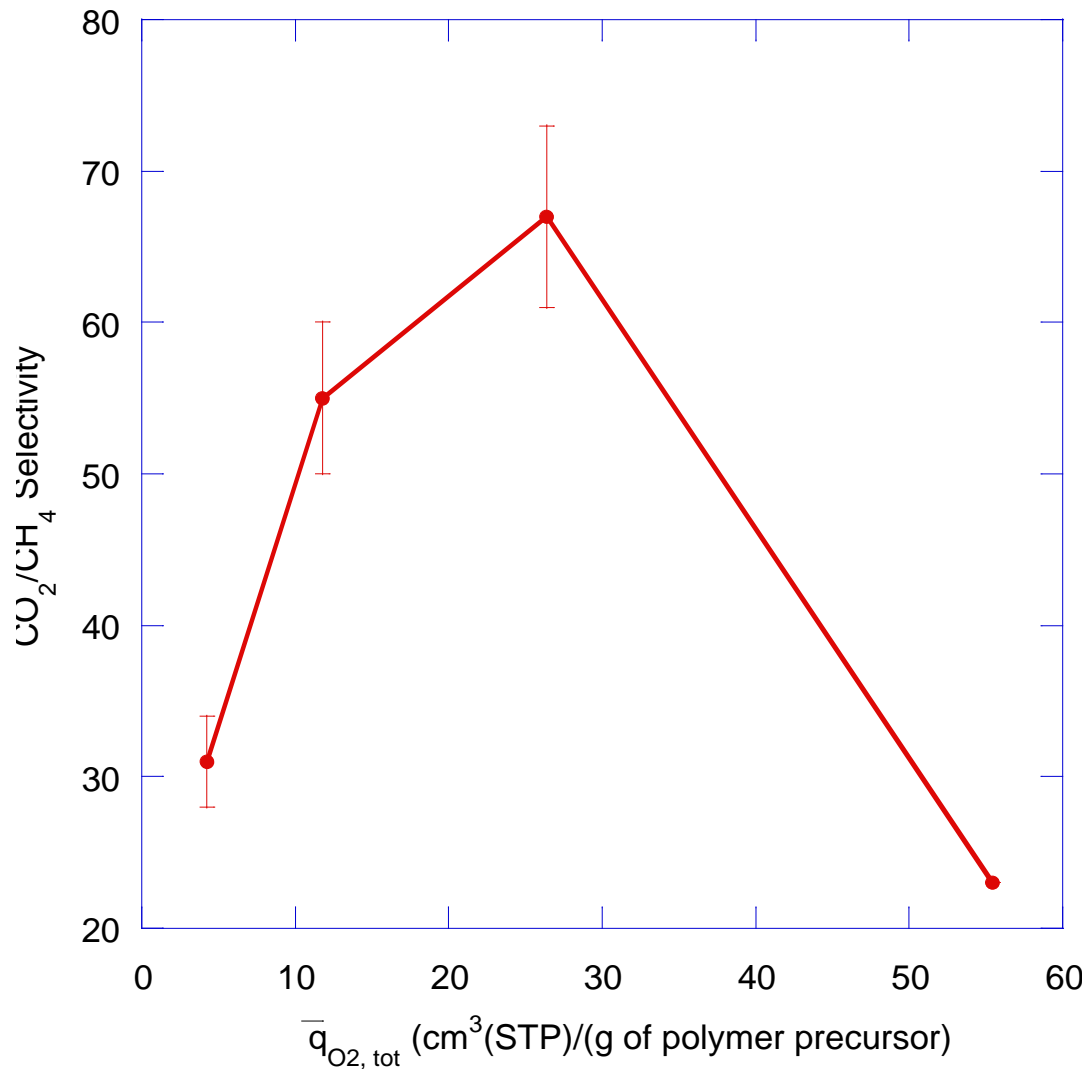


Figure 4.6: Trend on CO<sub>2</sub>/CH<sub>4</sub> selectivity as a function of the total amount of oxygen.

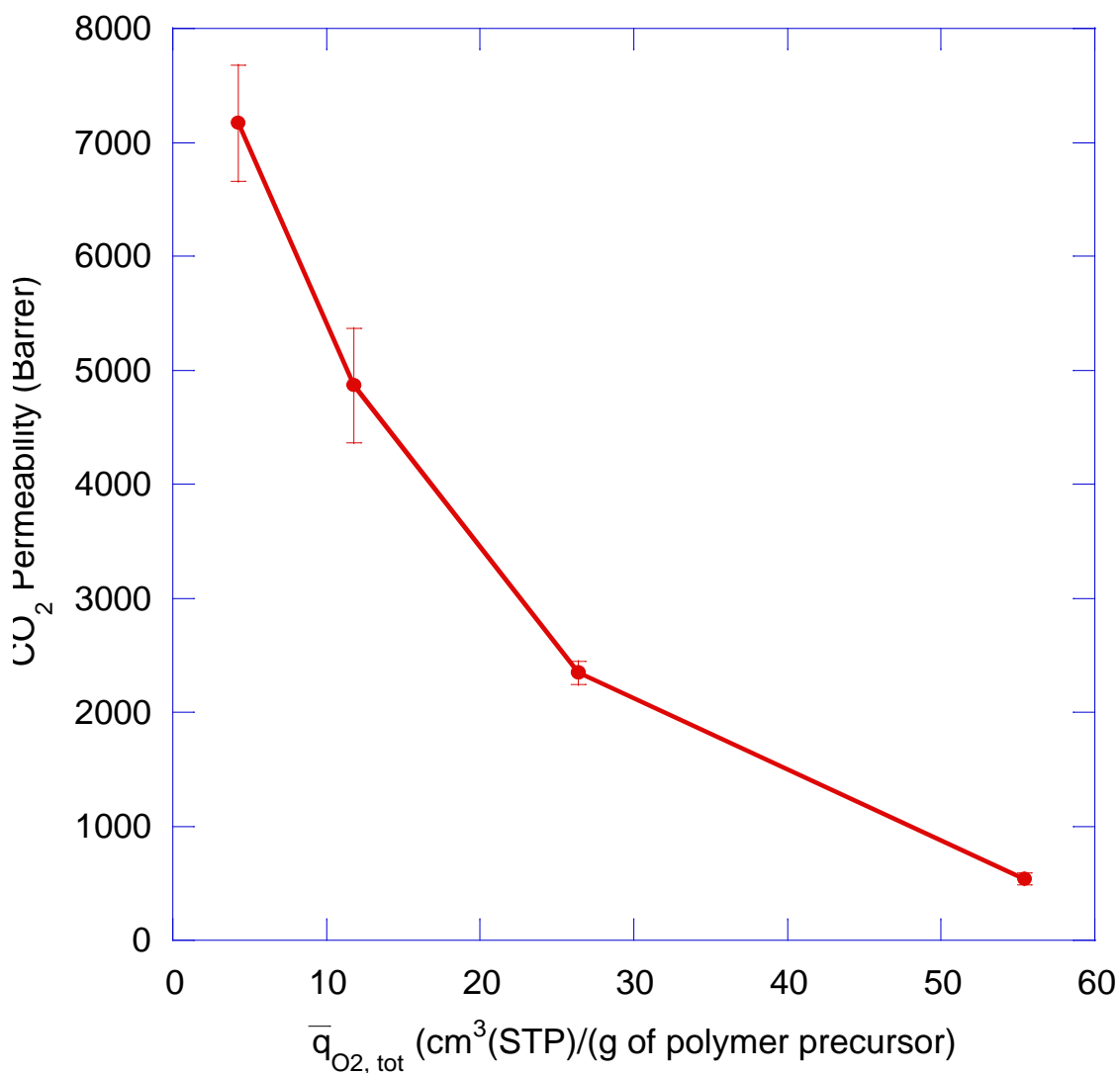


Figure 4.7: Trend on CO<sub>2</sub> permeability as a function of the total amount of oxygen.

This phenomenon is shown clearly by data with 50 ppm O<sub>2</sub>/Ar inert pyrolysis, possibly suggesting that the amount of oxygen was so high in this case that most of the oxygen used for the purpose of “doping” may have filled most of the “active” sites of ultramicropores, reducing both selectivity and permeability. This hypothetical explanation can also be understood in terms of a shift in the ultramicropore size distribution as shown hypothetically in Figure 4.8. Specifically, for the few remaining pathways in such a case are hypothesized to be larger and less susceptible to selectivity

enhancement by the oxygen chemisorption mechanism described earlier. In such a case, the permeability decreases as the total amount of oxygen exposed increases, but eventually selectivity actually drops due to only less selective paths remaining open for transport.

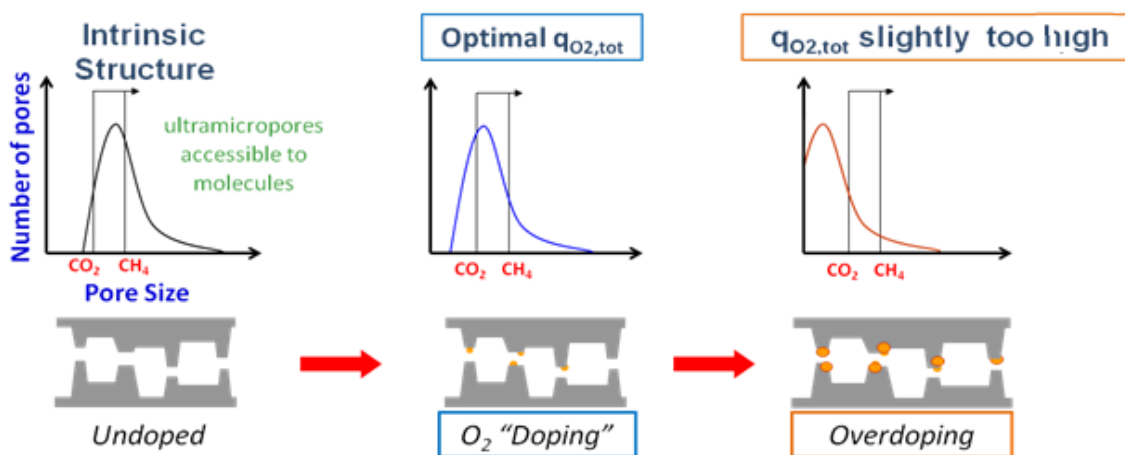


Figure 4.8: Hypothetical effective “diffusivity based ultramicropore distribution” along with CMS slit like structures: (a) undoped “intrinsic” structure when pyrolyzed under no oxygen presents, (b) optimal selective structure with adequate amount of oxygen doped, (c) overdoped structure when slightly higher oxygen was introduced during pyrolysis.

The previous section discussed a correlation between total amount of oxygen available and oxygen consumed. One may note a discrepancy between the total amount of oxygen available and the CMS separation performance when inert and vacuum pyrolysis atmospheres are compared. According to Figure 4.4, vacuum pyrolysis supplied the lowest total amount of oxygen available. Theoretically, this would result in the most permeable and least selective CMS membranes when compared with other pyrolysis experiments conducted in this work; however, the experimental results show that the separation performance of CMS membranes via vacuum pyrolysis lies between CMS membranes pyrolyzed under 8 to 30 ppm oxygen level. The oxygen profile in Figure 4.3 shows the oxygen level prior to the vacuum pyrolysis to be about 10 ppm. The

oxygen level measured in this work under the vacuum is equivalent of an oxygen concentration measured at 1 atmosphere pressure; i.e. a total pressure of 0.005 torr with 21 % O<sub>2</sub> is equivalent to an oxygen concentration of 10 ppm at 1 atm. This suggests the possibility of the oxygen concentration being a governing factor of “doping” process, rather than total amount of oxygen exposed: further investigations were conducted and discussed in section 4.3.

#### **4.2.2 Matrimid<sup>®</sup> CMS membranes**

Similar to the experiments conducted on 6FDA/BPDA-DAM polymer, the effect of oxygen exposure was investigated experimentally on the commercially available polymer, Matrimid<sup>®</sup>. The polymer precursor was pyrolyzed in the same manner under (i) vacuum and (ii) an inert gas of argon with 1-100 ppm level oxygen. A correlation between the total amount of oxygen available and the amount of consumption existed as illustrated in Figure 4.4 for 6FDA/BPDA-DAM. This section further seeks to verify the oxygen “doping” process by conducting FTIR analysis and evaluating separation performance on CMS membranes with various oxygen exposures.

##### **4.2.2.1 FTIR**

Figure 4.9 shows the FTIR result from CMS samples prepared with inert pyrolysis. While typical CMS membranes show no significant peaks [23], the spectra in Figure 4.9 shows C=O group appearing in the vicinity of 1700 cm<sup>-1</sup>, indicating that the oxygen “doping” method was successfully applied to CMS membranes.

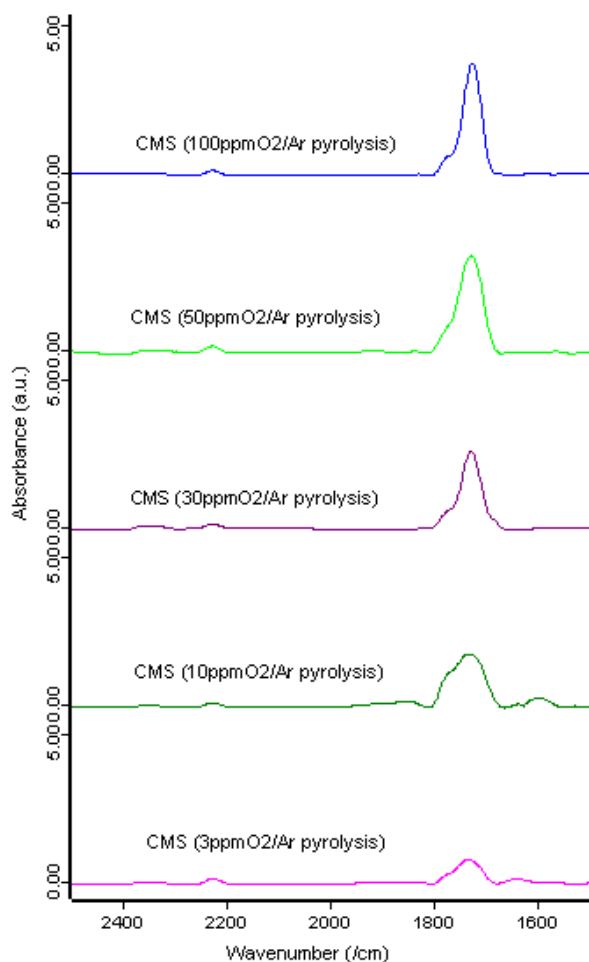


Figure 4.9: FTIR spectra of Matrimid<sup>®</sup> CMS membranes.

#### 4.2.2.2 Correlation between oxygen exposure and CMS transport properties

##### *4.2.2.2.1 Permeation*

The result of CO<sub>2</sub>/CH<sub>4</sub> separation performance is shown in Figure 4.10. It demonstrates that the attractive separation performance, which is above the upper bound curve, can be achieved with pyrolysis under (i) vacuum and (ii) inert pyrolysis *when* the pyrolysis atmosphere is properly controlled. These results are consistent with the observation with 6FDA/BPDA-DAM that oxygen exposure has a correlation with separation performance.

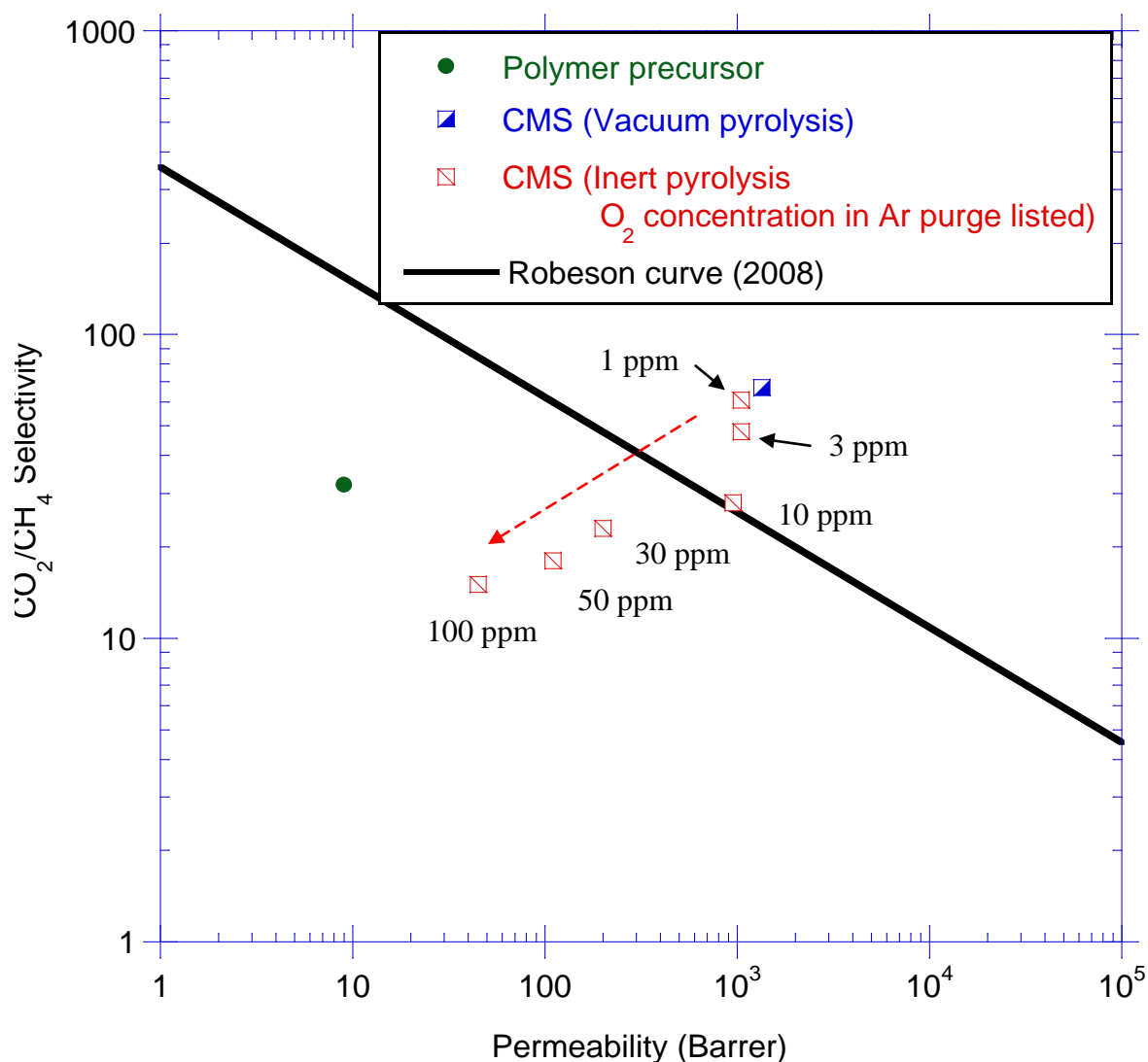


Figure 4.10: Separation performance of Matrimid<sup>®</sup> CMS dense films. Tests were conducted at 35 °C with an upstream pressure of ~50 psia. A circular data point represents polymeric properties and square points represent properties of CMS membranes. On vacuum pyrolysis, oxygen concentration was ~1 ppm. A dash arrow line represents a trend between separation performance and oxygen concentration prior to pyrolysis [24]. Experiments were repeated and all had less than 10% deviation.

The results on Figure 4.10 show that the oxygen doping method caused decreases in *both* permeability and selectivity. This trend is different from the trend observed with the 6FDA/BPDA-DAM CMS membranes (shown on Figure 4.5).

#### *4.2.2.2.2 Equilibrium sorption*

In addition, sorption equilibrium was measured on CMS samples pyrolyzed with 1, 30, and 100 ppm oxygen in argon inerts at 550 °C. The sorption isotherms are presented in Figure 4.11-Figure 4.13, and the Langmuir model coefficients derived from the isotherms are shown in Table 4.2-Table 4.4. These sorption isotherms and aforementioned permeabilities are used to predict mixed gas separation performance which will be discussed in next chapter.



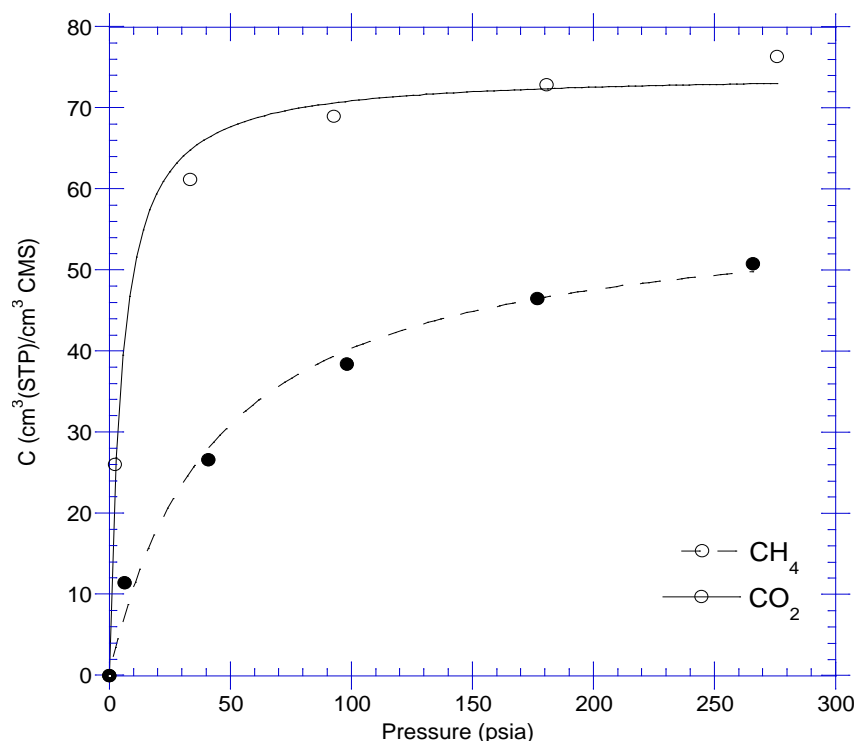


Figure 4.11: Sorption isotherms for Matrimid<sup>®</sup> CMS membranes prepared with 1 ppm O<sub>2</sub>/Ar inert pyrolysis. Test temperature was 35 °C. The experiments were repeated, had deviation less than 5%, and fitted with Langmuir isotherm model described in lines.

Table 4.2: Langmuir hole filling capacity  $C_H'$  and Langmuir affinity constant  $b$  calculated based on Matrimid<sup>®</sup> CMS sorption isotherms on Figure 4.11.

Gas	$C_H'$ (cc(STP)/cc CMS)	$b$ (psia <sup>-1</sup> ) ●
CO <sub>2</sub>	74.3	0.02
CH <sub>4</sub>	57.9	0.005

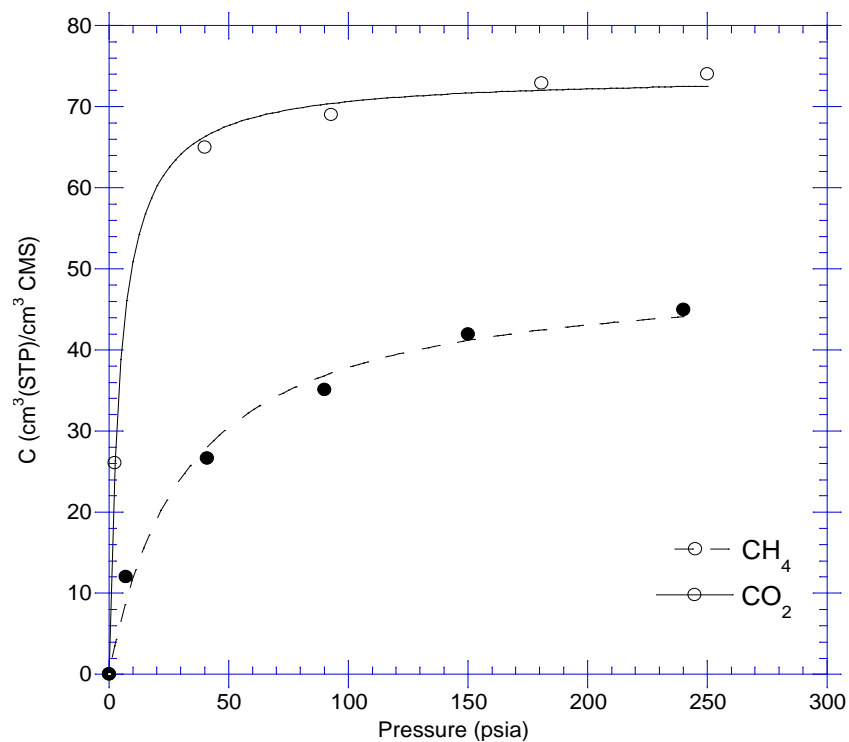


Figure 4.12: Sorption isotherms for Matrimid® CMS membranes prepared with 30 ppm O<sub>2</sub>/Ar inert pyrolysis. Test temperature was 35 °C. The experiments were repeated, had deviation less than 5%, and fitted with Langmuir isotherm model described in lines.

Table 4.3: Langmuir hole filling capacity  $C_H'$  and Langmuir affinity constant  $b$  calculated based on Matrimid® CMS sorption isotherms on Figure 4.12.

Gas	$C_H'$ (cc(STP)/cc CMS)	$b$ (psia <sup>-1</sup> )
CO <sub>2</sub>	73.6	0.02
CH <sub>4</sub>	57.6	0.005

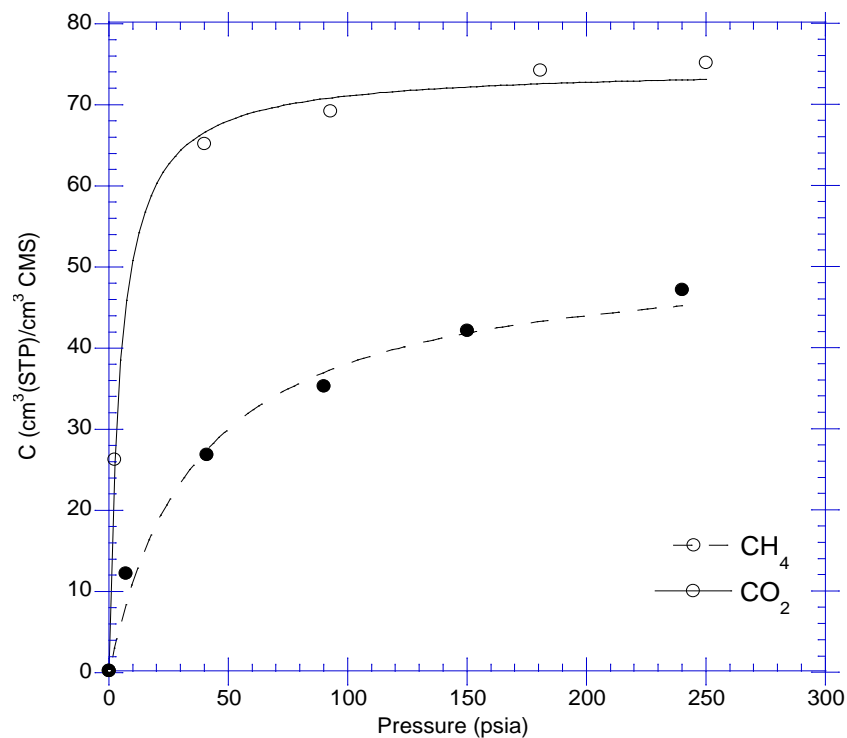


Figure 4.13: Sorption isotherms for Matrimid<sup>®</sup> CMS membranes prepared with 100 ppm O<sub>2</sub>/Ar inert pyrolysis. Test temperature was 35 °C. The experiments were repeated, had deviation less than 5%, and fitted with Langmuir isotherm model described in lines.

Table 4.4: Langmuir hole filling capacity  $C_H'$  and Langmuir affinity constant  $b$  calculated based on Matrimid<sup>®</sup> CMS sorption isotherms on Figure 4.13.

Gas	$C_H'$ (cc(STP)/cc CMS)	$b$ (psia <sup>-1</sup> )
CO <sub>2</sub>	74.5	0.02
CH <sub>4</sub>	58.2	0.005

Results of the sorption isotherms of the three CMS samples are almost identical. In fact, sorption selectivities among these samples are almost the same as shown in Figure 4.14.

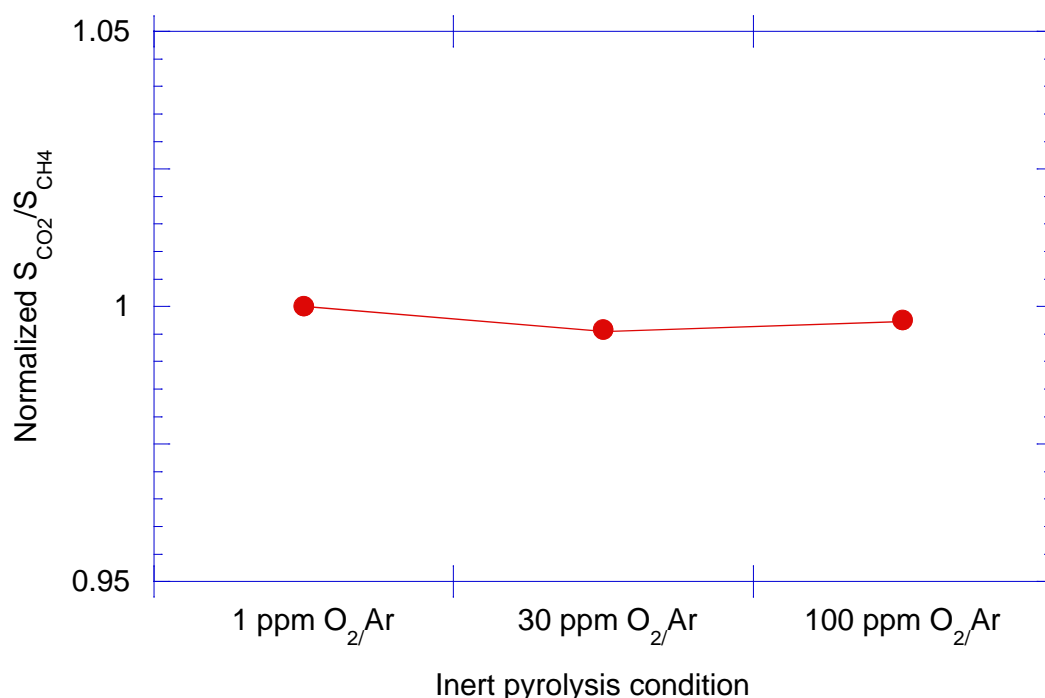


Figure 4.14: Normalized sorption selectivity values of CMS membranes pyrolyzed at 1, 30, and 100 ppm  $\text{O}_2/\text{Ar}$ . The normalization was based on  $S_{\text{CO}_2}/S_{\text{CH}_4}$  of 1ppm  $\text{O}_2/\text{Ar}$  CMS membranes.

*This finding is significant since it essentially implies that the oxygen doping is likely taking place at ultramictopores, rather than micropores and affecting diffusion selectivities, as we hypothesized in section 4.1.2. Therefore, it is speculated that the discrepancy observed on the different trend observed between 6FDA/BPDA-DAM and Matrimid<sup>®</sup> CMS membranes is caused by the difference in intrinsic CMS structures for the two samples. It is hypothesized that Matrimid<sup>®</sup> CMS membranes, created from an intrinsically lower free volume precursor, has a less sorptive and less selective intrinsic*

structure than 6FDA/BPDA-DAM CMS membranes. Therefore, oxygen doping not only reduces pore sizes of ultramicropore- and micro-pores but also further closes selective pores, leading to a decrease in both permeability and selectivity. This hypothesis was tested by several characterizations as discussed in the next section.

### **4.2.3 Structural differences between 6FDA/BPDA-DAM and Matrimid<sup>®</sup> CMS membranes**

#### **4.2.3.1 TGA-FTIR**

The decomposition process of each polymer was investigated using TGA-FTIR [24]. Polymeric samples were heated under argon purge, and the evolved gases were sent to an FTIR chamber to analyze the chemical composition. Figure 4.15 and Figure 4.16 show decomposition results of 6FDA/BPDA-DAM and Matrimid<sup>®</sup>. Polymer 6FDA/BPDA-DAM produced HF (4250-4500 cm<sup>-1</sup>), CH<sub>4</sub> (3017 cm<sup>-1</sup>), CHF<sub>3</sub> (1150, 1178 cm<sup>-1</sup>), CO<sub>2</sub> (2110 cm<sup>-1</sup>), and CO (2190 cm<sup>-1</sup>). On the other hand, Matrimid<sup>®</sup> produced mainly CH<sub>4</sub> (3017 cm<sup>-1</sup>), CO<sub>2</sub> (2110 cm<sup>-1</sup>) and CO (2190 cm<sup>-1</sup>).

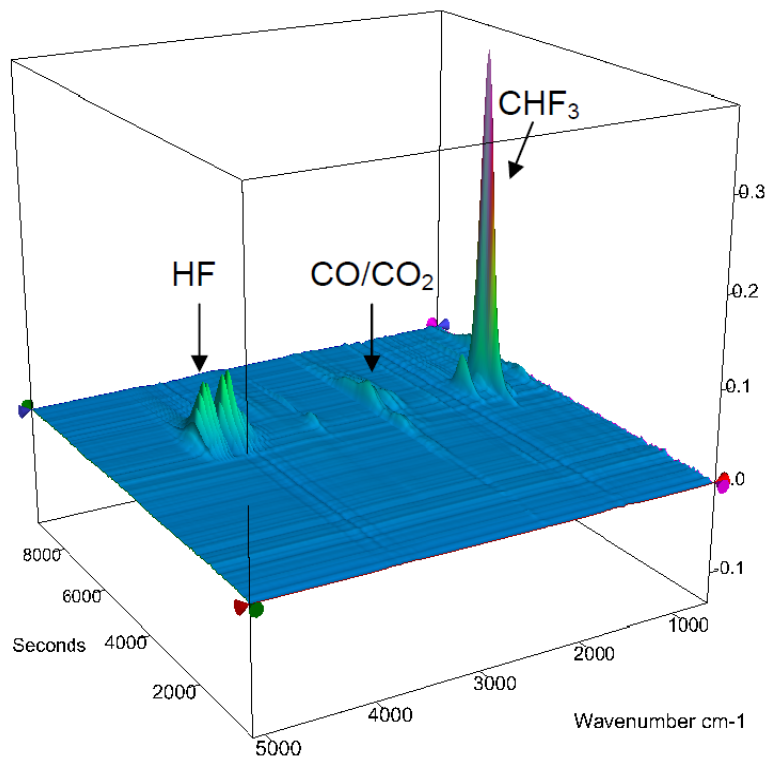


Figure 4.15: TGA-FTIR result of 6FDA/BPDA-DAM [23].

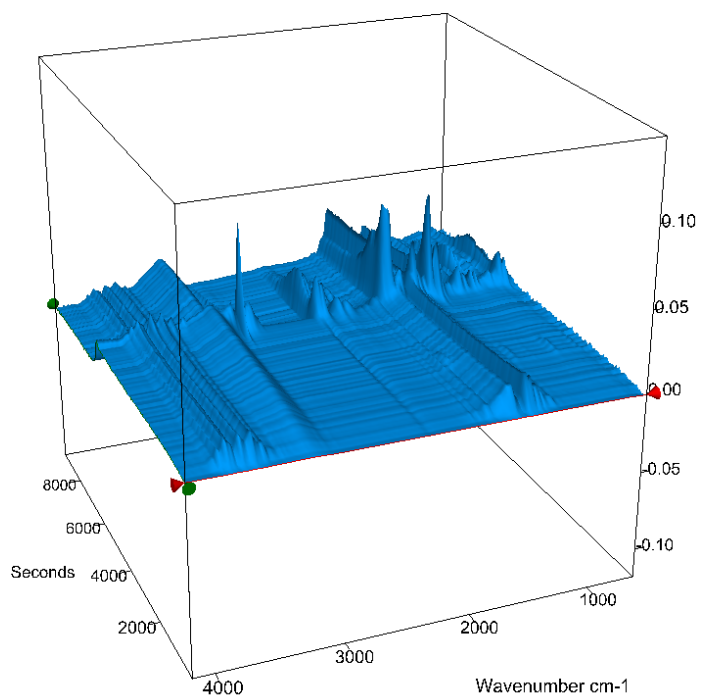


Figure 4.16: TGA-FTIR result of Matrimid<sup>®</sup> [24].

There are three stages of pyrolysis when polymers are heated up to 1200 °C: (i) the precarbonation, (ii) the carbonization, and (iii) dehydrogenation [25]. A temperature range between 100 °C and up to the polymer decomposition temperatures, i.e. 450 °C for 6FDA/BPDA-DAM and 425 °C for Matrimid<sup>®</sup>, would be considered as the precarbonation stage. During this first stage, molecules, such as excess monomer and solvent are removed. Polymeric films turn black and linear conjugated C-C systems start to form near the decomposition temperature [25]. In the carbonization stage, rapid weight loss is observed due to the removal of entities, such as oxygen, nitrogen, and CF<sub>3</sub> [25]. As the large fluorinated compounds are produced and diffuse out of membrane films, more open ultramicropore structures are believed to be formed with 6FDA/BPDA-DAM than with Matrimid<sup>®</sup>, which lacks these fluorinated moieties.

As Figure 4.15 and Figure 4.16 show, major by-products evolve in this regime. An exact temperature range of this stage is difficult to define. However, it is speculated to be between the decomposition temperature and the temperature where the rate of weight loss is significantly reduced (an elbow of the decomposition weight loss curve). Evolution of CO, CO<sub>2</sub>, and CH<sub>4</sub> were also observed for Matrimid<sup>®</sup> by Barsema et al [26]. At the end of this stage, a loose network of linear conjugated systems is formed [25]. In the dehydrogenation stage, hydrogen is gradually eliminated, typically between 500 and 1200 °C. Presumably this results in the turbostratic structure with defective sites in each graphene sheets as suggested in Figure 4.17. These defect sites can then react with oxygen as previously proposed in section 4.1.2.

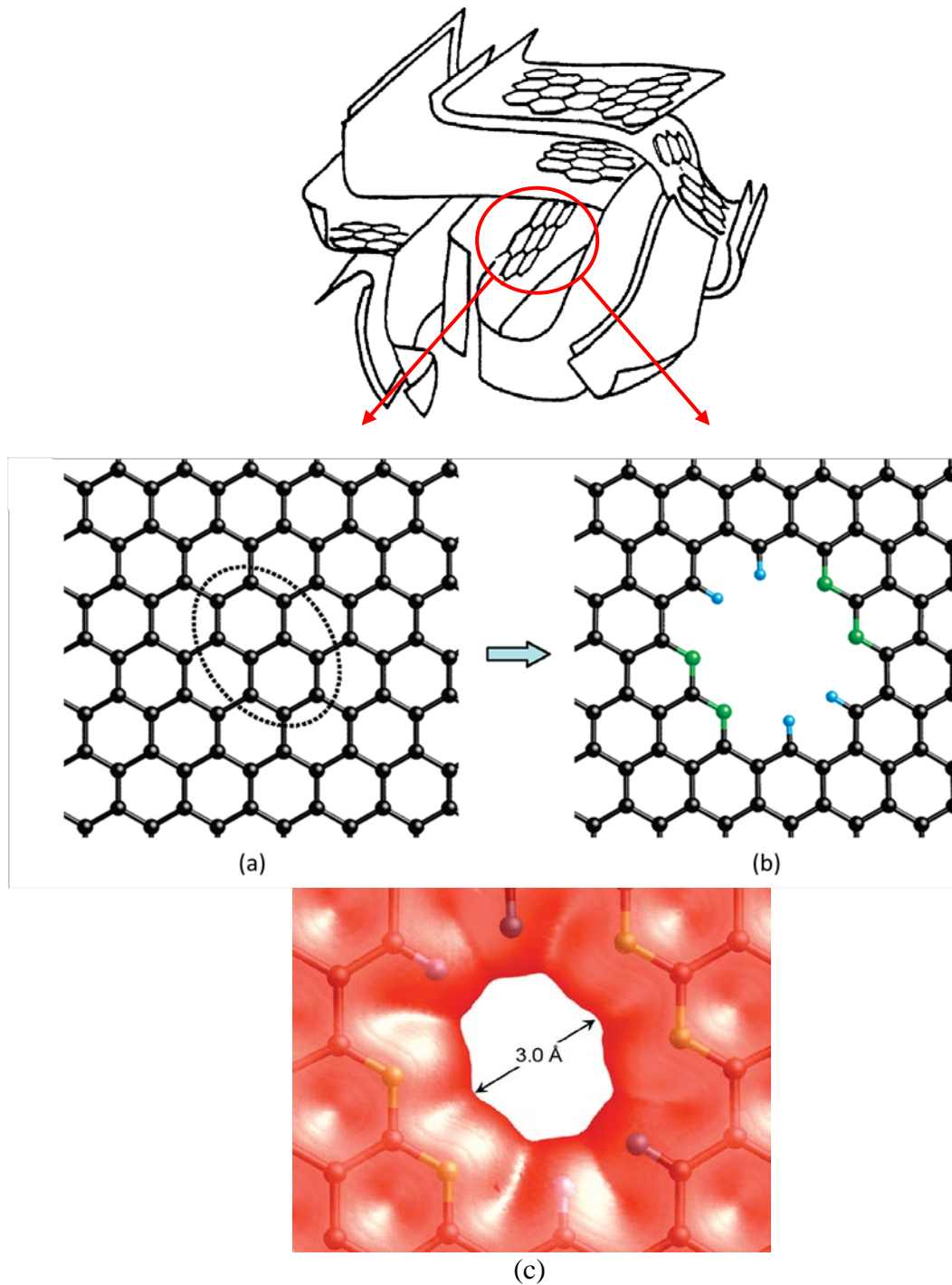


Figure 4.17: Schematic of folded graphite-like layers (top) [27] and graphene sheets (bottom): (a) the carbon atoms in the dotted circles are removed by electron beam, and (b) four dangling bonds are saturated by hydrogen (cyan), while the other four dangling bonds together with their carbon atoms are replaced by nitrogen atoms (green). The pore electron density isosurface of the nitrogen functionalized porous graphene presumably has 3.0 Å pore window, adapted from [28].



Jenkins and Kawamura note that the rate of the hydrogen removal is a characteristic of a given heat-treatment temperature [25]. Elemental analysis on carbon membranes pyrolyzed in similar manners shows 95-99 % of aromatic carbon content [9, 18, 29, 30]; moreover, the percentage of carbon element is dependent on pyrolysis temperature [25].

#### 4.2.3.2 Sorption isotherms

Gas sorption was examined to characterize sorption coefficients, hole filling capacity and affinity constant [24]. Each polymeric film was pyrolyzed under a flow of 200cc/min 1ppm O<sub>2</sub>/Ar to produce CMS membranes. The lowest concentration of oxygen in argon mixture available was chosen to prepare CMS membranes with structures closest to their “intrinsic structures.”

The sorption coefficients depend on the micropore sizes of carbon material and the critical temperature of the molecule, which reflects condensability and affinity of penetrants for the carbon. If the ultramicropore size is small enough to effectively exclude one gas molecule while transmitting the smaller molecule in a pair, true molecular sieving occurs. In this case, no uptake of the sieved component would be shown on the sorption isotherm. For carbon material, however, a distribution of ultramicropore exists. Therefore, only regions connected with perfect molecular sieving pore windows would be inaccessible to a larger gas molecule.

Figure 4.18 and Figure 4.19 show sorption isotherms measured with six gases, He, CO<sub>2</sub>, O<sub>2</sub>, N<sub>2</sub>, CH<sub>4</sub>, and SF<sub>6</sub>. The sorption isotherms were fitted to the Langmuir equation model in Equation 3. The hole filling capacities,  $C_H'$ , and affinity constants,  $b$ , are shown in Table 4.5 and Table 4.6, along with the kinetic diameters of the test gases.

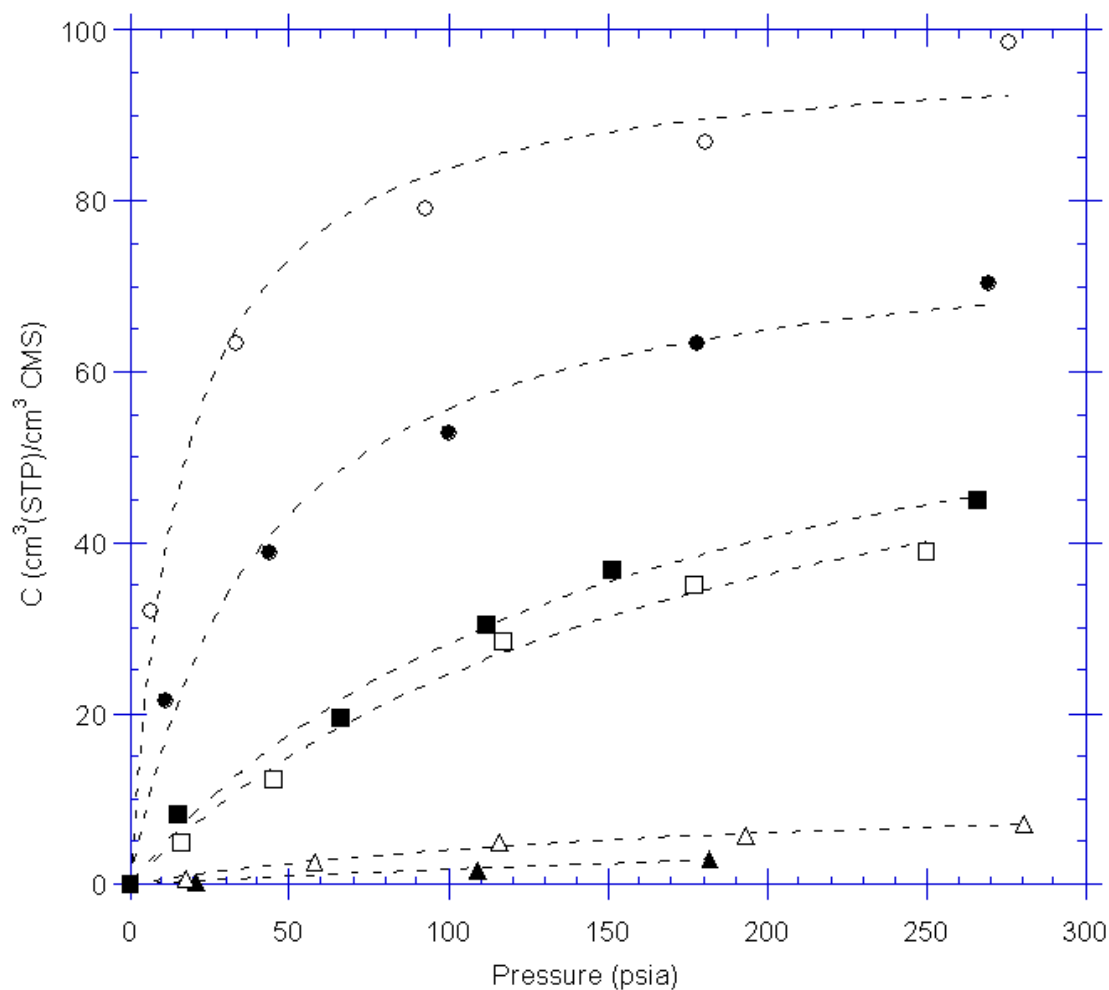


Figure 4.18: Sorption isotherms for 6FDA/BPDA-DAM CMS membranes prepared with 1 ppm O<sub>2</sub>/Ar inert pyrolysis. The isotherms were obtained with six different gases: ○ CO<sub>2</sub>, ● CH<sub>4</sub>, ■ O<sub>2</sub>, □ N<sub>2</sub>, △ He, ▲ SF<sub>6</sub>. The experiments were repeated, had less than 5% of deviations, and fitted with Langmuir isotherm model described in dot lines.

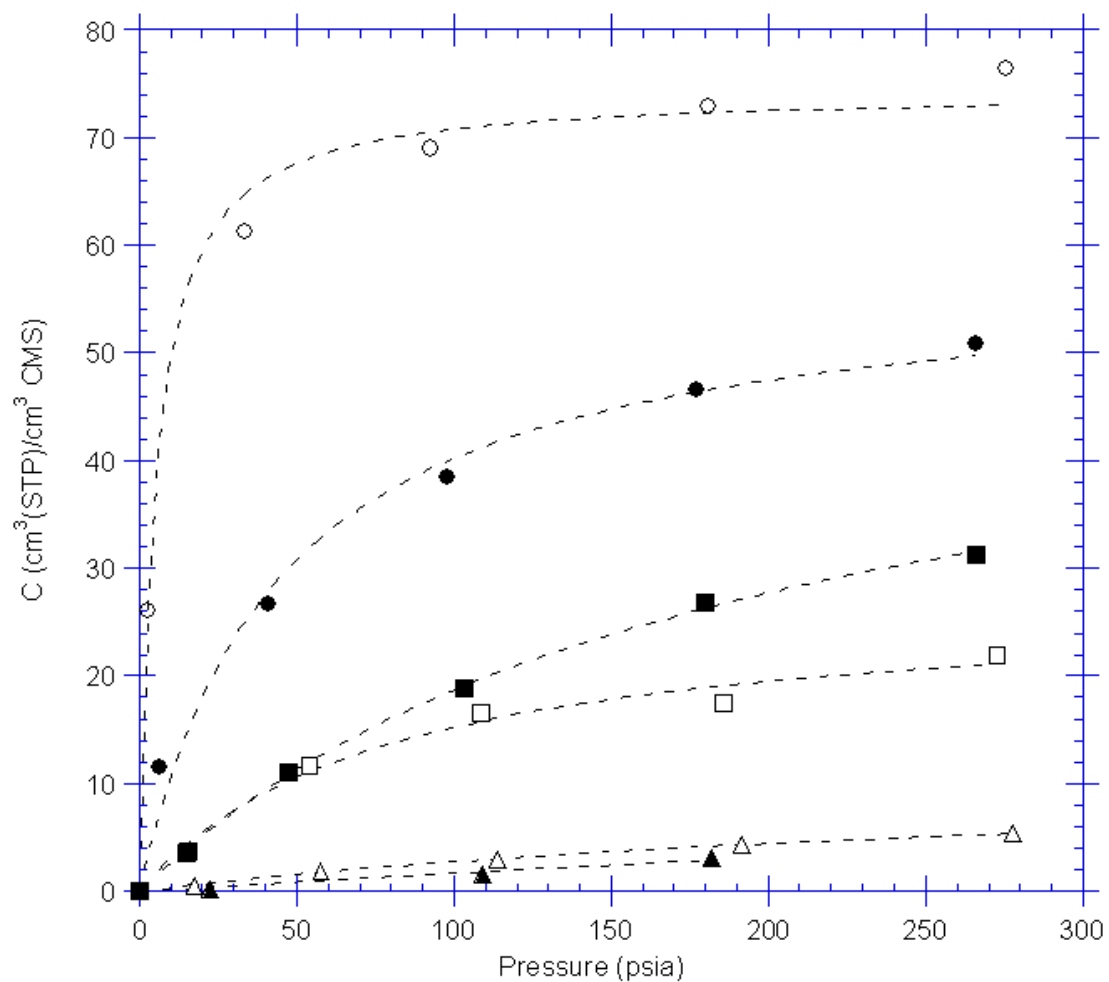


Figure 4.19: Sorption isotherms for Matrimid® CMS membranes prepared with 1 ppm O<sub>2</sub>/Ar inert pyrolysis. The isotherms were repeated and obtained with six different gases: ○ CO<sub>2</sub>, ● CH<sub>4</sub>, ■ O<sub>2</sub>, □ N<sub>2</sub>, △ He, ▲ SF<sub>6</sub>. The experiments were repeated, had less than 5% of deviations, and fitted with Langmuir isotherm model described in dot lines.

Table 4.5: Langmuir hole filling capacity  $C_H'$  and Langmuir affinity constant  $b$  calculated based on 6FDA/BPDA-DAM CMS sorption isotherms.

Gas	Kinetic diameter (Å) [31]	$C_H'$ (cc(STP)/cc CMS)	$b$ (psia <sup>-1</sup> )
He	2.6	13.0	0.005
CO <sub>2</sub>	3.3	98.0	0.06
O <sub>2</sub>	3.46	72.2	0.006
N <sub>2</sub>	3.64	69.4	0.01
CH <sub>4</sub>	3.8	78.0	0.025
SF <sub>6</sub>	5.5	12.7	0.002

Table 4.6: Langmuir hole filling capacity  $C_H'$  and Langmuir affinity constant  $b$  calculated based on Matrimid<sup>®</sup> CMS sorption isotherms.

Gas	Kinetic diameter (Å) [31]	$C_H'$ (cc(STP)/cc CMS)	$b$ (psia <sup>-1</sup> )
He	2.6	11.7	0.003
CO <sub>2</sub>	3.3	74.3	0.02
O <sub>2</sub>	3.46	68.5	0.006
N <sub>2</sub>	3.64	27.1	0.01
CH <sub>4</sub>	3.8	57.9	0.005
SF <sub>6</sub>	5.5	11.6	0.0005

In all gas measurements, 6FDA/BPDA-DAM CMS membranes showed higher sorption coefficients and hole filling capacities than Matrimid<sup>®</sup> CMS membranes. This indicates a larger available micropore volume in 6FDA/BPDA-DAM CMS membranes than for Matrimid<sup>®</sup> CMS membranes. The ratio of  $(C_H')_{CO_2}$  values for 6FDA/BPDA-DAM vs. Matrimid<sup>®</sup> CMS membranes' is about 1.3. This ratio is similar to the reported value of 1.4 for the ratio of micropore volume for the 6FDA/BPDA-DAM vs. Matrimid<sup>®</sup> CMS samples by density functional theory (DFT) analysis in Steel and Koros [32].

The trend of isotherms for both sets of CMS membranes is similar. The similarity can also be seen with the order of magnitudes on Langmuir constants, namely  $C_H'$  and  $b$ , in both CMS membranes. This is likely caused by the fact that CMS samples were treated in the same manner and resulted in similar overall gross structure. As previously mentioned, pyrolysis treatment above 550 °C results in more than 95 % carbon in the final structure [9, 18], and the percentage presumably depends upon the intensity of heat treatment [25]. Despite its small molecular size, the sorption coefficients for He were significantly lower than other gases. This is attributed to its non-condensable nature. On the other hand, the lowest sorption coefficients observed for both CMS materials was found for the highly condensable gas, SF<sub>6</sub>. It is speculated that this is caused by the small population of ultramicropores in the range between 5 and 6 Å. In fact, bimodal pore size distributions seen by various researchers suggest that the minimum for typical CMS materials lies around the size of an SF<sub>6</sub> molecule [33-35]. This could explain the order of Langmuir affinity constants in both CMS membranes with SF<sub>6</sub> being the lowest, because access of a large spherical molecule SF<sub>6</sub> to the regular microvoids is simply too low to enable accurate measurement of the affinity constants for typical regular micropores. A comparison of R<sup>2</sup> values for the affinity constants on SF<sub>6</sub> versus other gases shows poor fitting of the model: ~0.6 and 0.95 respectively, providing further evidence of this observation.

#### 4.2.3.3 “Molecular-ruler”

Pore size distributions in the ultramicropore region were investigated in this study using various gas molecules as probes [24]. Diffusion coefficients were obtained from permeation and sorption experiments using Equation 2.13. Similar to sorption isotherm experiments, CMS membranes were prepared under inert pyrolysis of 200 cc/min 1ppm O<sub>2</sub>/Ar to produce CMS membranes with close to “intrinsic” structures. Once samples

were prepared, the sorption and transport experiments were conducted at 35 °C with a pressure of 50 psia using the test gases listed in Table 4.7, namely He (2.6 Å), CO<sub>2</sub> (3.3 Å), O<sub>2</sub> (3.46 Å), N<sub>2</sub> (3.64 Å), CH<sub>4</sub> (3.80 Å), and SF<sub>6</sub> (5.5 Å). Table 4.7 lists permeability coefficients, Table 4.8 lists sorption coefficients, and Table 4.9 shows diffusion coefficients for 6FDA/BPDA-DAM and Matrimid<sup>®</sup> CMS membranes.

Table 4.7: Permeability of 6FDA/BPDA-DAM and Matrimid<sup>®</sup> CMS membranes pyrolyzed under 1 ppm O<sub>2</sub>/Ar inert gas. Tests were conducted at 35 °C with a pressure of 50 psia. Units are in Barrer with % deviation of less than 10%.

Polymer precursor	He	CO <sub>2</sub>	O <sub>2</sub>	N <sub>2</sub>	CH <sub>4</sub>	SF <sub>6</sub>
6FDA/BPDA-DAM	2530	7170	1530	204	247	0.6
Matrimid <sup>®</sup>	605	1049	301	63	17	0.13

Table 4.8: Sorption coefficients of 6FDA/BPDA-DAM and Matrimid<sup>®</sup> CMS membranes in ccSTP/(ccCMS-psia). Experiments were repeated and had less than 10% of deviation.

Polymer precursor	He	CO <sub>2</sub>	O <sub>2</sub>	N <sub>2</sub>	CH <sub>4</sub>	SF <sub>6</sub>
6FDA/BPDA-DAM	0.049	1.41	0.43	0.46	0.82	0.018
Matrimid <sup>®</sup>	0.031	1.28	0.37	0.18	0.23	0.006

Table 4.9: Diffusion coefficients of 6FDA/BPDA-DAM and Matrimid<sup>®</sup> CMS membranes in 10<sup>-8</sup> cm<sup>2</sup>/s. Experiments were repeated and had less than 10% of deviation.

Polymer precursor	He	CO <sub>2</sub>	O <sub>2</sub>	N <sub>2</sub>	CH <sub>4</sub>	SF <sub>6</sub>
6FDA/BPDA-DAM	2680	262	237	22.8	15.5	1.72
Matrimid <sup>®</sup>	1020	42.4	42.1	18.0	3.85	1.14

Permeabilities of 6FDA/BPDA-DAM CMS membranes are higher than for Matrimid<sup>®</sup> CMS membranes; presumably due to higher free volume of the polymer precursor and resultant larger  $C_H'$  as a result of evolution of  $CF_3$  group during the heating process as seen on TGA-FTIR. Table 4.8 confirms that transport in CMS membranes is not sorption dominant with regard to selectivity. For  $CO_2/CH_4$  separation, sorption selectivity is less than half of diffusion selectivity. In the case of  $O_2/N_2$  separation on both 6FDA/BPDA-DAM and Matrimid<sup>®</sup> CMS membranes, the sorption selectivity is in the range between 0.9 and 2, which is similar to results observed by Singh and Koros [36]. The results of diffusion coefficients suggest that 6FDA/BPDA-DAM CMS membranes have a larger average number of accessible ultramicropore windows than Matrimid<sup>®</sup> CMS membranes. For all tested gases, diffusion coefficients are much higher for 6FDA/BPDA-DAM CMS membranes than that of Matrimid<sup>®</sup> CMS membranes. For instance,  $D_{He}$  is more than double, and  $D_{CO_2}$  is more than six times higher than Matrimid<sup>®</sup> CMS membranes. In addition, diffusion selectivity indicates that 6FDA/BPDA-DAM CMS membranes have more selective pore structures. For  $CO_2/CH_4$  separation, the diffusion selectivity is ~17 on 6FDA/BPDA-DAM CMS membranes while it is ~11 for Matrimid<sup>®</sup> CMS membranes. By interpreting results of diffusion coefficients, effective semi-quantitative pore size distributions for the ultramicropore region were constructed and are shown in Figure 4.20. The distributions were drawn to match the ratio of diffusion coefficients relative to the area of accessible ultramicropores for each respective molecule for the gas separations among  $CO_2$ ,  $O_2$ ,  $N_2$ ,  $CH_4$  gases. In addition, the total area under the curve was adjusted to be about 2.6 times larger for 6FDA/BPDA-DAM CMS membranes than that of Matrimid<sup>®</sup> CMS membranes to reflect the relative diffusion coefficients of He in the two polymers. This is based on an assumption that He samples all pores accessible to any gas molecule in both CMS membranes from the two precursors.

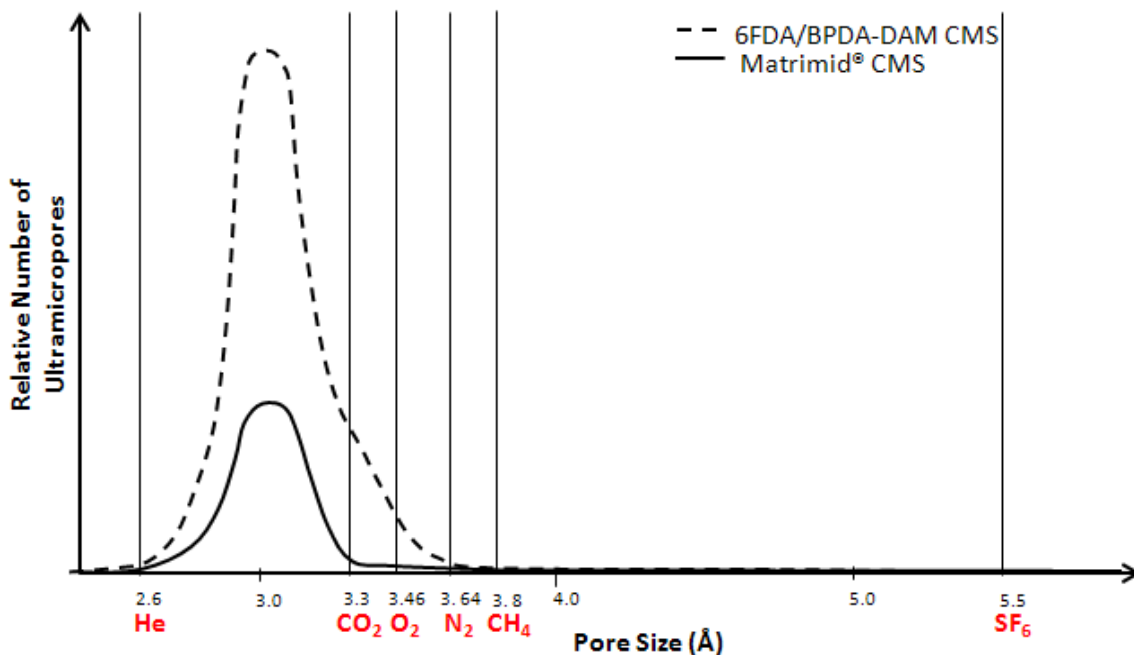


Figure 4.20: Diffusion coefficient based ultramicropore size distribution. The dot line represents the distribution of 6FDA/BPDA-DAM CMS membrane and the solid line represents the distribution of Matrimid<sup>®</sup> CMS membranes. The x-axis is linearly scaled with an indication of molecule's kinetic diameters.

Specifically, the overall shape of the curve was built with an assumption that the number of ultramicropores that are accessible to the SF<sub>6</sub> molecule provides a useful metric of the minimal number of large size ultramicropores to which a value of unity was assigned. Then the area which represents number of additional ultramicropores accessible for the rest of the gas molecules was scaled to be proportional to the diffusion coefficients. Finally, distribution curves were drawn to satisfy the ratios of diffusion coefficients among challenging separation gas pairs listed in Table 4.10.



Table 4.10: Diffusion selectivity among challenging gas separations. This was referenced to construct ultramicropore size distribution curves.

Polymer precursor	He/N <sub>2</sub>	CO <sub>2</sub> /CH <sub>4</sub>	O <sub>2</sub> /N <sub>2</sub>
6FDA/BPDA-DAM	117	16.9	10.3
Matrimid <sup>®</sup>	56.7	11.0	2.33

The diffusion coefficient data on Table 4.10 and the diffusion coefficient based ultramicropore size distribution on Figure 4.20 suggest that 6FDA/BPDA-DAM CMS membranes have a larger number of large pores and a more selective pore structure than Matrimid<sup>®</sup> CMS membranes.

Note that in Figure 4.20, the shape of the distribution between He (2.6 Å) and CO<sub>2</sub> (3.3 Å) was drawn for convenience with uncertainty and is not important for this discussion. Clarification of the shape in this range requires additional work with probes between 2.6 and 3.3 Å, such as neon molecule.

#### 4.2.4 Effect of pyrolysis temperature

Previous sections have shown that Matrimid<sup>®</sup> CMS membranes have closed and less selective intrinsic pore structures that result in a decrease in both permeability and selectivity with an increase in oxygen exposure. In order to utilize the oxygen doping method on the Matrimid<sup>®</sup> precursor, experiments were designed to create CMS membranes with more open intrinsic pore structures. Like Figure 4.21 shows, researchers have shown that higher temperatures tend to produce more selective yet less permeable CMS membranes [5, 6, 8] presumably due to systematic relaxation of the CMS matrix.

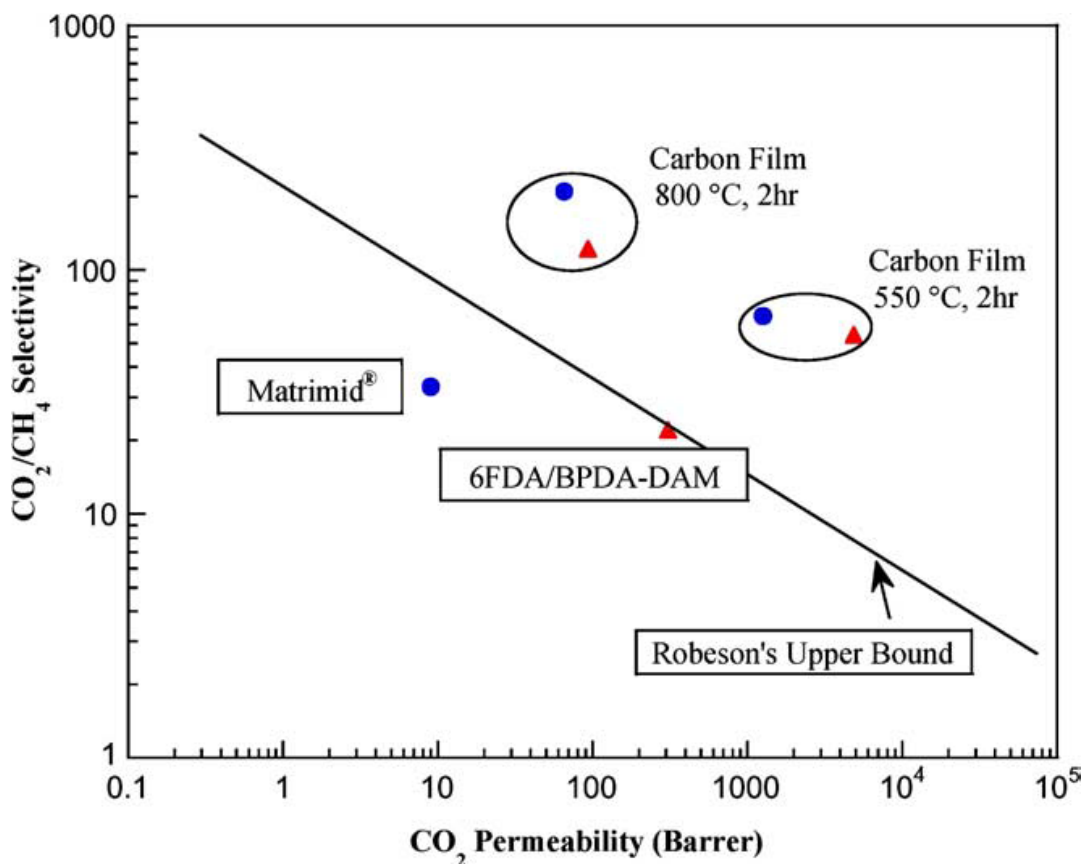


Figure 4.21: Effect of pyrolysis temperature reported by Steel [8]. All data was from vacuum pyrolysis.

This suggests that higher pyrolysis temperatures result in more selective and less permeable CMS structure. In principle, lowering the pyrolysis temperature should lead to more open intrinsic CMS structure so that one can take advantage of the oxygen doping method. In order to test this hypothesis, a slightly lower pyrolysis temperature of 500 °C with 1 ppm oxygen in argon gas was chosen to demonstrate the effect of temperature and the doping process. Results are shown in Figure 4.22.

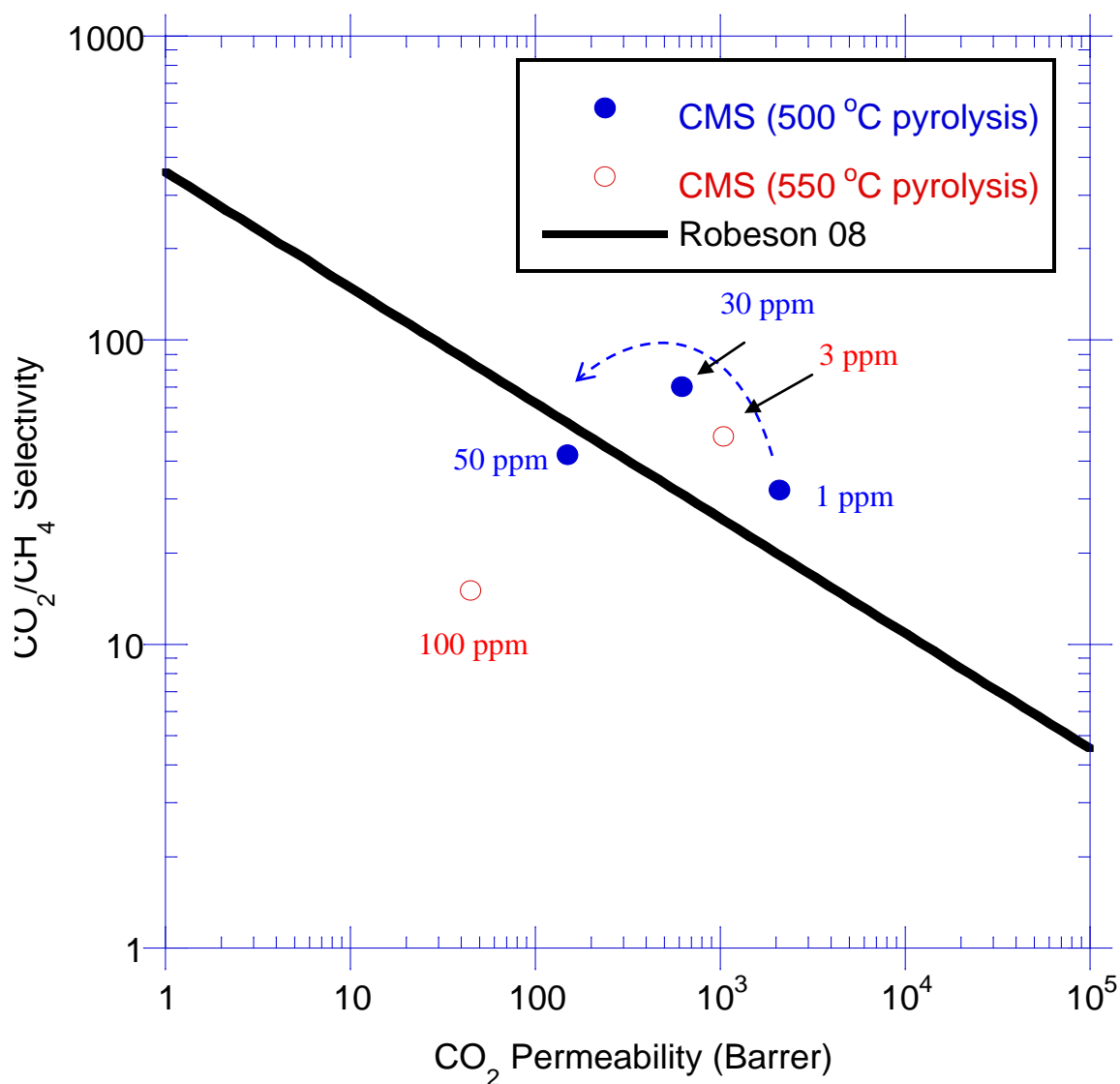


Figure 4.22: Separation performance of Matrimid® CMS membranes pyrolyzed by different temperatures, 500 and 500 °C, with oxygen “doping” process. Oxygen concentration in argon inert is listed. A dot line represents a trend observed for CMS films pyrolyzed at 500 °C. All data were repeated and had deviation of less than 10%.

As predicted, the lower pyrolysis temperature produces more permeable, but less selective CMS membranes with “near-intrinsic” structures, when CMS membranes are exposed to low amounts of oxygen. In addition, exposure to higher oxygen concentration enables use of the “doping” method, since the selectivity enhancement was more than double from 1 ppm O<sub>2</sub>/Ar to 30 ppm O<sub>2</sub>/Ar. When 50 ppm O<sub>2</sub>/Ar was used, the

selectivity decreased, compared with 30 ppm O<sub>2</sub>/Ar. This may be due to “over doping” as seen on 6FDA/BPDA-DAM CMS membranes on Figure 4.5.

### **4.3 EFFECT OF OXYGEN CONCENTRATION ON CMS FORMATION**

The method above allows one to enhance membrane performance by >100 times in permeability with doubled selectivity when CMS pyrolysis atmosphere is optimized, compared with separation performance of polymeric precursors [24, 37]. Although the total amount of oxygen exposure was hypothesized to govern effectiveness and amount of oxygen chemisorbed at the selective pore windows, this version has been refined to suggest that the oxygen-carbon reaction at the edges may be equilibrium limited, rather than kinetically controlled by observations from Figure 4.5 and Figure 4.10. Oxidation of carbon is complex due to the fact that the oxygen-carbon reaction involves chemical kinetics with consequent heat transfer and mass transfer processes at a number of levels. Gaseous oxygen molecules move from the surrounding bulk atmosphere to the carbon surface and are adsorbed to form surface intermediates, which may rearrange, desorb, and return to the gas phase [11, 12, 38]. Moreover, emitted decomposition by-products can be reacted in the external bulk gas phase. This section seeks to identify the limiting factor of the doping process during formation of CMS membranes.

#### **4.3.1 Review**

Three regimes are considered during the oxidation process: (i) oxygen fully penetrates the solid and all active sites are available for the reaction, (ii) oxidant penetration is partial and oxygen diffusion into the solid is insufficient to supply all reaction needs, and (iii) reaction only takes place at the outer surface [39, 40] for the available contact time. Investigation of the influence of diffusional resistance relative to

reaction resistance can be carried out using a fundamental analysis of the Thiele modulus,  $\theta$ , which is defined as:

$$\theta = \frac{d}{2} \left( \frac{\sigma_P k \beta}{D_e \sigma_{OX}} \right)^{\frac{1}{2}} \quad (4.4)$$

where  $d$  is the particle diameter in meters,  $\sigma_P$  is its density in  $\text{kg/m}^3$ ,  $k$  is the carbon reaction rate in  $\text{kg/kg-s}$ ,  $\beta$  is the stoichiometric mass ratio of oxygen to carbon,  $D_e$  is the effective diffusion coefficient in  $\text{m}^2/\text{s}$ , and  $\sigma_{OX}$  is the bulk gas concentration of oxygen in  $\text{kg/m}^3$  [41]. The Thiele modulus is applied by means of an effectiveness factor, which varies between 0 and 1 [41, 42]. The effectiveness factor represents the fraction of internal surface which can react when exposed to the surface concentration of reactant gas [42]. When the Thiele modulus is larger than 1, the reaction rate hinders the ability of diffusion to supply oxygen to the reactive surface and the effectiveness factor is much smaller than 1. When the Thiele modulus is smaller than unity, there is no resistance to pore diffusion. In terms of formation of CMS membranes, factors like pyrolysis temperature, film thickness, and pore structure strongly influence the process and determine the three regimes described earlier. A preliminary calculation can be made to identify one of three oxidation process regimes from the Thiele modules in Equation 6. The bulk oxygen concentration,  $\sigma_{OX}$ , of our interests is in 1-100 ppm, which corresponds to  $1.41 \times 10^{-6}$  to  $1.41 \times 10^{-4} \text{ kg/m}^3$ . The density,  $\sigma_P$ , of CMS membranes is reported to be in the order of  $10^3 \text{ kg/m}^3$ , depending on polymeric precursors [8]. At temperatures of 500-800 °C, where typical CMS membranes are produced, carbon oxidation produces chemisorbed CO as the dominant product [43]. According to Stanmore et al., this results in a  $\beta$  value of 4/3 [38]. Effective diffusion coefficients of oxygen in CMS membranes at high temperatures are in the order of  $10^{-8} \text{ m}^2/\text{s}$ , according to Singh [18]. According to de Soete, the reaction is in the first order when oxygen adsorption dominates, and overall

reaction rate constants can be in the range of 0.5-0.9 kg/kg-s [15, 44, 45]. When either homogeneous dense films or asymmetric hollow fibers have a selective skin thickness of  $d = 0.1\text{-}30\text{ }\mu\text{m}$ , calculation of the Thiele modulus based on these literature values results in a value of 0.6 to 2500. Since this range clearly spans values less than and greater than one, it suggests the possibility of pore diffusion resistance control of the oxidation reaction. Nevertheless, there is considerable uncertainty in the above parameters, so this study probes this issue experimentally in detail.

While the above theoretical calculation suggests possible pore diffusion resistance of oxygen during high temperature pyrolysis in carbon membranes, some researchers have seen inconsistent separation performance of CMS membranes pyrolyzed under atmosphere in which oxygen exists for possible oxidation reaction. Variations have been reported in CMS separation performance with respect to polymer precursor thickness [23], and researchers have seen separation performance independent of inert flow rates as mentioned in section 4.1 [7, 23, 46]: observations and the theoretical calculation have not reached an agreement. Therefore it is essential to draw a more definite conclusion by identifying the controlling factor in the oxygen doping process by a series of well controlled experiments, specifically, by means of oxygen consumption during pyrolysis and separation performance of the resulting CMS membranes.

#### **4.3.2 Effect of thermal soak time**

Effect of thermal soak time on the oxygen doping process was investigated by comparing oxygen consumption during pyrolysis and the separation performance between CMS membranes prepared at 550 °C with two different thermal soak times of two and eight hours. First, 6FDA/BPDA-DAM polymer precursor was pyrolyzed with an eight hour soak time under 200 cc(STP)/min inert flow of 7 ppm oxygen in argon gas. The result was compared with data of a two hour thermal soak time previously reported

[37]. Table 4.11 shows amounts of oxygen available and consumed during the pyrolysis process. While the total amount of oxygen available during the eight hour soak time is higher than during the two hour soak, the consumption amount *stays almost the same*. Moreover, Figure 4.23 shows that the data falls within the range of correlation observed in the previous study between the total amount of oxygen and the amount of oxygen consumption. This result indicates that a longer thermal soak time led to only a slight increase in the oxygen consumption.

Table 4.11: Normalized values of the total amount of oxygen at different soak time obtained with 6FDA/BPDA-DAM. Inert pyrolysis under 200 cc/min of 7 ppm O<sub>2</sub>/Ar was conducted by eight hour soak time while the other was pyrolyzed for two hours 8 ppm O<sub>2</sub>/Ar. Weight of precursors on eight hour soak time was slightly higher than two hour soak time, which resulted in similar normalized values of total oxygen available amount. Experiments were repeated and have a standard deviation of less than 10%.

Thermal soak time (hrs)	Total O <sub>2</sub> available (ccSTP/g)	Total O <sub>2</sub> consumed (ccSTP/g)
2	11.8	5.24
8	12.5	6.75

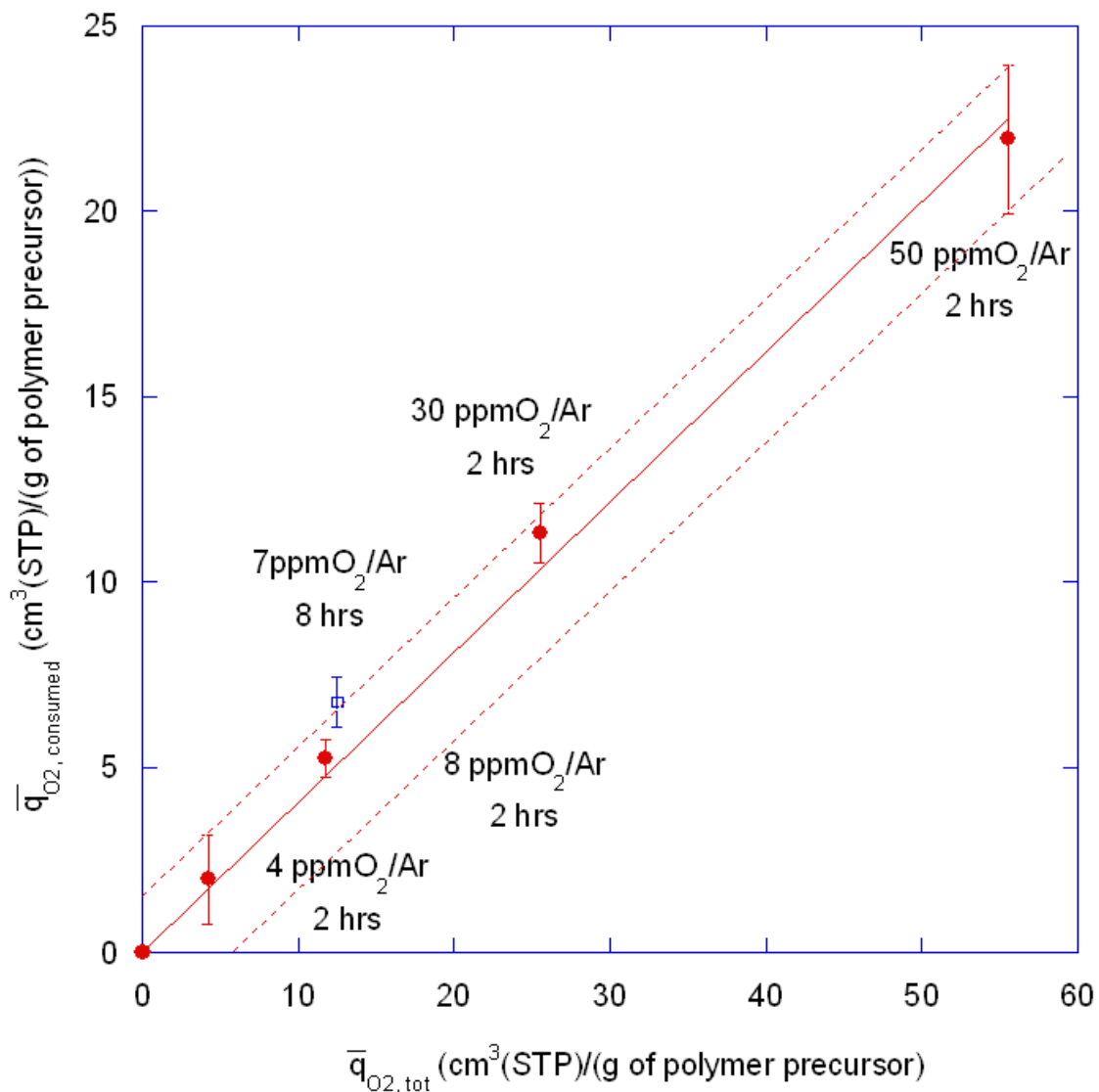


Figure 4.23: Correlation between the total amount of oxygen and the amount of oxygen consumption normalized by weight of polymer precursors. Circles (●) represent data of two hour thermal soak time from previous study [37], and the rectangular (□) represents data of eight hour thermal soak time. Inert compositions are listed along with data points. The data with longer thermal soak time falls within the trend seen with two hour soak time [47].



In addition, the separation performance of 6FDA/BPDA-DAM CMS membranes from two thermal soak periods was evaluated. As shown in Figure 4.24, CMS membranes prepared with an eight hour soak time have a slightly higher  $\text{CO}_2$  permeability and lower  $\text{CO}_2/\text{CH}_4$  selectivity compared with that of a two hour soak time. Based on these facts, it was speculated that the oxygen concentration may play a more major role during the doping process with oxygen than the period of soaking per se.

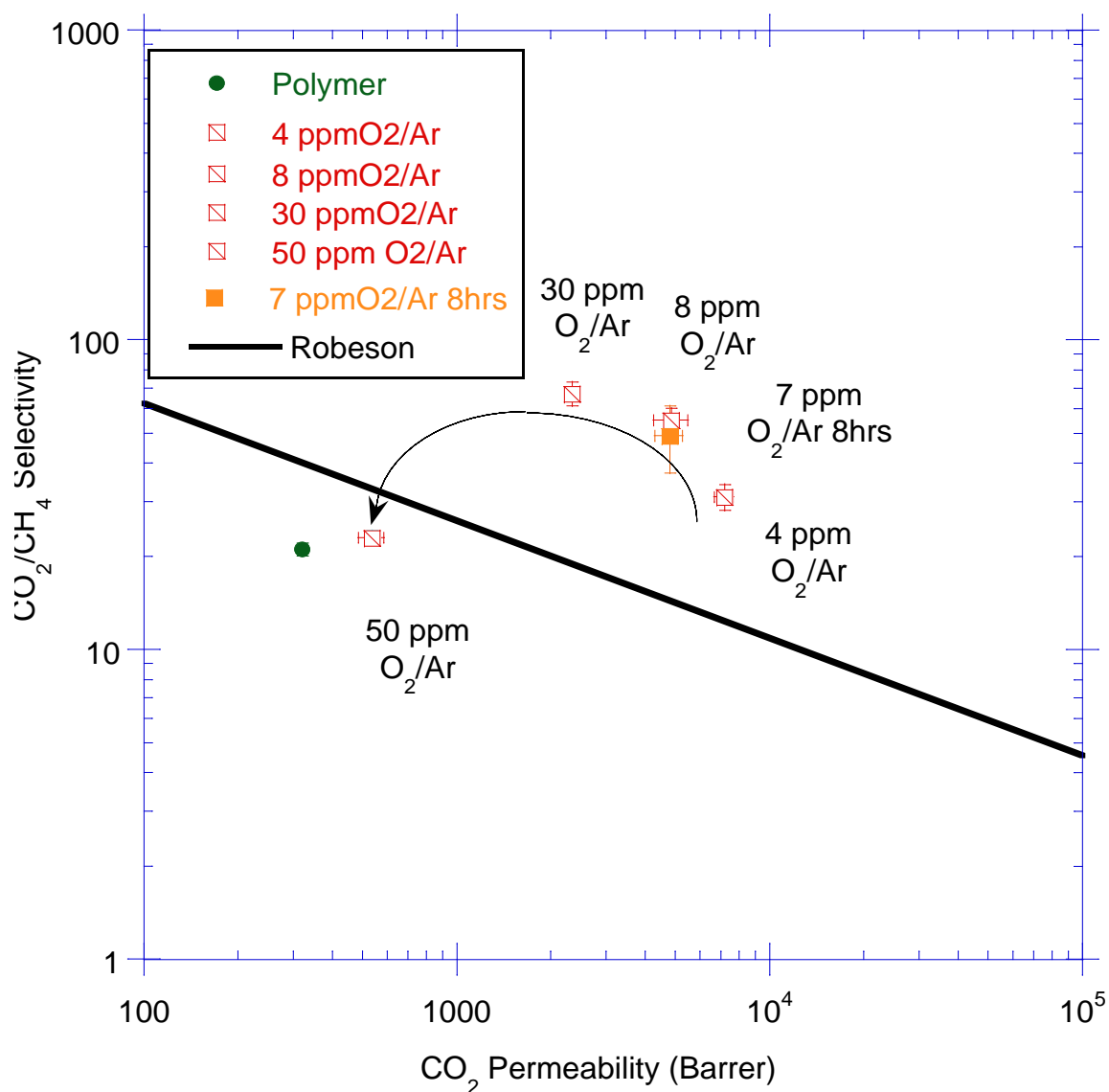


Figure 4.24: Separation performance of 6FDA/BPDA-DAM CMS films. A filled circle (●) represents CMS pyrolyzed with eight hour thermal soak time, and open circles (○) represent CMS pyrolyzed with two hour soak time. Each was repeated at 35 °C [47].

The effect of thermal soak time on Matrimid<sup>®</sup> as a polymer precursor was also investigated. A pyrolysis atmosphere of 200 cc(STP)/min inert flow with ~30 ppm oxygen in argon was used. Oxygen consumption and separation performance results are shown in Table 4.12 and

Figure 4.25, respectively. The results show that samples with a shorter soak time consumed a smaller amount of oxygen compared with a longer one; however,

*Figure 4.25 indicates that their separation performances are similar.* During the Matrimid<sup>®</sup> pyrolysis process, large amounts of tan colored by-products adsorbed on the pyrolysis tube wall unlike the pyrolysis of 6FDA/BPDA-DAM. Based on this observation, it is speculated that the difference in oxygen consumption could be caused by the oxidation of the by-products, which has little effect on the membrane properties.

Table 4.12: Normalized values of the total amount of oxygen at different soak time obtained with Matrimid<sup>®</sup>. Inert pyrolysis under 200 cc/min of ~30 ppm O<sub>2</sub>/Ar was conducted in both cases. Experiments were repeated and have a standard deviation of less than 10%.

Thermal soak time (hrs)	Total O <sub>2</sub> available (ccSTP/g)	Total O <sub>2</sub> consumed (ccSTP/g)
2	154.2	50.0
8	216.1	90.2

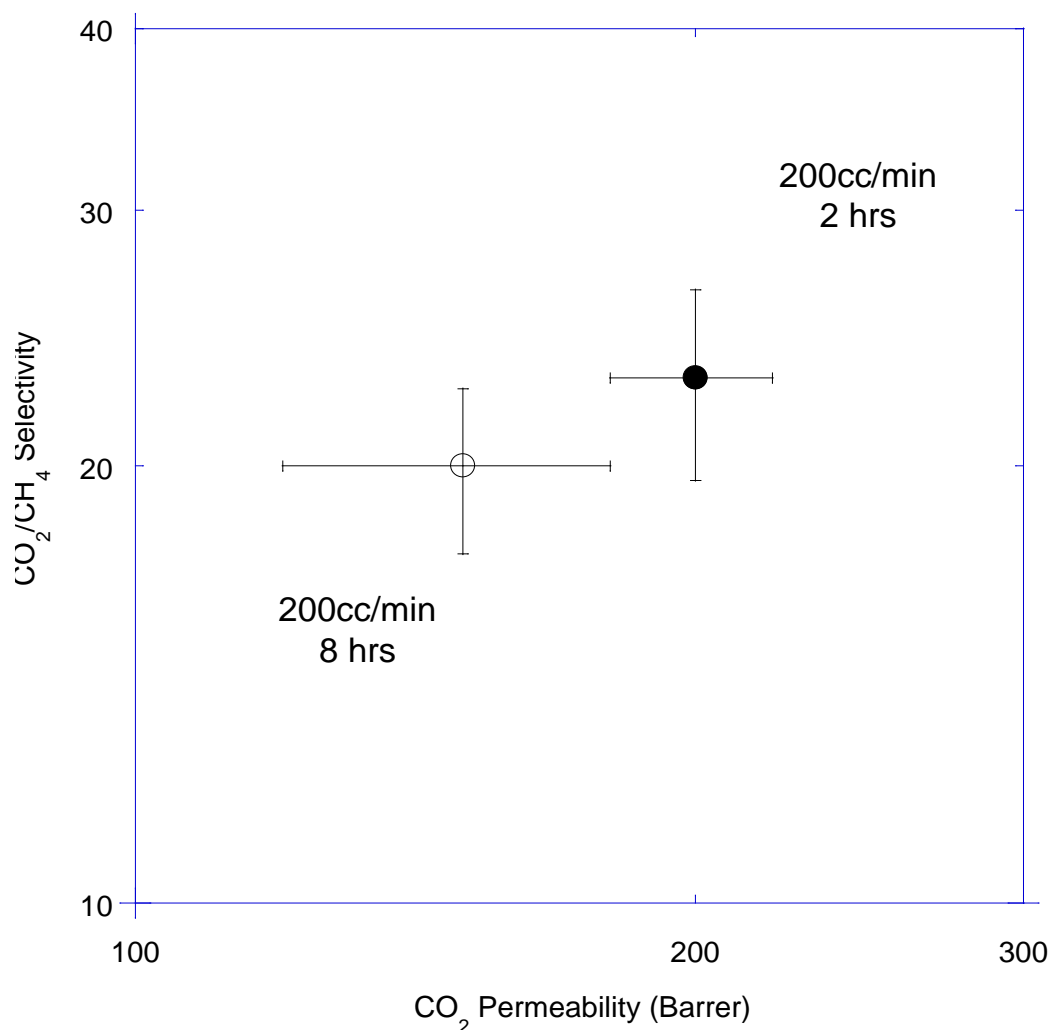


Figure 4.25: Separation performance of Matrimid<sup>®</sup> CMS films pyrolyzed with two different thermal soak times of two hours (●) and eight hours (○). The thickness of the films was ~80  $\mu\text{m}$ . Inert carrier of ~30 ppm O<sub>2</sub>/Ar was used with a flow rate of 200 cc(STP)/min. All was repeated at 35 °C[47].

A combination of the oxygen consumption and the separation performance properties indicates that the effect of *duration of oxygen exposure to the separation performance is relatively small*. This led us to hypothesize that the oxygen doping process during the pyrolysis to produce attractive CMS membranes is governed by oxygen concentration rather than total amount of oxygen exposed. A series of well

controlled experiments was conducted to identify the limiting factor on the oxygen “doping” process to support this hypothesis. Three limiting factors are considered regarding the oxygen doping effect in dense films: external transport, internal transport, and chemical reaction. They were studied with respect to oxygen consumption and CO<sub>2</sub>/CH<sub>4</sub> separation performance.

#### 4.3.3 Effect of inert flow rate: external transfer limitation

Researchers have shown that inert flow rate during pyrolysis does *not* affect separation performances [7, 23]. These studies showed that the external transport is not the limiting factor in determining the resulting CMS membrane performance. In order to demonstrate this phenomenon in terms of the oxygen exposure, two sets of experiments were conducted as shown in Figure 4.26. A gas mixture of 30 ppm of oxygen in argon was used as an “inert” with two different flow rates: 50 and 200 cc(STP)/min. Two polymeric films (total of ~0.02g) were pyrolyzed with the thermal protocol of 550 °C and a two hour thermal soak time for consistency. It was hypothesized that if external mass transfer dominates the mechanism, oxygen consumption and separation performance would be dependent on the inert flow rates.

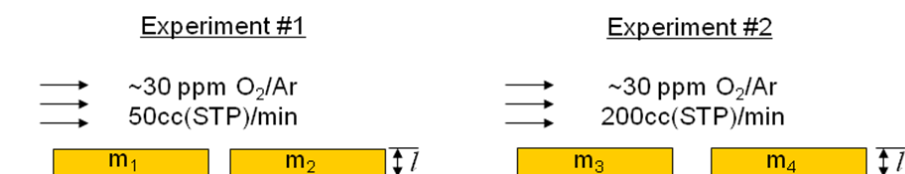


Figure 4.26: Schematic of experiments to investigate external transfer limitation by applying two different inert flow rates. Total of ~0.02g polymeric films,  $m_1 + m_2 = m_3 + m_4$  were pyrolyzed at 550 °C with two hour soak time. Experiments were repeated twice.

Table 4.13 shows the result of oxygen consumption on the two different flow rates. This further confirms that the flow rates *do not affect* the amount of oxygen consumption as noted above. In addition, Figure 4.27 shows that the separation performances are almost the same for different flow rates, which also supports our hypothesis that *rate effects due to external transport resistance are negligible factors in fixing membrane performance*.

Table 4.13: Normalized values of the total amount of oxygen at different inert flow rates of 50 and 200 cc(STP)/min with Matrimid<sup>®</sup>. Inert gas of ~30 ppm O<sub>2</sub>/Ar was used in both cases. Experiments were repeated and have a standard deviation of less than 10%.

Inert flowrate (cc(STP)/min)	Total O <sub>2</sub> available (ccSTP/g)	Total O <sub>2</sub> consumed (ccSTP/g)
50	67.3	45.4
200	154.2	50.0

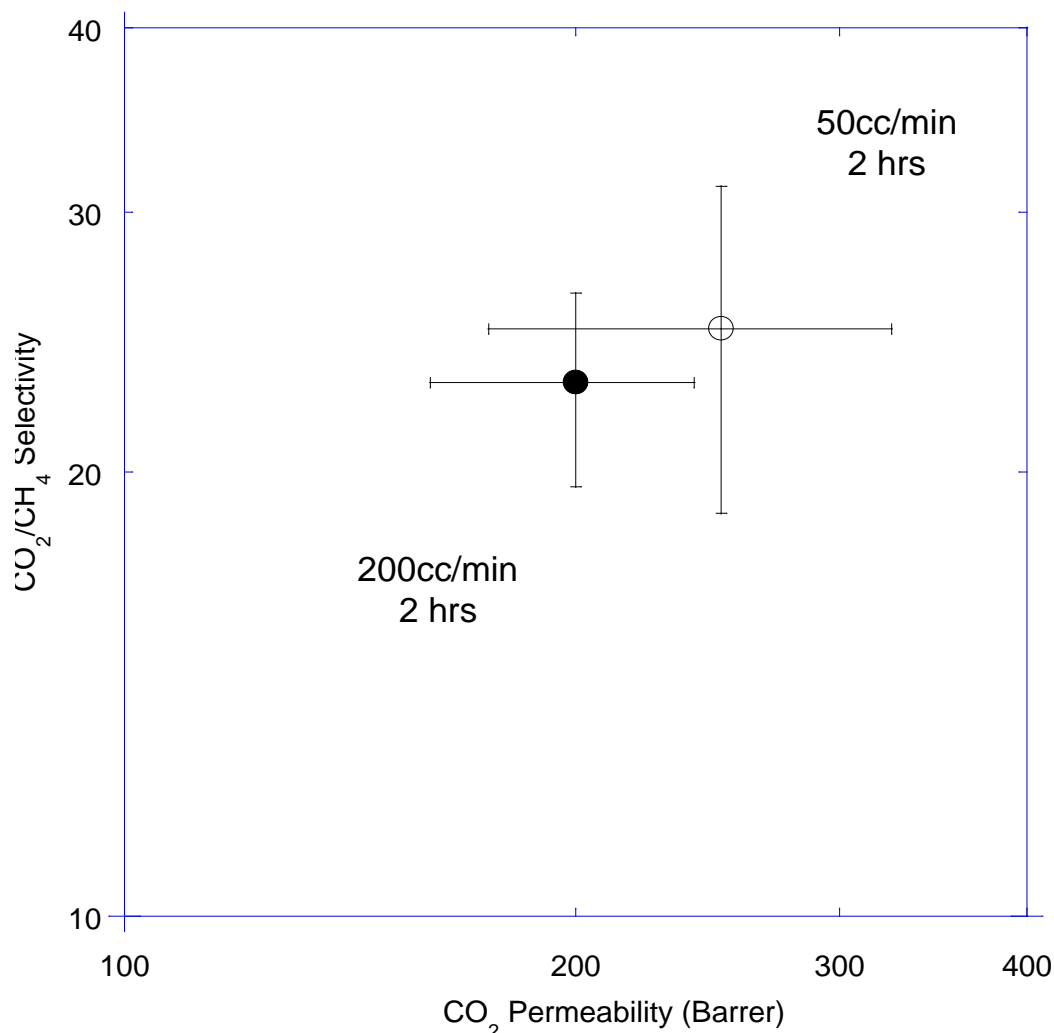


Figure 4.27: Separation performance of Matrimid<sup>®</sup> CMS films pyrolyzed with two different inert flow rates of 200 (●) and 50 (○) cc(STP)/min. Inert carrier of ~30 ppm O<sub>2</sub>/Ar was used. All was repeated at 35 °C.

Clearly when CMS membranes experience longer thermal soak times, both the total amount of oxygen available and consumed should increase; however, consumption stayed almost consistent despite a higher inert (and oxygen) flow rate. Since the separation performances for the two different thermal soak times are almost the same, this discrepancy can be explained by suggesting that CMS oxidation may be equilibrium limited while by-products, or “molecular debris,” externally follow a kinetically limited reaction mechanism.

#### 4.3.4 Effect of precursor film thickness: internal transfer limitation

The above investigation shows that the transport mechanism is not likely dominated by the external transport. Next, another investigation was conducted to determine any role of internal mass transfer limitations. This investigation consisted of two experiments as shown in Figure 4.28.

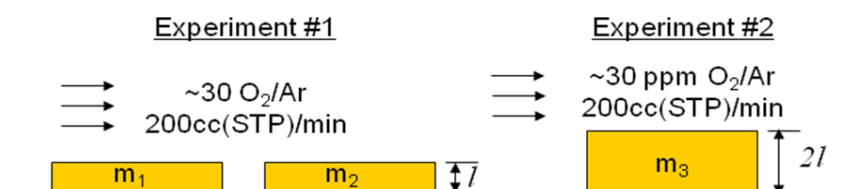


Figure 4.28: Schematic design of experiments testing the internal mass transfer limitation. About 0.02g of polymer precursor,  $m_1 + m_2 = m_3$ , was prepared. Gas mixture of argon and a slightly higher than 30 ppm of oxygen in argon gas was used as an inert with the flow of 200 cc(STP)/min. Experiments were repeated twice.

The first experiment consisted of pyrolysis of two polymer films ( $m_1$  and  $m_2$ ) which each film had a thickness of 60  $\mu\text{m}$ . The second experiment consisted of a film ( $m_3$ ) whose mass was essentially a sum of  $m_1$  and  $m_2$  with a thickness of 120  $\mu\text{m}$ . It was hypothesized that if the internal mass transfer dominated the mechanism, the oxygen consumption and separation performance would depend strongly on the film thickness. Recall that about four times longer exposure to a given amount oxygen showed almost no effect on CMS oxygen uptake, so these experiments sought to further probe if the process of doping is an equilibrium limited, internal reaction process. The results are shown in Table 4.14 and Figure 4.29.

Table 4.14: Normalized values of the total amount of oxygen with different polymer precursor thickness. Inert gas of ~35 ppm O<sub>2</sub>/Ar was used in both cases. Experiments were repeated and have a standard deviation of less than 10%.

Thickness of polymer precursor	Total O <sub>2</sub> available (ccSTP/g)	Total O <sub>2</sub> consumed (ccSTP/g)
60 $\mu$ m	180	47
120 $\mu$ m	182	52

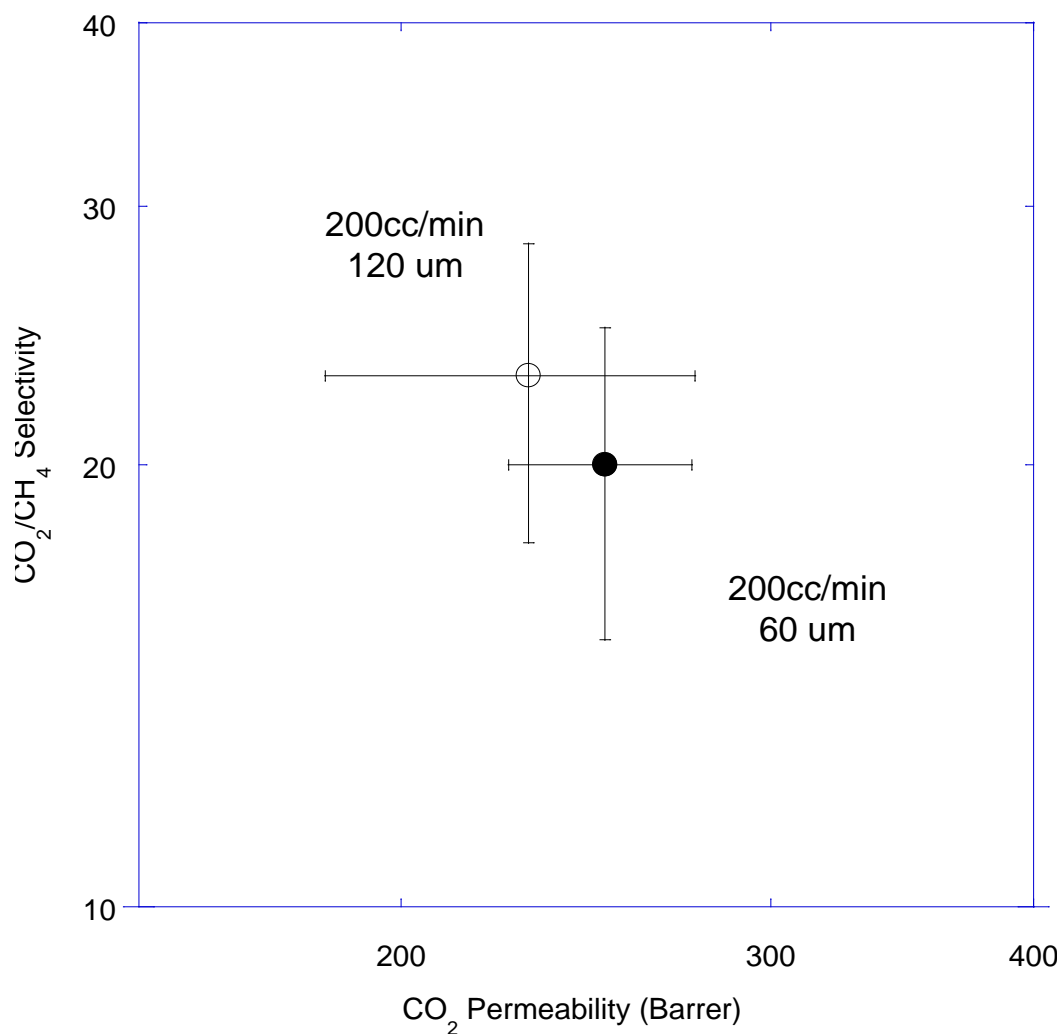


Figure 4.29: Separation performance of Matrimid<sup>®</sup> CMS films pyrolyzed with two different precursor thickness, 60 (●) and 120 (○)  $\mu$ m. Inert carrier of ~35 ppm O<sub>2</sub>/Ar was used. All was repeated at 35 °C.



Results of oxygen consumption in Table 4.14 indicate that oxygen consumption is almost the same regardless of the film thickness as long as the sample masses are the same. In addition, the separation performance of CO<sub>2</sub>/CH<sub>4</sub> in Figure 4.29 is similar as well. *This indicates that the oxygen doping process is unlikely to be internal mass transfer limited.*

#### **4.3.5 Oxygen-carbon reaction mechanism: chemical reaction limitation consideration**

The above experiments show that the CMS membrane separation performance and oxygen consumption during the high temperature pyrolysis are not likely influenced by the thickness of the polymer precursors, inert, or oxygen, flow rates, nor thermal soak time during pyrolysis. The summation of all these facts implies that a carbon-oxygen equilibrium reaction governs the oxygen doping process via a chemisorption process. The oxygen chemisorption mostly likely takes place at the same time polymer precursors decompose, and evolved products diffuse out of the membranes. This indicates that the actual full mechanism can be very complex.

#### **4.4 POSSIBLE MECHANISM OF OXYGEN “DOPING” PROCESS DURING PYROLYSIS**

As previous sections described, an oxygen doping process was successfully developed to tune separation properties of CMS membranes by controlling the CMS structure. The method was built based on well-known scientific facts that (i) oxygen reacts with active carbon edges at high temperature during pyrolysis [11, 12, 14, 38] and that (ii) the adsorption step which involves surface oxides dominate the reaction process and is endothermic and reversible in the temperature range between 350 and 700 °C [15, 48]. According to Marsh et al., several carbon-oxygen complexes could be produced as a result of the oxidation as shown in Figure 4.30.

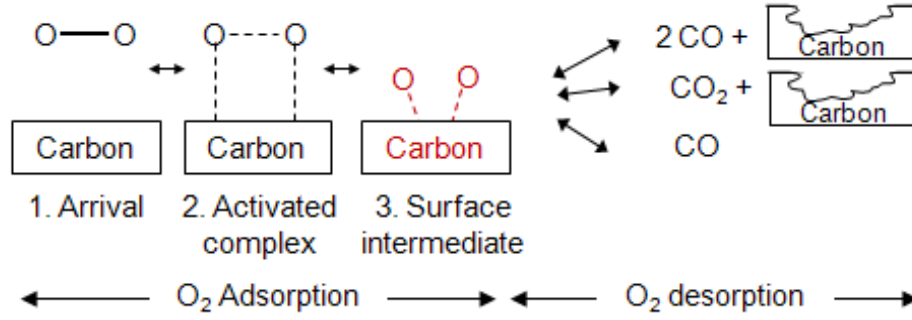
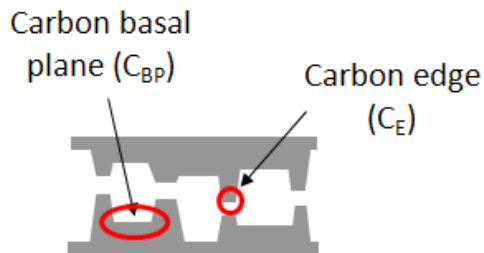
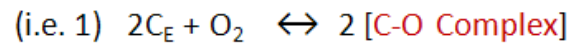


Figure 4.30: Possible carbon-oxygen reactions suggested by Marsh et al. [12]. In the temperature of the interests, the O<sub>2</sub> adsorption dominates the reaction [15, 48]; therefore, there is no actual carbon loss with “O<sub>2</sub> doping” CMS production.

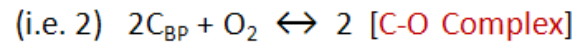
As previously mentioned, the reaction is likely endothermic and reversible around the temperature our CMS samples were pyrolyzed; either at the carbon edges or basal planes. Equilibrium oxidation reactions associate with the equilibrium constants,  $K_{eqbm}$ , as shown in Figure 4.31.



Some of reactions taking places are:



$$K_{eqbm} = \frac{[C_{CO2}]_{\text{cmplx}}}{[C_{CE}][C_{O2}]}$$



$$K_{eqbm} = \frac{[C_{CO2}]_{\text{cmplx}}}{[C_{CBP}][C_{O2}]}$$

Figure 4.31: Carbon-oxidation equilibrium reactions.

These constants are temperature dependent via the following correlation:

$$RT \ln(K_{eqbm}) = -\Delta G \quad (4.5)$$

where R is the gas constant, T is the temperature,  $K_{eqbm}$  is the equilibrium constant, and  $\Delta G$  is Gibbs free energy. Gibbs free energy is defined as:

$$\Delta G = \Delta H - T\Delta S \quad (4.6)$$

where  $\Delta H$  is the enthalpic component based on the change in molecular interactions and  $\Delta S$  comprises any entropic element which accounts for the change in the number of possible configurations of the molecule from one state to another [49]. Hypothetically, this concept enables us to “post-tune” the CMS structures. For example, if too much oxygen was doped, both permeability and selectivity would be lower than expected. One could expose the CMS samples to lower oxygen concentration at the pyrolysis temperature so that the CMS samples would supposedly have a higher permeability and possibly increased selectivity.

The oxygen-carbon mechanism can be very complex. Here we seek to understand the pyrolysis process of polymer membranes with oxygen exposure by normalization of literature and our findings. Section 4.2.3.1 described the three stages that occur during the polymer decomposition process: precarbonation, carbonation, and dehydrogenation [25]. In this study, oxygen was continuously supplied during the pyrolysis process. Precarbonation mostly involves removal of excess solvent and monomer [25], and as illustrated in Figure 4.3, consumption of oxygen does not start until temperature is close to the decomposition temperature. During the carbonation stages, it is believed that a majority of the oxygen was consumed by by-products. Meanwhile, a transformation from

polymeric to CMS membranes takes place [25], and the “intrinsic” CMS structure results a product of the high temperature pyrolysis process. Once most of the by-products are evolved, the dehydrogenation process begins, but consumption of oxygen by the by-products continues at a significantly decreased rate, and a larger amount of oxygen became available to the CMS membranes compared with previous two stages. As section 4.3 described, the oxidation of the by-products is likely controlled kinetically while the oxidation of the active carbon edges for “doping” is likely equilibrium controlled. Therefore, the likelihood of oxygen molecules adsorbing on the surface and penetrating through CMS membranes to react with active carbon edges depend on oxygen concentration in the bulk flow. The oxidation “doping” process also depends on the temperature which is related to the energetics of the chemisorption [15, 50]. Effects of the temperature on the “doping” process are complex since one also needs to consider the effect of pyrolysis temperature on the formation of the “intrinsic” CMS structure in the absence of oxygen chemisorption. Section 4.2.4 depicted an experiment involving pyrolysis temperature of 500 °C. Comparing separation performance of CMS membranes with 550 °C, it seems that the effect of temperature to the “doping” process is less significant compared to its importance on the formation of the intrinsic CMS structures. One should note, however, that a distribution of reactivity of carbon edges is speculated to exist to form carbonyl groups among ultramicropores, and the overall “doping” process is complex.

## 4.5 SUMMARY

In this chapter, correlations observed during the development of a pyrolysis method were presented. This enables the control of separation performance of CMS membranes. This method utilized oxygen chemisorptions or “O<sub>2</sub> doping” on selective pore windows at high temperature. Initially the method was developed using a 6FDA based polymer and extended to a commercially available polymer Matrimid<sup>®</sup>. Observed correlations were shown (i) between the total oxygen exposure  $q_{O_2, \text{ tot}}$  and oxygen consumption,  $q_{O_2 \text{ consumed}}$ , and (ii) between  $q_{O_2, \text{ tot}}$  and CMS CO<sub>2</sub>/CH<sub>4</sub> separation performance. Moreover, a series of controlled experiments allowed us to show that the oxygen-carbon reaction appears to be equilibrium limited and that a correlation exists between oxygen concentration in the inert gas and CMS CO<sub>2</sub>/CH<sub>4</sub> separation performance. These findings are significant for two major reasons: (i) they enable one to predict the trends in separation performance with the doping method after knowing the intrinsic structures created in low oxygen exposure pyrolysis conditions at a given temperature and (ii) they require only monitoring a primary variable of the oxygen concentration during the pyrolysis process for the doping method in inert pyrolysis.

#### 4.6 REFERENCES

- [1] Centeno TA, Fuertes AB. Supported carbon molecular sieve membranes based on a phenolic resin. *J Membr Sci* 1999; 160:201-11.
- [2] Koresh JE, Soffer A. Molecular sieve permselective membrane. Part I. Presentation of a new device for gas mixture separation. *Sep Sci Technol* 1983; 18(8):723-34.
- [3] Sedigh MG, Jahangiri M, Liu PK, Sahimi M, Tsotsis TT. Structural characterization of polyetherimide-based carbon molecular sieve membranes. *AIChE J* 2000; 46(11):2245-55.
- [4] Steel KM, Koros WJ. Investigation of porosity of carbon materials and related effects on gas separation properties. *Carbon* 2003; 41(2):253-66.
- [5] Vu DQ. Formation and characterization of asymmetric carbon molecular sieve and mixed matrix membranes for natural gas purification. Austin TX USA, University of Texas at Austin, PhD thesis, 2001.
- [6] Barsema JN, Vegt NFA, Koops GH, Wessling M. Carbon molecular sieve membranes prepared from porous fiber precursor. *J Membr Sci* 2002; 205(1-2):239-46.
- [7] Geiszler VC, Koros WJ. Effects of polyimide pyrolysis conditions on carbon molecular sieve membrane properties. *Ind Eng Chem Res* 1996; 35(9):2999-3003.
- [8] Steel KM. Carbon membranes for challenging gas separations. Austin TX USA, The University of Texas at Austin, PhD thesis, 2000.
- [9] Suda H, Haraya K. Gas permeation through micropores of carbon molecular sieve membranes derived from Kapton polyimide. *J Phys Chem B* 1997; 101(20):3988-94.
- [10] Grisdale RO. The properties of carbon contacts. *J Appl Phys* 1953; 24(10):1288-96.
- [11] Kinoshita K. Carbon: electrochemical and physicochemical properties. Berkeley CA USA: Wiley-Interscience; 1988.
- [12] Marsh H. Introduction to carbon science. Borough Green, England: Butterworth & Co. Ltd; 1989.
- [13] Ishiguro T, Suzuki N, Fujitani Y, Morimoto H. Microstructural changes of diesel soot during oxidation. *Combust Flame* 1991; 85(1-2):1-6.
- [14] Laine NR, Vastola FJ, Walker PL Jr. The importance of active surface area in the carbon-oxygen reaction. *J Phys Chem* 1963; 67(10):2030-4.

- [15] deSoete G. Catalysis of soot combustion by metal oxides. Western States Section Meeting of the Combustion Institute; 1988 March 21-22, 1988; Salt Lake City UT USA. 1988.
- [16] Jones CW, Koros WJ. Carbon molecular sieve gas separation membranes-II. Regeneration following organic exposure. *Carbon* 1994; 32(8):1427-32.
- [17] Jones CW, Koros WJ. Characterization of ultramicroporous carbon membranes with humidified feeds. *Ind Eng Chem Res* 1995; 24:158-63.
- [18] Singh A. Membrane materials with enhanced selectivity: an entropic interpretation. Austin TX USA, The University of Texas at Austin, PhD thesis, 1997.
- [19] Coutinho EB, Salim VMM, Borges CP. Preparation of carbon hollow fiber membranes by pyrolysis of polyetherimide. *Carbon* 2003; 41:1808-14.
- [20] Fuertes AB, Centeno TA. Carbon molecular sieve membranes from polyetherimide. *Micropor Mesopor Mater* 1998; 26:23-6.
- [21] Sedigh MG, Xu L, Tsotsis TT, Sahimi M. Transport and morphological characteristic of polyetherimide-based carbon molecular sieve membranes. *Ind Eng Chem Res* 1999; 38:3367-80.
- [22] Robeson LM. The upper bound revisited. *J Membr Sci* 2008; 320(1-2):390-400.
- [23] Williams PJ. Analysis of factors influencing the performance of CMS membrane for gas separation. Atlanta GA USA, Georgia Institute of Technology, PhD thesis, 2006.
- [24] Kiyono M, Williams PJ, Koros WJ. Effect of polymer precursor on carbon molecular sieve structure and separation performance properties, accepted. *Carbon* 2010.
- [25] Jenkins GM, Kawamura K. Polymeric carbons - carbon fiber, glass and char. London: Cambridge University Press; 1976.
- [26] Barsema JN, Klijnstra SD, Balster JH, Vegt NFAVd, Koops GH, Wessling M. Intermediate polymer to carbon gas separation membranes based on Matrimid PI. *J Membr Sci* 2004; 328(1-2):93-102.
- [27] Stoeckli HF. Microporous carbons and their characterization: The present state of the art. *Carbon* 1990; 28(1):1-6.
- [28] Jiang D, Cooper VR, Dai S. Porous graphene as the ultimate membrane for gas separation. *Nano Lett* 2009; 9(12):4019-24.
- [29] Jones CW, Koros WJ. Carbon molecular sieve gas separation membranes-I. Preparation and characterization based on polyimide precursors. *Carbon* 1994; 32(8):1419-25.

- [30] Vu DQ, Koros WJ, Miller SJ. High pressure CO<sub>2</sub>/CH<sub>4</sub> separation using carbon molecular sieve hollow fiber membranes. *Ind Eng Chem Res* 2002; 41(3):367-80.
- [31] Mulder M. Basic principles of membrane technology. 2nd ed. Dordrecht Netherlands: Kluwer Academic Publishers; 1997.
- [32] Steel KM, Koros WJ. An investigation of the effects of pyrolysis parameters on gas separation properties of carbon materials. *Carbon* 2005; 43:1843-56.
- [33] Campo MC, Magalhaes FD, Mendes A. Comparative study between a CMS membrane and a CMS adsorbent: Part I - Morphology, adsorption equilibrium and kinetics. *J Membr Sci* 2010; 346(1):15-25.
- [34] Lee H, Suda H, Haraya K. Characterization of the post-oxidized carbon membranes derived from poly(2,4-dimethyl-1,4-phenylene oxide) and their gas permeation properties. *Sep Purif Technol* 2008; 59(2):190-6.
- [35] Stoeckli F, Centeno TA. On the characterization of microporous carbons by immersion calorimetry alone. *Carbon* 1997; 35(8):1097-100.
- [36] Singh A, Koros WJ. Significance of entropic selectivity for advanced gas separation membranes. *Ind Eng Chem Res* 1996; 35(4):1231-4.
- [37] Kiyono M, Williams PJ, Koros WJ. Effect of pyrolysis atmosphere on separation performance of carbon molecular sieve membranes. *J Membr Sci* 2010; 359(1-2):2-10.
- [38] Stanmore BR, Brillhac JF, Gilot P. The oxidation of soot: a review of experiments, mechanisms and models. *Carbon* 2001; 38(15):2247-68.
- [39] Smith BC. Infrared spectral interpretation: a systematic approach. 1st ed. New York: CRC Press; 1999.
- [40] Welty JR, Wicks CE, Wilson RE, Rorrer GL. Fundamentals of momentum, heat, and mass transfer. New York: John Wiley & Sons, Inc; 2001.
- [41] Walker PJ, Rusinko FJ, Austin LG. Gas reactions of carbon. In: Eley DD, Frankenburg WG, editors. *Advances in catalysis and related subjects*, New York: Academic Press Inc; 1959, p. 133-76.
- [42] Levenspiel O. Chemical reaction engineering. 3rd ed. Hoboken NJ: John Wiley & Sons, Inc; 1999:376-417.
- [43] Lear AE, Brown TC, Haynes BS. Formation of metastable oxide complexes during the oxidation of carbons at low temperatures. *Twenty-Third Symposium (International) on Combustion*; 1990; At the University of Orléans, Orléans France. 1990. p. 1191-7.



- [44] Neeft J, Nijhuis T, Smakman E, Makkee M, Moulijn J. Kinetics of the oxidation of diesel soot. *Fuel* 1997; 76(12):1129-36.
- [45] Gilot P, Bonnefoy F, Marcucilli F, Prado G. Determination of kinetic data for soot oxidation. Modeling of competition between oxygen diffusion and reaction during thermogravimetric analysis. *Combust Flame* 1993; 95:87-100.
- [46] Park HB, Nam SY, Jang JG, Lee YM. Preparation, characterization, and gas permeation properties of carbon molecular sieve membranes derived from dense P84-polyimide film. *Korean Membrane Journal* 2002; 4(1):25-35.
- [47] Kiyono M, Williams PJ, Koros WJ. Generalization of effect of oxygen exposure on formation and performance of carbon molecular sieve membranes, accepted. *Carbon* 2010.
- [48] Ong JN Jr. On the kinetics of oxidation of graphite. *Carbon* 1964; 2(3):281-97.
- [49] Prausnitz JM, Lichtenthaler RN, Azevedo EGd. *Molecular thermodynamics of fluid-phase equilibria*. Upper Saddle River, NJ: Prentice-Hall, Inc.; 1999.
- [50] Hill CG Jr. *An introduction to chemical engineering kinetics & reactor design*. New York: John Wiley & Sons, Inc.; 1977.

## **CHAPTER 5**

### **ASYMMETRIC HOLLOW FIBER CMS MEMBRANES FOR NATURAL GAS (CO<sub>2</sub>/CH<sub>4</sub>) SEPARATION**

#### **5.1 OVERVIEW**

The effective inert pyrolysis method was developed in Chapter 4 based on fundamental studies with homogeneous dense CMS membranes. The method describes introduction of trace amount of oxygen during pyrolysis. This project not only focused on the process development but also translation of the dense film work with the oxygen “doping” method to asymmetric hollow fibers, since this is an industrially preferred form of the membranes [1, 2]. This chapter advances the previous chapter by applying the pyrolysis method to form asymmetric hollow fiber CMS membranes. Asymmetric hollow fiber membranes provide higher mechanical strength than dense films due to a combination of a thin integral “skin” on the outer surface of the membrane supported by a microporous support layer. In addition, the high transmembrane pressure differences capable of being handled, and the high surface area to volume ratios and high packing densities achieved from such cylindrical morphologies make this membrane structure industrially favorable. Like dense films, asymmetric hollow fiber CMS membranes are prepared by pyrolysis of polymers. Section 5.2 describes preparation of such polymer fibers including precursor screening, section 5.3 describes oxygen “doping” effect on CMS fibers using single gas testing, and section 5.4 investigates mixed gas separation performance of these CMS fibers.

## 5.2 DEFECT-FREE POLYMER PRECURSOR DEVELOPMENT

Previously, it was observed that Ultem<sup>®</sup> films were fragmented and broken into pieces around the softening point (Section 4.2). Indeed, most Ultem<sup>®</sup> based CMS membranes are supported on ceramic or aluminum [3-6]. On the contrary, Ultem<sup>®</sup> hollow fiber spinning has been well practiced in industry, and the raw material cost of Ultem<sup>®</sup> is lower than Matrimid<sup>®</sup> [7]. This allows Ultem<sup>®</sup> to be more favored precursor for economical scaling if adequate properties can be achieved. The following section revisits investigation of Ultem<sup>®</sup> as a precursor, specifically for asymmetric hollow fiber morphology and describes CMS precursor preparation used in this study.

### 5.2.1 Defect-free polymeric fiber spinning

Asymmetric hollow fiber CMS membranes were prepared by spinning and pyrolyzing polymeric fibers. Many researchers have reported that separation performance is enhanced by pyrolysis of the defect-free asymmetric hollow fibers [4, 8-10]. In particular, Centeno and Fuertes observed 36% increase in CO<sub>2</sub>/CH<sub>4</sub> permselectivity as a result of reducing the defectiveness of polymer precursor by thickening the polymer coating and reducing pin hole defects [4]. This indicates the importance of defectiveness influencing CMS hollow fiber performance. In this work, defect-free asymmetric hollow fiber polymeric membranes were produced by the method called spinning. The polymeric fibers were then pyrolyzed to use the oxygen doping method described on Chapter 4. The spinning was conducted by making a polymer solution, commonly called a “dope”. The dope of Ultem<sup>®</sup> and Matrimid<sup>®</sup> was prepared using phase diagrams by previous group members. The specific mixing procedure was adapted from Clausi and Koros [11]. Dope compositions for each polymer are shown in Table 5.1 and Table 5.2.

Table 5.1: Dope composition of Ultem<sup>®</sup>.

Component	wt%
Ultem <sup>®</sup> (polymer)	33.0
NMP (solvent)	51.0
THF (solvent)	10.0
Ethanol (non-solvent)	4.7
LiNO <sub>3</sub> (pore former)	1.3

Table 5.2: Dope composition of Matrimid<sup>®</sup>.

Component	wt%
Matrimid <sup>®</sup> (polymer)	26.2
NMP (solvent)	53
Ethanol (non-solvent)	14.9
THF	5.9

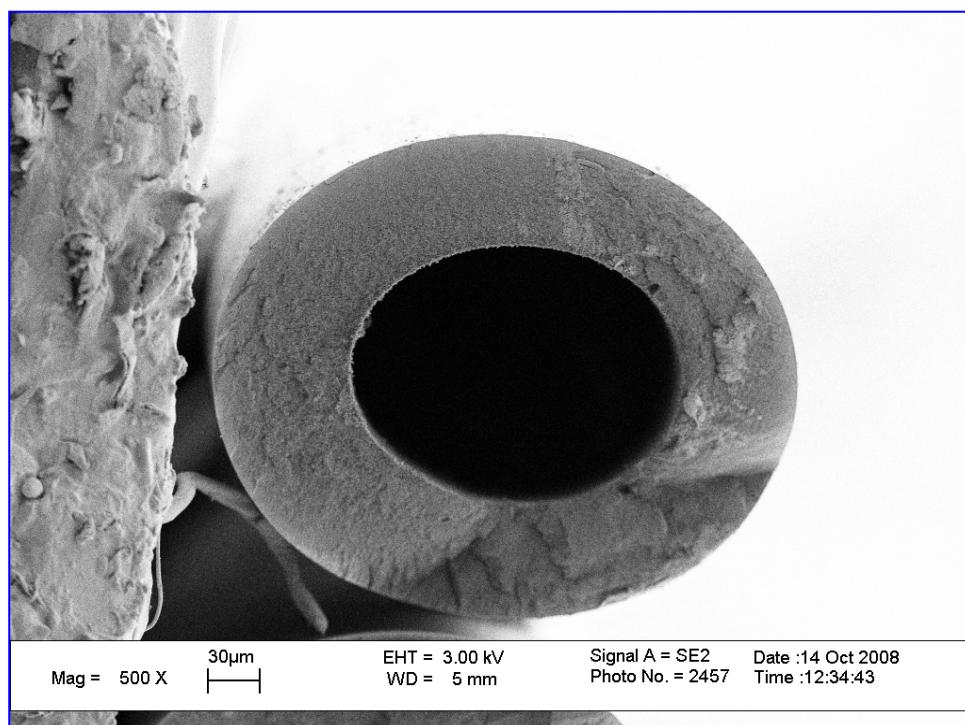
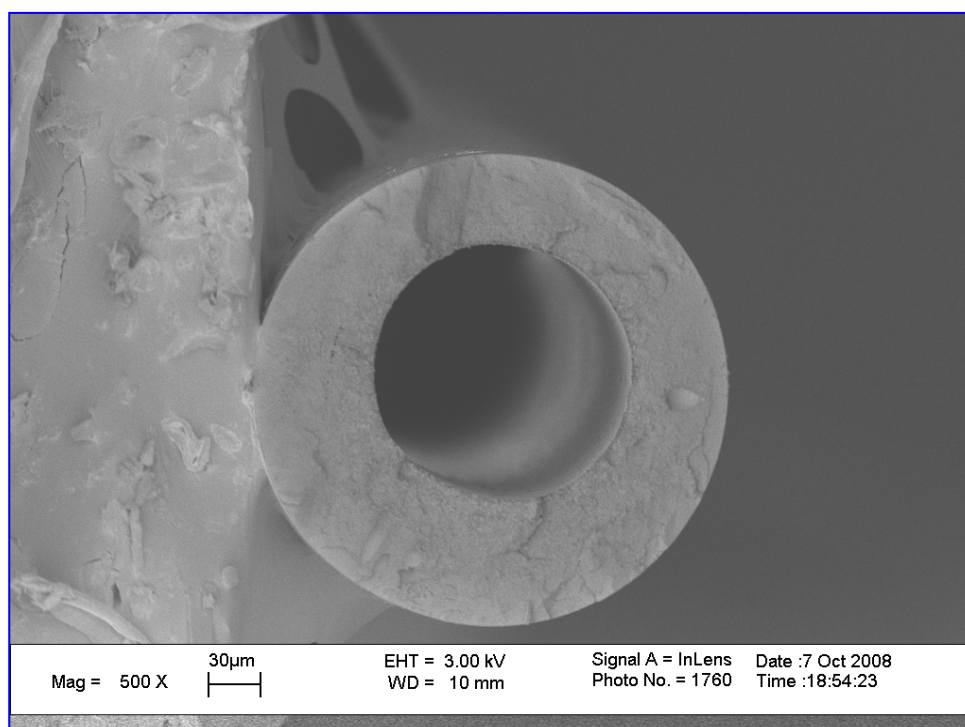
The dopes were used to spin the fibers using the dry jet/wet quench method described in Chapter 3. Table 5.3 shows typical spinning conditions used in this work for defect-free fiber production. The bore fluid consisted of a mixture of de-ionized (DI) water (18 MΩ; Model: D4521, Barnstead International, Dubuque, IA) and NMP (Aldrich) with the composition of 90:10 wt% NMP: DI water. A 40 micron filter (Swagelok) were attached upstream of the a monolithic spinneret [12] to trap large particles which could potentially block the spinneret channels. The spinneret and filter blocks were heated up to 55 °C using multiple heating tapes (BriskHeat<sup>TM</sup>, Barnstead International) regulated by the temperature controllers (Omega Engineering Inc.,

Stamford, CT). The nascent membranes were extruded into the air gap and into the quench bath, passed under a PTFE guide roll in the bath and collected on a rotating drum which diameter is 0.32 m, partially immersed in tap water.

Table 5.3: Optimized spinning conditions for defect-free asymmetric hollow fiber membranes.

Polymer	Ultem <sup>®</sup>	Matrimid <sup>®</sup>
Dope flow rate (ml/hr)	240	180
Bore flow rate (ml.hr)	80	60
Air-gap height (cm)	15	20
Take-up rate (m/min)	55	76
Draw ratio	4.3	2.6
Quench bath (water) temperature (°C)	25	25
Fiber O.D. (microns)	260	250

Once fibers were removed from the drum by cutting them using a razor blade, they were placed in DI water for three days. The water bath was changed daily. On the fourth day, the fibers were solvent exchanged by immersing in three successive aliquots of methanol and hexane for 20 minutes each. The fibers were removed from the hexane bath and dried in the hood for an hour. Then the fibers were dried in a vacuum oven at 75 °C for overnight. The SEM images of each fiber are shown in Figure 5.1.



(b)

Figure 5.1: SEM images of asymmetric hollow fiber precursors: Ultem® (top) and Matrimid® (bottom).

The separation performance of the Ultem<sup>®</sup> and Matrimid<sup>®</sup> fibers are shown in Table 5.4 along with selectivity results obtained on dense films. Their separation performance shows successful spinning of defect-free asymmetric hollow fiber membranes.

Table 5.4: Separation performance of Ultem<sup>®</sup> and Matrimid<sup>®</sup> asymmetric hollow fibers. Measurements were repeated and data has less than 5% deviations. CO<sub>2</sub>/CH<sub>4</sub> selectivity from dense film study is also listed as a reference.

Polymer	Fiber		Film
	P <sub>O<sub>2</sub></sub> (GPU)	O <sub>2</sub> /N <sub>2</sub>	O <sub>2</sub> /N <sub>2</sub>
Ultem <sup>®</sup>	0.79	7.2	7.6
Matrimid <sup>®</sup>	3.85	7.0	7.1

### 5.2.2 Pyrolysis of defect-free asymmetric hollow polymeric fibers

The defect-free asymmetric hollow fibers were then pyrolyzed using the 550 °C pyrolysis protocol. Unlike broken Ultem<sup>®</sup> CMS films, the Ultem<sup>®</sup> CMS fibers were intact; however, the hollow morphology was destroyed as a result of the softening point. The details are shown in Figure 5.2 below.

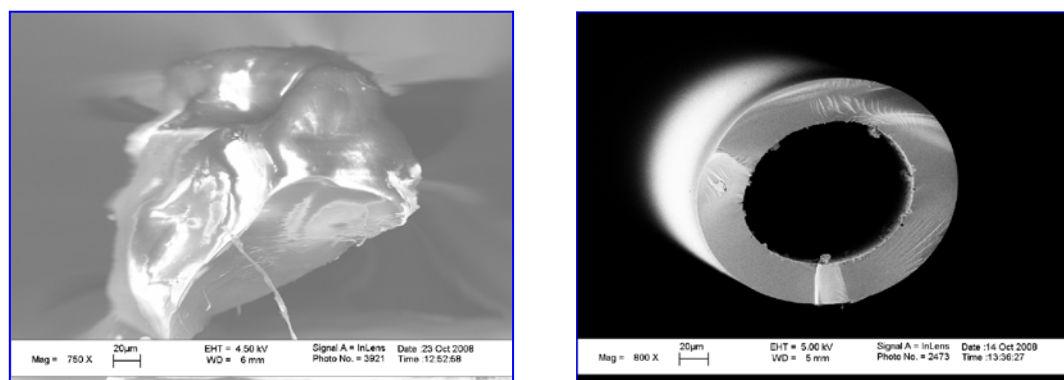


Figure 5.2: SEM images of asymmetric hollow fiber CMS membranes: Ultem<sup>®</sup> CMS fiber (left) and (b) Matrimid<sup>®</sup> CMS fiber (right).

Barbosa-Coutinho et al. reports pyrolysis of Ultem<sup>®</sup> hollow fibers with an additive such as polyvinylpyrrolidone (PVP) [13] without hollow morphology destroyed; however, they do not provide evaluations of the separation performance. The morphology shown in the article suggests that their CMS fibers were quite defective. This indicates that an additional technology is required to produce Ultem<sup>®</sup> hollow fiber CMS membranes. The overall results on material selection for CMS dense films and fibers indicate that Matrimid<sup>®</sup> is easier to process for formation of processable CMS membranes. Therefore, Matrimid<sup>®</sup> was chosen to be our preferred precursor.

### **5.3 EFFECT OF PYROLYSIS ATMOSPHERE ON ASYMMETRIC HOLLOW FIBER CMS MEMBRANES**

#### **5.3.1 Review**

The effect of pyrolysis atmosphere on asymmetric hollow fiber CMS membranes has been investigated by several researchers. Suda and Haraya reported that CMS prepared from polyimide Kapton<sup>®</sup> at 1000 °C in either argon or in vacuum of  $10^{-5}$  torr showed relatively minor differences [14]. Geiszler and Koros conducted work on asymmetric hollow fiber CMS membranes using 6FDA/BPDA-DAM and reported negligible differences between fibers produced under argon, helium, and carbon dioxide inerts for both O<sub>2</sub>/N<sub>2</sub> and H<sub>2</sub>/N<sub>2</sub> separations [15]. A previous chapter has shown that the oxygen concentration was a governing factor influencing separation performance of CMS membranes, and attractive CMS membranes can be produced by tuning oxygen concentration. In this chapter, the effect of oxygen exposure on asymmetric hollow fiber membranes was investigated based on the dense film study.



### 5.3.2 Effect of oxygen exposure during pyrolysis process

CMS asymmetric hollow fiber membranes were prepared by pyrolyzing the polymeric fibers at 550°C for two hours with exposure to the oxygen-containing argon inerts, specifically 1, 30, and 100 ppm. Permeation measurements were conducted with a mixed gas feed of 50/50 CO<sub>2</sub>/CH<sub>4</sub>. The feed pressure of 80 atm and the permeate pressure of 1 atm were used at a temperature of 35°C. The experiments were repeated to demonstrate reproducibility.

#### 5.3.2.1 Shrinkage

When polymeric fibers were pyrolyzed, polymer shrinkage was observed in both axial and radial directions regardless of the oxygen exposure, and the deviations among samples pyrolyzed under a given oxygen exposures were small. The polymer fibers were shortened by ~30-35% and Table 5.5 shows shrinkage in radial direction (fiber radius). Densification of the wall as a result of pyrolysis made the measurement of the CMS wall thickness difficult to distinguish between the skin and the transition layer.

Table 5.5: Dimensions of Matrimid<sup>®</sup> polymeric and CMS fibers, pyrolyzed under various oxygen exposure. Measurements were the average of three samples, and the deviation was less than 10%.

	Precursor Fiber	CMS (1 ppm O <sub>2</sub> /Ar)	CMS (30 ppm O <sub>2</sub> /Ar)	CMS (100 ppm O <sub>2</sub> /Ar)
O.D. (μm)	250	196	192	198
I.D. (μm)	135	122	123	125

Among the CMS samples at different oxygen doping levels, the difference in relative shrinkage was negligible, and the level of oxygen exposure did not affect overall fiber

dimensions. This trend was similar to the weight loss of dense film. In section 4.2.1.1, it was reported that the percentages of the average weight losses was in a range of 32-35 % in all cases and deviations among CMS films exposed to different oxygen levels were not considered to be significant beyond experimental uncertainty.

#### 5.3.2.2 Correlation between oxygen exposure and consumption

Like the dense film study, total amount of oxygen available and amount of oxygen consumed by polymeric precursors were calculated using Equation 4.2 and 4.3. The results are shown on Table 5.6.

Table 5.6: Amount of oxygen available and consumed during Matrimid<sup>®</sup> asymmetric polymeric hollow fiber pyrolysis process. All was repeated and has standard deviation less than 10%.

Membrane	O <sub>2</sub> available (approx ccSTP/fiber)	O <sub>2</sub> consumed (approx ccSTP/fiber)
CMS (1 ppm O <sub>2</sub> /Ar)	0.067	0.033
CMS (30 ppm O <sub>2</sub> /Ar)	2.06	1.08
CMS (100 ppm O <sub>2</sub> /Ar)	6.04	3.01

The amount of oxygen consumed was proportional to concentration of oxygen and about 49-52% of oxygen available was consumed in all cases. The similarities between fibers and films indicate the validity of film studies.

### 5.3.2.3 Correlation between oxygen exposure and CMS separation performance

Once oxygen consumption was monitored during pyrolysis, the resulting CMS fibers were characterized for separation performance. The 50/50 CO<sub>2</sub>/CH<sub>4</sub> mixed gas at a pressure of 80 atm was fed to shell side of the membrane module. The results are shown in Figure 5.3.

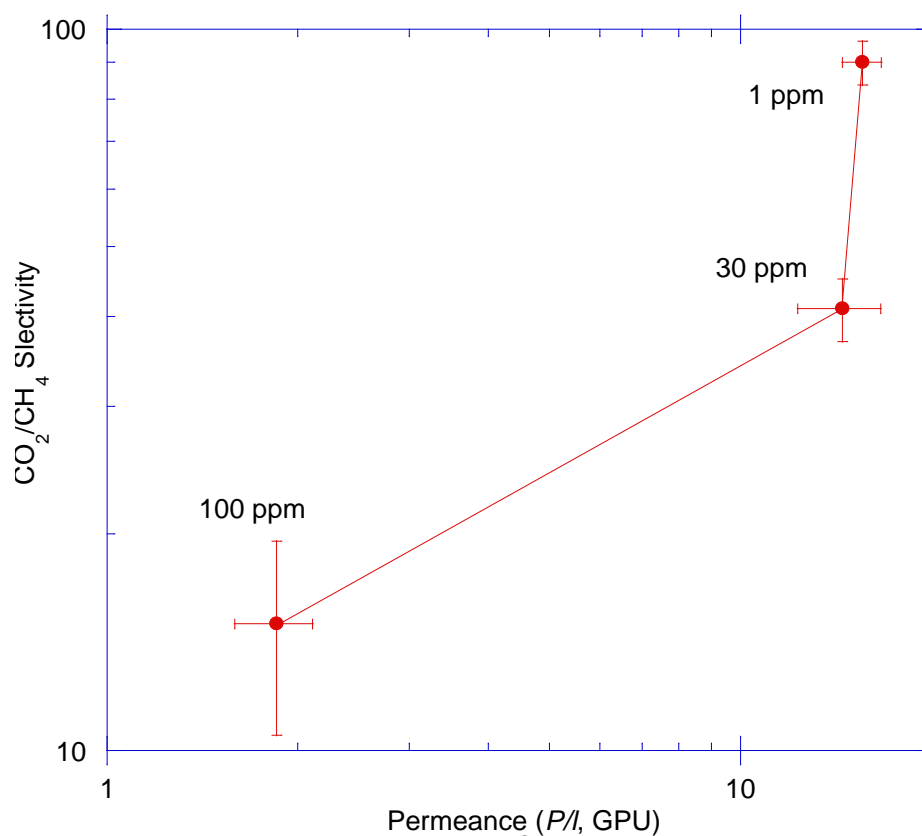


Figure 5.3: Separation performance of Matrimid<sup>®</sup> CMS membranes using 50/50 CO<sub>2</sub>/CH<sub>4</sub> mixed gas with  $P_{\text{feed}} = 80$  atm and  $P_{\text{permeate}} = 1$  atm at 35° C. Stage cut less than 1% was used.

In the previous chapter, 550° C pyrolyzed Matrimid<sup>®</sup> CMS film showed the trend of decrease in both permeability and selectivity as oxygen concentration in inert atmosphere increased. Figure 5.3 showed essentially the same trend: an increase in oxygen concentration during pyrolysis resulted in decrease of both permeance and selectivity. It appears that at the higher oxygen doping levels, performance of the

asymmetric hollow fiber CMS and estimated dense film performance (scaled by a thickness ranging from 30 to 100% collapse of the asymmetric hollow fiber wall thickness) tend to converge. Figure 5.4 shows the CMS data along with the upper bound curve and the currently best performing polymer membranes.

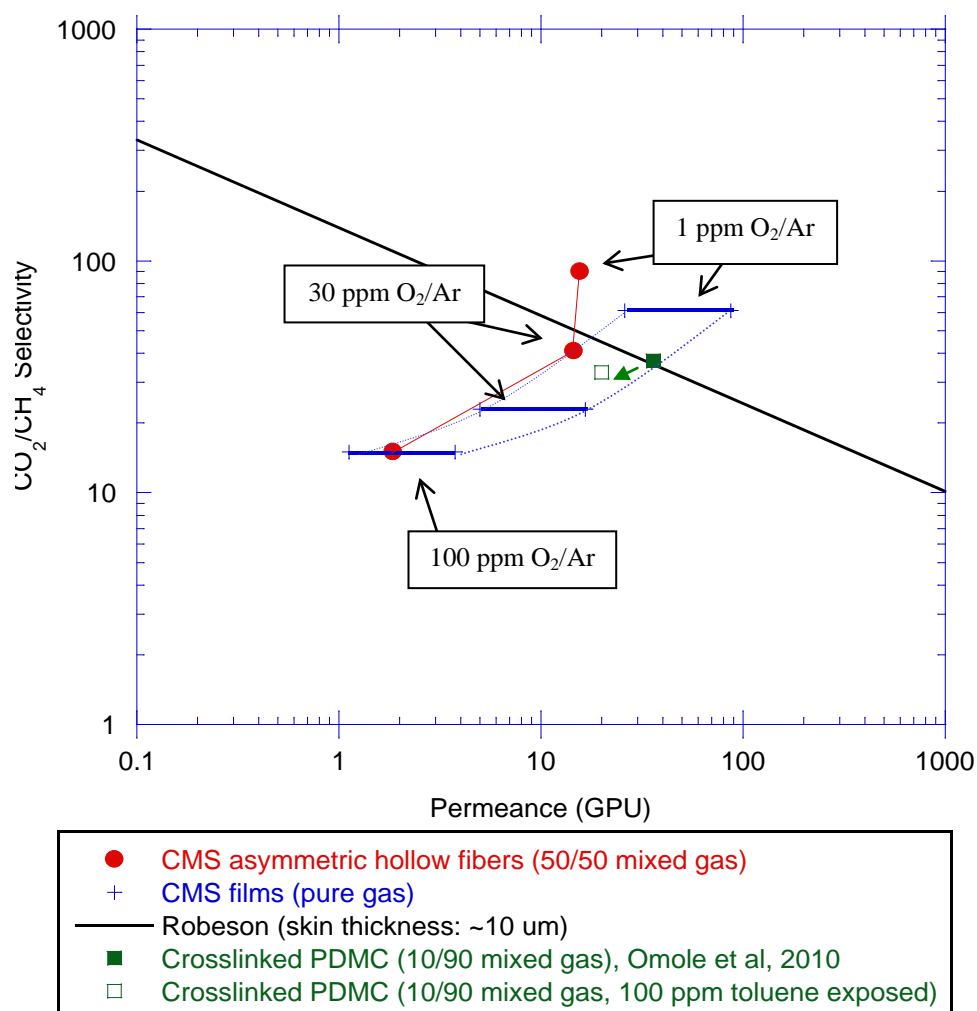


Figure 5.4: Comparison between Matrimid<sup>®</sup> CMS film and asymmetric hollow fiber membranes tested at 35 °C. The red circles represent transport properties obtained on asymmetric hollow fiber membranes with 50/50  $\text{CO}_2/\text{CH}_4$  mixed gas of  $P_{\text{feed}} = 80$  atm and  $P_{\text{permeate}} = 1$  atm, and the blue lines represent properties based on dense film experimental data obtained with single gas feed of  $\sim 3$  atm. The permeability of the dense films was converted to a unit of permeance with 30 to 100% skin thickness of the  $40 \mu\text{m}$  wall. Robeson curves were converted with assumption of  $10 \mu\text{m}$  of fiber skin thickness. Rectangular points represent separation performance of cross-linked PDMC. The filled point was measured at 35 °C with 10/90  $\text{CO}_2/\text{CH}_4$  mixed gas of  $P_{\text{feed}} = 57$  atm and  $P_{\text{permeate}} = 1$  atm, and the open was measured with 100 ppm toluene exposure [16].

In Figure 5.4, the Robeson upper bound curve, which was built based on processable polymer membrane performance, was converted from a unit of permeability (Barrer) to permeance (GPU) based on an assumption that the asymmetric hollow fibers have a skin thicknesses of 10 $\mu$ m. While thinner skin thickness is preferred to increase productivity, thinner polymer membranes tend to plasticize more easily thus separation performance would be significantly reduced [17]. In fact, the plasticization usually occurs immediately after CO<sub>2</sub> exposure on fibers with membrane thickness <500 nm [18]. This implies that polymer fibers which may be close to the trade-off curve could suffer from plasticization under realistic conditions and lose its ability. In 2010, Omole et al. reported robust cross-linked PDMC fibers (skin thickness:  $\sim$ 3 $\mu$ m) developed for anti-plasticizing membrane materials; however, these materials allow uptake by anti-plasticizing aromatic contaminants that should be totally removed by the fine pore size of the current CMS materials. In the presence of even 100 ppm aromatic, the robust cross-linked fibers lose up to 43% of permeance, leading from the filled to the open rectangular data point and dashed line performance as shown in Figure 5.4 [18]. CMS membranes, on the other hand, do not plasticize and are known to be stable at high CO<sub>2</sub> partial pressure exposure or aromatic contaminants [19].

In Figure 5.4, both CMS film and asymmetric hollow fiber membranes pyrolyzed with 1 ppm O<sub>2</sub>/Ar inert atmosphere provide excellent performance, well exceeding the upper bound curve. As noted, the small pores of the CMS should exclude contaminants, such as toluene, but this issue needs to be further investigated on oxygen doped CMS fibers. While the trend of decrease in the transport properties between films (red circular points) and fibers (blue lines) are similar, two key findings should be addressed related to (i) possible densification and/or collapse of the CMS fibers and (ii) CO<sub>2</sub>/CH<sub>4</sub> selectivity.

When CO<sub>2</sub> permeance of CMS films and fibers is compared, CMS fibers pyrolyzed with 30 and 100 ppm O<sub>2</sub>/Ar lie in the range of permeance obtained on the CMS films. These results indicate that about 30-45% of the wall thickness of the CMS

fiber is the selective skin. On the other hand, a permeance value of the CMS fibers pyrolyzed with 1 ppm O<sub>2</sub>/Ar is less than expected from the CMS dense films. This suggests possible densification or collapse as a result of pyrolysis. Exact reasons for this observation are unknown and further investigation needs to be conducted. One possibility of the densification or collapse may be the result of complex morphology of asymmetric hollow fiber membranes. The polymer chain arrangements of the fibers may be different from films since fibers are produced essentially by polymer extrusion process while films are produced by solution casting.

When CO<sub>2</sub>/CH<sub>4</sub> selectivity was compared between films and fibers, selectivity of the CMS fibers were higher than CMS films. This could be caused by the difference between mixed gas and single gas experiments: a competition for the Langmuir sorption sites between CO<sub>2</sub> and CH<sub>4</sub> could attribute this deviation. In the previous chapter, sorption equilibrium isotherms were measured on CMS dense films. As Equation 5.1 shows, the sorption selectivity of the mixed gas is essentially the same as the ratio of the product of the sorption capacity,  $C_H'$ , and the affinity constant,  $b$ .

$$\frac{C_{CO_2}/p_{CO_2}}{C_{CH_4}/p_{CH_4}} = \frac{\frac{(C_H')_{CO_2} b_{CO_2}}{(1+b_{CO_2} p_{CO_2} + b_{CH_4} p_{CH_4})}}{\frac{(C_H')_{CH_4} b_{CH_4}}{(1+b_{CO_2} p_{CO_2} + b_{CH_4} p_{CH_4})}} = \frac{(C_H')_{CO_2} b_{CO_2}}{(C_H')_{CH_4} b_{CH_4}} = \frac{S_{CO_2}}{S_{CH_4}} \quad (5.1)$$

As section 4.2.2.2.1 identified, sorption selectivity was almost constant regardless of the oxygen doping level, implying that much higher sorption of CO<sub>2</sub>, compared with CH<sub>4</sub>, on all oxygen doped samples. Therefore, it is likely that the selectivity of mixed gas is much higher than single gas due to the competition effect.

Using the permeation and sorption data obtained on CMS dense films in section 4.2.2.2, selectivity of CMS membranes of the mixed gas tests was modeled and compared with experimental values obtained on asymmetric hollow fiber CMS membranes. The

mixed gas selectivity was predicted using equations based on solution-diffusion mechanism, viz.:

$$P_{i,mix} = D_{Hi}S_{i,mix} \quad (5.2)$$

$$S_{i,mix} = \frac{C_{i,mix}}{p_i} \quad (5.3)$$

$$C_{i,mix} = \frac{C_{Hi}b_i p_i}{1+b_i p_i + b_j p_j} \quad (5.4)$$

$$\alpha_{i/j,mix} = P_{i,mix}/P_{j,mix} \quad (5.5)$$

where  $P_{i, mix}$  is the permeability,  $D_{Hi}$  is the diffusion coefficient through the Langmuir environments,  $S_{i, mix}$  is sorption capacity,  $C_{i, mix}$  is the amount of penetrants absorbed, and  $\alpha$  is the selectivity in the binary mixture of the component “ $i$ ” and “ $j$ ”. In this model, a condition of total pressure,  $p$ , of 80 atm and 50/50 CO<sub>2</sub>/CH<sub>4</sub> mixed gas was used. The result is presented in Figure 5.5.

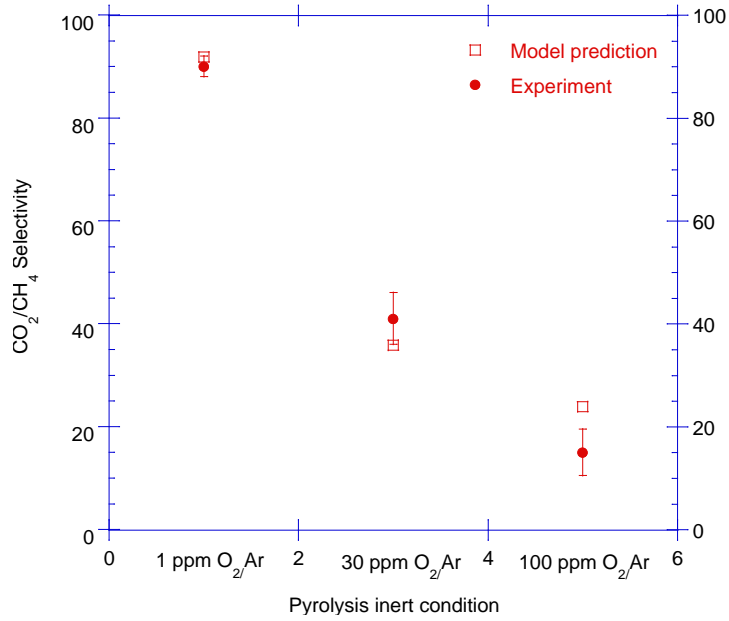


Figure 5.5: Comparison of CO<sub>2</sub>/CH<sub>4</sub> selectivity between experimental (asymmetric hollow fibers) and model (dense films) made under 50/50 CO<sub>2</sub>/CH<sub>4</sub> mixed gas at a feed pressure of 80 atm at 35 °C.

Permselectivity observed was in reasonable agreement with the model prediction. The experimental value was slightly higher than the prediction when low level of oxygen was used while it was slightly lower than prediction. As previously motioned, the high sorption capacity of CO<sub>2</sub> is likely contributing this difference, making CMS membranes more attractive at high pressure applications.

## 5.4 SUMMARY

In this chapter, “inert” pyrolysis process developed on dense films was successfully adapted to produce asymmetric hollow fiber CMS membranes. The translation from the films to fibers is inevitable for commercial scale up since asymmetric hollow fiber morphology offer much higher surface area to volume ratios compared with films. Defect-free asymmetric hollow fiber CMS membranes were prepared using a commercially available polymer Matrimid® and the oxygen doping method was applied. Similar trends as films were observed on various aspects: % oxygen consumption, weight loss, and CO<sub>2</sub>/CH<sub>4</sub> separation performance.

The characterizations of the fibers were made with a realistic condition of a high pressure mixed gas feed instead of single gas feed. And it demonstrated that the “oxygen doped” CMS fibers not only withstand the high pressure mechanically but also are able to show excellent performance, well exceeding the precursor efficiency. Additional sorption isotherm experiments showed that the oxygen doping takes place at ultramicropores, rather than micropores, which validated our hypothesis of the oxygen doping method further. A comparison between theoretical and experimental separation performance indicated that mixed gas separation performance of CMS membranes can be predicted theoretically and competition between CO<sub>2</sub> and CH<sub>4</sub> is likely negligible.



## 5.5 REFERENCES

- [1] Baker RW. Future directions of membrane gas separation technology. *Ind Eng Chem Res* 2002; 41:1393-411.
- [2] Ekiner OM, Vassilatos G, inventors; E.I. du Pont de Nemours and Co., assignee. Polymeric membranes. US patent 5,102,600. 1992.
- [3] Centeno TA, Fuertes AB. Supported carbon molecular sieve membranes based on a phenolic resin. *J Membr Sci* 1999; 160:201-11.
- [4] Centeno TA, Fuertes AB. Carbon molecular sieve membranes derived from a phenolic resin supported on porous ceramic tubes. *Sep Purif Technol* 2001; 25:379-84.
- [5] Sedigh MG, Jahangiri M, Liu PK, Sahimi M, Tsotsis TT. Structural characterization of polyetherimide-based carbon molecular sieve membranes. *AIChE J* 2000; 46(11):2245-55.
- [6] Sedigh MG, Xu L, Tsotsis TT, Sahimi M. Transport and morphological characteristic of polyetherimide-based carbon molecular sieve membranes. *Ind Eng Chem Res* 1999; 38:3367-80.
- [7] Kim BH. U.S. list prices for polyimides. *Polymer Science and Technology Vol. 12*, No. 5; [October 2001; cited]; Available from: <http://www.chem.org/PDF/PST/PT12/PT12-5-0746.pdf>.
- [8] Geiszler VC, Koros WJ. Polyimide precursors for carbon molecular sieve membranes. Austin, TX, University of Texas at Austin, 1997.
- [9] Jones CW, Koros WJ. Carbon molecular sieve gas separation membranes-I. Preparation and characterization based on polyimide precursors. *Carbon* 1994; 32(8):1419-25.
- [10] Vu DQ. Formation and characterization of asymmetric carbon molecular sieve and mixed matrix membranes for natural gas purification. Austin TX USA, University of Texas at Austin, PhD thesis, 2001.
- [11] Clausi DT, Koros WJ. Formation of defect free polyimide hollow fiber membranes for gas separations. *J Membr Sci* 2000; 167:78-89.
- [12] Pesek SC. Aqueous quenched asymmetric polysulfone flat sheet and hollow fiber membranes prepared by dry/wet phase separation. Austin TX USA, University of Texas at Austin, 1993.
- [13] Barbosa-Coutinho E, Salim VMM, Borges CP. Preparation of carbon hollow fiber membranes by pyrolysis of polyetherimide. *Carbon* 2003; 41:1707-14.

- [14] Suda H, Haraya K. Gas permeation through micropores of carbon molecular sieve membranes derived from Kapton polyimide. *J Phys Chem B* 1997; 101(20):3988-94.
- [15] Geiszler VC, Koros WJ. Effects of polyimide pyrolysis conditions on carbon molecular sieve membrane properties. *Ind Eng Chem Res* 1996; 35(9):2999-3003.
- [16] Omole IC, Adams RT, Miller SJ, Koros WJ. Effects of CO<sub>2</sub> on a high performance hollow-fiber membrane for natural gas purification. *Ind Eng Chem Res* 2010; 49:4887-96.
- [17] Wessling M, Lidon Lopez M, Strathmann H. Accelerated plasticization of thin-film composite membranes used in gas separation. *Sep Purif Technol* 2001; 24:223-33.
- [18] Omole IC. Crosslinked polyimide hollow fiber membranes for aggressive natural gas feed streams. Atlanta GA USA, Georgia Institute of Technology, PhD thesis, 2008.
- [19] Vu DQ, Koros WJ, Miller SJ. Effect of condensable impurities in CO<sub>2</sub>/CH<sub>4</sub> gas feeds on carbon molecular sieve hollow-fiber membranes. *Ind Eng Chem Res* 2003; 42(5):1064–75.

## **CHAPTER 6**

### **CHARACTERIZATION OF CMS MEMBRANES UNDER AGGRESSIVE OPERATING CONDITIONS**

#### **6.1 INTRODUCTION**

This chapter contains the experimental characterization results for asymmetric hollow fiber CMS membranes under realistic very aggressive operating conditions. This step is necessary not only to demonstrate CMS separation ability for realistic testing conditions but also to promote large scale CMS production for future work. In chapter 5, the effective inert pyrolysis method, developed in chapter 4, was adapted to asymmetric hollow fiber membranes and the efficacy of the production method was demonstrated. In this chapter, the CMS membranes are further characterized under more realistic conditions. Section 6.2 demonstrates CMS membrane performances with various permeate pressures and section 6.3 investigates the effect of humidity on both homogeneous dense and asymmetric hollow fiber CMS membranes.

#### **6.2 PRACTICAL CONSIDERATION OF PERMEATE PRESSURE**

The permeance, or permeability, gives fundamental insight on the events occurring in the membrane as penetrants permeate through. As previously mentioned, the ratio of the fast gas permeance to the slow gas permeance is called the permselectivity. However, this permselectivity is ideal relative to the actual separation performance, which is represented by the separation factor. As the membrane's permeate pressure increases from idealistic vacuum conditions, the separation factor deviates from the

permselectivity even though the membrane material itself may not be affected significantly. Most of the work reported in the literature is done under vacuum permeate conditions; however, the relationship between the pressure ratio and selectivity is important because of the practical limitation. Compressing the feed stream to very high pressure or drawing a very low vacuum on the downstream requires large amounts of energy and expensive pumps [1].

In this work, ambient permeate pressures are used, and both permselectivities and separation factors are reported to reflect practical separation performance values. The separation factor can be derived from the operating pressures and feed compositions using mass balance equations. The expression for the separation factor at a negligible stage cut is given by Equation 6.1 and 6.2:

$$y_{CO_2} = \frac{R}{2} \cdot \left[ x_{CO_2} + \frac{1}{R} + \frac{1}{\alpha-1} - \sqrt{\left( x_{CO_2} + \frac{1}{R} + \frac{1}{\alpha-1} \right)^2 - \frac{4 \cdot \alpha \cdot x_{CO_2}}{(\alpha-1)R}} \right] \quad (6.1)$$

$$SF = \frac{\frac{y_{CO_2}}{y_{CH_4}}}{\frac{x_{CO_2}}{x_{CH_4}}} \quad (6.2)$$

In the equations above,  $y_{CO_2}$  and  $y_{CH_4}$  are the permeate mole fraction for  $CO_2$  and  $CH_4$  respectively,  $x_{CO_2}$  and  $x_{CH_4}$  are the feed mole fractions for  $CO_2$  and  $CH_4$  respectively,  $R$  is the pressure ratio (feed pressure/permeate pressure), and  $\alpha$  is the intrinsic membrane selectivity ( $\alpha_{CO_2/CH_4}$ ). Based on these equations, the relationship between the pressure ratio and selectivity can be observed in Figure 6.1.

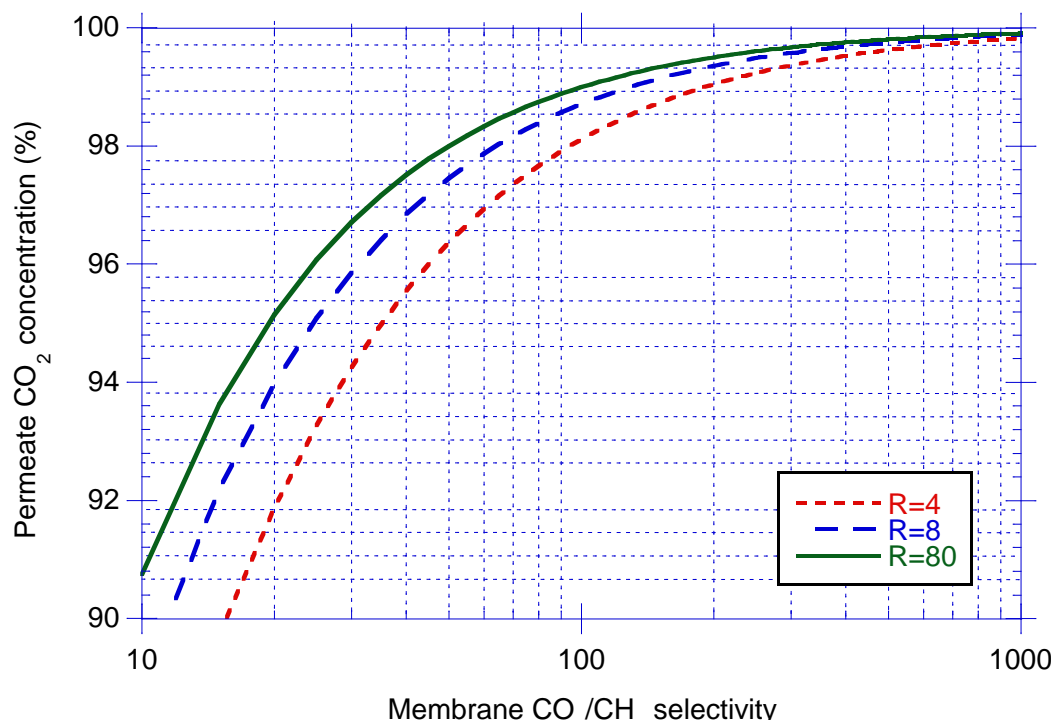


Figure 6.1: Calculated permeate CO<sub>2</sub> concentration as a function of selectivity with various pressure ratios ( $R$ ). The feed CO<sub>2</sub> concentration is 50%.

Figure 6.1 indicates the benefit of highly selective membranes. For instance, under the condition at which the pressure ratio is 4, increasing the membrane selectivity from 60 to 100 can increase % CO<sub>2</sub> concentration in permeate stream by 1%, thus increasing purity of CH<sub>4</sub> in the retentate stream. The graph also shows the effect of pressure ratio. The pressure ratio between 4 and 80 can be equivalent to having permeate pressure between 1 and 20 atm at a feed pressure of 80 atm. At a given permeation % CO<sub>2</sub> concentration, highly selective membrane is required as pressure ratio becomes small. Indeed, Baker reports the practical values of the pressure ratio to be in a range of 5 to 20 [1].

The best performing CMS membranes, pyrolyzed with 200 cc(STP)/min 1ppm O<sub>2</sub>/Ar was used as a model object. The feed pressure was kept constant at 80 atm, and the permeate pressure was varied between 1 to 20 atm. The permeate pressure was varied

by integrating a backpressure regulator (KBP series, pressure range: 0-500 psig, Swagelok) on the permeate side as shown in Figure 6.2.

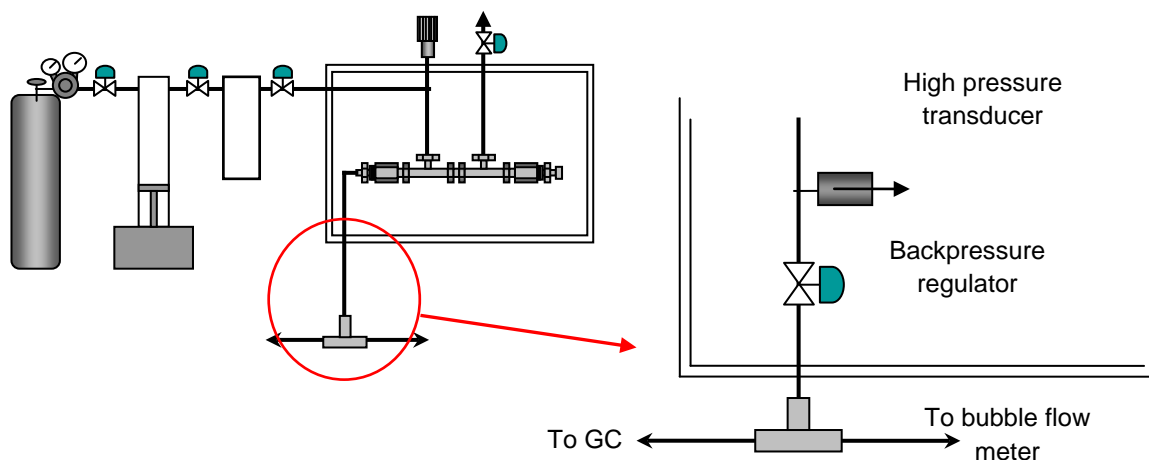


Figure 6.2: Schematic of fiber permeation system modified to measure separation performance with various permeate pressures.

Results are shown in Table 6.1. As predicted, a significant reduction in separation factor was observed when permeate pressure was increased. The deviations between experimental and theoretical are speculated to be caused by the competition effect as the previous chapter described. It should also be noted that it was difficult to set the backpressure regulator to the target as the knob was relatively large. Nevertheless, the results indicate that the equations 6.1 and 6.2 well described CMS membrane behavior considering standard deviation.

Table 6.1. CMS membrane performance, pyrolyzed with 1ppm O<sub>2</sub>/Ar, and various permeate pressures. Experiments were conducted at feed pressure of 80 atm with 50/50 CO<sub>2</sub>/CH<sub>4</sub> at 35 °C.

P <sub>permeate</sub> (atm)	Pressure ratio	CO <sub>2</sub> Permeance (GPU)	SF <sub>Experimental</sub>	SF <sub>Theoretical</sub>
1	80	15.6 ± 1.2	90 ± 6.2	93
10	8	19.3 ± 2.0	62 ± 4.3	68
20	4	17.0 ± 1.0	42 ± 6.2	46

## 6.3 PRACTICAL CONSIDERATION OF HUMIDITY EXPOSURE

### 6.3.1 Review

Various researchers reported that the adsorption of water is strongly influenced by various factors such as the nature of carrier, temperature, and the humidity's partial pressure. The sorption mechanism differs depending on the vapor concentration, and water adsorption has been shown to follow Langmuir isotherm [2-5]. According to Gawryz et al. only active polar centers seem to be involved at relatively low humidity and this adsorption is so weak that the negative effect on separation can be easily removed [6]. When relative humidity is more than 25%, the negative effect on separation may be substantial. Hydrogen bonding between neighboring water molecules leads to clusters of adsorbed water, which may trap the carrier gas molecules. Other researchers also documented carbon materials experiencing severe losses of transport properties under humid rich environment [2-5]. Currently, an adequate solution to this phenomenon has not been fully explored. Jones and Koros developed a coating method on the CMS fiber using unique polymeric materials and saw significant improvements. This method utilizes Teflon AF2400 which is highly hydrophobic yet does not prohibitively reduce the flux of other permeating species. As a result of this coating, %  $O_2$  flux loss was improved by 40% while maintaining the selectivity of  $O_2/N_2$  separation [4]. In the study, permeation was carried out under a feed pressure of 105 psi and the CMS fiber membrane was exposed to humid air for 24 hours.

In this work, two important experiments were conducted. Section 6.3.2 reports analysis of experiments conducted on CMS dense films exposure to 80% relative humidity up to 30 days. Morphology, specifically physical appearance, as well as separation performance was investigated. Furthermore, regeneration of the lost separation performance was intended to be treated by heat treatment under vacuum. Section 6.3.3 studies the effect of humidified feed on asymmetric hollow fiber CMS membranes.

These studies not only demonstrate CMS membranes durability against humidity but also show the stability of CMS membranes prepared with the oxygen “doping” method.

### **6.3.2 CMS dense films**

#### **6.3.2.1 Humidity exposure**

Both 6FDA/BPDA-DAM and Matrimid<sup>®</sup> CMS dense films were prepared using the 550 °C temperature protocol. The oxygen concentration of 3 ppm in argon was used on Matrimid<sup>®</sup>, and 4 ppm was used on 6FDA/BPDA-DAM to produce each CMS membranes. Multiple CMS films were produced in one batch of pyrolysis, and one of them was immediately loaded to a permeation system while some were (i) kept in a vacuum oven at room temperature and (ii) kept in a humidity controlled box depicted in Figure 6.3. The system consists of a sample box which has an analog RH indicator and a Teflon<sup>®</sup> sealing door from Sigma-Aldrich. In addition, a digital RH and temperature monitor was integrated to make sure RH was controlled. The 80% RH was accomplished by saturating the inside air with NaCl solution. A duration of 1 week and 1 month (30days) was chosen to demonstrate humidity effects on CMS films.



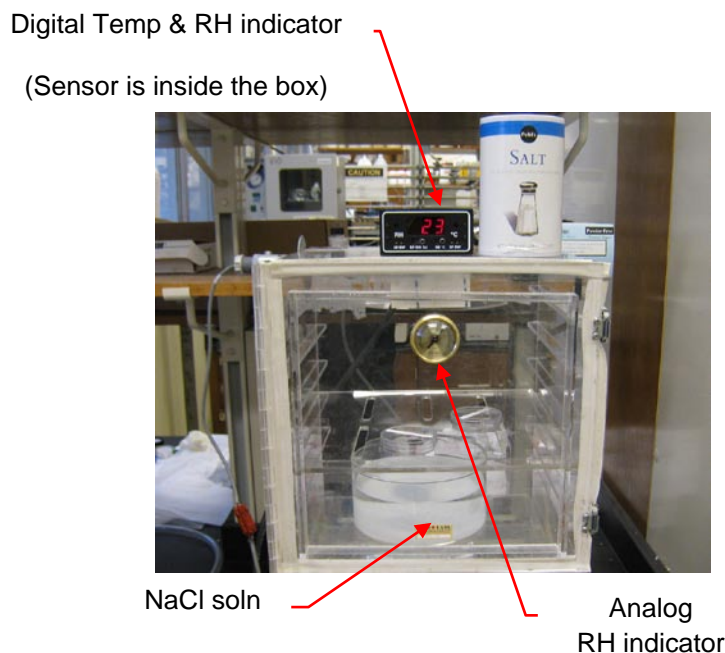


Figure 6.3: Schematic of a humidity controlled sample box.

When Matrimid<sup>®</sup> CMS films were studied, it was noticed that the appearance had been changed after 1 month as shown in Figure 6.4. This could be caused by adsorption of water on the surface of CMS membranes.



Figure 6.4: Matrimid<sup>®</sup> CMS dense films exposed to humidified conditions.

When Matrimid<sup>®</sup> CMS films were kept in vacuum, it was noticed that some, not all, of the films became crinkled and non-testable. The specific reasons for this are unknown.

The films were then evaluated for their separation performance. The separation performance of CMS membranes kept in vacuum did not change, and normalized values

of both permeability and selectivity for these “unexposed” values were essentially unchanged. On the other hand, CMS membranes exposed to humidified air showed different results. Results of CMS films exposed to humidity are shown in Figure 6.5 and Figure 6.6.

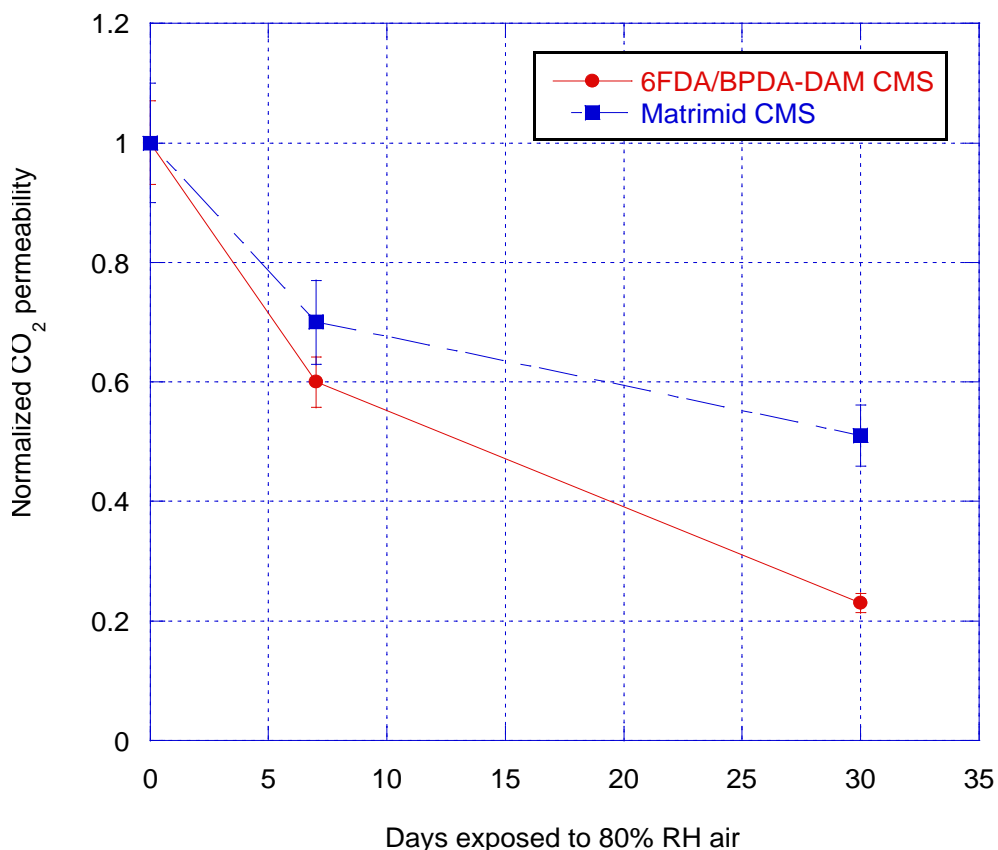


Figure 6.5: Effect of humidity during ageing process on normalized  $\text{CO}_2$  permeability values ( $P_{\text{CO}_2}/P_{\text{CO}_2,0}$ ).  $P_{\text{CO}_2,0}$  of 6FDA/BPDA-DAM CMS was 7169 Barrer and  $P_{\text{CO}_2,0}$  of Matrimid<sup>®</sup> CMS was 1050 Barrer. The experiments were conducted at 35 °C. They were repeated and had less than 10% deviation.

As expected, a significant reduction in permeability was observed. In fact, most of the loss in permeability took place in a week, and the extent of permeability reduction decreased afterwards. For Matrimid<sup>®</sup> based CMS, a ~35% reduction in permeability was observed after a week, and a ~40% of reduction was observed after a month. For 6FDA

based CMS, a ~40% of permeability was observed after a week, and a ~80% of reduction was observed after a month. The 6FDA based CMS films seem to be influenced more by exposure to the humid environment. Higher free volume of the 6FDA material, compared with Matrimid<sup>®</sup>, is speculated to be responsible for this observation.

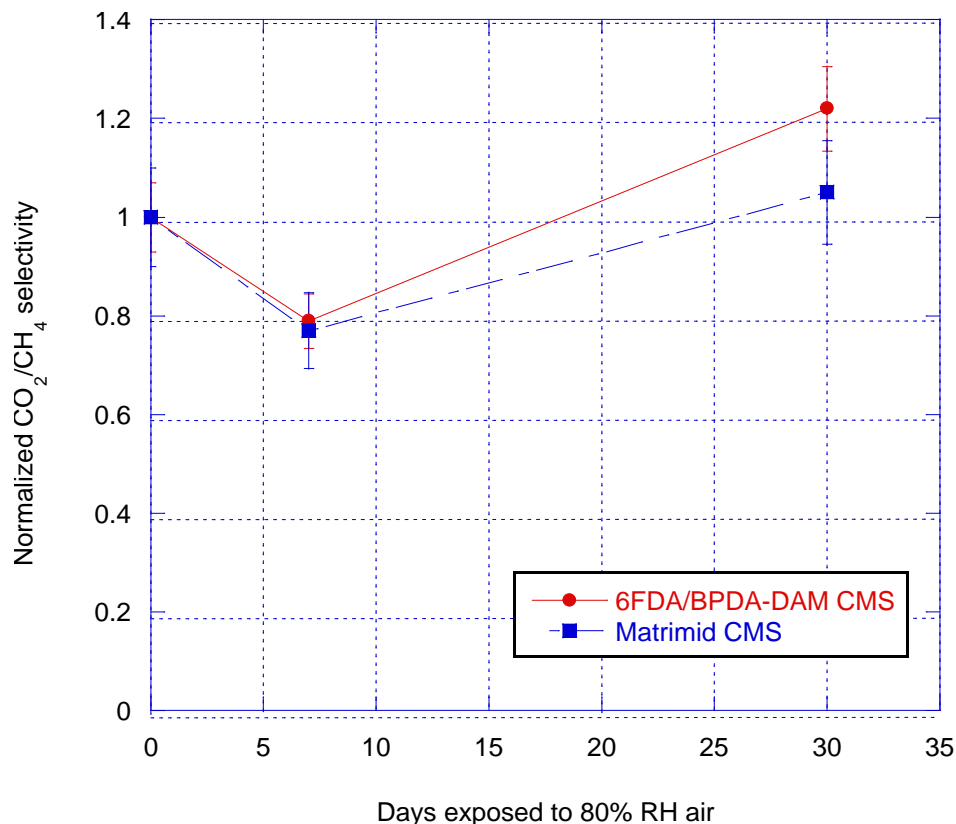


Figure 6.6: Effect of humidity during ageing process on normalized CO<sub>2</sub>/CH<sub>4</sub> selectivity.  $\alpha_0$  of 6FDA/BPDA-DAM CMS is 31 and  $\alpha_0$  of Matrimid<sup>®</sup> CMS is 48. The experiments were repeated and had less than 10% deviation.

Selectivity, on the other hand, showed unexpected results. It was decreased by ~20% after 7 days of exposure but increased to higher the initial selectivity value after a month for both 6FDA and Matrimid<sup>®</sup> based CMS membranes. The samples were not dried at high temperature after exposure and were only evacuated at 35 °C. Similar

phenomena were reported by Menendez and Fuertes [7]. While exact reasons remain unknown, one possible hypothesis for the selectivity decrease is that the selective pores, (which only CO<sub>2</sub> can go through), become clogged by water vapor as depicted in Figure 6.7. This could result in reduction of both permeability and selectivity. According to Figure 6.6, this phenomenon took place in a week and led to a decrease in both permeability and selectivity.



Figure 6.7: Possible explanation of water adsorption taking place after a week.

After one month, the samples were loaded into permeation cell in which they were evacuated at 35 °C for overnight. As a result, it was found that the selectivity was increased and in fact, it was enhanced by humidity exposure. CMS membranes have sorption-diffusion mechanism. One possibility is that water being dissolved in CMS membranes and enhances CO<sub>2</sub> sorption, thus increasing selectivity. The other possibility is that water vapor formed clusters on the pore mouth which was originally available to CH<sub>4</sub>. This water adsorption eventually made “new” selective pore slits which is now only available to CO<sub>2</sub> as depicted in Figure 6.8. This could lead to the increase in selectivity while a decrease in permeability was still observed. At this point, we cannot speculate further, but the result is clearly an encouraging outcome.

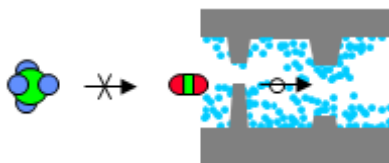


Figure 6.8: Possible explanation of water adsorption taking place after 1 month.

In addition to permeation, sorption isotherms were measured on the CMS membranes. Results of sorption isotherms are shown in Figure 6.9 and Figure 6.10 and the Langmuir coefficients are listed in Table 6.2 and Table 6.3.

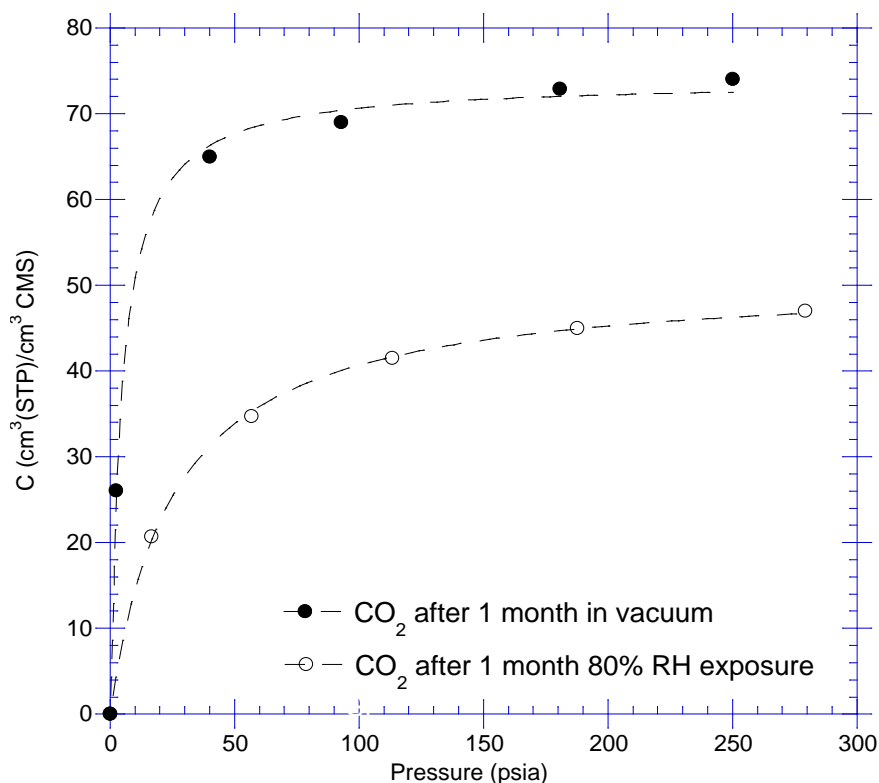


Figure 6.9: CO<sub>2</sub> sorption isotherm for Matrimid® CMS membranes with different levels of humidity exposure: 80% RH vs. in vacuum (~0% RH) in a month. The experiment was conducted at 35 °C.

Table 6.2: Langmuir hole filling capacity  $C_H'$  and Langmuir affinity constant  $b$  calculated based on Matrimid® CMS sorption isotherms on Figure 6.9.

Gas	$C_H'$ (cc(STP)/cc CMS)	$b$ (psia <sup>-1</sup> )
CO <sub>2</sub> (after 1 month in vacuum)	72.2	0.02
CO <sub>2</sub> (after 1 month in 80% RH)	50.4	0.04

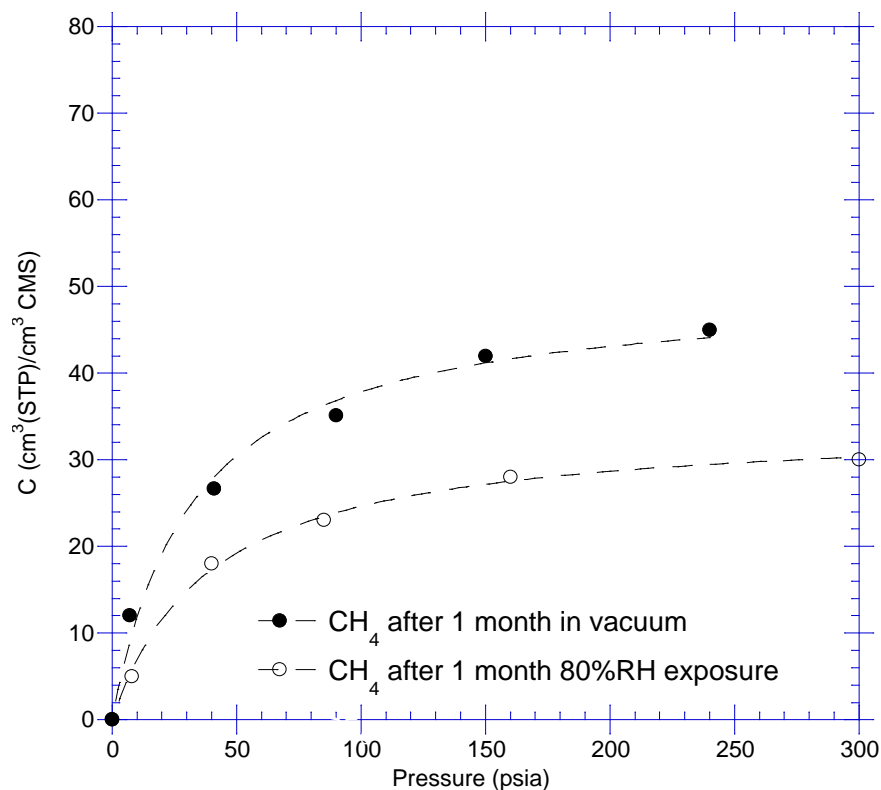


Figure 6.10: CH<sub>4</sub> sorption isotherms of Matrimid<sup>®</sup> CMS membranes with different levels of humidity exposure. : 80% RH vs. in vacuum (~0% RH) in a month. The experiment was conducted at 35 °C.

Table 6.3: Langmuir hole filling capacity  $C_H'$  and Langmuir affinity constant  $b$  calculated based on Matrimid<sup>®</sup> CMS sorption isotherms on Figure 6.10.

Gas	$C_H'$ (cc(STP)/cc CMS)	$b$ (psia <sup>-1</sup> )
CH <sub>4</sub> (after 1 month in vacuum)	50.2	0.006
CH <sub>4</sub> (after 1 month in 80% RH)	33.0	0.005

Results of sorption isotherm showed that both CO<sub>2</sub> and CH<sub>4</sub> sorption capacity,  $C_H'$ , was decreased by ~30%. The sorption selectivity remained almost the same before and after the humidity exposure, implying that the small selectivity increase observed in Figure 6.6 was caused by increase in diffusion selectivity.

### 6.3.2.2 Regeneration study

Once CMS samples were exposed to humidity conditions, regeneration of the films was attempted. CMS films were dried at 105 °C overnight in a vacuum oven and transport properties were measured. The results of permeability are shown in Figure 6.11.

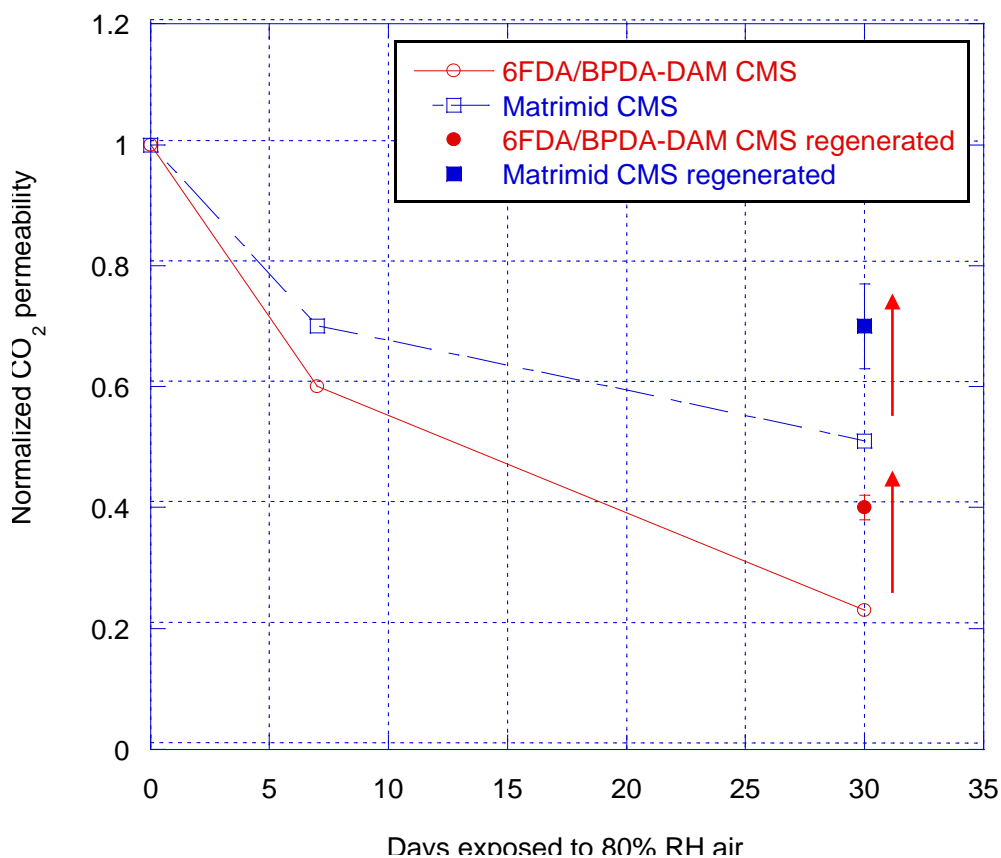


Figure 6.11: Recovery from humidity effect on CO<sub>2</sub> permeability of CMS membranes. Data in red represents separation properties of regenerated CMS membranes.

The result indicates that the short regeneration procedure recovered more than 20% of permeability reduced by humidity exposure for both 6FDA based and Matrimid<sup>®</sup> CMS membranes; however, it is obvious that the negative effect was not eliminated completely. Longer or more aggressive regeneration might recover even more of the function. To probe this issue, additional experiment showed that the change in selectivity was negligible, indicating that the regeneration removed moisture sorbed in micropores without affecting ultramicropore structures. TGA experiments were conducted on the CMS membranes exposed to humidified air for 30 days, and the result is shown in Figure 6.12.

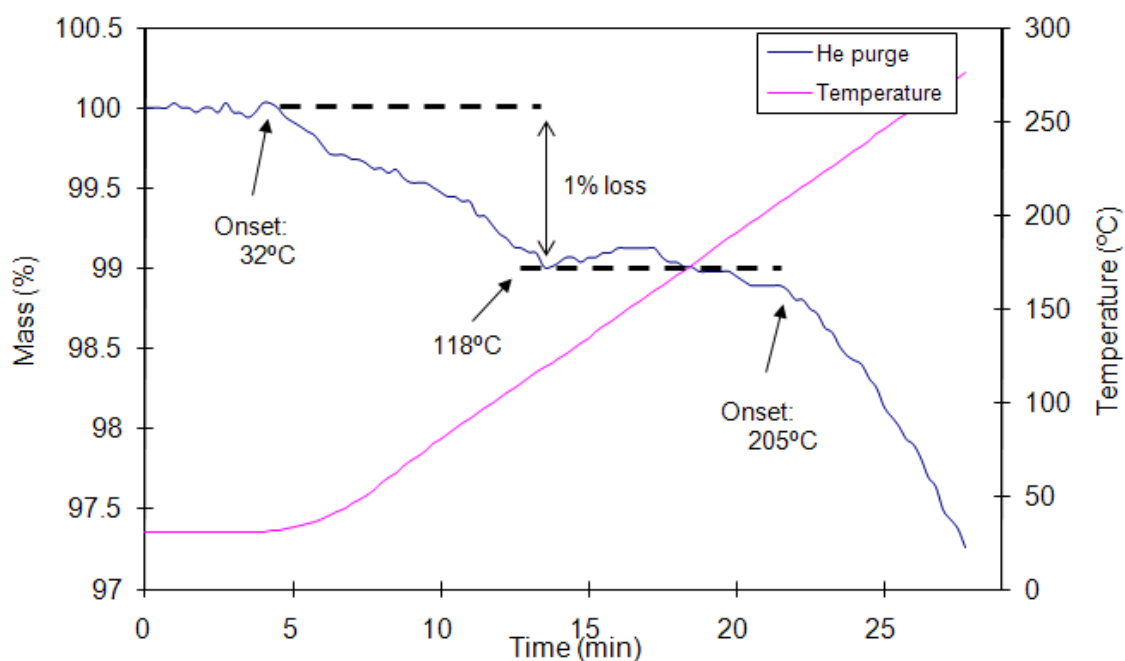


Figure 6.12: TGA profile of 6FDA/BPDA-DAM CMS membranes exposed to 80%RH for 1 month.

The result shows that the possible water removal takes place in the temperature range of 32-120 °C. Similar observation was seen for Matrimid<sup>®</sup> CMS membranes. Since the regeneration in this study occurred at 105 °C, it is speculated that residual water remained



which contributed to the partial recovery of the permeability. It is possible that a higher temperature (120 °C) regeneration could almost completely regenerate the performance but heat resistance of the aluminum adhesive masking materials did not permit exploring this issue and alternative masking materials need to be utilized. It is also speculated that regeneration by propylene exposure could be another regeneration method since CMS is known to swell under those conditions [8]. This further study needs to be addressed as a future work.

### **6.3.3 Asymmetric hollow fiber CMS membranes**

The effect of humidify was also evaluated on asymmetric hollow fiber CMS membranes. Matrimid<sup>®</sup> asymmetric hollow fibers were pyrolyzed using the 550 °C protocol under the best performance conditions: 1 ppm O<sub>2</sub>/Ar with a flow of 200 cc(STP)/min. Humidified stream was integrated in the existing permeation system to measure the separation performance with 50/50 CO<sub>2</sub>/CH<sub>4</sub> mixed gas feed containing ~80%RH at 35 °C. The stainless steel canister was integrated to allow feed gas to bubble through the water phase. A pressure release valve was integrated for safety. A moisture trap (SUPELCO, PA) was introduced in line prior to GC to prevent damaging the GC. Prior to measurements, a blank run was conducted to detect any effect of the moisture trap in the GC signals. Actual percentage relative humidity was measured by the portable humidity indicator used previously in Section 6.3.2.1. A schematic of the system is shown in Figure 6.13. As seen in the figure, the single modules were fed in shell side to keep consistent with previous experiments.

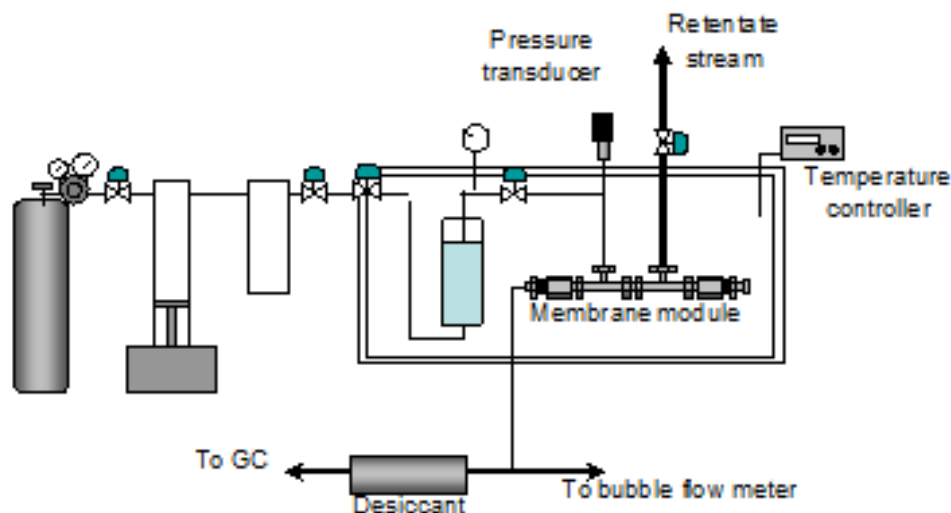


Figure 6.13: Schematic of the permeation system used to measure separation performance of asymmetric hollow fiber CMS membranes under humidified feed conditions.

The effect of humidity was investigated using asymmetric hollow fiber CMS membranes, then the fibers were coated with Teflon AF2400 (DuPont, DE) to demonstrate efficacy of the coating method developed by a previous group member. Polymer, Teflon AF2400, is produced by polymerization of 2,2-bis(trifluoromethyl)-4,5-difluoro-1,3-dioxole (BDD) and tetrafluoroethylen (TFE) as shown in Figure 6.14.

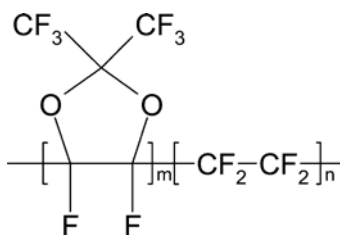


Figure 6.14: Chemical structure of Teflon AF2400 which consists of m:n mole fraction of 87:13 [9, 10].

The reaction produces amorphous, a high free volume and glass transition polymer. The transport properties are well studied [11-16], and it is known to have one of the highest permeabilities of all known polymers [16]. The permeation properties of interest include  $P_{CO_2} = 2800$  and  $P_{CH_4} = 340$  Barrers [17]. A ~25wt% solution of Teflon AF2400 (400S1-100-1, DuPont, DE) was purchased and used to soak the shell-side of a hollow fiber module. A duration of 30 minutes was used, and the solution was drained from the module. In order to remove any residual solvents, both feed and permeate streams were pulled under vacuum overnight.

The separation performance was measured at 35 °C with a 50/50 CO<sub>2</sub>/CH<sub>4</sub> mixed gas feed of 80 atm. Knowing the permeability of the barrier material from the literatures, the thickness of the coating material was calculated using an equation for the resistance in series, viz. [4],

$$\left(\frac{l}{P}\right)_{CO_2, composite} = \left(\frac{l}{P}\right)_{CO_2, CMS} + \left(\frac{l}{P}\right)_{CO_2, Teflon AF} \quad (6.3)$$

where  $P$  represents permeability and  $l$  is the thickness of the material. From the calculation, coating of 2.3-3.0 μm in thickness was identified.

Table 6.4 shows CO<sub>2</sub>/CH<sub>4</sub> separation performance of CMS membranes before and after the coating with dry feed gas and with humidified feed.

Table 6.4: Separation performance of Matrimid<sup>®</sup> CMS membranes evaluated under 50/50 CO<sub>2</sub>/CH<sub>4</sub> mixed gas feed of 80 atm at 35 °C. CMS membranes were prepared by 550 °C with 1ppm O<sub>2</sub>/Ar. Tests were repeated at least twice and deviation was less than 10%.

CMS properties		Dry feed		Wet feed	
		No coating	Teflon AF coating	No coating	Teflon AF coating
CMS (1 ppm O <sub>2</sub> /Ar)	P <sub>CO2</sub>	15.6	15.4	6.8	9.2
	α <sub>CO2/CH4</sub>	90	87	80	84

When CMS membranes are exposed to humidity, permeance was reduced by more than 50%. As stated in the previous section, it was speculated that the moisture sorbes in micropore sites which reduce sorption capacity. The % CO<sub>2</sub> permeance loss was about 58%, which is similar to what Jones and Koros observed on O<sub>2</sub>/N<sub>2</sub> separation [4] which validates our experiments and also implies that the oxygen doping on CMS membranes does not likely influence the separation performance of CMS under humidified condition. When the Teflon coating was applied, the reduction due to humidity exposure was reduced but not eliminated. It is recommended to explore other hydrophobic coating materials or to investigate the exact mechanism of the humidity effect on CMS materials. This conclusion is similar to what Jones and Koros suggested, after exploring other coating materials, such as poly(4-methyl-1-pentene) (PMP) or Teflon AF1600 [4].

## 6.4 SUMMARY

In this chapter, CMS membranes were characterized under aggressive conditions, namely (i) change in permeate pressure and (ii) exposure to humidity. An increase in the pressure ratio resulted in a decrease in the separation factor due to a reduction in the chemical potential driving force. The CMS separation performance correlated well with the theoretical separation factor expression when the pressure ratio was within the values used in industry; however, further investigation should be conducted to address the deviation of excellent CMS separation performance which theory somewhat underestimated at high pressure ratio (or driving force). The deviation may have been due to competitive sorption effects that enable CO<sub>2</sub> to favorably depress CH<sub>4</sub> sorption on permeation in mixed gases.

When CMS films were exposed to humidified air for a period of 30 days, permeability was reduced by more than 50% but the selectivity remained almost constant. This and a significant reduction in the sorption isotherms indicated that the water adsorbed in micropore site, instead of critical ultramicropores. Similar observation was made on CMS asymmetric hollow fiber membranes that the permeance was significantly reduced with a small effect on selectivity. These imply a high tolerance of “oxygen doped” CMS membranes to humidity, and there is no apparent reaction or effect from humidity exposure. Additional experiments on asymmetric hollow fiber CMS membranes on Teflon coating demonstrated the ability to prevent the humidity effect on CMS membranes.

## 6.5 REFERENCES

- [1] Baker RW. Membrane technology and applications. New York: McGraw-Hill; 2000.
- [2] Jones CW, Koros WJ. Carbon molecular sieve gas separation membranes-I. Preparation and characterization based on polyimide precursors. Carbon 1994; 32(8):1419-25.
- [3] Jones CW, Koros WJ. Characterization of ultramicroporous carbon membranes with humidified feeds. Ind Eng Chem Res 1995; 24:158-63.
- [4] Jones CW, Koros WJ. Carbon composite membranes: A solution to adverse humidity effects. Ind Eng Chem Res 1995; 34:164-7.
- [5] Lagorsse S, Campo MC, Magalhaes FD, Mendes A. Water adsorption on carbon molecular sieve membranes: Experimental data and isotherm model. Carbon 2005; 43:2769-79.
- [6] Gawrys M, fastyn P, Gawloeski J. Prevention of water vapor adsorption by carbon molecular sieves in sampling humid gases. J Chrom A 2001; 933:107-16.
- [7] Menendez I, Fuertes AB. Aging of carbon membranes under different environment. Carbon 2000; 39:733-40.
- [8] Jones CW, Koros WJ. Carbon molecular sieve gas separation membranes-II. Regeneration following organic exposure. Carbon 1994; 32(8):1427-32.
- [9] Pauly S. Permeability and diffusion data. New York: John Wiley & Sons; 1989.
- [10] Resnick PR, Buck WH, editors. Teflon AF amorphous fluoropolymers. New York: John Wiley & Sons; 1997.
- [11] Alentiev AY, Shantarovich VP, Merkel TC, Freeman BD, Yampolskii YP. Macromolecules 2002; 35:9513-22.
- [12] Alentiev AY, Yampolskii YP, Shantarovich VP, Nemser SM, Plate NA. J Membr Sci 1997; 126:123-32.
- [13] Dasgupta PK, Genfa Z, Poruthoor SK, Caldwell S, Dong S. High-sensitivity gas sensors based on gas-permeable liquid core waveguides and long-path absorbance detection. Anal Chem 1998; 70(22):4661-9.
- [14] Merkel TC, Bondar V, Nagai K, Freeman BD, Yampolskii YP. Gas sorption, diffusion, and permeation in poly(2,2-bis(trifluoromethyl)-4,5-difluoro-1,3-dioxole-co-tetrafluoroethylene). Macromolecules 1999; 32(25):8427-40.
- [15] Merkel TC, He Z, Pinnau I, Freeman BD, Meakin P, Hill AJ. Sorption and transport in poly(2,2-bis(trifluoromethyl)-4,5-difluoro-1,3-dioxole-co-tetrafluoroethylene) containing nanoscale fumed silica. Macromolecules 2003; 36(22):8406-14.

- [16] Pinnau I, Toy LG. Gas and Vaport transport properties of amorphous perfluorinated copolymer membraens based on 2,2-bistrifluoromethyl-4,5-difluoro-1,3-dioxole/tetrafluoroethylene. J Membr Sci 1996; 109:125-33.
- [17] Nemser SM, Roman IC, inventors; Preparation and uses of permselective perfluorodimethyldioxole polymer membranes for gas separations patent 9015662. 1990.

## CHAPTER 7

### SUMMARY AND RECOMMENDATIONS

#### 7.1 SUMMARY AND CONCLUSIONS

The goal of this project was *to develop an economically preferred method to produce industrially viable CMS membranes*. To start with the project, a high performance 6FDA based polyimide was synthesized and a CMS membrane was produced using vacuum pyrolysis to benchmark against the literature. In order to produce CMS membranes in a more economical way, inert pyrolysis was chosen over traditional vacuum pyrolysis. A hypothesis was made that oxygen exposure during pyrolysis would result in carbon-oxygen chemisorption reactions at ultramicropores which essentially results in efficiency (selectivity) enhancement.

The effect of oxygen exposure during pyrolysis was evaluated by first changing oxygen concentration in purge gas using the aforementioned 6FDA derived polyimide. The results indicated that (i) inert pyrolysis can be used to produce attractive CMS membranes that well exceed the polymer trade-off curve, (ii) the data deviation of the CMS separation performance can be reduced to less than 10% from 20% of previously reported by controlling and carefully monitoring oxygen concentration, and (iii) a correlation between oxygen exposure and separation performance exists. Once the “oxygen doping” method was developed, it was demonstrated on a commercially available polymer Matrimid<sup>®</sup> precursor. A similar correlation was observed with a surprisingly different trend. This led to the investigation of the structure of CMS membranes. Sorption and permeation experiments were utilized to calculate diffusion coefficients of both 6FDA and Matrimid<sup>®</sup> derived CMS membranes. Using various gas molecules as probes, diffusion coefficient based pore size distributions were constructed.



As a result, it was concluded that one can control and predict separation performance using the oxygen doping method once the intrinsic or “undoped” CMS structures are known.

The oxygen doping method was developed with a hypothesis that oxygen exposure would control the chemisorption process. The oxygen exposure can be tuned in two ways: (i) by changing oxygen concentration and (ii) by changing total oxygen exposure amount. Previously, it was believed that the amount of oxygen exposure dominates the oxygen doping process. A series of well controlled studies were conducted, namely (i) effect of thermal soak time, (ii) effect of precursor thickness, and (iii) effect of inert flow rates. The result indicated that the oxidation process is likely governed by reaction equilibrium, rather than reaction kinetics, which was to be a key finding factor in this project.

The oxygen doping process was then translated from homogeneous dense films to asymmetric hollow fiber membranes. This step was important for CMS commercialization to attain high surface area to volume ratios. Using defect-free asymmetric hollow fiber membranes, the oxygen doping method was successfully translated from films to fibers. CMS fibers were characterized under realistic conditions of high pressure mixed gas feed with negligible stage-cut. This also implies that an ability to control or predict separation performance of CMS fibers like films once intrinsic CMS structure is known. In addition, the effect of permeate pressure as well as humidity exposure was investigated and it was demonstrated that the oxygen doping process would not likely to affect the resulting CMS material unstable under these conditions.

## **7.2 RECOMMENDATIONS**

This research was successful in developing highly attractive CMS membranes, and during the course of the development, several potential research areas were discovered and explained below.

### **7.2.1 Properties of CMS membranes**

#### 7.2.1.1 Morphology

As Chapter 2 explained, literature suggests two hypothetical CMS structures: (i) turbostratic structure in which short graphene sheets ( $<30 \text{ \AA}$ ) are entangled in 3D orientation [1] and (ii) short “defective” graphene sheets oriented randomly as a result of polymer pyrolysis [2]. While both fits the bimodal pore size distribution model, the latter picture seems to fit the idea of having “defects to react with oxygen” to make pores even more selective on the graphene sheets as reported in Jiang’s simulation work [3]. The exact structure of CMS membranes remains unknown, but understanding the CMS formation and structure would lead to better control of the doping process developed in this work and also may be a key to solve the low permeance issue of asymmetric hollow fiber CMS membranes. A combination of various characterization techniques, such as high resolution transmission electron microscope (TEM) often used in the lithography research field [4, 5], and transport properties may be a good starting point for this objective, especially to understand structure of ultramicropore regions.

As discussed in chapter 2, CMS structures are known to be affected by various factors, such as the polymer precursor and the pyrolysis temperatures, and it is also important to conduct thorough investigation on this matter. For instance, Lafyatis et al.

have examined the effect on CMS pore structure of adding PEG of various average molecular weights to PFA resin. They found that the added PEG resulted in a distinct effect of molecular weight on CMS structures [6]. While their focus was on microporous region, this implies that even change in molecular weight could result in slight difference in CMS structure, hence separation performance.

#### 7.2.1.2 Physical properties

For production of commercial CMS module, it is important to understand mechanical strength of CMS fibers. Flexibility (ability to bend) of CMS fibers was observed to be exceedingly high compared with the CMS dense films. While polymer dense fibers are flexible, the pyrolyzed CMS films are rather brittle and made it difficult to successfully mask them. Asymmetric hollow fiber morphology, on the other hand, made both polymer and CMS materials flexible and mechanically easy to process as depicted in Figure 7.1. Negligible deviation was observed on the flexibility among CMS fibers exposed to various oxygen levels during module construction. To understand the morphology and for CMS fibers to be commercialized the physical ability and stability should be further addressed.

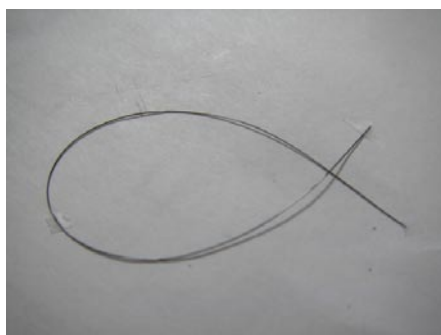


Figure 7.1: Matrimid<sup>®</sup> CMS fibers twisted to depict its flexibility.

Several mechanical test methods could be used to investigate both film and fiber flexibility [7]. Most of them are based on uniaxial bending. For example, the Kawabata Evaluation System for Fabrics (KESF) includes a test measuring the bending moment of a strip of material as a function of its curvature, thus providing the uniaxial bending rigidity which is proportional to the material stiffness [8]. On the other hand, the test method used in the ISO 5979 standard measures the uniaxial flexibility of elastomer coated textile fabrics; its principle consists in forming a loop with the material, the maximum height formed by this loop being proportional to the material stiffness [9]. In addition, ASTM D 1388 standard characterizes the flexibility properties of fibers, the bending length is measured according to two procedures, the cantilever test and the heart loop test, which allows the flexural rigidity to be calculated [10].

### **7.2.2 “Other “dopants”**

The oxidation of carbon can be achieved with oxygen, carbon dioxide, water vapor, or nitrogen dioxide [11]. According to Jacquot et al., the reactivity of nitrogen dioxide, NO<sub>2</sub>, towards carbon is far greater than that of oxygen at low temperature of 500 °C [12]. Study shows that chemisorption takes place with surface species like C-NO<sub>2</sub>, C-ONO, and C-N-NO<sub>2</sub> [13, 14]. It would be interesting to investigate the comparison between the two dopants, especially related to stability and ageing of such CMS membranes.

### **7.2.3 “Doping” method for other gas separations**

Natural gas consists of various impurities, as mentioned in the introduction chapter. The impurities include heavy hydrocarbons and other components, such as moisture and H<sub>2</sub>S. One of the most difficult hydrocarbon separations is alkane/ alkene separation. According to our hypothesis, pore size distribution shifts as the degree of

oxygen doping increases. Based on this hypothesis, one could demonstrate the effect of the oxygen doping method and optimize these challenging separation performances. In this work, the effect of a humidified feed was investigated on one of the best performing CMS membranes and with better coating technique, it was concluded that the humidity effect is likely to be treated. For H<sub>2</sub>S separations, preliminary work using Matrimid<sup>®</sup> CMS membranes (pyrolyzed under 1ppm O<sub>2</sub>/Ar), resulted in H<sub>2</sub>S/CH<sub>4</sub> selectivity of ~23.1 with H<sub>2</sub>S permeability of 1.1, using 10/90 H<sub>2</sub>S/CH<sub>4</sub> feed at 50 psia at 35 °C. Using the same membrane, CO<sub>2</sub>/CH<sub>4</sub> selectivity was reported to be 85.4 when a ternary mixture of 15% H<sub>2</sub>S, 15% CO<sub>2</sub> and balance CH<sub>4</sub> was fed (H<sub>2</sub>S permeability of 9.9 Barrer). The exact mechanism of H<sub>2</sub>S transport in CMS is not known, and the transport properties, such as energetic and entropic contributions should be addressed.

#### **7.2.4 Prevention of permeance loss**

Permeance of CMS membranes on asymmetric hollow fibers are observed to be slightly lower than expected from dense film study. This phenomenon has been observed by various researchers. In order to resolve this issue, integration of various techniques in the pyrolysis method is recommended. One such example is the pyrolysis of dual layer polymer membranes. In this study, 6FDA based CMS membranes were found to be more permeable than Matrimid<sup>®</sup> CMS membranes. Having bulky 6FDA based polymer on the outer skin layer could provide more permeable fibers, and having the more economical polymer, Matrimid<sup>®</sup>, on the inside would reduce the cost compared with utilizing single layer 6FDA based fibers. Several researchers have successfully demonstrated the efficacy and productivity of cross-linking hollow fiber membranes, but the CMS membranes of cross-linked polymer membranes may not be a solution. For instance, Tin et al. showed that both selectivity and permeability of cross linked Matrimid<sup>®</sup> CMS membranes are not improved by cross linking. In fact, a degree of cross linking

increased, both parameters started to decrease [15]. Instead of modifying the structure of the polymer precursor, it is also suggested to increase the rate of heating. As previously mentioned, increasing the ramp rate results in an increase in permeability with a decrease in selectivity. Suda and Haraya reported that the CO<sub>2</sub> permeance increased from 0.5 to 13.3 Barrer by increasing from 1.3 to 13.3 K/min with decrease in CO<sub>2</sub>/N<sub>2</sub> selectivity from 122 to 83 [16].

#### **7.2.5 Alternative regeneration method**

Chapter 6 demonstrated effect of humidity exposure on CMS membranes. In this work, heat treatment was used as a method of the regeneration. The results shows recovery of the reduced permeability, but it was not completely eliminated. Another possibility is to expose CMS membranes to propylene to remove sorbed water on CMS membranes since Jones and Koros demonstrated that propane acts as a cleaning agent when CMS is exposed to organic contaminants [17].

#### **7.2.6 Alternative hydrophobic coating**

In this work, Teflon AF was utilized as a coating material for CMS membranes. One of the alternative methods is to use highly branched polymers which provide a barrier layer to inhibit access of water vapor or nonpolar oil contaminants to the surface of CMS membranes. One such example is dendrimers. The nature of the dendrimers can be tuned to enable the creation of diverse properties against various contaminants. Literature suggests that the highly branched hydrocarbon dendrimers, such as shown in Figure 7.2 are much larger than gas molecules and have hydrophobic high free volume natures. This enables a coating comprising such dendrimers to hinder access of water to the CMS membrane surface by adding selective water resistance while causing minimal resistance to desired gas molecules being separated by the CMS structure. This material

may be similarly effective and much less costly than highly expensive amorphous hydrophobic Teflon<sup>®</sup> coating that are known to fulfill this protective coating on CMS [18, 19]. Such novel dendrimers are prepared with several routes, such as use of the Diels-Alder reaction [20, 21]. Hydrocarbon dendrimers with functional groups, such as fluorine [22] and carboxylic acids [21], are interests since this allows one to possibly tune the hydrophobicity and/or hydrophilicity [21] of the coating and therefore overall performance of CMS membranes.

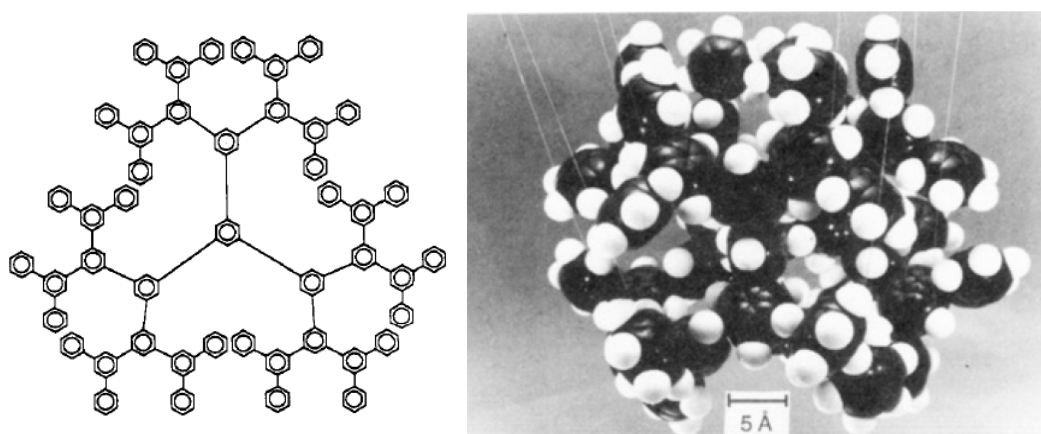


Figure 7.2: Example of hydrocarbon dendrimers: (left) chemical structure and (right) space-filling molecular model [23].

### 7.2.7 Scale-up of CMS membrane production

This work has been currently expanded to the asymmetric hollow fiber CMS membrane production from a laboratory scale to a commercial scale using the method developed in this work. While our current pyrolysis set-up allows producing 1~3 fibers in one batch, this next generation pyrolysis setting allows producing more than 200 fibers at once. Preliminary results are encouraging and it is speculated that the CMS fibers would alter the current polymer membranes in near future.

### 7.3 REFERENCES

- [1] Jenkins GM, Kawamura K. Polymeric carbons - carbon fiber, glass and char. London: Cambridge University Press; 1976.
- [2] Pierson HO. Handbook of carbon, graphite, diamond, and fullerenes. New York: Noyes Publication; 1993.
- [3] Jiang D, Cooper VR, Dai S. Porous graphene as the ultimate membrane for gas separation. *Nano Lett* 2009; 9(12):4019-24.
- [4] Girit CO, Meyer JC, Erni R, Rossell MD, Kisielowski C, Yang L, et al. Graphene at the edge: stability and dynamics. *Science* 2009; 323:1705-8.
- [5] Meyer JC, Girit CO, Crommie MF, Zettl A. Hydrocarbon lithography on graphene membranes. *Appl Phy Lett* 2008; 92:123110-3.
- [6] Lafyatis DS, Tung J, Foley HC. Poly (furfuryl alcohol)-derived carbon molecular sieves: dependence of adsorptive properties on carbonization temperature, time, and poly (ethylene glycol) additives. *Ind Eng Chem Res* 1991; 30(5):865-73.
- [7] Brown RP. Handbook of polymer testing: physical methods. New York: CRC Press; 1992.
- [8] Kawabata S, editor. The Standardization and Analysis of Hand Evaluation. Osaka: The Textile Machinery Society of Japan; 1980.
- [9] ISO 5979. Rubber or plastics coated fabrics – Determination of flexibility – Flat loop method; 1982.
- [10] ASTM D 1388. Standard test method for stiffness of fabrics. Annual Book of ASTM Standards; 1996.
- [11] Stanmore BR, Brilhac JF, Gilot P. The oxidation of soot: a review of experiments, mechanisms and models. *Carbon* 2001; 38(15):2247-68.
- [12] Jacquot F, Logie V, Brilhac JF, Gilot P. Comparison of soot reactivity in the presence of oxygen or NO<sub>2</sub>. Nanoparticle Congress of ETH; August, 2000; Zurich. August, 2000.
- [13] Chughtai AR, Gotdon SA, Smith DM. Kinetics of the hexane soot reaction with NO<sub>2</sub>/N<sub>2</sub>O<sub>2</sub> at low concentration. *Carbon* 1994; 32:405-16.
- [14] Chughtai AR, Welch WF, Akhter MS, Smith DM. A spectroscopic study of gaseous products of soot- oxides of nitrogen.water reactions. *Appl Spectrosc* 1990; 44:294-8.
- [15] Tin PS, Chung T-S, Kawi S, Guiver MD. Novel approaches to fabricate carbon molecular sieve membranes based on chemical modified and solvent treated polyimides. *Micropor Mesopor Mater* 2004; 73:151-60.



- [16] Suda H, Haraya K. Gas permeation through micropores of carbon molecular sieve membranes derived from Kapton polyimide. *J Phys Chem B* 1997; 101(20):3988-94.
- [17] Jones CW, Koros WJ. Carbon molecular sieve gas separation membranes-II. Regeneration following organic exposure. *Carbon* 1994; 32(8):1427-32.
- [18] Koros WJ, Jones CW, inventors; Composite carbon fluid separation membranes patent US 5288304. 1993.
- [19] Jones CW, Koros WJ. Carbon composite membranes: A solution to adverse humidity effects. *Ind Eng Chem Res* 1995; 34:164-7.
- [20] Morgenroth F, Reuther E, Müller K. *Angew Chem, Int Ed Eng* 1997; 36.
- [21] Zhang H, Grim PCM, Vosch T, Wiesler U-M, Berresheim AJ, Müller KM, et al. Discrimination of dendrimer aggregates on mica based on adhesion force: a pulsed force mode atomic force microscopy study. *Langmuir* 2000; 16:9294-8.
- [22] Walker KL, Kahr MS, Wilkins CL, Xu Z, Moore JS. Analysis of hydrocarbon dendrimers by laser desorption time-of-flight and fourier transform mass spectrometry. *J Am Soc Mass Spectrom* 1994; 5:731-9.
- [23] Miller TM, Neenan TX, Zayas R, Bair HE. Synthesis and characterization of a series of monodisperse, 1,3,5-phenylene-based hydrocarbon dendrimers including C<sub>27</sub>H<sub>18</sub> and their fluorinated analogues. *J Am Chem Soc* 1992; 114:1018-25.

# APPENDIX A

## MANUFACTURE OF LAB-SCALE HOLLOW FIBER MODULES [1, 2]

### A.1 INTRODUCTION

Prior to permeation testing, hollow fiber modules are prepared. The module serves as the interface between the permeation system (gas cylinder, tubing, valves, etc.) and the CMS or polymeric membrane. This appendix consists of lists of the parts and procedures to construct a double-ended hollow-fiber module for laboratory-scale experiments. This design has been used in a number of prior studies and is reported in work by Djoekita [3].

### A.2 PARTS

The main parts required to make a hollow fiber module are listed in Table A.1.

Table A.1: Parts required for manufacture of double-ended lab scale hollow fiber module.

Name	Manufacture	Materials
Ferrules	Swagelok	Brass or Stainless Steel
Nut	Swagelok	Brass or Stainless Steel
Female Adapter	Swagelok	Brass or Stainless Steel
Male Adapter	Swagelok	Brass or Stainless Steel
Tee	Swagelok	Brass or Stainless Steel
Metal Tubing	Swagelok	Brass or Stainless Steel
Cap	Swagelok	Brass or Stainless Steel
Plug	Swagelok	Brass or Stainless Steel
ID Tag		
Tygon Tubing	Fisher	
“5 Minute” Epoxy	GC Electronics or Devcon	

### **A.3 PROCEDURE**

A “blank” module is first prepared then fibers are put into the module and the ends sealed with Teflon tape and epoxy. Finally, the module is prepared to be put into the permeation testing system.

#### **Step 1: The “blank” module (Figure A.1)**

- a. Stainless Steel (S.S.) parts.
  - i) Cut a 2~ 12 cm piece of 1/4” S.S. tubing.
  - ii) Bore out the ends with a 1/4” countersink tool used as the bit in a drill press.
  - iii) Test the ends for burrs with a Q-tip.
  - iv) Add a S.S. nut, ferrule and tee (either S.S or Brass) to each end.
- b. Brass Parts
  - i) Attach a Brass nut and ferrule to a Brass female 1/4” NPT adapter.
  - ii) Attach the S.S. tee from step 1a (iv) to the Brass nut on the female adapter.
  - iii) Repeat steps (i) and (ii) for the other end of the module. Both ends should be identical.
- c. Attach an ID tag to the middle of the tubing and a weighting paper hold into cone-shaped to the end of the tubing.

#### **Step 2: Adding the hollow fibers**

- d. Prepare nominally 1 (for CMS) or 25 (polymer) hollow fibers.
- e. Tie a 2-ft. long string to the end of the fibers.
- f. Slide the string through the Blank Module, pulling the fibers through as well.

This part needs to be done carefully and slowly as the fibers can break easily.
- g. Remove the string from fibers.
- h. Tape the other, non-tied, end of the fibers together with Scotch tape so that they can easily be threaded through 1/4” tubing.

- i. Slide the fibers so that equal length sections extend from each end of the module.

### **Step 3: Sealing the module**

- j. Pack a Teflon tape “worm” into one of the Female Adapters and around the fibers. Be careful not to crush the fibers, and assure a good seal between the fibers and the brass wall of the female adapter. (A “worm” is a 5-cm long roll made up of ~16 layers of Teflon tape.)
- k. Put a 1-cm piece of 3/16” Tygon Tubing onto a Brass Male ¼” NPT Adapter. (Figure A.1(c)).
- l. Add a 1:1 ratio of the GC electronics or Stycast brand epoxy Hardener and Resin into a disposable container. Mix for 30 seconds.
- m. Pour the epoxy into the Brass Female Adapter, filling it slightly beyond the top.
- n. Slide the fibers through the piece from step 3l. Screw the Male Adapter into the Female Adapter until the epoxy fills the Tygon tubing piece.
- o. Wait ~10 minutes, then flip the module and repeat steps 3a-e for the other end of the module.

### **Step 4: Prepare the Module for Permeation Tests**

- p. Once the epoxy has fully cured (30 minutes after mixing for the GC Electronics ‘5 minute’ epoxy), break off the Tygon tubing piece by tapping it on the countertop. The fibers should be all open, with an encapsulating seal of epoxy around them.
- q. Put a Brass nut and ferrule on the Male Adapter on each end of the module.
- r. Put a Plug into one end of the module, and a Cap on the nearest Tee fitting, and a Port connector on the furthest Tee fitting.

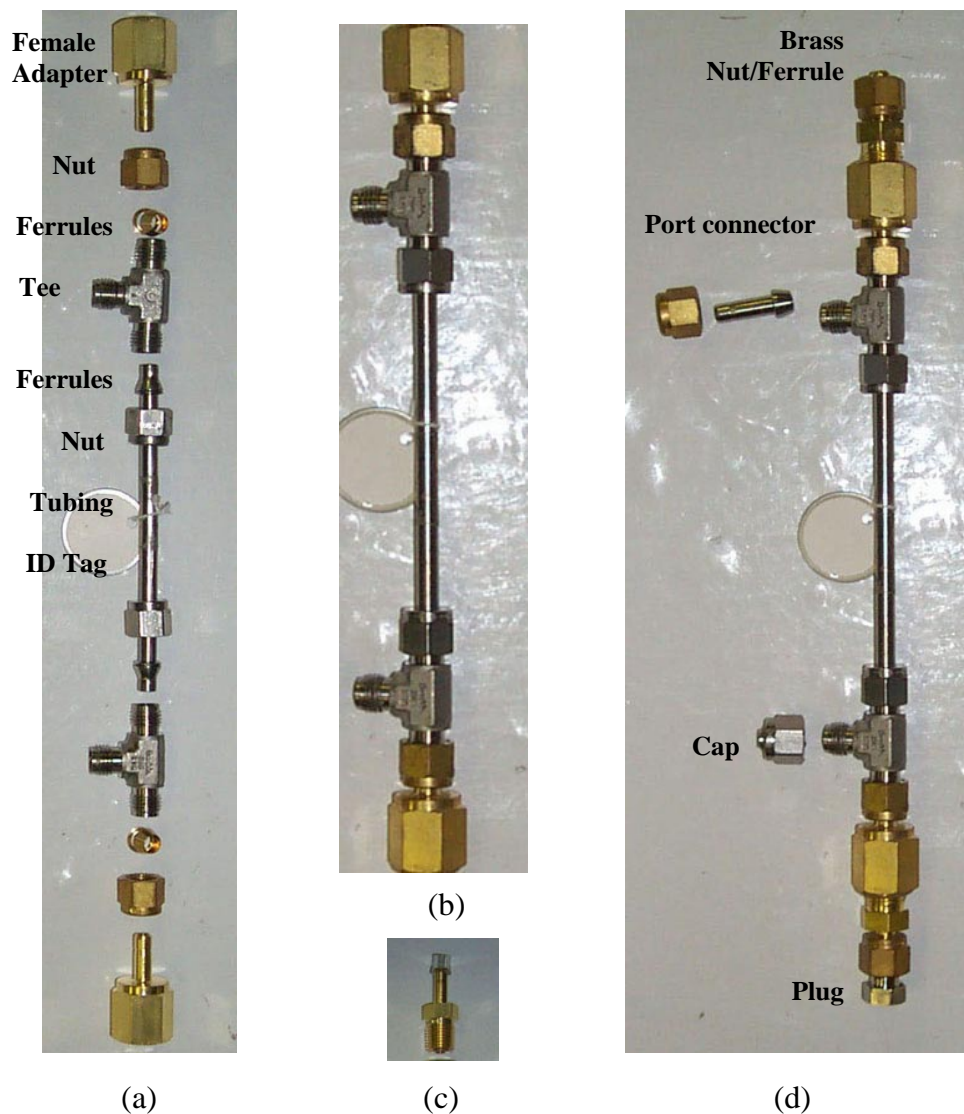


Figure A.1: Picture of fiber modules in production: (a) Parts for a “blank” module, (b) the “blank” module, (c) a brass male adapter with Tygon tubing piece, and (d) the final module for permeation tests.

#### A.4 REFERENCES

- [1] Curruthers SB. Integral skin formation in hollow fiber membranes for gas separations. Austin, TX USA, University of Texas at Austin, PhD thesis, 2001.
- [2] Wallace DW. Crosslinked hollow fiber membranes for natural gas purification and thier manufacture from novel polymers. Austin TX USA, University of Texas at Austin, 2004.
- [3] Djoekita G, Vu DQ, Koros WJ. Pervaporative introduction of organic vapors into high-pressure gas feeds. J Appl Polym Sci 2001; 80(2):311-5.